SYNTHESIS AND CHARACTERIZATION OF SOME LOW AND NEGATIVE THERMAL EXPANSION MATERIALS

A Dissertation
Presented to
The Academic Faculty

by

Tamás Varga

In Partial Fulfillment
of the Requirements for the Degree
Doctor of Philosophy in Chemistry

Georgia Institute of Technology

May 2005

SYNTHESIS AND CHARACTERIZATION OF SOME LOW AND NEGATIVE THERMAL EXPANSION MATERIALS

Approved by:

Dr. Angus P. Wilkinson, Chairman
School of Chemistry and Biochemistry
Georgia Institute of Technology

Dr. L. Andrew Lyon
School of Chemistry and Biochemistry
Georgia Institute of Technology

Dr. Jiří Janata
School of Chemistry and Biochemistry
Georgia Institute of Technology

Dr. Meilin Liu
School of Materials Science & Engineering
Georgia Institute of Technology

Dr. Z. John Zhang
School of Chemistry and Biochemistry
Georgia Institute of Technology

Date Approved: April 14, 2005

To

my parents

and

my wife Szilvia

ACKNOWLEDGEMENTS

First of all, I would like to thank my advisor Dr. Angus P. Wilkinson who made this work possible. His continuous support, thoughtful guidance and understanding helped me to learn a lot and made my time at Georgia Tech very beneficial to me. I also would like to express my thanks to my thesis committee members, professors Dr. Jiří Janata, Dr. Z. John Zhang, Dr. L. Andrew Lyon and Dr. Meilin Liu, for kindly sharing their time and providing comments and feedbacks that helped to make this thesis better.

I thank to the School of Polymer, Textile and Fiber Engineering at Georgia Tech for making the measurements at the Thermal Analysis Center possible. I also thank to Dr. Michael Haluska and Dr. Iuliana Cernatescu for their assistance with x-ray powder diffraction data collection using their instrument. Another thank you goes to Dr. Johannes Leisen for his assistance with some solid state ^{31}P-NMR experiments that did not make it into this thesis, but I found them a great learning experience.

I would also like to thank to the past and present members of the Wilkinson Group whom I worked with for their assistance, help and the friendly atmosphere they provided. I especially thank Dr. Cora Lind for getting me started in the lab and for all her contributions to this work as a collaborator. I also thank Dr. Andrew C. Jupe for his collaboration in the collection and analysis of x-ray absorption spectroscopy data as well as for answering my questions. Thanks are also extended to Kathy White for providing a sample and data for the pyrosphosphate work, Mehmet Cetinkol for assistance with sample preparation for the work on $A_2M_3O_{12}$-type structures and Michael M. Morant for his contribution to Chapter 6. Support from Dr. Hakan Arslan and Mehmet Kutukcu is also appreciated.

This work would not have been possible without the contribution of several other collaborators, including Dr. Ross J. Angel at Virginia Tech, Dr. William A. Bassett at Cornell University and Dr. Chang-Sheng Zha at the Cornell High Energy Synchrotron Source.

This work has benefited from the use of many research facilities in the country. Experiments were carried out at the High Temperature Materials Laboratory, which is sponsored by the Office of Transportation Technologies, U.S. Department of Energy. I would like to thank to Dr. E. Andrew Payzant for his help with x-ray diffraction data collection and providing information for the data analysis.

Part of the neutron diffraction studies were performed at the National Center for Neutron Research and the National Institute of Standards and Technology (NIST). I acknowledge the support of NIST, U.S. Department of Commerce for providing the neutron facility used in this work and thank Dr. Brian H. Toby for his assistance with the data collection.

Most of the synchrotron x-ray diffraction work discussed in this thesis was carried out at the Cornell High Energy Synchrotron Source (CHESS), Cornell University, which is supported by the National Science Foundation and the National Institutes of Health/National Institute of General Medical Sciences under award DMR-0225180. I am grateful to the staff of CHESS, particularly Dr. Ken D. Finkelstein and Dr. Tony Lloyd.

I acknowledge the High Pressure Lab in the Mineral Physics Institute of the State University of New York at Stony Brook for providing access to their high-pressure apparatus and technical support. The help from Dr. Baosheng Li and Dr. Wei Liu in the syntheses of the amorphous samples is greatly appreciated.

Part of the synchrotron experiments were carried out at the National Synchrotron Light Source, Brookhaven National Laboratory, which is supported by the U.S. Department of Energy, Division of Materials Sciences and Division of Chemical Sciences, under Contract No. DE-AC02-98CH10886. Help from the staff of beamlines X14A and X11A is acknowledged. In particular, I thank Dr. Jianming Bai (University of Tennessee) and Dr. Scott Speakman (Oak Ridge National Laboratory) for assistance with the x-ray diffraction data collection at X14A and Dr. Bruce Ravel (Argonne National Laboratory) for his help with our x-ray absorption spectroscopy experiments at X11A.

Neutron diffraction studies were also carried out at the Intense Pulsed Neutron Source in Argonne National Laboratory, which is funded by the U.S. Department of Energy, BES-Materials Science under contract W-31-109-ENG-38. I thank Simine Short for her assistance with the neutron data collection.

Funding for this work was provided by the National Science Foundation under grant DMR-0203342. Partial support from the College of Sciences/Georgia Tech Research Corporation for my attendance at the 2004 Gordon Research Conferences' Solid State Chemistry I. section is also acknowledged.

Last, but certainly not least, many thanks to my family and my close friends for their support and encouragement.

TABLE OF CONTENTS

LIST OF TABLES

LIST OF FIGURES

SUMMARY

The research presented in this thesis focuses on the synthesis, characterization of several low and negative thermal expansion materials and the study of their high-pressure behavior as well as thermal expansion properties. The results of this work contribute to the understanding of the structure-property relationships in materials exhibiting negative thermal expansion, such as the mechanism of some pressure-induced phase transformations. It also explores possibilities to control the thermal expansion properties in some low thermal expansion phases. Finally, the present thesis contributes to the knowledge of the high-pressure research community through some challenging experimental work and a study of hydrostaticity of some widely used pressure media.

In **Chapter 3**, pressure-induced phase transitions in materials of the $Sc_2W_3O_{12}$ family are discussed based on *in-situ* high-pressure diffraction studies. An unusual "bulk modulus collapse" phase transition is seen in the compounds studied. The mechanism for volume contraction on compression is different from the mechanism for volume negative thermal expansion, and the degree of anisotropy is also different on compression then on heating. Some trends in the high-pressure behavior with the properties of the octahedral 3+ cation are also discussed.

Chapter 4 is an *in-situ* high-pressure combined x-ray diffraction and spectroscopy study of the mechanism of the pressure-induced amorphization (PIA) in cubic ZrW_2O_8 and cubic $ZrMo_2O_8$ through following the changes in the local metal coordination environments on compression. The validity of some proposed mechanisms for the amorphization are examined and the differencies between the two compounds are

discussed. The driving force for the PIA seems to be either a kinetically hindered phase transformation to a high-pressure crystalline phase or a kinetically frustrated decomposition, or the combination of the two. To the best of our knowledge, this is the first report of a combined *in-situ* x-ray diffraction and *in-situ* x-ray absorption spectroscopic study under high pressure.

Chapter 5 complements the results of Chapter 4 with a study of the pressure-induced amorphization in cubic ZrW_2O_8 and cubic $ZrMo_2O_8$ ex-situ through the examination of the local coordination environments in samples that had been previously amorphized and the recovered to ambient conditions.

The possibility of stabilizing the low thermal expansion high-temperature structure in AM_2O_7 compounds to lower temperatures through a combination of cation insertion and substitution is explored in **Chapter 6**. Chemical modification through the method studied is not successful in stabilizing the high-temperature structure to around room temperature.

In **Chapter 7**, we attempt to control the thermal expansion properties in materials of the $(M^{III}_{0.5}M^{V}_{0.5})P_2O_7$ type through the choice of the M^{III} and M^{V} cations as well as through manipulating the ordering of the cations by different heat treatment conditions. Although controlled heat treatment conditions resulted in only short-range cation ordering, the choice of the M^{III} cation has an interesting effect on the thermal expansion behavior of the materials studied.

Finally, in **Chapter 8** we examine the useful (hydrostatic) pressure range of different grades of fluorinert as pressure-transmitting media. All of the fluorinerts studied became nonhydrostatic at relatively low pressures (~1 GPa).

CHAPTER 1

INTRODUCTION

1.1 Thermal expansion

The thermal expansion behavior of solid materials is important in many industrial processes and other practical applications. Good control of thermal expansion can be crucial in precision positioning of, for instance, optical device parts and matching the thermal expansion of components that are bonded together. Thermal expansion is also closely related to the thermal shock resistance of materials. Materials with a high CTE show poor thermal shock resistance, as rapid heating or cooling can result in temperature gradients that will cause cracks. Due to their intrinsic nature, expansion coefficients will usually be different for any pair of materials. While differences in thermal expansion can sometimes be useful (e.g. thermostatic bimetals), different thermal expansion coefficients for two materials sharing an interface are in general a problem, as this can lead to cracks or separation at the interface. Highly anisotropic behavior (e.g. large difference in the expansion along the crystallographic axes) can also result in microcracks in polycrystalline bodies. Low thermal expansion coefficients as well as control of the thermal expansion are therefore desirable.

Thermal expansion of solids is a physical property that depends on the nature of the interatomic potential. As two atoms are brought together, attractive forces dominate the overall potential energy of the system until their distance becomes too short and bonding

electrons cannot overcome the short-range repulsions. At this point, the potential energy increases. The interatomic potential function of a simple harmonic oscillator is shown in Figure 1.1. The attractive interactions lead to a decrease in the potential energy as the two atoms come close together and bond formation begins. The repulsive interaction of the electrons is reflected on the left side of the curve from the minimum and rising with decreasing interatomic distance. If the temperature of this system is increased from T_1 to T_2, there is no change in the average bond distance, R (indicated by the arrows) and thus no expansion is observed.

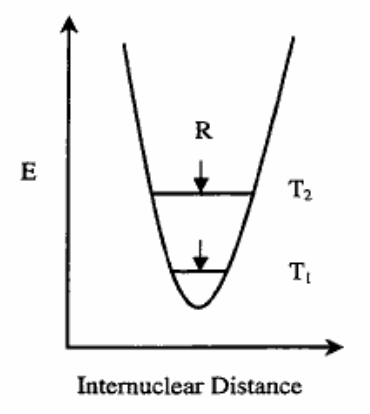

Figure 1.1: Potential energy diagram of a harmonic oscillator

However, in reality atoms vibrate in an anharmonic fashion. This anharmonicity is due to an asymmetric potential energy well. The variation of the potential function with interatomic separation for an anharmonic oscillator is represented in Figure 1.2. At one particular temperature T_1, the intersection of the horizontal line with the curve marks the extreme values of the internuclear distance where oscillation energy is all potential energy. The midpoint of the line marks the average value. As the temperature is increased to T_2, the average bond length shifts to larger distances due to the asymmetry of the potential well. This increase in the average bond length contributes to the thermal

expansion. The extent of the asymmetry is dependent on the bond strength in the region that is thermally sampled. A stronger bond results in a more symmetric potential well. This means a smaller bond expansion on thermal excitation for the stronger bond.

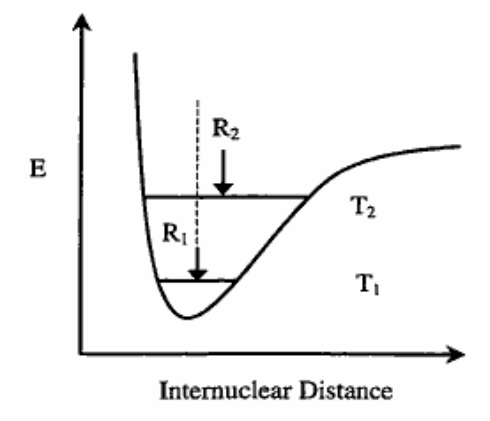

Figure 1.2: Potential energy diagram for an anharmonic oscillator

In order to quantitatively measure and compare the extent of thermal expansion in solids, the thermal expansion coefficient can be calculated. This describes the dimensional change that occurs with a change in temperature at constant pressure. The linear coefficient of thermal expansion (CTE) α is defined as:

$$\alpha = \frac{d(\ln L)}{dT} = \frac{L - L_0}{L_0 (T - T_0)}, \tag{1}$$

where L_0 and L are the values of the lattice constant at temperatures T_0 and T, respectively. In non-cubic materials, different values of α are usually observed for the different lattice constants. The volume coefficient of thermal expansion α_V is defined as:

$$\alpha_V = \frac{d(\ln V)}{dT} = \frac{1}{V_T}\frac{dV_T}{dT}, \tag{2}$$

where V is the volume and T the temperature. α_V can be approximated as the sum of the α's of the different lattice parameters:

$$\alpha_V \cong \alpha_a + \alpha_b + \alpha_c \quad (3)$$

This above summation can be confirmed by the following derivation. Let a_T, b_T and c_T represent lattice parameters at temperature T and a_0, b_0 and c_0 represent initial lattice parameters. If α, β and γ are the different thermal expansion coefficients associated with lengths a, b and c, then:

$$a_T = a_0 (1 + \alpha T)$$

$$b_T = b_0 (1 + \beta T)$$

$$c_T = c_0 (1 + \gamma T)$$

The volume at temperature T is defined by:

$$V_T = a_T \text{ x } b_T \text{ x } c_T = a_0 \text{ x } b_0 \text{ x } c_0 (1 + \alpha T) (1 + \beta T) (1 + \gamma T) =$$

$$= V_0(1 + \alpha T) (1 + \gamma T + \beta T + \beta\gamma T^2) =$$

$$= V_0(1 + \gamma T + \beta T + \beta\gamma T^2 + \alpha T + \alpha\gamma T^2 + \alpha\beta T^2 + \alpha\beta\gamma T^3) =$$

$$= V_0[1 + T(\gamma + \beta + \alpha) + T^2(\beta\gamma + \alpha\gamma + \alpha\beta) + T^3(\alpha\beta\gamma)]$$

Differentiating this expression gives:

$$\frac{1}{V_0}\frac{dV_T}{dT} = (\alpha + \beta + \gamma) + 2T(\beta\gamma + \alpha\gamma + \alpha\beta) + 3T^2(\alpha\beta\gamma)$$

As the last two terms are generally considered negligible, the volume coefficient of thermal expansion can be approximated by the sum of the thermal expansion coefficients of each cell dimension.

Thermal expansion is related to the anharmonicity of lattice vibrations as was illustrated by Figure 1.2. In the quasiharmonic approximation, which takes thermal expansion related to atomic vibrations into consideration, the contribution of each lattice vibration mode (phonon mode) of energy E to the thermal expansion is $\frac{1}{KV}\Gamma_i C_{Vi}$, where

K is the bulk modulus, V is the unit cell volume, Γ_i is the mode Grüneisen parameter and C_{Vi} is the contribution of the phonon mode of energy E to the specific heat.[1] This relationship is reflected in the Grüneisen equation for the volume coefficient of thermal expansion:

$$\alpha_V(T) = \frac{\Gamma B C_V(T)}{V_0}, \tag{4}$$

where B is the isothermal compressibility and V_0 is the molar volume at T = 0 K.[2] The Grüneisen parameter is defined as the volume dependence of mode frequencies according to:

$$\Gamma_i = -\frac{d ln\omega_i}{d \ln V}, \tag{5}$$

where ω_i is the frequency of the ith mode and V is the volume.[3] The molar specific heat at constant volume can be defined as the sum of the contributions of all the vibration modes:

$$C_V = \frac{1}{Z}\Sigma\, p_i C_i, \tag{6}$$

where Z is the number of formula units per unit cell, p_i is the number of phonons of frequency ω_i and C_i is the specific heat contribution from a single mode of frequency ω_i.[3] The contribution of each phonon mode to the thermal expansion is proportional to the positive specific heat via the Grüneisen parameter as shown in equations 4-6. Each mode has an independent Grüneisen coefficient. As the compressibility and the volume will always have positive values, the signs and magnitude of the Grüneisen parameters and thus the contribution of the associated vibrational modes to the overall expansion will determine the actual thermal expansion displayed by the material. Equation (4) also

illustrates that the expansion coefficient is not a constant, but can vary with temperature. As this variation is usually small, it is common to use average values of α for the temperature range over which the measurements were carried out.

Materials can be arbitrarily classified into three groups based on their thermal expansion:[2]

High Expansion Group: $\alpha > 8 \times 10^{-6} K^{-1}$

Intermediate Group: $2 < \alpha < 8 \times 10^{-6} K^{-1}$

Low Expansion Group: $\alpha < 2 \times 10^{-6} K^{-1}$

From the perspective of the problems related to thermal expansion and in the context of the research described in the present thesis, the last group is the most interesting. Several families of low thermal expansion materials have been known for over 60 years. The earliest materials were based on the metal alloy Invar ($Fe_{65}Ni_{35}$), the oxides cordierite ($Mg_2Al_4Si_5O_{18}$) and zircon ($ZrSiO_4$) as well as silica glass (SiO_2).[2] Later, in 1948, low expansion materials β-spodumene ($LiAlSi_2O_6$) and β-eucryptite ($LiAlSiO_4$) among the lithium aluminum silicates were discovered.[4, 5] With the discovery of the NZP family ($NaZr_2P_3O_{12}$, where Na and Zr sites can be substituted in a variety of ways) in the early 1980's, which provided a new class of well controllable low α materials, interest in low thermal expansion materials became even greater.[6] In Table 1.1, some important low expansion materials as well as their coefficient of thermal expansion (CTE) are listed.

The low thermal expansion exhibited by the above materials can be attributed to different structural characteristics. In the next several paragraphs a brief discussion is given of the structural features responsible for their unusual thermal expansion behavior.

Cordierite, $Mg_2Al_4Si_5O_{18}$, is a low expansion silicate that has the beryl structure consisting of a flexible framework of rigid SiO_4 and one AlO_4 corner sharing tetrahedra, which are connected by additional AlO_4 tetrahedra and MgO_6 octahedra. It has been shown that it is the expansion of the Mg-O bonds in combination with the stiffness of the Si-O and Al-O bonds that leads to the contraction along the c axis, as the increase in Mg-O bond distance pulls the sheets closer together (see also section 1.2.6).[7] Its thermal expansion can be affected by substitution of other metals (e.g. Fe, Mn, Ga, Ge and Ca) into the structure.[8, 9]

Table 1.1: Coefficient of thermal expansion of some low CTE materials[2]

Material	Average CTE ($^oC^{-1}$ x 10^6)	Temperature range (^oC)
Beryl, $Be_3Al_2Si_6O_{18}$	2.0	25-1000
Cordierite, $Mg_2Al_4Si_5O_{18}$	1.4	25-800
PMN, $Pb(Mg_{1/3}Nb_{1/3})O_3$	1.0	-100-100
β-Spodumene, $Li_2O{\cdot}Al_2O_3{\cdot}4SiO_2$	0.9	25-1000
$Ca_{0.75}Sr_{0.25}Zr_4P_6O_{24}$ (NZP)	0.6	25-1000
SiO_2 glass	0.5	25-1000
Zerodur	0.12	20-600
$SiO_2{\cdot}TiO_2$ glasses	0.05-(-0.03)	25-800
Invar	0.01	5-30
NZP, $NaZr_2P_3O_{12}$	-0.4	25-1000
β-Eucryptite, $Li_2O{\cdot}Al_2O_3{\cdot}2SiO_2$	-6.2	25-1000

In ferroelectric relaxor materials of the perovskite structure, e.g. $Pb(Mg_{1/3}Nb_{2/3})O_3$ (PMN),[10] in analogy to the magnetostriction observed in Invar and related materials, a mechanistically equivalent electrostrictive contribution is responsible for the expansion behavior. Perovskite ferroelectrics show a paraelectric-ferroelectric phase transition

brought about by the displacement of the octahedral B cation in the ABO_3 general formula. Above their Curie temperature they are paraelectric, but at lower temperatures they become ferroelectric as the B cation is displaced from the center of the octahedron causing polarization. Due to a mixture of two or more cations on the same lattice site in PNM-type compounds, microcompositional inhomogeneities are present resulting in different Curie temperatures for different microregions and thus in a mixture of paraelectric and ferroelectric phases. The phase coexistence in the ferroelectric-paraelectric transition region results in an electrostrictive contribution to the thermal expansion making it very low.[11]

The expansion coefficient of $Na_{1+x}Zr_2P_{3-x}Si_xO_{12}$ (NASICON) changes from strongly positive to slightly negative with decreasing x. This phenomenon reported by Boilot[6] led to the discovery of the family of low expansion materials with $NaZr_2P_3O_{12}$ (NZP) and $CaTi_4P_6O_{24}$ (CTP) as the parent compounds. Their framework is composed of corner-sharing ZrO_6 octahedra and PO_4 tetrahedra, which form tube-like structures. The sodium ions occupy six-coordinated sites in the channels that result in face sharing of ZrO_6 and NaO_6 octahedra. Similarly to silicates, the polyhedra are rigid (both the Zr-O and the P-O bonds are strong), so that their expansion can be neglected over a large temperature range. As the Na-O bonds expand with increasing temperature, the tubes are stretched along the c axis but pulled together perpendicular to the c axis. This leads to an expansion along c and contraction along a and b. Na, Zr and P can be substituted by a variety of cations, which offers the possibility of tailoring the thermal expansion coefficients.[2]

$CaZr_4P_6O_{24}$ (CZP) and $SrZr_4P_6O_{24}$ (SZP) show reverse anisotropy.[12] While CZP contracts along *a* and *b* and expands along *c*, SZP shows the opposite behavior with

contraction along c and expansion along *a* and *b*. A 1:1 solid solution of the two materials could be synthesized that showed close to zero thermal expansion both along the *a*/*b*- and *c*-axes. Lattice dynamical calculations have shown that the behavior of all alkaline earth zirconium phosphates can be explained by polyhedral distortions resulting from coupled rotations of rigid PO_4 and ZrO_6 polyhedra.[13]

The common structural feature of silicates and the different crystalline and amorphous polymorphs of silica are the SiO_4 tetrahedra. The thermal expansion behavior depends strongly on these rigidly bonded SiO_4 tetrahedra that are connected through corner sharing and form a flexible and open framework. α-Quartz, for example, shows highly anisotropic and positive volume expansion at all temperatures, while β-quartz has near-zero or even negative expansion coefficients.[14, 15] Transverse vibrational motions of the oxygen atoms in the open framework structure shorten the Si-Si distances, counteracting the small expansion of the strong Si-O bonds.[16]

The expansion coefficient of vitreous silica can be modified by the addition of other oxides to the glass. TiO_2 lowers the CTE, resulting in strong negative expansion at low temperatures and near zero expansion at room temperature. This is the basis of Corning Glass Works' Ultra Low Expansion (U.L.E.) titanium silicate, which is applied in optical mirror substrates.[17] Zerodur, a glass-ceramic composite produced by Schott, consists of ~30 % glassy phase of SiO_2 and $AlPO_4$, which exhibits low thermal expansion, and ~70 % crystalline doped lithium aluminum silicate with a negative CTE.[18]

In Invar, which is an iron-nickel alloy with an approximate composition of $Fe_{65}Ni_{35}$ discovered in 1897,[19] and other related materials, the anomalously low thermal expansion seen at temperatures below their Curie temperature has been attributed to a

magnetostrictive component in their expansion behavior. Due to compositional inhomogeneities on the micro-scale, thermal energy is absorbed in a transition process from the ferromagnetic state to a disordered non-collinear configuration that results in a magnetostrictive contraction, which counteracts the "normal" positive thermal expansion.[20, 21]

The discovery of the lithia alumina silica (LAS) system was a milestone in the history of low thermal expansion materials. First, ultra-low thermal expansion was observed in β-spodumene ($LiAlSi_2O_6$),[4] and later, it was reported that β-eucryptite ($LiAlSiO_4$) and solid solutions of the two compounds showed negative thermal expansion.[5] The expansion behavior of β-spodumene and β-eucryptite is a direct consequence of their crystal structures. β-spodumene has a three-dimensional aluminosilicate framework of corner sharing tetrahedra. The distribution of silicon and aluminum in the tetrahedra is random. The tetrahedra form five-membered rings that are connected by common tetrahedra. The lithium cations occupy the channels of the zeolite-like structure. The expansion behavior of β-spodumene can be explained by the strain present in the five-membered rings. Thermal energy results in an increase of the Li-O distances and thereby in a puckering of the tetrahedra in the rings, which relieves the strain. This leads to expansion of the c-axis and contraction of the a and b axes due to reorientations of the tetrahedra.[22]

The volume negative thermal expansion of β-eucryptite results from the spiral arrangement of its tetrahedral network. When the material is heated, the spirals are subject to a torsional stress due to the larger expansion of the Li-O bonds as compared to the Si-O and Al-O bonds. Contraction relieves the torsional stress. Another ways of

viewing this phenomenon are that the contraction is 1) due to a positive expansion of layers in the structure leading to contraction in other directions as in cordierite[7] or 2) a dynamic disordering of the lithium cations, which change sites between tetrahedral and octahedral coordination.[7, 22]

1.2 Negative thermal expansion

Materials that display negative thermal expansion (NTE) are being investigated both because of technological interest and scientific curiosity. The technological interest arises from their potential applicability in composites, which may facilitate control of thermal expansion and allow the design of materials with specific expansion coefficients. Matching the thermal expansion of another device part can be important to avoid cracks or separation at interfaces between two materials, and zero expansion is needed when exact positioning of electronic or optical components in a device is crucial. NTE materials have, therefore, received considerable attention during the last years.[7, 23-28]

The phenomenon that matter (gas, liquid or solid) expands when it is heated is considered common knowledge. It used to be taught in school as an empirical law of nature. However, it was found to be pseudo-knowledge when the first crystalline materials exhibiting negative thermal expansion (NTE) were discovered. The simple energy diagram in section 1.1 (see Figure 1.2), which provides a common view of thermal expansion as being positive, does not explain how some materials contract on heating. This highlights the nature of thermal expansion as being not so much a basic physical quantity as a material property. Other factors must be considered when trying to understand how negative expansion can occur.

As we have seen through the examples of low thermal expansion materials in section 1.1, there are some general structural features that can be associated with compounds exhibiting low and negative thermal expansion, which include 1) strongly bonded polyhedra linked in three dimensions, 2) open, flexible structure, and 3) ferromagnetic or ferroelectric microdomains.[2] Thus the linkages and rotations of the polyhedral network should also be examined when trying to understand bulk thermal expansion. An open, flexible framework of rigid corner sharing polyhedra is likely to accommodate transverse vibrational modes of the oxygen atoms, which can lead to a significant negative contribution to the thermal expansion if the Grüneisen parameters are large enough. It has been stated earlier that the signs and magnitude of the Grüneisen parameters and thus the contribution of the associated vibrational modes to the overall expansion will determine the actual thermal expansion of the material. It has been shown for several NTE materials including cubic ZrW_2O_8, HfW_2O_8 and $ZrMo_2O_8$ that the NTE behavior is driven by low-frequency vibrational modes that are associated with large negative Grüneisen parameters.[29-31] Also, dimensional changes induced by thermal energy can be somewhat compensated if a ferroic microdomain distribution tends to change with temperature.

The "thermal anomaly of water" is probably the earliest observation of negative thermal expansion.[32] Water has its highest density at 4 °C and therefore displays NTE between 0 and 4 °C. The first time that a solid was shown to contract on heating was in 1907, during experiments on quartz, silica glass and some metals by Scheel. His measurements in liquid air and up to 100 °C revealed that both crystalline and glassy quartz have negative expansion coefficients at low temperatures.[33]

There are several materials that show NTE at low temperatures (e.g. Invar, SiO_2 glass) or over a narrow temperature range (e.g. water, Cu_2O, ferroelectric materials around their phase transition). Some materials display anisotropic expansion behavior, they contract along one or two axes and expand along the other axes, which can give rise to both small positive and small negative volume expansion (e.g. NZP and Li-Al silicates). Most of these compounds have been discussed in section 1.1.

Most of the research related to NTE materials have focused on materials that fall into the following five network types: the AM_2O_7 family,[34-37] the AM_2O_8 family[38-41], the $A_2M_3O_{12}$ family,[42-45] AO_2 networks or framework silicates and aluminophosphates (zeolites)[46-50] and AMO_5[51, 52] networks. It should be noted that some MO_3 network structures, which also consist of rigid, corner-sharing metal-oxygen octahedra, show very low thermal expansion especially relative to typical metal oxides. These materials have the cubic ReO_3 structure[53] and include NbO_2F and TaO_2F.[54] While NbO_2F shows positive expansion, the value of CTE for TaO_2F is very small, it is of a magnitude comparable to experimental errors, therefore it cannot be stated with certainty if it exhibits NTE or not.[54]

1.2.1 The AM_2O_7 family

In cubic materials with the AM_2O_7 structure, the tetrahedral M cation can be P, V or As and the octahedral A cation can be Si, Ti, Ge, Zr, Nb, Mo, Sn, Hf, W, Re, Pb, Ce, Th, U or Pu.[34] For M = V, only the Zr and Hf,[34] for M = As, only the Zr and Th compounds are known.[55, 56] Many of these compounds crystallize in the cubic space group $Pa\bar{3}$, and, hence, exhibit isotropic thermal expansion. Cubic ZrP_2O_7 and ZrV_2O_7 can be taken as prototypes for the behavior of many of these materials. They exist in a 3 x 3 x 3

superstructure with the same $Pa\bar{3}$ space group at room temperature. This low temperature phase shows normal positive thermal expansion. Many of these materials undergo a phase transition on heating that involves the loss of this complex superstructure. The resulting disordered high temperature structure (see Figure 1.3) exhibits small positive expansion (low or low intermediate range) for most of the phosphates, only the uranium and thorium analogues show NTE in the high temperature phase.[34, 35] The vanadates display strong NTE at high temperatures.[57, 58]

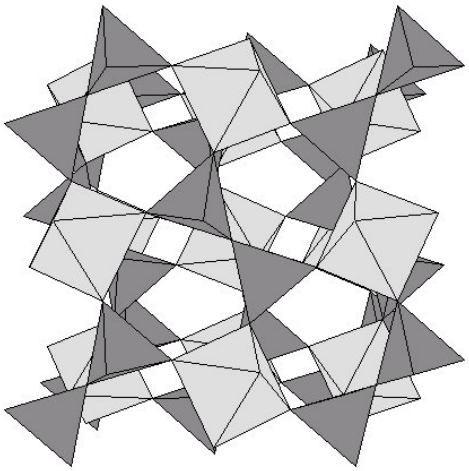

Figure 1.3: High temperature (ideal) crystal structure of ZrP_2O_7 in space group $Pa\bar{3}$. Bright: ZrO_6 octahedra, dark: PO_4 tetrahedra.

The 3 x 3 x 3 superstructure was first reported in GeP_2O_7[59] and a model was first proposed for SiP_2O_7.[60] Since then, it has been studied in many different compounds including ZrP_2O_7,[35] TiP_2O_7,[61, 62], GeP_2O_7,[63] ZrV_2O_7[36, 37, 64] and HfV_2O_7.[65] In the high temperature disordered structure, the pyrophosphate and pyrovanadate groups are constrained by symmetry to have unfavorable 180° P-O-P and V-O-V bond angles. The formation of the superstructure is driven by the tendency to avoid these linear P-O-P and V-O-V units as it allows most of these bonds to bend. The symmetry of the superstructure

as well as the static or dynamic disorder that leads to an average 180° bond angle have been studied by solid state NMR.[61, 63, 66-69] In the case of, for instance ZrP_2O_7[70] and ZrV_2O_7,[37] an intermediate incommensurate structure exists between the low temperature and high temperature forms.

The thermal expansion behavior and control of thermal expansion in these compounds is discussed in detail in section 1.5 and Chapters 6 and 7.

1.2.2 The AM_2O_8 family

The report of negative thermal expansion in cubic ZrW_2O_8 over an extremely wide range (0.3 – 1050 K, see Figure 1.4)[39] generated a large amount of recent research focusing on the properties of different NTE materials and the mechanism behind this unusual behavior. Cubic ZrW_2O_8 (or α-ZrW_2O_8) was first prepared in 1959.[71] It is the only ternary phase that appears in the atmospheric pressure ZrO_2-WO_3 phase diagram.[72, 73] The material has been known to exhibit NTE over a smaller temperature range (50-700 °C) since 1968.[74] However, greater interest arose only after its crystal structure had been fully solved and the wider temperature range for the NTE has been reported.

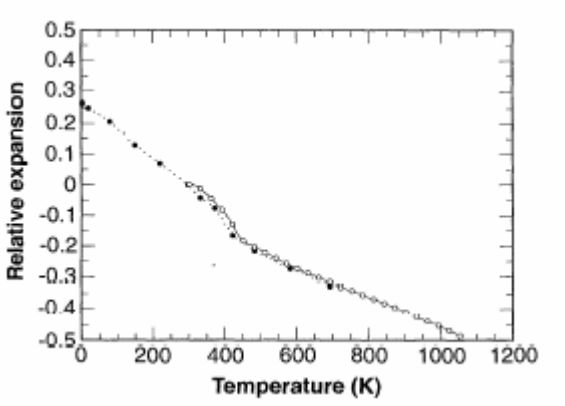

Figure 1.4: Isotropic negative thermal expansion in cubic ZrW_2O_8. Open circles are dilatometer, solid circles are neutron diffraction data. Taken from Mary et al.[39]

The structure of cubic ZrW_2O_8 consists of corner sharing ZrO_6 octahedra and WO_4 tetrahedra (see Figure 1.5). There are two crystallographically distinct WO_4 units. Each ZrO_6 octahedron is surrounded by six WO_4 tetrahedra, while each WO_4 is only connected to three ZrO_6, leaving one terminal oxygen per WO_4 unit. These polyhedra are rather rigid, while the open framework allows for vibrational motions of the bridging oxygens and rocking motions of the polyhedra. The intimate relationship between negative thermal expansion and lattice vibrational modes has been confirmed by Raman spectroscopic studies[3, 31], low temperature specific heat measurements[75] and phonon density of states (DOS) studies by neutron scattering[76, 77] for cubic ZrW_2O_8. It was found from the temperature dependence of the lattice constants that the NTE originates from low-frequency vibrational modes,[29, 78] which is also supported by the phonon DOS measurements. These low-frequency modes are inferred to be rigid, as the polyhedra remain mostly undistorted, and are called rigid unit modes (RUMs) (see section 1.2.6). Cubic ZrW_2O_8 and HfW_2O_8 are isostructural and show very similar thermal expansion behavior.

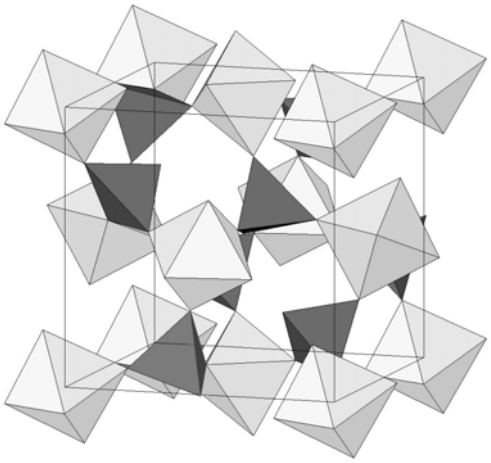

Figure 1.5: Crystal structure of α-ZrW_2O_8. Bright: ZrO_6 octahedra, dark: WO_4 tetrahedra.

Cubic ZrW_2O_8 is only thermodynamically stable at high temperatures, between 1380 and 1530 K. It can be quenched to room temperature and remains metastable up to 1050 K, where it decomposes to ZrO_2 and WO_3.[39] It exhibits isotropic linear negative thermal expansion throughout its metastable temperature range. However, the expansion curve in Figure 1.4 shows a discontinuity around 430 K, which is due to a cubic-to-cubic phase transition (α- to β-ZrW_2O_8). The expansion coefficients are different below and above 430 K ($-8.8 \times 10^{-6}\ K^{-1}$ and $-4.9 \times 10^{-6}\ K^{-1}$, respectively).[38] The ordered acentric α-phase (that crystallizes in space group $P2_13$) becomes a disordered β-phase, which is centrosymmetric and has $Pa\bar{3}$ symmetry. This reversible order-disorder phase transition and the orthorhombic form of ZrW_2O_8 are discussed later.

Zirconium and hafnium molybdates have also been known for some time. Zirconium molybdates and zirconium molybdate hydrates have been studied as catalysts for e.g. oxidation,[79] ion exchangers[80] and fission products in nuclear reactors.[81] However, until

1998, $ZrMo_2O_8$ has been known to exist only in a low temperature monoclinic form with space group C2/c[82, 83] and a trigonal phase with space group $P\bar{3}c$.[82, 84, 85] Neither of these polymorphs exhibits NTE. Cubic $ZrMo_2O_8$ was first prepared by our research group.[40] Like cubic ZrW_2O_8, cubic $ZrMo_2O_8$ displays NTE over almost its entire range of stability. However, unlike cubic ZrW_2O_8 it does not undergo reversible phase transitions at ambient pressure. The molybdate irreversibly transforms to the trigonal polymorph at about 400 ^oC. It adopts the β-ZrW_2O_8 structure below 400 ^oC. Its thermal expansion coefficient is very similar to that of β-ZrW_2O_8 (~5 x 10^{-6} K^{-1} over the 11-573 K range).[40] The lack of any structural phase transition between 0 and about 673 K may be beneficial from the perspective of applications, as there are no associated discontinuities in the thermal expansion coefficient.

1.2.3 The $A_2M_3O_{12}$ family

Another large group of NTE materials are the tungstates and molybdates in the $A_2M_3O_{12}$ family (A = a variety of 3+ ions, M = Mo or W).[42] There are several different structures known for these compounds.[86-89] However, the orthorhombic $Sc_2(WO_4)_3$ structure (space group Pnca) is only found for A = Al, Sc, Cr, Fe, Y, In or the smaller rare earths from Lu to Ho and M = Mo, W. These orthorhombic materials show negative thermal expansion.[25-28, 42-44, 90, 91] $Sc_2W_3O_{12}$ consists of corner-sharing ScO_6 octahedra and WO_4 tetrahedra (see Figure 1.6).[88] Each ScO_6 octahedra is bound to six MO_4 tetrahedra and each MO_4 unit is connected to four ScO_6 units. It displays anisotropic thermal expansion with the *a*- and *c*-axes contracting and the *b*-axis expanding on heating. The contraction can be viewed as arising from a dynamic cooperative tilting of

the quasi-rigid polyhedral units that make up the framework.[43] The cooperative rocking motion of the polyhedra will always result in a slight distortion of the polyhedra. As the M-O bonds are stronger than most A-O bonds, the distortion is expected to be larger in the octahedra. The changes of the expansion behavior with the A cation size are also intimately related to the $Sc_2W_3O_{12}$ structure. The b axis tend to contract when Sc is substituted with an A^{3+} ion of larger size (e.g. Y, Lu, Er, Yb).[44, 91, 92] With an increasing size of the A^{3+} cation, the thermal contraction along the b-axis becomes more negative.[92] The reason is that $A_2M_3O_{12}$ compounds with larger A^{3+} ion size can be more flexible towards rocking motion of the polyhedra. The main force that keeps the polyhedra regular is the repulsive interaction between oxygens.[93] This interaction becomes weaker as the size of the polyhedra increases.

Several members of the $Sc_2(WO_4)_3$ family have been shown to undergo a structure-collapse phase transition to a monoclinic structure on cooling.[86, 87, 89, 94, 95] The monoclinic structure does not show negative volume expansion.[94]

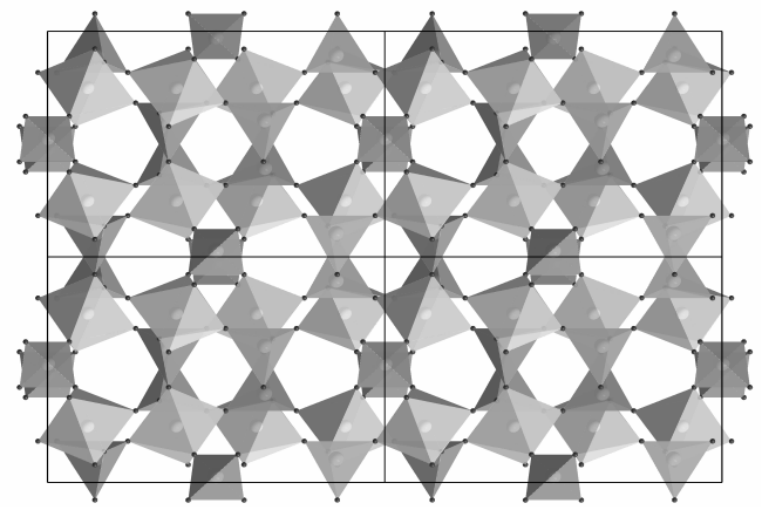

Figure 1.6: Crystal structure of orthorhombic $Sc_2W_3O_{12}$ (space group Pnca) viewed down the *a*-axis. The octahedra are ScO_6 (brighter), the tetrahedra are WO_4 (darker) and the tiny balls are oxygen atoms.

It should be noted that the anisotropic thermal expansion behavior results in different values for the CTE when it is determined by different methods. Dilatometer experiments give systematically more negative values than diffraction, suggesting that there is an intrinsic and an extrinsic contribution to the negative thermal expansion.[45] Due to the anisotropic expansion behavior, microcracks can develop during thermal cycling of the material leading to an extrinsic negative expansion that can change between cycles. This is a hindrance from the applications point of view as the thermal expansion behavior is not necessarily repeatable as temperature is cycled.

1.2.4 The AO_2 family of framework silicates and aluminophosphates

A large number of zeolitic framework silicates and aluminophosphates are known. They consist of corner-sharing, almost rigid SiO_4 tetrahedra or alternating AlO_4 and PO_4 tetrahedra (see Figure 1.7). Their open framework structures consisting of rigid units,

make zeolites good candidate NTE materials. Many materials of this type have been reported to display NTE and theoretical investigations predict NTE for many zeolites as well as SiO_2 and $AlPO_4$ framework materials.[46] Strong negative thermal expansion has been observed in, for example, siliceous faujasite,[47] $AlPO_4$-17,[48] siliceous zeolites ITQ-1, ITQ-3, SSZ-23,[50] as well as chabazite and ITQ-4.[49] Chabazite was found to have one of the most negative CTEs known. Unlike other flexible framework structures (AM_2O_7, AM_2O_8 and $A_2M_3O_{12}$ families), the above zeolitic materials display no obvious changes in average A-O-A or O-A-O bond angles with temperature. Based on this observation, it has been suggested that the vibrational motion of the oxygen atoms in zeolites are harmonic and dynamic, resulting in an overall decrease in A-A distances without time-average bending the A-O-A angles.[48] A recent pair distribution function (PDF) analysis of the structure of chabazite confirmed that it can be modeled as rigid polyhedra that can move in a way that causes the structure to contract.[96]

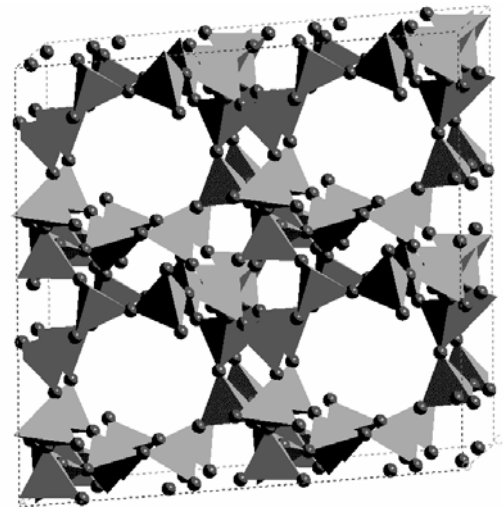

Figure 1.7: The open framework structure of chabazite. The balls are oxygen atoms of the SiO_4 tetrahedra.

Two characteristics of zeolites are that, 1) in addition to Si and Al, they contain extraframework cations in their channels and 2) they may absorb large amounts of water. The extraframework cations as well as the absorbed water can have a pronounced influence on the expansion behavior of the materials.[47] For these reasons, study of their thermal expansion behavior is usually carried out on purely siliceous zeolites or aluminophosphates, where there are no extraframework cations.

1.2.5 The AMO_5 family

In the AMO_5 compounds, the A cation can be V, Nb, Mo, Sb, Ta and W, and the M cation can be P, V, As and Mo. This structure consists of corner-sharing AO_6 octahedra and MO_4 tetrahedra (see Figure 1.8) similar to the AM_2O_7, AM_2O_8 and $A_2M_3O_{12}$ families of materials. The overall symmetries vary from tetragonal (e.g. A = V, Nb, Mo, Ta and W) to monoclinic (e.g. A = Nb, Ta, W).[52, 97] Two high temperature phases of $NbOPO_4$ (tetragonal and orthorhombic, see Figure 1.8),[51, 52] $TaOPO_4$ and orthorhombic $TaOVO_4$[98] were found to display negative thermal expansion.

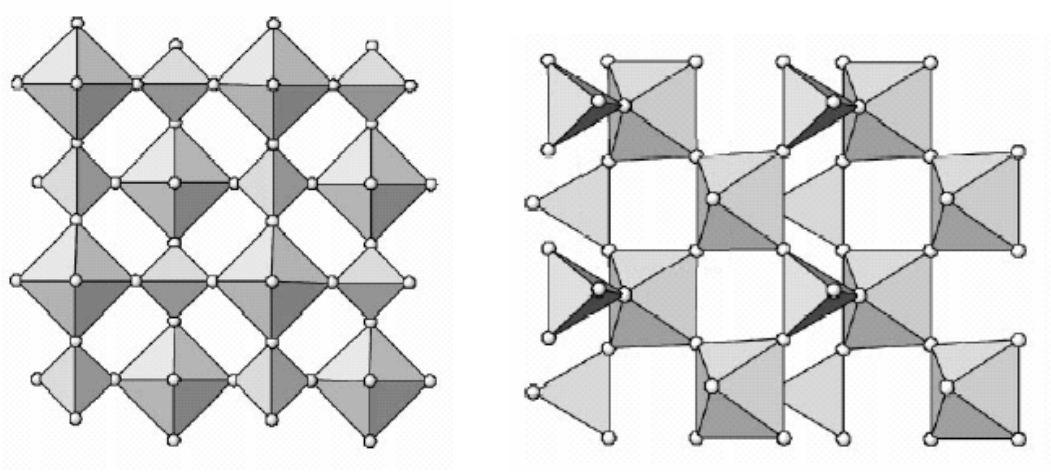

Figure 1.8: Structures of the high-temperature tetragonal form (left) and the orthorhombic form (right) of $NbOPO_4$ consisted of NbO_6 octahedra and PO_4 tetrahedra. Taken from Amos and Sleight.[51]

1.2.6 Mechanisms for NTE

As is clear from the review of the different low thermal expansion materials in section 1.1, the thermal expansion actually displayed by the material can be the result of different structural features. Consequently, several different mechanisms for NTE have been identified.[25] It should be noted that, in the context of the below discussion, contraction along only one or two crystallographic axes not leading to a volume negative expansion, is also of interest.

One mechanism pertains to ferroelectric oxides with the perovskite structure. NTE exists in e.g. $BaTiO_3$ and $PbTiO_3$ just below their tetragonal-to-cubic phase transition. In the low-temperature, tetragonal structure the TiO_6 and BaO_{12} or PbO_{12} polyhedra become more regular with increasing temperature. Due to a decrease in anion-anion repulsion in the more regular polyhedra, the average metal-oxygen distances become shorter.[99] The resulting thermal expansion along the a and b axes, and the contraction along the c axis gives a small volume contraction in the tetragonal structure.[25]

NTE in the silicates cordierite ($Mg_2Al_4Si_5O_{18}$) and β-eucryptite ($LiAlSiO_4$) as well as NZP ($NaZr_2P_3O_{12}$) is caused by the normal positive thermal expansion of certain metal-oxygen bonds.[7] For cordierite and β-eucryptite, positive thermal expansion along axes *a* and *b* is coupled with NTE along *c*. On the contrary, for NZP, *c*-axis positive thermal expansion is coupled with contraction along the *a*- and *b*-axes. In these compounds, the thermal expansion of the Al-O, Si-O, P-O and Zr-O bonds are small enough to ignore. Figure 1.9 shows the schematic of a portion of the cordierite structure.

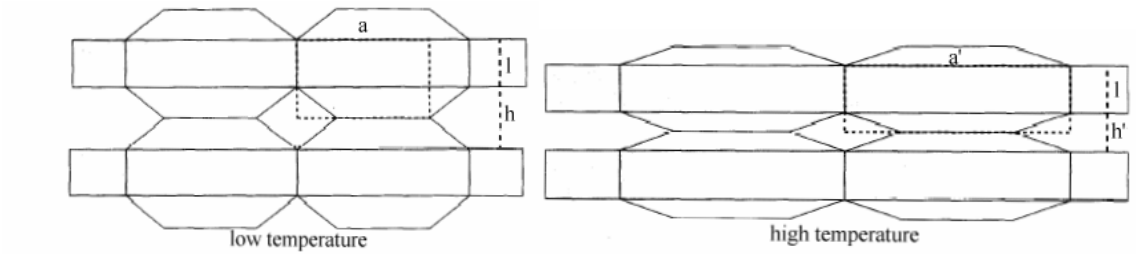

Figure 1.9: Schematic of the thermal expansion in cordierite networks. As the layers (of constant thickness l) undergo positive thermal expansion (a' > a), they are pulled closer together (h' < h). Taken from Sleight.[7]

With the lengthening of the Mg-O bonds with temperature, there is an expansion only in the horizontal direction. Expansion in the vertical direction is inhibited by the cation-cation repulsion across the shared edge. The thickness of horizontal layers does not change significantly as they expand laterally. A vertical contraction is caused by the horizontal expansion of the layers as schematically shown in Figure 1.9. In both cordierite and β-eucryptite, there are polyhedra within the layers that share only edges. In NZP, there is face sharing of ZrO_6 and NaO_6 octahedra along the c axis, forming tubes. It is the expansion of the Na-O distances that pulls the layers together in the other directions.[24]

In the case of β-eucryptite and some members of the NZP family other factors should be considered as well for a complete picture on their thermal expansion properties. A third mechanism is based on the interstitial cations within the network changing sites as a function of temperature. Cation conductivity in these materials is significant, indicating reasonable cation mobility. Modeling studies have shown that the change in the distribution of the interstitial (Li^+, Na^+) cations may critically influence the observed thermal expansion.[25]

The mechanism, which can be considered the most important one in open framework oxides exhibiting isotropic thermal expansion, is based on the transverse thermal motion of oxygen in M-O-M linkages (M = metal). This mechanism is relevant to basically all open framework oxide materials discussed in sections 1.2.1-5, where the oxygen is coordinated to just two metal atoms.[24-26] Provided that the M-O bonds in the structure are sufficiently strong and therefore show insignificant expansion (the polyhedra are rigid), the average metal-metal distance will decrease as the bridging oxygen in an M-O-M unit vibrates with increasing amplitude (see Figure 1.10). In a three dimensional solid, each vibration will result in a rocking motion of the polyhedra that are connected by the respective oxygen. For NTE to occur, all polyhedra must tilt back and forth in a cooperative fashion. Figure 1.10 depicts an example of how such a cooperative motion can result in a reduction in the average metal-metal distances.

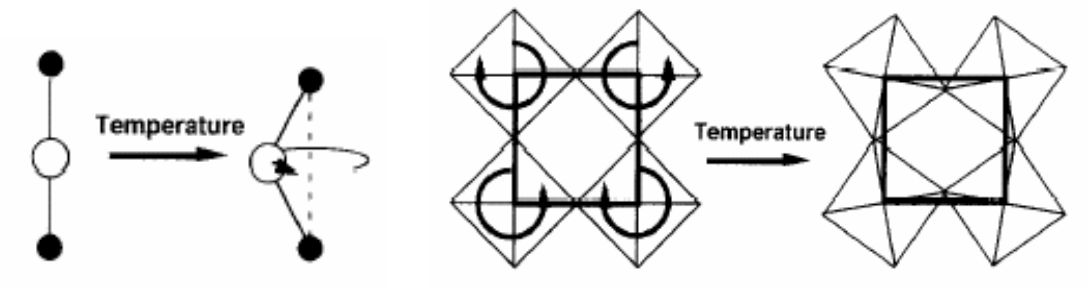

Figure 1.10: Transverse vibrational motion of an oxygen atom in a M-O-M linkage resulting in a decrease of the average metal-metal distance. A cooperative rotation of the polyhedra causes a decrease in the average metal-metal distances. Taken from Evans *et al*.[27]

This mechanism has been proposed to be responsible for the NTE in many members of the AM_2O_7, AM_2O_8, $A_2M_3O_{12}$, AO_2 and AMO_5 families of materials, where the following requirements are met: a) open framework structure, b) oxygen in two-fold

coordination, c) strong metal-oxygen bonds and d) rigid polyhedra that can freely tilt back and forth with little or no change in shape.[24, 25]

From the lattice dynamics point of view, one has to consider lattice vibrational modes in the solid in order to understand NTE. Lattice vibrational modes, also called phonon modes, are cooperative vibrational modes of all atoms in a solid. If the polyhedra in the material are essentially rigid and they can rock back and forth without significant distortions or interference with other polyhedra, then low-energy vibrational modes may be present that can result in NTE.[29, 39, 76, 77, 100-102] The observed thermal expansion of a material depends on the nature of the various modes present (sign of the Grüneisen parameter) as well as their energies, as only the modes that are excited at a given temperature contribute to the thermal expansion. The low-energy modes involving no polyhedra distortions (also called rigid unit modes) can exhibit negative Grüneisen parameters and may be excited at low temperatures. Negative Grüneisen parameters for these low-energy modes can result in a decrease in unit cell size, that is, NTE. Direct evidence for the role of low-energy modes in the NTE of cubic ZrW_2O_8 has been obtained from heat capacity,[75] as well as phonon density of states measurements.[29, 76] The low-frequency modes that actually contribute to the NTE behavior of cubic ZrW_2O_8 have been identified by high-pressure inelastic neutron diffraction[77] and high-pressure Raman spectroscopic studies.[3, 103]

1.2.7 Practical aspects

Besides scientific curiosity, NTE materials are also being investigated due to technological interest. The technological interest in NTE materials is primarily due to

their applicability in composites with tailored thermal expansion. It has been demonstrated that the use of a composite containing a positive expansion material (e.g. Al_2O_3, SiO_2, ZrO_2, MgO and CaO) and an NTE material such as cubic ZrW_2O_8 or HfW_2O_8 can prevent undesired expansion of optical fiber gratings and compensate for the changes in the dimensions and refractive index of optical fibers.[104, 105] The Cu/ZrW_2O_8 composite may have high thermal conductivity and low thermal expansion at the same time.[106, 107] The use of NTE materials in composites facilitates the control of thermal expansion.[105] In principle, the overall expansion coefficient of a composite material can be precisely tailored to a specific expansion coefficient value. Zero thermal expansion composites are employed in optical mirrors (large mirror blanks for telescopes) as substrates. Low expansion ceramics are being used for their resistance to thermal shock. The cookware industry uses these glass ceramics for ceramic top kitchen appliances. Matching the thermal expansion of device parts is important in electronic and biomedical applications. There is interest in the electronics industry to tailor the thermal expansion properties of printed circuit boards and heat sinks to match those of silicon. Dental fillings need to have their thermal expansion coefficients matched to those of teeth. Some materials that display NTE down to very low temperatures can be used in low-temperature sensing applications.[28]

The most important characteristics for an NTE material to be widely applicable are: 1) isotropic, preferably linear NTE over a wide temperature range including room temperature, 2) large range of stability (phase transitions on the application of temperature or pressure are undesirable, as is decomposition), 3) chemical inertness

(towards other materials in the composite) and 4) the possibility of cost-effective, large-scale production.

1.3 High-pressure studies of materials

The desire to better understand geophysical/geochemical phenomena and to know more about the physical and chemical properties of the Earth's crust as well as planetary materials led scientists originally to develop and utilize tools for high-pressure (and high-temperature) research. This enables us to study the properties of Earth materials in the laboratory under high-pressure-temperature environments that can mimic the conditions of the Earth's mantle and core as well as the interiors of other major planets. In general, high-pressure research can contribute to a better understanding of crystal chemistry and the structural principles underlying the solid state. Application of high pressures facilitates the synthesis of new materials that are not accessible through ambient pressure routes. Materials' characteristics can be studied under variable pressure and temperature conditions and their properties can be tuned for specific applications. Finally, through mapping the P-V-T parameter space of the materials, their phase diagrams can be established, which may shed light on the existence or possibility of preparing new phases.

The most important developments in the field of high-pressure science include: devices for the containment of pressure and the application of pressure to samples (multi-anvil devices,[108, 109] diamond anvil cells,[109, 110] moissanite anvils,[111] etc.), high-pressure measurement methods and tools (ruby fluorescence technique,[112] other fluorescence sensors[113]) and the use of advanced light sources (synchrotron radiation, laser heating

techniques) for probing the structure and studying the properties of materials under extreme conditions on an atomic level.

More and more effects of high pressure on materials have been observed and examined. The most studied changes include: structural phase transitions, shifting of vibration modes, band shape and intensity changes, splitting of degenerate vibrations, doubling of vibrations as well as changes in mechanical, electronic, magnetic and thermal properties.[114] Some of these changes, such as phase transitions, changes in vibrational frequencies and in certain physical properties, can also be brought about by changing temperature. The present thesis discusses structural phase transitions in low and negative thermal expansion materials brought about by the application of pressure or temperature and the effect of the occurring phase transitions on the physical properties (structure, thermal expansion and applicability) of these materials. However, changes in the frequencies of some phonon modes with pressure also have a major role in the high-pressure behavior of NTE materials as is discussed later in this chapter.[3, 30, 77, 103, 115-119]

Pressure-induced structural phase transitions that are of interest in the current thesis include crystalline to crystalline phase transitions, when transformation to another crystalline polymorph with different symmetry occurs, and crystalline to amorphous phase transitions, when the material loses its long-range order.[120] In crystalline to crystalline phase transitions the symmetries of the two phases usually have a subgroup to supergroup relationship and the low-symmetry structure can often be described as a distorted version of the high-symmetry structure.[120] Structural phase transitions are a common feature of many framework materials. A classic example is the temperature-induced α-β phase transition in quartz.[121]

1.3.1 Pressure-induced amorphization

Pressure-induced amorphization (PIA) is a widespread and intriguing phenomenon, which occurs among framework structures. PIA can be defined as the formation of an amorphous phase by the application of high (static or dynamic) pressure. For some materials, the amorphization can occur on the decompression of a high-pressure crystalline phase. Since the discovery of the amorphization of hexagonal ice under compression,[122] PIA has been extensively studied in different types of materials.[123-132] The first in-situ evidence of a crystalline to amorphous phase transition under high pressure was found for SnI_4 by x-ray diffraction[133] and Raman scattering.[134] Given that PIA is of fundamental interest to naturally occurring processes, such as phase transformations in minerals, and with the growing number of compounds found to undergo PIA, research targeted at the understanding of the mechanism of the amorphization process has been widely pursued.[125, 127, 128, 135-137] Sharma and Sikka outlined the following rules for pressure-induced crystalline to amorphous phase changes:[127, 138] (1) The pressure-induced amorphous phase is a kinetically preferred one. It arises from the frustration of the parent metastable crystalline phase in transforming to the high-pressure equilibrium state due to the requirement of thermal energy to overcome the energy barrier; (2) The equilibrium phase is usually of higher coordination or is dissociated; (3) The structural frustration arises as, e.g. while achieving higher coordination, some of the non-bonded distances become too short and make a repulsive contribution to the free energy. Further compression results in the loss of long-range order by taking advantage of the enhanced entropy.

The models for PIA found in the literature generally follow two different levels of description of the phenomenon: thermodynamic models and structural (sometimes referred to as microscopic) mechanisms (see Figure 1.11).[127]

Thermodynamically, the pressure-amorphized phase is often considered a metastable intermediate between two crystalline forms and is believed to be evolving as a result of kinetic hindrance of equilibrium phase transitions. If the kinetic barrier for the conversion of the low-density crystalline material to the amorphous form is lower than that for the transformation into the high-density crystalline form, then pressure-induced amorphization may occur.[127] Other ways of viewing PIA from a thermodynamic point of view are as pseudo-melting (also called thermodynamic melting or high-pressure melting) of a crystalline phase,[127, 129] dynamical lattice instability[137] as well as (hindered) chemical decomposition.[131, 136] There are several limitations to view PIA as a form of melting, which make pseudo-melting a model that is not generally acceptable.[127] The material should have a melting curve that shows a negative trend with pressure. This means that at some pressure, the melting point would become lower than the temperature of the experiment and thus the material becomes a glass. The high-pressure amorphous phase of the material should have a structure similar to that of the usual glassy phases obtained by thermal quenching from the liquid phase. This is not satisfied for many known pressure-amorphized phases. Amorphous materials formed by compression are usually denser than those quenched at ambient pressure from melts, because they incorporate structural units with distorted shape and/or higher coordination numbers than those present in the melt-quenched glasses. A hallmark of phase changes under pressure

is that the decrease in volume is often accompanied by an increase in the average local coordination number of the atoms.[139-142]

Due to the great diversity of the materials exhibiting PIA, numerous structural mechanism have also been proposed, some of which can be related and thus simultaneously applicable. Among the many structural factors considered as possible PIA mechanism, steric constraints preventing the formation of the high-density crystalline form,[127, 143] and random packing of polytetrahedral units resulting in orientational disorder,[126, 127, 144] have evolved into widely accepted structural models. The above models cannot always be viewed as explicit mechanisms, more than one mechanism may be simultaneously applicable. For example, the polytetrahedral model,[144] which is based on the transformation of the original polyhedra to higher-coordination polyhedra for closer packing on pressure, may combine with the steric constraints model.[127, 143] The latter mechanism is based on the argument that the shape of the rigid polyhedral building blocks may not favor close-packing and this leads to a destabilization of the crystal structure. The combination of these two mechanisms can be important in the amorphization of NTE materials, where the framework is composed of rigid polyhedral units. A reasonably realistic scenario is that the polyhedra may change their shape/distort a little bit initially (increase coordination), but further distortion at higher pressure results in the collapse of the structure (loss of long-range order).

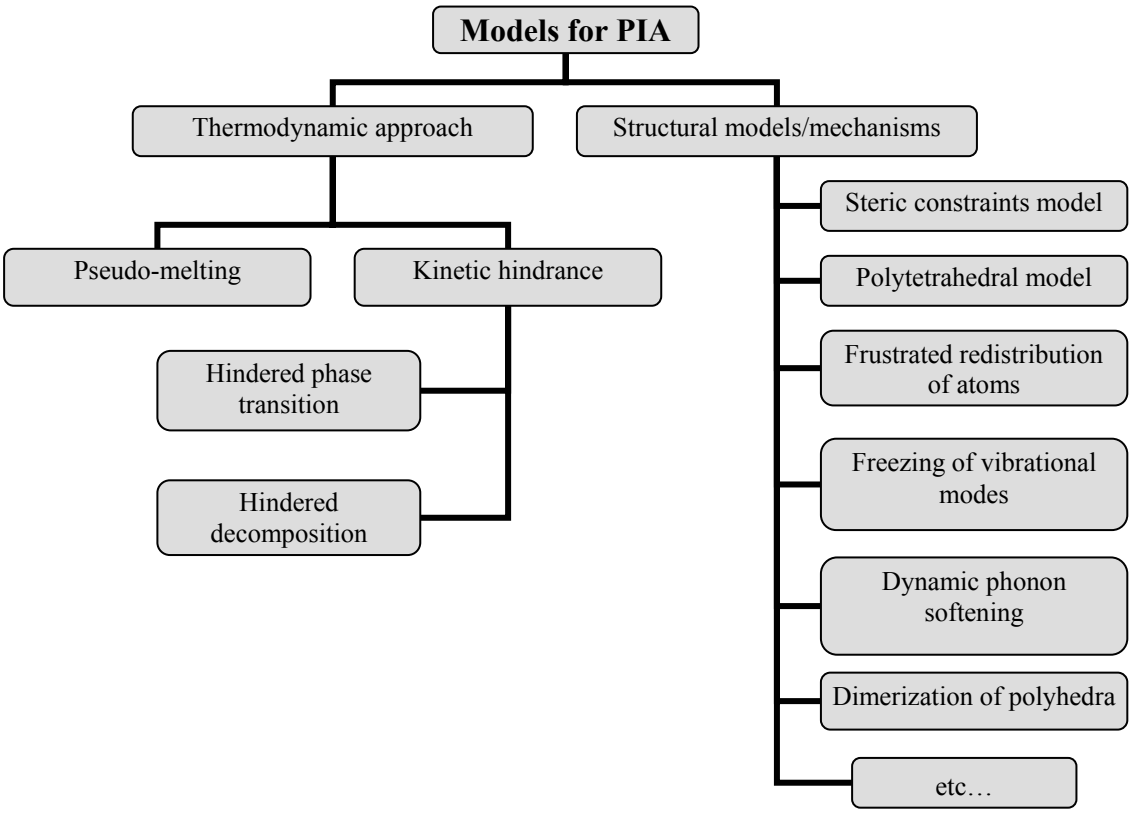

Figure 1.11: General mechanisms for pressure-induced amorphization.

Amorphization can be observed *in-situ* with a variety of structural probes such as x-ray diffraction, Raman, IR, or Brillouin spectroscopies. In samples quenched down to ambient pressure, other methods, such a high-resolution electron microscopy may be used as well.[128] However, it should be noted that as every technique probes a particular length scale (about 10 Angstroms and up for x-ray diffraction, less for Raman spectroscopy or still less for electron microscopy), thus detection of amorphization depends on the characterization tool used. The sample e.g. may be ordered at short length scales, while disordered at longer scales.[145] Also, a seemingly amorphous material by x-

ray diffraction may show nanocrystalline domains. For the purposes of the present research, by an amorphous material we mean that the material shows no sign of long-range order by x-ray diffraction, i.e. it is x-ray amorphous.

1.4 High-pressure behavior of NTE materials

As discussed earlier in section 1.2, most NTE materials have framework structures composed of relatively rigid polyhedra. The forces that act within the polyhedral units are much stronger than the ones that act between them making the structure largely flexible. The flexible bond angles may vary on compression or heating without breaking of the bonds, which may result in transformations to a new phase. These flexible framework structures have relatively low density and thus some void spaces in them. The density of cubic ZrW_2O_8 in volume per formula units is 192 $Å^3$ (d = 5.08 g/cm^3). If ZrW_2O_8 was of comparable density to its binary oxides, then it would have a density of about 141 $Å^3$ per formula unit based on the densities of the binary oxides ZrO_2 (35 $Å^3$/formula unit, d = 5.89 g/cm^3) and WO_3 (53 $Å^3$/formula unit, d = 7.16 g/cm^3). Cubic $ZrMo_2O_8$ (190.3 $Å^3$/formula unit) is less dense than the most stable ambient pressure and temperature monoclinic polymorph (143.1 $Å^3$/formula unit) (not an NTE material), which contains Zr and Mo with higher coordination numbers than those found in the cubic material.[40] It is also less dense than trigonal $ZrMo_2O_8$ (173.8 $Å^3$/formula unit).[40]

NTE materials necessarily have some lattice modes that soften on volume reduction.[3, 77, 103, 115-119] The presence of these lattice modes is necessary, as such modes are responsible for the NTE behavior. High-pressure inelastic neutron scattering measurements revealed that low-energy phonons (below 8 meV) in cubic ZrW_2O_8 show

an unusual softening, i.e. decrease in frequency, on compression and this softening corresponds to large negative Grüneisen parameters.[77] High-pressure Raman studies showed that phonons of higher energy (between 8-50 meV) also have negative Grüneisen parameters and thus contribute to the NTE in ZrW_2O_8,[3, 103]

Due to the combination of their highly flexible framework structure, relatively low density and the presence of lattice modes that soften on compression, NTE materials are likely candidates to exhibit unusual high-pressure behavior. Volume-reducing phase transitions and/or amorphization can be expected to occur at relatively low pressures in NTE materials.

These framework structures are generally quite soft, i.e., highly compressible. Low bulk moduli are common amongst NTE and related materials, for example cubic ZrW_2O_8 (72.5 GPa by neutron diffraction),[146] cubic $ZrMo_2O_8$ (44.6 GPa)[147] cubic ZrP_2O_7 (39 GPa),[148] cubic ZrV_2O_7 (18 GPa)[148] and cubic NbO_2F[149] (24.8(11) GPa), presumably arising from the low density and framework flexibility that is characteristic of them. For comparison, the bulk modulus of some non-flexible-framework materials; the metal oxide hematite (γ-Fe_2O_3): 203 GPa,[150] body-centered cubic Fe: 165 GPa[151] and magnesite ($MgCO_3$): 117 GPa,[152] softer materials include LiF: 65.3 GPa,[151] NaCl: 25 GPa[153] and CsCl: 18.1.[153]

1.4.1 Pressure-induced crystalline to crystalline phase transitions in NTE materials

Phase transitions at low pressures have been reported for many NTE materials (cubic $ZrMo_2O_8$,[154, 155] cubic $HfMo_2O_8$,[155] cubic ZrW_2O_8,[3, 103, 146, 156-158] cubic HfW_2O_8,[118, 159] cubic ZrV_2O_7,[160] $Sc_2Mo_3O_{12}$,[161] $Sc_2W_3O_{12}$[162] (this work) and $Al_2W_3O_{12}$[163, 164]). In general,

these pressure-induced phase transitions involve tilting of rigid polyhedral units with a concomitant decrease in unit cell volume and lowering of the symmetry. Another very important characteristic of these phase transitions is that the linear thermal expansion coefficient exhibited by the ambient pressure structure can be changed significantly. In ZrW_2O_8, the cubic-to-orthorhombic phase transformation results in a reduction of the negative coefficient of thermal expansion by almost an order of magnitude.[156, 157] In some materials with the orthorhombic $Sc_2W_3O_{12}$ structure, NTE is likely to be lost completely in the monoclinic structure which is formed on compression.[161-163] The monoclinic phase is known to show positive thermal expansion for compositions that adopt this structure at ambient pressure.[94, 161, 163] This variation or loss of the NTE property on compression adversely affects their applicability in structural materials, as they may be subjected to high pressures during processing of composites with tailored thermal expansion.[106, 107, 165]

1.4.2 Pressure-induced amorphization in NTE materials

In addition to the softening of the low-frequency phonon modes, another possible link between NTE and PIA has been suggested some time ago. Theoretical simulations revealed that in tetrahedral networks showing NTE, such as ice and silicon, on compression, changes in bond angle that are not correlated over long length scales can lead to amorphization.[135] This theory involving uncorrelated tilting of polyhedra was extended to NTE materials containing mixed tetrahedral-octahedral units as it seemed to be the operating mechanism that led to disorder in cubic ZrW_2O_8.[166] PIA at low pressures were reported for many other NTE materials including $ZrMo_2O_8$,[154] $Sc_2Mo_3O_{12}$,[167] $Sc_2W_3O_{12}$[168] and $Lu_2W_3O_{12}$.[132] However, it is not clear whether the flexibility of their

frameworks and the corresponding ability of the polyhedral units to tilt freely on compression alone can be considered responsible for the PIA in NTE materials as there were observations of other possible mechanisms. *In-situ* neutron diffraction experiments on ZrW_2O_8 revealed an increase of coordination on compression, that is, the tungsten is 4+1-coordinate in the high-pressure orthorhombic phase formed above 0.21 GPa.[156] Raman studies of ZrW_2O_8 were interpreted as indicating amorphization at 2.2 GPa due to a kinetically hindered pressure-induced decomposition into its constituent oxides.[3, 103] The preparation of a new ZrW_2O_8 polymorph with a cation-disordered α-U_3O_8-type structure by heating a pressure-amorphized sample under pressure suggests that the amorphization process may involve an increase in coordination number.[169] The Zr and W cations in this structure display 6+1 coordination,[169] indicating that the tetrahedral coordination of tungsten in cubic ZrW_2O_8 and the predominantly 4+1 coordination of tungsten in orthorhombic ZrW_2O_8[156] is unstable at high pressure.

In order to find direct evidence on the nature of the pressure-induced amorphous phase (cation coordination numbers, interatomic distances) and thus the mechanism of amorphization, *in-situ* studies carried out at high pressure using "local probe" techniques are indispensable. Investigation of the structure of glassy phases requires either "local structural probes" that are not sensitive to the extent of ordering or the utilization of more sophisticated scattering techniques. The need for in-situ studies has necessitated making the structural characterization techniques suitable for use at high pressure. The applicable characterization tools are discussed in more detail in Chapters 2 and 4.

1.5 Temperature-induced phase transitions in low and negative thermal expansion materials

Temperature-induced phase transitions are commonly found in low thermal expansion and NTE materials. This has to do with their flexible framework structure where atomic displacements are feasible through small distortions of the polyhedra. Temperature-induced order-disorder phase transitions have been observed in cubic ZrW_2O_8,[38, 39, 170-172] HfW_2O_8,[38, 171] ZrV_2O_7,[37, 64] HfV_2O_7,[65] ZrP_2O_7,[34, 35] TiP_2O_7[62] and other materials of the AM_2O_7 general formula.[34, 35]

The α- to β phase transition in ZrW_2O_8 is a cubic to cubic transformation from acentric space group $P2_13$ to centrosymmetric $Pa\bar{3}$ symmetry. It involves a rearrangement of the WO_4 tetrahedra. A schematic representation of the inversion of the WO_4 groups is given in Figure 1.12. The terminal oxygen, O4, is mobile at elevated temperatures. Migration of O4 from its original site to a vacant site is inferred to be the source of the disorder. This migration is then accompanied by the migration of oxygen atom O3 from tungsten W2 to the adjacent W1, and the concerted migration of W1's original terminal oxygen. In the high-temperature disordered phase, the two tungstens become related to each other by an inversion center. The inversion center results in two possible sites for O4, both with only 50 % occupancy. This leads to disorder of the O3 and W sites and results in a split W site with 50 % occupancy for each W atom.[38, 39]

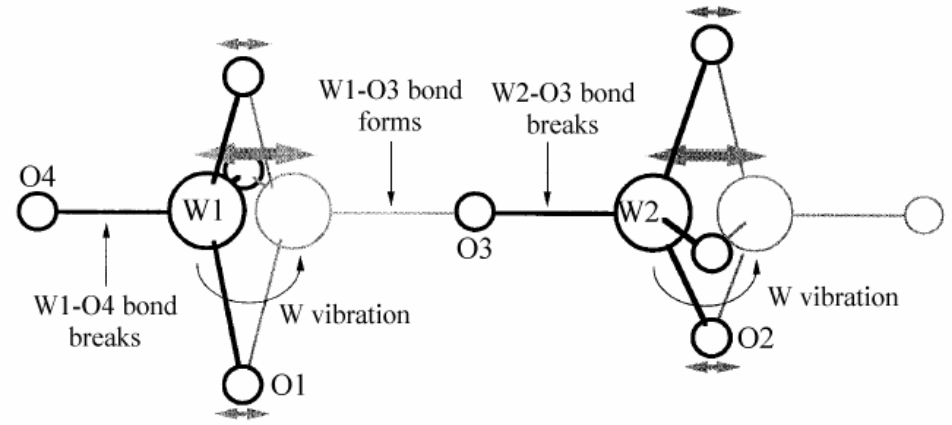

Figure 1.12: Schematic representation of the inversion of the WO_4 groups in α-ZrW_2O_8 resulting in the disordered β-ZrW_2O_8. Taken from Evans *et al*.[38]

The phase transition causes a discontinuity in the thermal expansion curve of the material (see Figure 1.4) and results in an increase of the coefficient of thermal expansion by a factor of two: CTE before the phase transition is ~ -8.8 x 10^{-6} K^{-1} (0-400 K) and ~ -4.9 x 10^{-6} K^{-1} after (430-950 K).[40] The isostructural HfW_2O_8 displays similar expansion and phase transition behavior.[38] In addition to the second-order α-β phase transition in ZrW_2O_8, a first-order phase transition from the α- to a proposed γ-phase was also observed by power-compensated differential scanning calorimetry. It was claimed that the value of the CTE was more negative for the γ-phase, stable between 123 and 164 ^oC, than for the other two.[173]

Most compounds of the cubic AM_2O_7 family show an order-disorder phase transition from a low-temperature superstructure to a high-temperature disordered structure as already discussed in section 1.2.1. This has practical importance as the high-temperature phase, as opposed to the normal expansion low-temperature phase, displays low thermal expansion in e.g. ZrP_2O_7,[34, 174, 175] and the thermal expansion can even be negative in the cases of ThP_2O_7, UP_2O_7, ZrV_2O_7, HfV_2O_7.[34, 57, 58, 174]

Examples of temperature-induced displacive phase transitions are given by compounds of the $A_2M_3O_{12}$ family. Several materials with the orthorhombic $Sc_2W_3O_{12}$ structure have been shown to undergo a volume-reducing phase transition to a monoclinic structure on cooling.[86, 87, 89, 94, 95] These orthorhombic to monoclinic phase transitions can also be seen under compression for several members of the family. Heating or cooling under approximately constant pressure conditions can sometimes be thought of as decompression or compression, respectively, under constant temperature, although temperature and pressure are not fully interchangeable. The monoclinic structure does not show negative volume expansion,[94] which has important implications with respect to the applicability of these materials in composites. These phase transitions are first-order. The high-pressure phase transitions of $A_2M_3O_{12}$ compounds are discussed in detail in Chapter 3.

Reconstructive phase transitions are also known in some NTE materials. These phase transitions usually involve a major reorganization of the structure (breaking and formation of bonds) and are therefore generally irreversible. They usually constitute an abrupt change of structure and are first-order. The cubic to trigonal phase transition in $ZrMo_2O_8$ is an example of a first-order reconstructive phase transition. The trigonal (space group $P\bar{3}1c$)[82, 84, 85] and the monoclinic ($C2/c$)[82, 83] polymorph are thermodynamically more stable than the cubic ($Pa\bar{3}$) one. The metastable cubic polymorph thus converts into the trigonal phase on heating at temperatures above 390 ^oC.[40] *Ex-situ* x-ray diffraction studies carried out on samples that were recovered from a high-pressure multi-anvil apparatus showed that by exposing the cubic phase to pressures

up to 4 GPa, the monoclinic phase can be obtained, which, at low pressures (< 1.3 GPa) is mixed with trigonal $ZrMo_2O_8$.[154]

1.5.1 Control of thermal expansion by doping

For compounds exhibiting low or negative thermal expansion in a phase that is only stable at high temperatures, there is a practical interest in lowering the temperature of the phase transition and thus stabilizing the low or negative thermal expansion structure over a wider temperature range, preferably including room temperature. One way to do this is by changing the chemical composition of the material through cation replacement or insertion. The widely used low thermal expansion ceramics β-eucryptite and β-spodumene are basically stuffed β-quartz and keatite structures, respectively.[176, 177] β-quartz shows low thermal expansion, but it is only stable at high temperatures.[178] However, the replacement of some of the silicon with Li^+ and Al^{3+} ions stabilizes the β-quartz structure by suppressing its transformation to α-quartz, which shows normal positive thermal expansion. The resulting $LiAlSiO_4$ compositions retain the β-quartz structure to low temperatures including room temperature and display low thermal expansion over a wide temperature range.[178]

Solid solution formation in the $ZrV_{2-x}P_xO_7$ and $HfV_{2-x}P_xO_7$ systems has been reported to suppress the order-disorder phase transitions that are shown by the end-member phosphates and vanadates.[34] For the mid region of the ZrV_2O_7-ZrP_2O_7 solid solution ($x \geq 0.3$), the phase transitions above room temperature were completely suppressed resulting in low thermal expansion around room temperature. Similar results were obtained for the system with the Hf-analogues. Two explanations are given for the depression of the

temperature of the phase transition. One considers it a normal solid solution effect analogous to freezing point depression. The disorder inherent in the solid solution interferes with the long-range cooperative forces required for the phase transition. Another explanation is supported by ^{31}P NMR results: it reveals the prevalence of VPO_7^{4-} groups in the $ZrP_{2-x}V_xO_7$ system as opposed to a mixture of $V_2O_7^{4-}$ and $P_2O_7^{4-}$ groups when x is close to 1.0. The linear P-O-V linkage is not known as unstable relative to the instabilities of linear P-O-P and V-O-V linkages. Therefore, the depression of the phase transitions might also be due to the presence of the P-O-V bonds.[34]

The temperature of the α-β phase transition in cubic ZrW_2O_8 was shown to decrease by the substitution of Zr^{4+} by Sc^{3+}, In^{3+} and Y^{3+} ions.[179] As the decrease was only seen in $Zr_{1-x}M_xW_2O_{8-y}$ compositions, where M = Sc^{3+}, In^{3+} or Y^{3+}, and not in $Zr_{1-x}Hf_xW_2O_8$ compositions, it was argued that it may be caused by the decrease of ordering in the α-phase due to the presence of oxygen defects. However, this study doesn't really have significance from an application's point of view, as the depression is relatively small (from ~ 440 K to ~ 360 K) and it is the α-phase that exhibits larger negative thermal expansion.

The possibility of controlling the phase transition and thus thermal expansion in cubic ZrP_2O_7 through stuffing and substitution of the structure is discussed in Chapter 6.

1.5.2 Control of thermal expansion by cation ordering

The extent of cation ordering in a solid material can significantly affect its properties, such as phase transitions, thermal and electric behavior, etc. The influence of the ordering of M^{III} and M^{V} cations on the ferroelectric properties has been shown in the perovskite

ferroelectrics $PbIn_{0.5}Nb_{0.5}O_3$ (PIN)[180-183] and $PbSc_{0.5}Ta_{0.5}O_3$ (PST).[184-188] For these materials, controlled slow annealing results in a long-range ordered arrangement of M^{III} and M^{V} ions, while quenching from high temperatures locks in a disordered arrangement of the cations. By carefully chosen heat treatment conditions, the degree of cation ordering can be controlled. In fully ordered samples of PIN and PST, a well-defined paraelectric to ferroelectric phase transition was observed, but in the disordered samples only a very diffuse phase transition is seen.[181, 182, 187, 188] As a result, the materials behaved as relaxors rather than normal ferroelectrics at low temperature.[185]

Studies on how cation ordering can be influenced by heat treatment conditions and whether it can be used to control the thermal expansion properties / manipulate the phase transitions in ZrP_2O_7-related materials are discussed in Chapter 7.

1.6 Goals/Overview

The thermal expansion properties of solid materials are influenced by both pressure and temperature as they can induce crystalline-to-crystalline or crystalline-to-amorphous phase transitions. Furthermore, chemical substitution/doping can in principle be used to manipulate the thermal expansion properties. The present thesis discusses the properties of different low and negative thermal expansion framework structures in the context of modification by pressure, temperature as well as chemical substitution. We set out to answer specific questions such as:

- How do different NTE materials with the orthorhombic $Sc_2W_3O_{12}$ structure behave under pressure? How does their structure change and why? What material's features

control the compressibility of these materials? Is there a trend in their high-pressure behavior with the identity of the A^{3+} cation? (Chapter 3)

- What is the mechanism of the pressure-induced amorphization in compounds of the AM_2O_8 framework? What differences (if any) do we observe in the amorphization mechanisms of frameworks composed of different types of polyhedra? (Chapters 4 and 5)
- Can a combination of cation insertion and substitution be effectively used to stabilize the low thermal expansion high-temperature structure in AM_2O_7 compounds to lower temperatures? (Chapter 6)
- Can cation order/disorder be influenced by heat treatment conditions in $M^{III}M^{V}(P_2O_7)_2$ compounds? Can it be used to manipulate the phase transitions and thus control the thermal expansion properties of these materials? (Chapter 7)

Additionally, in Chapter 8 we examine the utility of different grades of fluorinert as pressure-transmitting media. Fluorinerts have been widely used as liquid pressure-transmitting media for high-pressure (neutron) diffraction studies). Hydrostaticity is a very important issue in high-pressure materials research. It can affect the nature of phase transitions.

1.7 References

[1] P. Bruesch, *Phonons: Theory and Experiments*, Springer Verlag, Berlin, Germany (1982).

[2] R. Roy, D. K. Agrawal, and H. A. McKinstry: Very Low Thermal Expansion Coefficient Materials. *Annu. Rev. Mater. Sci.* **19**, 59 (1989).

[3] T. R. Ravindran, A. K. Arora, and T. A. Mary: High Pressure Behavior of ZrW_2O_8: Gruneisen Parameter and Thermal Properties. *Phys. Rev. Lett.* **84**, 3879 (2000).

[4] F. A. Hummel: Thermal expansion properties of natural lithia minerals. *Foote Prints* **20**, 3 (1948).

[5] F. A. Hummel: Thermal Expansion Properties of Some Synthetic Lithia Minerals. *J. Am. Ceram. Soc.* **34**, 235 (1951).

[6] J. P. Boilot, J. P. Salanie, G. Desplanches, et al.: Phase Transformation in $Na_{1+x}Si_xZr_2P_{3-x}O_{12}$ Compounds. *Mat. Res. Bull.* **14**, 1469 (1979).

[7] A. W. Sleight: Thermal Contraction. *Endeavour* **19**, 64 (1995).

[8] H. Ikawa, T. Otagiri, O. Imai, et al.: Thermal expansion of high-temperature cordierite and its solid solutions. *Yogyo Kyokaishi* **94**, 344 (1986).

[9] S. S. V. S. S. Vepa and A. M. Umarji: Effect of substitution on thermal expansion of cordierite ($Mg_2Al_4Si_5O_{18}$). *J. Am. Ceram. Soc.* **76**, 1873 (1993).

[10] H. D. Rosenfeld and T. Egami: A Model of Local Atomic Structure in the relaxor ferroelectric $Pb(Mg_{1/3}Nb_{2/3})O_3$. *Ferroelectrics* **150**, 183 (1993).

[11] D. K. Agrawal, R. Roy, and H. A. McKinstry: Ultra low thermal expansion phases: substituted 'PMN' perovskites. *Mat. Res. Bull.* **22**, 83 (1987).

[12] S. Y. Limaye, D. K. Agrawal, R. Roy, et al.: Synthesis, sintering and thermal expansion of $Ca_{1-x}Sr_xZr_4P_6O_{24}$ - an ultra-low thermal expansion ceramic system. *J. Mater. Sci.* **26**, 93 (1991).

[13] G. E. Lenain, H. A. McKinstry, J. Alamo, et al.: Structural model for thermal expansion in alkali metal zirconium phosphates $MZr_2P_3O_{12}$ (M = Li, Na, K, Rb, Cs). *J. Mater. Sci.* **22**, 17 (1987).

[14] T. H. K. Barron, J. F. Collins, T. W. Smith, et al.: Thermal expansion, Grüneisen functions and static lattice properties of quartz. *J. Phys. C: Solid State Phys.* **15**, 4311 (1982).

[15] P. R. L. Welche, V. Heine, and M. T. Dove: Negative thermal expansion in beta-quartz. *Phys. Chem. Minerals* **26**, 63 (1998).

[16] V. Heine, P. R. L. Welche, and M. T. Dove: Geometrical Origin and Theory of Negative Thermal Expansion in Framework Structures. *J. Am. Ceram. Soc.* **82**, 1793 (1999).

[17] C. L. Rathmann, G. H. Mann, and M. E. Nordberg: A New Ultralow-Expansion, Modified Fused-Silica Glass. *Appl. Opt.* **7**, 819 (1968).

[18] J. Petzoldt: Transparent metastable glass ceramics containing quartz solid solutions. *Glastechnische Berichte* **43**, 127 (1970).

[19] C.-É. Guillaume: Recherches sur les aciers au nickel. Dilatations aux températures élevées; résistance électrique. *C. R. Hebd. Seances Acad. Sci.* **125**, 235 (1897).

[20] D. A. Colling and W. J. Carr, Jr: Invar Anomaly. *J. Appl. Phys.* **41**, 5125 (1970).

[21] M. Van Schilfgaarde, I. A. Abrikosov, and B. Johansson: Origin of the Invar effect in iron-nickel alloys. *Nature* **400**, 46 (1999).

[22] M. F. Hochella, Jr. and G. E. Brown, Jr.: Structural mechanisms of anomalous thermal expansion of cordierite-beryl and other framework silicates. *J. Am. Ceram. Soc.* **69**, 13 (1986).

[23] A. W. Sleight, M. A. Thundathil, and J. S. O. Evans, Negative Thermal Expansion Materials, The Sate of Oregon on Behalf of Oregon State University, Corvallis, USA (1995).

[24] A. W. Sleight: Compounds that Contract on Heating. *Inorg. Chem.* **37**, 2854 (1998).

[25] A. W. Sleight: Negative thermal expansion materials. *Curr. Opin. Solid State Mater. Sci.* **3**, 128 (1998).

[26] A. W. Sleight: Isotropic Negative Thermal Expansion. *Annu. Rev. Mater. Sci.* **28**, 29 (1998).

[27] J. S. O. Evans, T. A. Mary, and A. W. Sleight: Negative thermal expansion materials. *Physica B* **241-243**, 311 (1998).

[28] J. S. O. Evans: Negative Thermal Expansion Materials. *J. Chem. Soc. Dalton Trans.*, 3317 (1999).

[29] W. I. F. David, J. S. O. Evans, and A. W. Sleight: Direct evidence for a low-frequency phonon mode mechanism in the negative thermal expansion compound ZrW_2O_8. *Europhys. Lett.* **46**, 661 (1999).

[30] Y. Yamamura, N. Nakajima, T. Tsuji, et al.: Heat capacity and Grüneisen function of negative thermal expansion compound HfW_2O_8. *Solid State Commun.* **121**, 213 (2002).

[31] K. Wang and R. R. Reeber: Mode Gruneisen parameters and negative thermal expansion of cubic ZrW_2O_8 and $ZrMo_2O_8$. *Appl. Phys. Lett.* **76**, 2203 (2000).

[32] D. B. Balashov and V. P. Orlov: Thermal anomaly of water. I. Regional boundaries. Entropy. Heat capacities. *Zh. Fiz. Khim.* **57**, 2465 (1983).

[33] K. Scheel: Experiments on the Expansion of Solids and Measurements of Quartz in the Direction of the Principal Axis, Platinum, Palladium, and Quartz-glass, to the Temperature of Liquid Air. *Ber. physik Ges.* **5**, 3 (1907).

[34] V. Korthuis, N. Khosrovani, A. W. Sleight, et al.: Negative Thermal Expansion and Phase Transitions in the $ZrV_{2-x}P_xO_7$ Series. *Chem. Mater.* **7**, 412 (1995).

[35] N. Khosrovani, V. Korthuis, A. W. Sleight, et al.: Unusual 180^o P-O-P Bond Angles in ZrP_2O_7. *Inorg. Chem.* **35**, 485 (1996).

[36] J. S. O. Evans, J. C. Hanson, and A. W. Sleight: Room-Temperature Superstructure of ZrV_2O_7. *Acta Crystallogr.* **B54**, 705 (1998).

[37] R. L. Withers, J. S. O. Evans, J. Hanson, et al.: An *In Situ* Temperature-Dependent Electron and X-ray Diffraction Study of Structural Phase transitions in ZrV_2O_7. *J. Solid State Chem.* **137**, 161 (1998).

[38] J. S. O. Evans, T. A. Mary, T. Vogt, et al.: Negative Thermal Expansion in ZrW_2O_8 and HfW_2O_8. *Chem. Mater.* **8**, 2809 (1996).

[39] T. A. Mary, J. S. O. Evans, T. Vogt, et al.: Negative Thermal Expansion from 0.3 to 1050 Kelvin in ZrW_2O_8. *Science* **272**, 90 (1996).

[40] C. Lind, A. P. Wilkinson, Z. Hu, et al.: Synthesis and Properties of the Negative Thermal Expansion Material Cubic Zirconium Molybdate. *Chem. Mater.* **10**, 2335 (1998).

[41] C. Closmann and A. W. Sleight: Low-Temperature Synthesis of ZrW_2O_8 and Mo-Substituted ZrW_2O_8. *J. Solid State Chem.* **139**, 424 (1998).

[42] J. S. O. Evans, T. A. Mary, and A. W. Sleight: Negative Thermal Expansion in a Large Molybdate and Tungstate Family. *J. Solid State Chem.* **133**, 580 (1997).

[43] J. S. O. Evans, T. A. Mary, and A. W. Sleight: Negative Thermal Expansion in $Sc_2(WO_4)_3$. *J. Solid State Chem.* **137**, 148 (1998).

[44] P. M. Forster, A. Yokochi, and A. W. Sleight: Enhanced Negative Thermal Expansion in $Lu_2W_3O_{12}$. *J. Solid State Chem.* **140**, 157 (1998).

[45] T. A. Mary and A. W. Sleight: Bulk thermal expansion for tungstate and molybdates of the type $A_2M_3O_{12}$. *J. Mater. Res.* **14**, 912 (1999).

[46] P. Tschaufeser and S. C. Parker: Thermal Expansion Behavior of Zeolites and $AlPO_4$s. *J. Phys. Chem.* **99**, 10609 (1995).

[47] M. P. Attfield and A. W. Sleight: Strong negative thermal expansion in siliceous faujasite. *Chem. Commun.*, 601 (1998).

[48] M. P. Attfield and A. W. Sleight: Exceptional Negative Thermal Expansion in $AlPO_4$-17. *Chem. Mater.* **10**, 2013 (1998).

[49] D. A. Woodcock, P. Lightfoot, L. A. Villaescusa, et al.: Negative Thermal Expansion in the Siliceous Zeolites Chabazite and ITQ-4: A Neutron Powder Diffraction Study. *Chem. Mater.* **11**, 2508 (1999).

[50] D. A. Woodcock, P. Lightfoot, P. A. Wright, et al.: Strong negative thermal expansion in the siliceous zeolites ITQ-1, ITQ-3 and SSZ-23. *J. Mater. Chem.* **9**, 349 (1999).

[51] T. G. Amos and A. W. Sleight: Negative thermal expansion in orthorhombic $NbOPO_4$. *J. Solid State Chem.* **160**, 230 (2001).

[52] T. G. Amos, A. Yokochi, and A. W. Sleight: Phase transition and negative thermal expansion in tetragonal $NbOPO_4$. *J. Solid State Chem.* **141**, 303 (1998).

[53] L. K. Frevel and H. W. Rinn: The Crystal Structure of NbO_2F and TaO_2F. *Acta Crystallogr.* **9**, 626 (1956).

[54] J. Z. Tao and A. W. Sleight: Very low thermal expansion in TaO_2F. *J. Solid State Chem.* **173**, 45 (2003).

[55] H. Onken: Uber Zirkonpyroarsenat. *Die Naturwissenschaften* **52**, 344 (1965).

[56] G. Le Flem, J. Lamic, and P. Hagenmuller: As_2O_5-ThO_2 system. *Bull. Soc. Chim. Fr.* **6**, 1880 (1966).

[57] D. F. Craig and F. A. Hummel: Zirconium Pyrovanadate Transitions. *J. Am. Ceram. Soc.* **55**, 532 (1972).

[58] R. C. Buchanan and G. W. Walter: Properties of Hot-Pressed Zirconium Pyrovanadate Ceramics. *J. Electrochem. Soc.* **130**, 1905 (1983).

[59] H. Vollenkle, A. Wittmann, and H. Nowotny: Uber Diphosphate vom Typ $Me(IV)P_2O_7$. *Monatsh. Chem.* **94**, 956 (1963).

[60] E. Tillmans, W. Gebert, and W. H. Baur: Computer Simulations of Crystal Structures Aplied to the Solution of the Superstructure of Cubic Silicondiphosphate. *J. Solid State Chem.* **7**, 69 (1973).

[61] J. Sanz, J. E. Iglesias, J. Soria, et al.: Structural Disorder in the Cubic 3x3x3 Superstructure of TiP_2O_7. XRD and NMR Study. *Chem. Mater.* **9**, 996 (1997).

[62] S. T. Norberg, G. Svensson, and J. Albertsson: A TiP_2O_7 superstructure. *Acta Crystallogr., Sect. C* **57**, 225 (2001).

[63] E. R. Losilla, A. Cabeza, S. Bruque, et al.: Syntheses, Structures, and Thermal Expansion of Germanium Pyrophosphates. *J. Solid State Chem.* **156**, 213 (2001).

[64] N. Khosrovani, A. W. Sleight, and T. Vogt: Structure of ZrV_2O_7 from -263 to 470 ^{o}C. *J. Solid State Chem.* **132**, 355 (1997).

[65] C. Turquat, C. Muller, E. Nigrelli, et al.: Structural investigation of temperature-induced phase transitions in HfV_2O_7. *Eur. Phys. J. Appl. Phys.* **10**, 15 (2000).

[66] I. J. King, F. Fayon, D. Massiot, et al.: A space group assignment of ZrP_2O_7 obtained by ^{31}P solid state NMR. *Chem. Commun.* **18**, 1766 (2001).

[67] C. Hudalla, H. Eckert, and R. Dupree: Structural Studies of $ZrV_{2-x}P_xO_7$ Solid Solutions Using ^{31}P-{^{51}V} and ^{51}V-{^{31}P} Rotation Echo Double Resonance NMR. *J. Phys. Chem.* **100**, 15986 (1996).

[68] R. J. Iuliucci and B. H. Meier: A Characterization of the Linear P-O-P Bonds in $M^{4+}(P_2O_7)$ Compounds: Bond-Angle Determination by Solid-State NMR. *J. Am. Chem. Soc.* **120**, 9059 (1998).

[69] X. Helluy, C. Marichal, and A. Sebald: Through-Bond Indirect and Through-Space Direct Dipolar Coupling ^{31}P MAS NMR Constraints for Spectral Assignment in the Cubic 3x3x3 Superstructure of TiP_2O_7. *J. Phys. Chem. B* **104**, 2836 (2000).

[70] R. L. Withers, Y. Tabira, J. S. O. Evans, et al.: A New Three-Dimensional Incommensurately Modulated Cubic Phase (in ZrP_2O_7) and it Symmetry Characterization via Temperature-Dependent Electron Diffraction. *J. Solid State Chem.* **157**, 186 (2001).

[71] J. Graham, A. D. Wadsley, J. H. Weymouth, et al.: A New Ternary Oxide, ZrW_2O_8. *J. Am. Ceram. Soc.* **42**, 570 (1959).

[72] L. L. Y. Chang, M. G. Scroger, and B. Phillips: Condensed Phase Relations in the Systems ZrO_2-WO_2-WO_3 and HfO_2-WO_2-WO_3. *J. Am. Ceram. Soc.* **50**, 211 (1967).

[73] C. A. Martinek and F. A. Hummel: Subsolidus Equilibria in the System ZrO_2-WO_3-P_2O_5. *J. Am. Ceram. Soc.* **53**, 159 (1970).

[74] C. Martinek and F. A. Hummel: Linear Thermal Expansion of Three Tungstates. *J. Am. Ceram. Soc.* **51**, 227 (1968).

[75] A. P. Ramirez and G. R. Kowach: Large Low Temperature Specific Heat in the Negative Thermal Expansion Compound ZrW_2O_8. *Phys. Rev. Lett.* **80**, 4903 (1998).

[76] G. Ernst, C. Broholm, G. R. Kowach, et al.: Phonon Density of States and Negative Thermal Expansion in ZrW_2O_8. *Nature* **396**, 147 (1998).

[77] R. Mittal, S. L. Chaplot, H. Schober, et al.: Origin of Negative Thermal Expansion in Cubic ZrW_2O_8 Revealed by High Pressure Inelastic Neutron Scattering. *Phys. Rev. Lett.* **86**, 4692 (2001).

[78] J. S. O. Evans, W. I. F. David, and A. W. Sleight: Structural investigation of the negative-thermal-expansion material ZrW_2O_8. *Acta Crystallogr., Sect. B* **55**, 333 (1999).

[79] F. Prinetto, G. Cerrato, G. Ghiotti, et al.: Formation of the Mo^{VI} Surface Phase on MoO_x/ZrO_2 Catalysts. *J. Phys. Chem.* **99**, 5556 (1995).

[80] A. Clearfield and R. H. Blessing: The Preparation and Crystal Structure of a Basic Zirconium Molybdate and its Relationship to Ion Exchange Gels. *J. Inorg. Nucl. Chem.* **34**, 2643 (1972).

[81] R. Pankajavalli and O. M. Sreedharan: Standard Gibbs energy of formation of $ZrMo_2O_8$. *J. Nucl. Mater.* **172**, 151 (1990).

[82] M. Auray, M. Quarton, and P. Tarte: Crystal Data for Two Molybdates $M(MoO_4)_2$ with M = Zr, Hf. *Powder Diffr.* **2**, 36 (1987).

[83] M. Auray and M. Quarton: Revised Crystal Data of $Zr(MoO_4)_2$, L.T. Form. *Powder Diffr.* **4**, 29 (1989).

[84] M. Auray, M. Quarton, and P. Tarte: New Structure of High Temperature Zirconium Molybdate. *Acta Crystallogr., Sect. C* **42**, 257 (1986).

[85] V. N. Serezhkin, V. A. Efremov, and V. K. Trunov: The Crystal Structure of α-$Zr(MoO_4)_2$, the High-tempertuare Modification of Zirconium Molybdate. *Russ. J. Inorg. Chem.* **32**, 1566 (1987).

[86] K. Nassau, H. J. Levinstein, and G. M. Loiacono: Trivalent Rare-Earth Tungstates of the Type $M_2(WO_4)_3$. *J. Am. Ceram. Soc.* **47**, 363 (1964).

[87] K. Nassau, H. J. Levinstein, and G. M. Loiacono: A comprehensive study of trivalent tungstates and molybdates of the type $L_2(MO_4)_3$. *J. Phys. Chem. Solids* **26**, 1805 (1965).

[88] S. C. Abrahams and J. L. Bernstein: Crystal Structure of the Transition-Metal Molybdates and Tungstates. II. Diamagnetic $Sc_2(WO_4)_3$. *J. Chem. Phys.* **45**, 2745 (1966).

[89] A. W. Sleight and L. H. Brixner: A New Ferroelastic Transition in Some $A_2(MO_4)_3$ Molybdates and Tungstates. *J. Solid State Chem.* **7**, 172 (1973).

[90] N. Imanaka, M. Hiraiwa, G. Adachi, et al.: Thermal contraction in $Al_2(WO_4)_3$ single crystal. *J. Cryst. Growth* **220**, 176 (2000).

[91] D. A. Woodcock, P. Lightfoot, and C. Ritter: Negative thermal expansion in $Y_2(WO_4)_3$. *J. Solid State Chem.* **149**, 92 (2000).

[92] S. Sumithra, A. K. Tyagi, and A. M. Umarji: Negative thermal expansion in $Er_2W_3O_{12}$ and $Yb_2W_3O_{12}$ by high temperature X-ray diffraction. *Mater. Sci. Eng., B* **116**, 14 (2005).

[93] P. M. Forster and A. W. Sleight: Negative thermal expansion in $Y_2W_3O_{12}$. *Int. J. Inorg. Mater.* **1**, 123 (1999).

[94] J. S. O. Evans and T. A. Mary: Structural phase transitions and negative thermal expansion in $Sc_2(MoO_4)_3$. *Int. J. Inorg. Mater.* **2**, 143 (2000).

[95] A. K. Tyagi, S. N. Achary, and M. D. Mathews: Phase transition and negative thermal expansion in $A_2(MoO_4)_3$ system (A = Fe^{3+}, Cr^{3+} and Al^{3+}). *J. Alloys Compd.* **339**, 207 (2002).

[96] M. M. Martinez-Inesta, I. Peral, T. Proffen, et al., Pair distribution function analysis of the structure of zeolite beta and of the negative thermal expansion mechanism of chabazite, *227th ACS National Meeting - Abstracts of Papers*, (2004).

[97] E. J. Baran, I. L. Botto, N. Kinomura, et al.: The infrared spectra of the two polymorphic forms of tungsten oxide phosphate ($WOPO_4$). *J. Solid State Chem.* **89**, 144 (1990).

[98] J.-Z. Tao, Theory of negative thermal expansion, Oregon State University, Corvallis, Oregon, (2003).

[99] I. D. Brown and R. D. Shannon: Empirical bond-strength-bond-length curves for oxides. *Acta Crystallogr., Sect. A* **29**, 266 (1973).

[100] A. K. A. Pryde, K. D. Hammonds, M. T. Dove, et al.: Origin of the Negative Thermal Expansion in ZrW_2O_8 and ZrV_2O_7. *J. Phys. Condens. Matter* **8**, 10973 (1996).

[101] A. K. A. Pryde, K. D. Hammonds, M. T. Dove, et al.: Rigid Unit Modes and the Negative Thermal Expansion in ZrW_2O_8. *Phase Transitions* **61**, 141 (1997).

[102] A. K. A. Pryde, M. T. Dove, and V. Heine: Simulation studies of ZrW_2O_8 at high pressure. *J. Phys.: Condens. Matter* **10**, 8417 (1998).

[103] T. R. Ravindran, A. K. Arora, and T. A. Mary: High-pressure Raman spectroscopic study of zirconium tungstate. *J. Phys.: Condens. Matter* **13**, 11573 (2001).

[104] D. A. Fleming, D. W. Johnson, and P. J. Lemaire, Article Comprising a Temperature Compensated Optical Fiber Refractive Index Grating, US Patent 5,694,503, Lucent Technologies, USA (1997).

[105] D. A. Fleming, P. J. Lemaire, and D. W. Johnson, Temperature compensated optical fiber refractive index grating, European Patent EP 97-306798 19970902, Lucent Technologies, Inc., USA (1998).

[106] C. Verdon and D. C. Dunand: High-Temperature Reactivity in the ZrW_2O_8-Cu System. *Scr. Mater.* **36**, 1075 (1997).

[107] H. Holzer and D. C. Dunand: Phase transformation and thermal expansion of Cu/ZrW_2O_8 metal matrix composites. *J. Mater. Res.* **14**, 780 (1999).

[108] E. K. Graham: The multianvil press. *Methods Exp. Phys.* **24**, 237 (1987).

[109] R. Miletich and R. J. Angel, in *NATO Science Series, Series C: Mathematical and Physical Sciences*, Vol. C543, p. 1, edited by K. Wright and R. Cartlow, Kluwer Academic Publishers (1999).

[110] G. J. Piermarini: High Pressure X-ray Crystallography With the Diamond Cell at NIST/NBS. *J. Res. NIST* **6**, 889 (2001).

[111] J.-a. Xu, H.-k. Mao, R. J. Hemley, et al.: The moissanite anvil cell: a new tool for high-pressure research. *J. Phys.: Condens. Matter* **14**, 11543 (2002).

[112] J. D. Barnett, S. Block, and G. J. Piermarini: An Optical Fluorescence System for Quantitative Pressure Measurement in the Diamond-Anvil Cell. *Rev. Sci. Instrum.* **44**, 1 (1973).

[113] R. Miletich, D. Allan, R., and W. Kuhs, F.: High-Pressure Single-Crystal Techniques. *Rev. Mineral. Geochem.* **41**, 445 (2001).

[114] B. Chen, High-pressure study on borides, nanocrystals and negative thermal expansion materials, PhD Thesis, University of Missouri, Kansas City, Missouri, (2001).

[115] R. Mittal, S. L. Chaplot, H. Schober, et al.: Origin of negative thermal expansion in cubic ZrW_2O_8 and $ZrMo_2O_8$: High pressure inelastic neutron scattering study. *Solid State Phys. (India)* **44**, 656 (2001).

[116] Y. Yamamura, N. Nakajima, T. Tsuji, et al.: Low-temperature heat capacities and Raman spectra of negative thermal expansion compounds ZrW_2O_8 and HfW_2O_8. *Phys. Rev. B* **66**, 014301 (2002).

[117] S. M. Bennington, J. Li, M. J. Harris, et al.: Phonon softening in ice Ih. *Physica B* **263-264**, 396 (1999).

[118] B. Chen, D. V. S. Muthu, Z. X. Liu, et al.: High-pressure Raman and infrared study of HfW_2O_8. *Phys. Rev. B* **64**, 214111 (2001).

[119] R. Mittal, S. L. Chaplot, A. I. Kolesnikov, et al.: Inelastic neutron scattering and lattice dynamical calculation of negative thermal expansion in HfW_2O_8. *Phys. Rev. B* **68**, 054302 (2003).

[120] S. K. Sikka and S. M. Sharma, Mechanisms of pressure induced phase transitions, *International Conference on Advances in Physical Metallurgy*, 399 (1994).

[121] R. A. Young, Mechanism of the phase transition in quartz, government report, O. o. T. S. United States Department of Commerce, AD, **276**, 156 (1962).

[122] O. Mishima, L. D. Calvert, and E. Whalley: 'Melting ice' I at 77 K and 10 kbar: a new method of making amorphous solids. *Nature* **310**, 393 (1984).

[123] R. J. Hemley, A. P. Jephcoat, H.-k. Mao, et al.: Pressure-induced amorphization of crystalline silica. *Nature* **334**, 52 (1988).

[124] M. B. Kruger and R. Jeanloz: Memory Glass: An Amorphous Material Formed from $AlPO_4$. *Science* **249**, 647 (1990).

[125] E. G. Ponyatovsky and O. I. Barkalov: Pressure-induced amorphous phases. *Mater. Sci. Rep.* **8**, 147 (1992).

[126] A. Jayaraman, S. K. Sharma, Z. Wang, et al.: Pressure-induced amorphization of $Tb_2(MoO_4)_3$: a high pressure Raman and x-ray diffraction study. *J. Phys. Chem. Solids* **54**, 827 (1993).

[127] S. M. Sharma and S. K. Sikka: Pressure Induced Amorphization of Materials. *Prog. Mater. Sci.* **40**, 1 (1996).

[128] P. Richet and P. Gillet: Pressure-induced amorphization of minerals: a review. *Eur. J. Mineral.* **9**, 907 (1997).

[129] J. Badro, P. Gillet, and J.-L. Barrat: Melting and pressure-induced amorphization of quartz. *Europhys. Lett.* **42**, 643 (1998).

[130] T. Sakuntala, A. K. Arora, N. V. Chandra Shekar, et al.: Pressure-induced amorphization and orientational disorder in potash alum. *J. Phys.: Condens. Matter* **12**, 4417 (2000).

[131] V. Dmitriev, V. Sinitsyn, R. Dilanian, et al.: In situ pressure-induced solid-state amorphization in $Sm_2(MoO_4)_3$, $Eu_2(MoO_4)_3$ and $Gd_2(MoO_4)_3$ crystals: chemical decomposition scenario. *J. Phys. Chem. Solids* **64**, 307 (2003).

[132] H. Liu, R. A. Secco, N. Imanaka, et al.: X-ray diffraction study of pressure induced amorphization in $Lu_2(WO_4)_3$. *Solid State Commun.* **121**, 177 (2002).

[133] Y. Fujii, M. Kowaka, and A. Onodera: The pressure-induced metallic amorphous state of SnI_4: I. A novel crystal-to-amorphous transition studied by x-ray scattering. *J. Phys. C: Solid State Phys.* **18**, 789 (1985).

[134] S. Sugai: The pressure-induced metallic amorphous state of SnI_4: II. Lattice vibrations at the crystal-to-amorphous phase transition studied by Raman scattering. *J. Phys. C: Solid State Phys.* **18**, 799 (1985).

[135] R. J. Speedy: Models for the amorphization of compressed crystals. *J. Phys.: Condens. Matter* **8**, 10907 (1996).

[136] A. K. Arora: Pressure-induced amorphization versus decomposition. *Solid State Commun.* **115**, 665 (2000).

[137] T. Yamanaka, T. Nagai, and T. Tsuchiya: Mechanism of pressure-induced amorphization. *Z. Kristallogr.* **212**, 401 (1997).

[138] S. K. Sikka: Negative thermal expansion and its relation to high pressures. *J. Phys.: Condens. Matter* **16**, S1033 (2004).

[139] M. Micoulaut: Structure of densified amorphous germanium dioxide. *J. Phys.: Condens. Matter* **16**, L131 (2004).

[140] M. P. Pasternak, G. K. Rozenberg, A. P. Milner, et al.: Pressure-induced amorphization of antiferromagnetic $FePO_4$. *J. Magn. Magn. Mater.* **183**, 185 (1998).

[141] L. Pauling: Principles determining the structure of high-pressure forms of metals: the structures of cesium(IV) and cesium(V). *Proc. Nat. Acad. Sci. USA* **86**, 1431 (1989).

[142] G. Shen, N. Sata, N. Taberlet, et al.: Melting studies of indium: determination of the structure and density of melts at high pressures and high temperatures. *J. Phys.: Condens. Matter* **14**, 10533 (2002).

[143] S. K. Sikka and S. M. Sharma: Close packing and pressure-induced amorphization. *Curr. Sci.* **63**, 317 (1992).

[144] R. R. Winters, G. C. Serghiou, and W. S. Hammack: Observation and explanation of the reversible pressure-induced amorphization of $Ca(NO_3)_2$ /$NaNO_3$. *Phys. Rev. B* **46**, 2792 (1992).

[145] S. A. T. Redfern: Length scale dependence of high-pressure amorhization: the static amorphization of anorthite. *Miner. Mag.* **60**, 493 (1996).

[146] J. D. Jorgensen, Z. Hu, S. Teslic, et al.: Pressure -induced cubic-to-orthorhombic phase transition in ZrW_2O_8. *Phys. Rev. B* **59**, 215 (1999).

[147] C. Lind, A. P. Wilkinson, Z. Hu, et al.: Synthesis and Properties of the Negative Thermal Expansion Material Cubic Zirconium Molybdate. *Chemistry of Materials* **10**, 2335 (1998).

[148] S. Carlson and A. M. Krogh Andersen: High-pressure properties of TiP_2O_7, ZrP_2O_7 and ZrV_2O_7. *J. Appl. Cryst.* **34**, 7 (2000).

[149] S. Carlson: High-pressure studies of the cubic to rhombohedral transformation in NbO_2F. *J. Appl. Crystallogr.* **33**, 1175 (2000).

[150] J. Z. Jiang, J. S. Olsen, L. Gerward, et al.: Enhanced bulk modulus and reduced transition pressure in γ-Fe_2O_3 nanocrystals. *Europhys. Lett.* **44**, 620 (1998).

[151] Y. Fei, in *Mineral Physics and Crystallography: A Handbook of Physical Constants*, Vol., p., American Geophysical Union, Washington, DC (1995).

[152] N. L. Ross: The equation of state and high-pressure behavior of magnesite. *Am. Mineral.* **82**, 682 (1997).

[153] D. L. Decker: High-Pressure Equation of State for NaCl, KCl, and CsCl. *J. Appl. Phys.* **42**, 3239 (1971).

[154] A. Grzechnik and W. A. Crichton: Structural transformations in cubic $ZrMo_2O_8$ at high pressures and high temperatures. *Solid State Sci.* **4**, 1137 (2002).

[155] C. Lind, D. G. VanDerveer, A. P. Wilkinson, et al.: New high pressure form of the negative thermal expansion materials zirconium molybdate and hafnium molybdate. *Chem. Mater.* **13**, 487 (2001).

[156] J. S. O. Evans, Z. Hu, J. D. Jorgensen, et al.: Compressibility, Phase Transitions, and Oxygen Migration in Zirconium Tungstate, ZrW_2O_8. *Science* **275**, 61 (1997).

[157] Z. Hu, J. D. Jorgensen, S. Teslic, et al.: Pressure-induced phase transformation in ZrW_2O_8 - Compressibility and thermal expansion of the orthorhombic phase. *Physica B* **241-243**, 370 (1998).

[158] J. M. Gallardo-Amores, U. Amador, E. Moran, et al.: XRD study of ZrW_2O_8 versus temperature and pressure. *Int. J. Inorg. Mater.* **2**, 123 (2000).

[159] J. D. Jorgensen, Z. Hu, S. Short, et al.: Pressure-induced cubic-to-orthorhombic phase transfromation in the negative thermal expansion material HfW_2O_8. *J. Appl. Phys.* **89**, 3184 (2001).

[160] S. Carlson and A. M. Krogh Andersen: High-pressure properties of TiP_2O_7, ZrP_2O_7 and ZrV_2O_7. *J. Appl. Crystallogr.* **34**, 7 (2000).

[161] W. Paraguassu, M. Maczka, A. G. Souza Filho, et al.: Pressure-induced structural transformations in the molybdate $Sc_2(MoO_4)_3$. *Phys. Rev. B* **69**, 094111(1 (2004).

[162] T. Varga, A. P. Wilkinson, C. Lind, et al.: In-situ high pressure synchrotron x-ray diffraction study of $Sc_2W_3O_{12}$ at up to 10 GPa. *submitted to Phys. Rev. B*, (2005).

[163] M. Maczka, W. Paraguassu, A. G. Souza Filho, et al.: High-pressure Raman study of $Al_2(WO_4)_3$. *J. Solid State Chem.* **177**, 2002 (2004).

[164] G. D. Mukherjee, S. N. Achary, A. K. Tyagi, et al.: High pressure AC resistivity and compressibility study on $Al_2(WO_4)_3$. *J. Phys. Chem. Solids* **64**, 611 (2003).

[165] D. K. Balch and D. Dunand, C.: Copper-Zirconium Tungstate Composites Exhibiting Low and Negative Thermal Expansion Influenced by Reinforcement Phase Transformations. *Metall. Mater. Trans. A* **35A**, 1159 (2004).

[166] C. A. Perottoni and J. A. H. de Jornada: Pressure-Induced Amorphization and Negative Thermal Expansion in ZrW_2O_8. *Science* **280**, 886 (1998).

[167] A. K. Arora, R. Nithya, T. Yagi, et al.: Two-stage amorphziation of scandium molybdate at high pressure. *Solid State Commun.* **129**, 9 (2004).

[168] R. A. Secco, H. Liu, N. Imanaka, et al.: Pressure-induced amorphization in negative thermal expansion $Sc_2(WO_4)_3$. *J. Mater. Sci. Lett.* **20**, 1339 (2001).

[169] A. Grzechnik, W. A. Crichton, K. Syassen, et al.: A New Polymorph of ZrW_2O_8 Synthesized at High Pressures and High Temperatures. *Chem. Mater.* **13**, 4255 (2001).

[170] T. Hashimoto, T. Katsube, and Y. Morito: Observation of two kinds of phase transition of ZrW_2O_8 by power-compensated differential scanning calorimetry and high-temperature X-ray diffraction. *Solid State Commun.* **116**, 129 (2000).

[171] Y. Yamamura, N. Nakajima, and T. Tsuji: Calorimetric and x-ray diffraction studies of α–to–β structural phase transitions in HfW_2O_8 and ZrW_2O_8. *Phys. Rev. B* **64**, 184109 (2001).

[172] Y. Yamamura, T. Tsuji, K. Saito, et al.: Heat capacity and order-disorder phase transition in negative thermal expansion compound ZrW_2O_8. *J. Chem. Thermodyn.* **36**, 525 (2004).

[173] T. Hashimoto, T. Katsube, and Y. Morito: Observation of two kinds of phase transition of ZrW_2O_8 by power-compensated differential scanning calorimetry and high-temperature X-ray diffraction. *Solid State Communications* **116**, 129 (2000).

[174] D. Taylor: Thermal Expansion Data: IV Binary Oxides with the silica structures. *Br. Ceram. Trans. J.* **83**, 129 (1984).

[175] T. A. Mary, V. Korthuis, N. Khosrovani, et al., in *Ceramic Transactions*, Vol. 52 (Low-Expasion Materials), p. 81, edited by D. P. Stinron and S. Y. Limaye, American Ceramic Society, Westerville, OH (1995).

[176] G. Muller, in *Low Thermal Expansion Glass Ceramics*, Vol., p. 13, edited by H. Bach, Springer (1995).

[177] D. C. Palmer: Stuffed Derivatives of the Silica Polymorphs. *Rev. Miner.* **29**, 83 (1994).

[178] H. Xu, P. J. Heaney, and A. Navrotsky: Thermal expansion and structural transformations of stuffed derivatives of quartz along the $LiAlSiO_4$-SiO_2 join: a variable-temperature powder synchrotron XRD study. *Phys. Chem. Miner.* **28**, 302 (2001).

[179] T. Tsuji, Y. Yamamura, and N. Nakajima: Thermodynamic properties of negative thermal expansion materials ZrW_2O_8 substituted for Zr site. *Thermochim. Acta* **416**, 93 (2004).

[180] A. A. Bokov, I. P. Rayevskii, V. G. Smotrakov, et al.: Kinetics of Compositional Ordering in $Pb_2B'B''O_6$ Crystals. *Phys. Status Solidi A* **93**, 411 (1986).

[181] P. Groves: The influence of B-site cation order on the phase transition behaviour of antiferroelectric lead indium niobate. *J. Phys. C: Solid State Phys.* **19**, 5103 (1986).

[182] P. Groves: Structural phase transitions and long-range order in ferroelectric perovskite lead indium niobate. *J. Phys. C: Solid State Phys.* **19**, 111 (1986).

[183] N. Yasuda and S. Shibuya: Ferroelectricity in disordered $Pb(In_{1/2}Nb_{1/2})O_3$. *J. Phys.: Condens. Matter* **1**, 10613 (1989).

[184] K. Z. Baba-Kishi, G. Cressey, and R. J. Cernik: X-ray and Electron Diffraction Studies of the Structure of Pseudo-Perovskite Compounds $Pb_2(Sc, Ta)O_6$ and $Pb_2(Mg,W)O_6$. *J. Appl. Crystallogr.* **25**, 477 (1992).

[185] L. E. Cross: Relaxor ferroelectrics. *Ferroelectrics* **76**, 241 (1987).

[186] M. P. Harmer, J. Chen, P. Peng, et al.: Control of Microchemical Ordering in Relaxor Ferroelectrics and Related Compounds. *Ferroelectrics* **97**, 263 (1989).

[187] N. Setter and L. E. Cross: The contribution of structural disorder to diffuse phase transitions in ferroelectrics. *J. Mater. Sci.* **15**, 2478 (1980).

[188] N. Setter and L. E. Cross: The role of B-site cation disorder in diffuse phase transition behavior of perovskite ferroelectrics. *J. Appl. Phys.* **51**, 4356 (1980).

CHAPTER 2

INSTRUMENTATION AND DATA ANALYSIS

2.1 Laboratory x-ray diffraction

Laboratory x-ray diffraction was extensively used in the characterization of the compounds described in this dissertation. The following paragraphs give an overview of the equipment and software that were used for data collection and analysis.

2.1.1 Powder x-ray diffraction at Georgia Tech

Most of the laboratory diffraction data presented in Chapters 6 and 7 were collected on a Scintag X1 diffractometer with a Cu tube and a Peltier-cooled solid state detector. The variable temperature measurements made use of a Scintag High-Low temperature stage that allowed data collection between –196 ^{o}C (with liquid nitrogen) and 300 ^{o}C under vacuum (see Figure 2.1). In order to correct for small variations in sample height due to changes in the size of the copper-stainless steel block that supports the sample holder and possible changes in the thickness of the sample between runs, all the samples for variable temperature measurements were mixed with a silicon internal standard (Alfa Aesar, Ward Hill, MA). The position of the strongest reflection for silicon was used for initial adjustment of the sample height at room temperature. In order to suppress the correlation between the sample height and the lattice constants of the sample in Rietveld refinements, the lattice constant of the standard was fixed at a value expected for each

temperature and the sample height for the standard and sample phases were constrained to be identical.

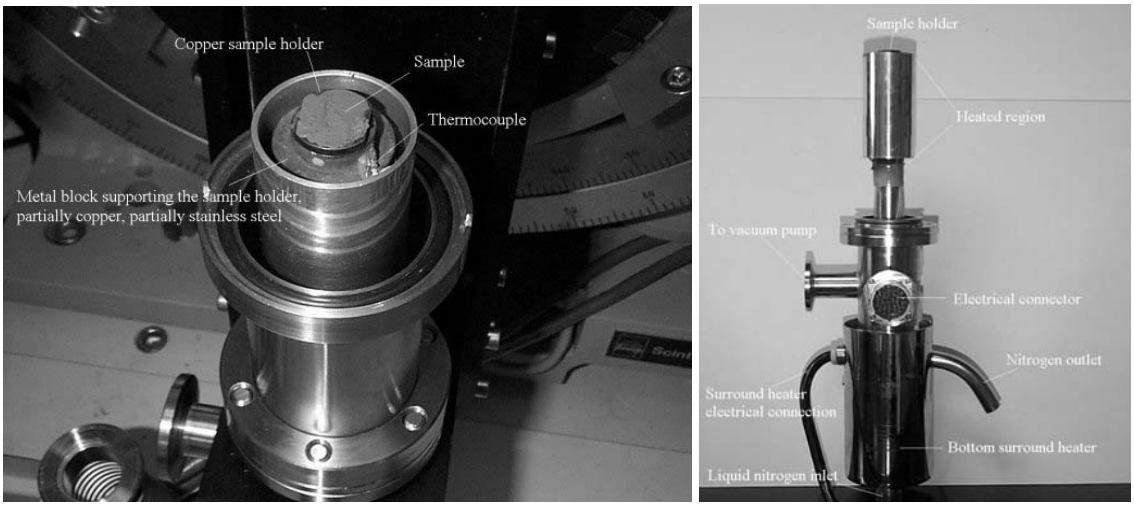

Figure 2.1: Experimental setup for variable temperature x-ray diffraction and the assembly of the high-low temperature stage. Taken from Lind.[1]

Some of the variable temperature measurements in Chapter 7 were carried out on an X'Pert PRO MPD diffractometer from PANalytical in the X-ray Analysis Group, Materials Science and Engineering, Georgia Tech. The PANalytical instrument's parallel beam configuration (PreFIX optics) with 0.04 degree Soller slits on the incident beam side and 0.09 degree parallel plate collimators on the diffracted beam side is very useful for variable temperature measurements due to its insensitivity to sample height variations. An Anton-Paar HTK1200 high-temperature furnace (see Figure 2.2) was used for these measurements.

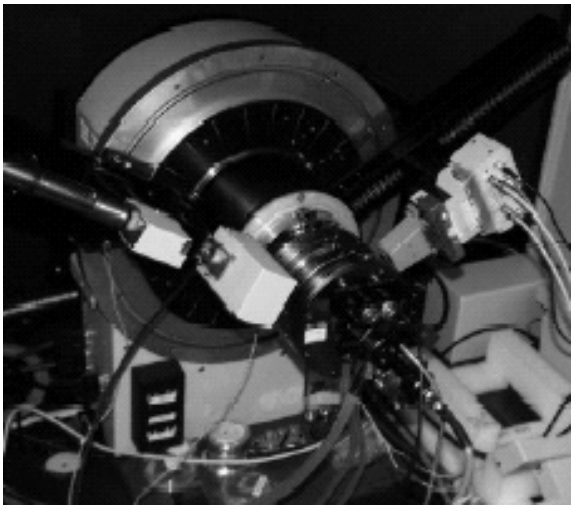

Figure 2.2: The Anton-Paar HTK1200 furnace. Taken from http://www.dur.ac.uk/john.evans/webpages/lab_xray_images.html.

2.1.2 Powder x-ray diffraction at Oak Ridge National Laboratory

Variable temperature x-ray diffraction experiments were carried out at the High Temperature Materials Laboratory, Oak Ridge National Laboratory (Oak Ridge, TN) on a Philips X'Pert PRO MPD x-ray powder diffractometer equipped with a high count rate proportional detector and an Anton-Paar XRK900 high-temperature stage. Polycapillary lens optics and parallel plate collimator with soller slits were used on the incident and diffracted beam sides, respectively. This configuration helped to eliminate the problem of the variation of sample height with temperature.

2.1.3 Single crystal diffraction at Virginia Tech and the Bayerisches Geoinstitut

The high-pressure single crystal x-ray diffraction measurements that constitute the basis of Chapter 8 were carried out on two Huber four-circle diffractometers with Eulerian-cradles, one at Virginia Tech (Blacksburg, VA) and one at the Bayerisches Geoinstitut (Bayreuth, Germany). The latter measurements were carried out by Ross J.

Angel, our collaborator on the work presented in Chapter 8. The physical parameters of the two diffractometers are very similar,[2] and described in detail in Chapter 8. These instruments are optimized for extremely precise measurements of lattice parameters at high-pressures in diamond-anvil cells.[3] The diffractometers were equipped with an unfiltered Mo sealed-tube X-ray source (Mo K_α radiation, 50 kV, 40 mA) without a monochromator to provide clean, stable and reproducible peak-profile shapes.

2.2 Synchrotron radiation and synchrotron x-ray diffraction

Synchrotron radiation is in many cases preferred over laboratory x-ray sources for a wide range of structural investigations. Synchrotrons are powerful radiation sources, their intensity is up to ~10^{10} times larger than that of laboratory x-ray tubes. Synchrotron radiation is produced when a charge (electron or positron) moving at relativistic speeds follows a curved trajectory. This trajectory is an enormous vacuum ring in which the electrons are radially accelerated by bending magnets, and therefore emit electromagnetic radiation (see Figure 2.3). In addition to its much higher intensity, which makes the observation of very weak signals possible, synchrotron radiation offers the following advantages:

- Much smaller angular divergence relative to laboratory x-rays (radiation from x-ray tube is almost uncollimated): the x-rays are emitted preferentially tangential to the ring resulting in very tight angular collimation in the vertical plane. This is very important when small samples are studied.
- Tunable energy from a broad spectral range by the use of monochromators in contrast to characteristic radiation from a tube source: the broad spectrum of white radiation

includes the x-ray region, and through the use of monochromator crystals monochromatic radiation of any energy can be selected (see Figure 2.4).

- Strongly polarized radiation in the plane of the acceleration of the electrons (possibility of linear, elliptical and circular polarization).
- Additional intensity can be gained by the use of insertion devices (wigglers, undulators): linear arrays of magnets that create more radiation.[4]
- The separated bunches of electrons provide a time structure to the radiation, which makes some highly specialized time-resolved measurements possible.

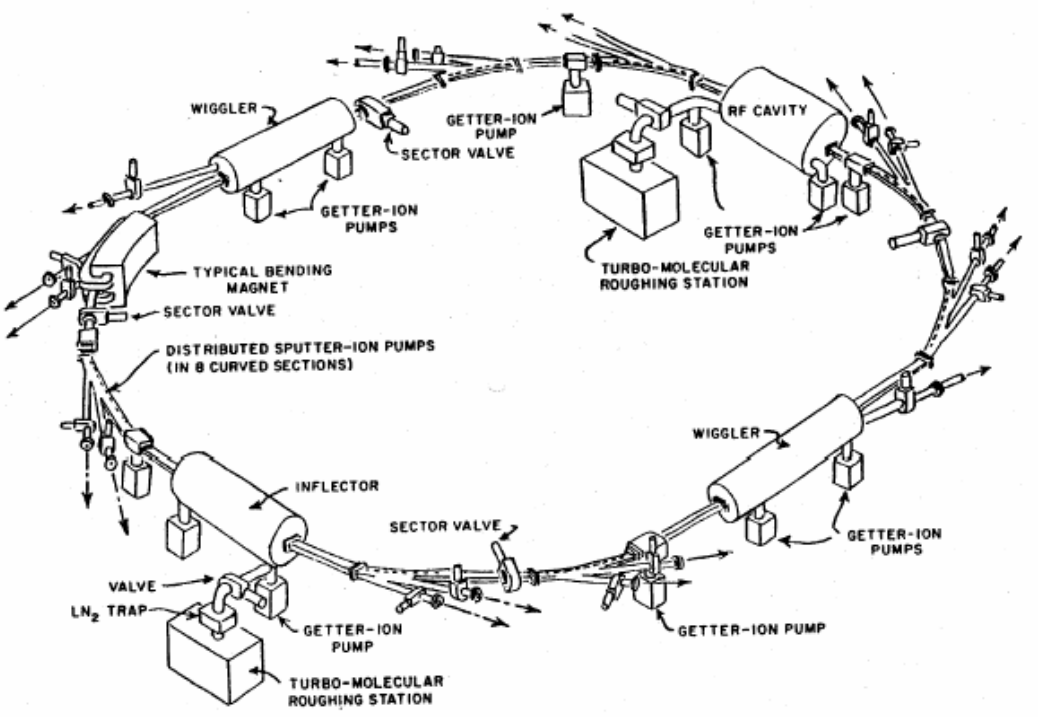

Figure 2.3: Schematic of the production of synchrotron radiation.

In our studies, the high intensity and tight angular collimation was invaluable for our high-pressure diffraction experiments where we looked at small samples in diamond anvil cells. A tunable source of x-rays was required for x-ray absorption spectroscopy

measurements. Furthermore, we needed synchrotron radiation when we desired diffraction data to higher Q (small d-spacing) values and better statistics at high Q than those achievable with copper radiation for our structural studies on doped ZrP_2O_7 phases (Chapter 6).

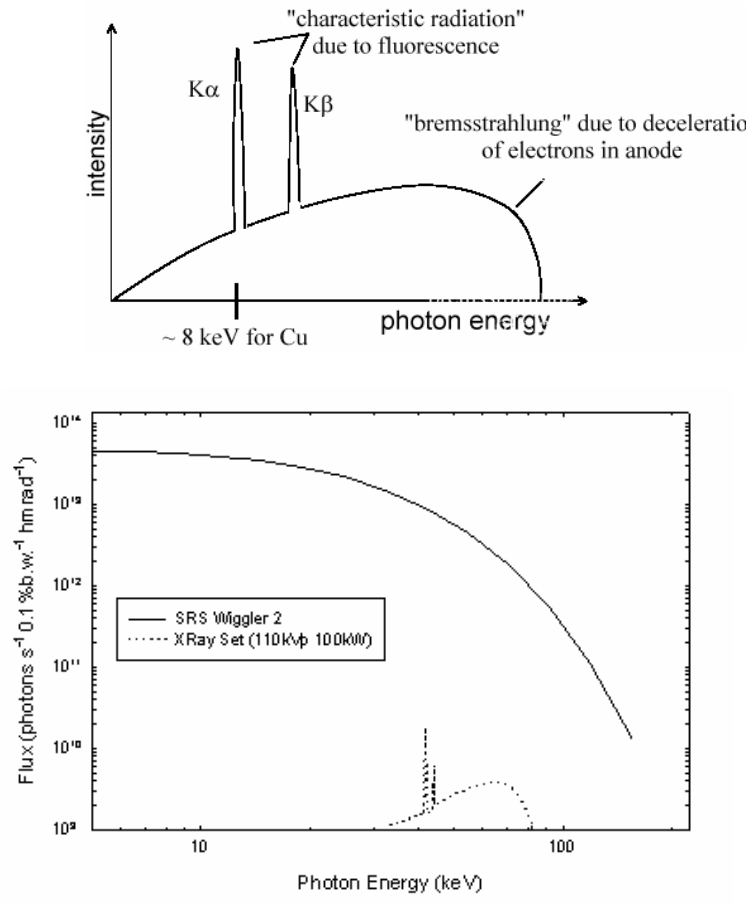

Figure 2.4: Comparison of the spectrum of laboratory x-ray radiation from a copper tube (top) with that of synchrotron radiation; the radiation spectrum from the Daresbury Synchrotron Radiation Source (bottom).[5]

Synchrotron x-ray diffraction measurements were performed at two different light sources for this thesis. High-pressure synchrotron x-ray diffraction measurements were carried out at the B-2 line of the Cornell High Energy Synchrotron Source (CHESS), Wilson Lab, Cornell University, Ithaca, NY. X-rays of the desired energy were selected

using a double-crystal monochromator and the beam was collimated and centered onto the sample cavity of the diamond anvil cell (DAC). Diffraction patterns were recorded on image plates (see setup in Figure 2.5).

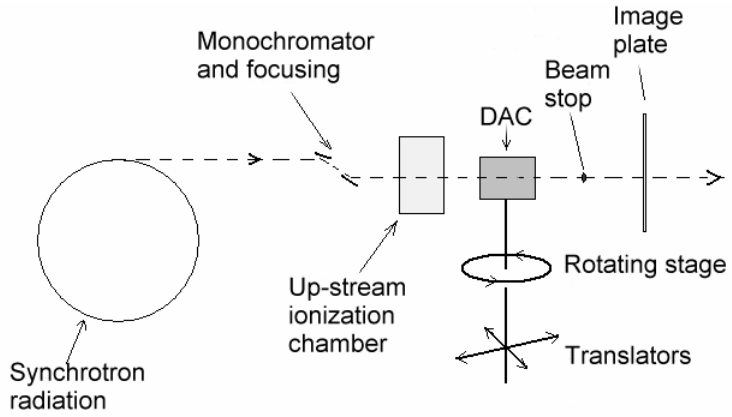

Figure 2.5: Scheme of the experimental setup for diffraction experiments at CHESS.

High-temperature synchrotron x-ray diffraction measurements were carried out at beamline X14A of the National Synchrotron Light Source, Brookhaven National Laboratory (BNL), Upton, NY. X-rays were monochromated using a Si(111) double-crystal monochromator. A gas proportional counter with krypton and CO_2 gas was used as detector. The samples were loaded into capillaries and placed in a capillary furnace for variable temperature measurements.

2.3 Powder neutron diffraction experiments

Neutrons, although a much more expensive source of radiation, are preferred over x-rays in many cases: (a) study of magnetic materials: neutrons have a spin and they can "see" magnetic order in solids as neutrons interact with electron spins, (b) study of light elements: neutrons are scattered by the atomic nuclei, not by electrons, and the scattering

power varies almost randomly and not systematically with atomic number (many light elements like H, O, Li are strong scatterers).

Neutrons for diffraction experiments can be produced from reactor sources or spallation sources. Neutrons from reactors have a Maxwellian distribution of speeds. The intensity is limited by the monochromation during which much of the neutrons are wasted. Spallation sources produce bursts of neutrons as opposed to a continuous beam. The energy distribution of the pulsed neutrons is different from the ideal gas-like distribution (see Figure 2.6). This results in significant neutron intensity over a wider energy range. Although the time average intensity of a spallation source at a particular wavelength is often much lower than in a reactor source, the overall usable neutron flux on the sample can be higher.

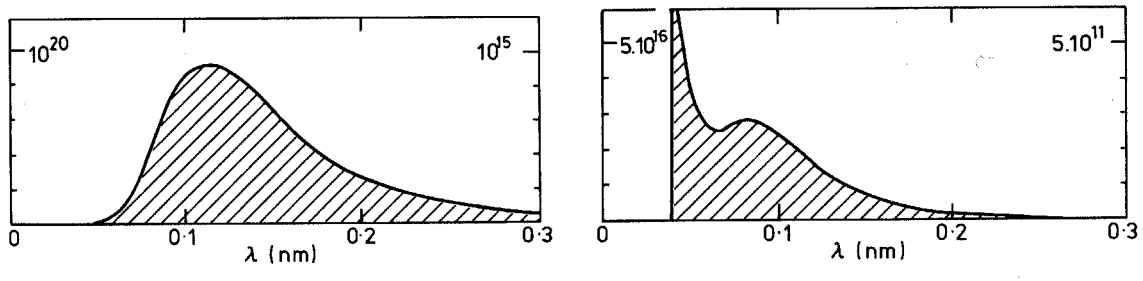

Figure 2.6: Comparison of the energy distribution of neutrons from the different sources: neutron flux from a reactor source (left), neutron flux from a spallation source (right). Taken from Windsor.[6]

Neutron diffraction experiments for this thesis were carried out at both reactor and spallation facilities. The neutron data reported in Chapter 6 were collected on the BT-1 high resolution powder diffractometer at the National Center for Neutron Research (NCNR) at NIST, Gaithersburg, MD. A schematic of the instrument is shown on Figure 2.7. A bank of detectors measures the scattered intensity as a function of scattering angle.

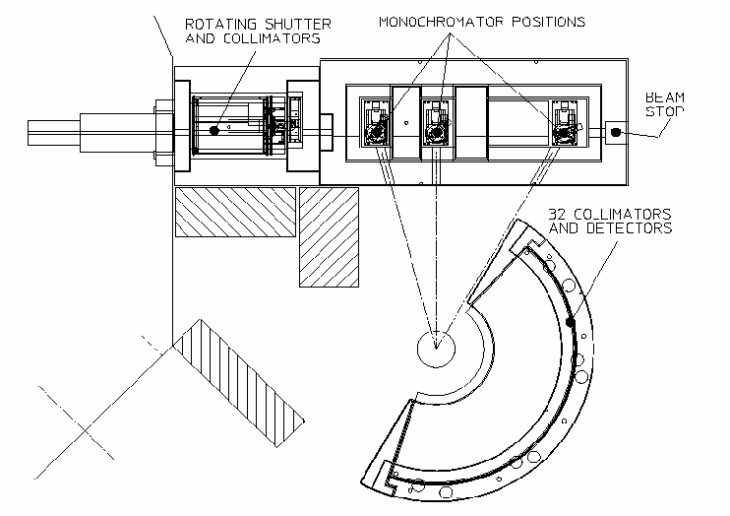

Figure 2.7: Schematic of the BT-1 neutron powder diffractometer at NIST. The diffractometer radius is ~1 m.[7]

Measurements for the neutron diffraction studies reported in Chapter 3 were performed on the Special Environment Powder Diffractometer (SEPD),[8] at the Intense Pulsed Neutron Source (IPNS) of Argonne National Laboratory, Argonne, IL. A schematic of the instrument is shown in Figure 2.8. Like most experiments performed at spallation sources, the experiment was a time-of-flight (TOF) type. In a typical neutron TOF experiment, the incoming neutron beam, the sample and the detectors are fixed. The detectors are arranged in "banks" at different angles. In each bank, the signal of all detectors that belong to the bank is averaged, giving an intensity-versus-time pattern of the diffracted neutron beam that can be converted to intensity versus d-spacing. The resolution of a TOF powder diffractometer depends on the incident and scattered flight path lengths. The neutrons with a range of energies come in pulses, their energy (and wavelength) can be determined by measuring the time it takes for the neutron to reach the detector banks.

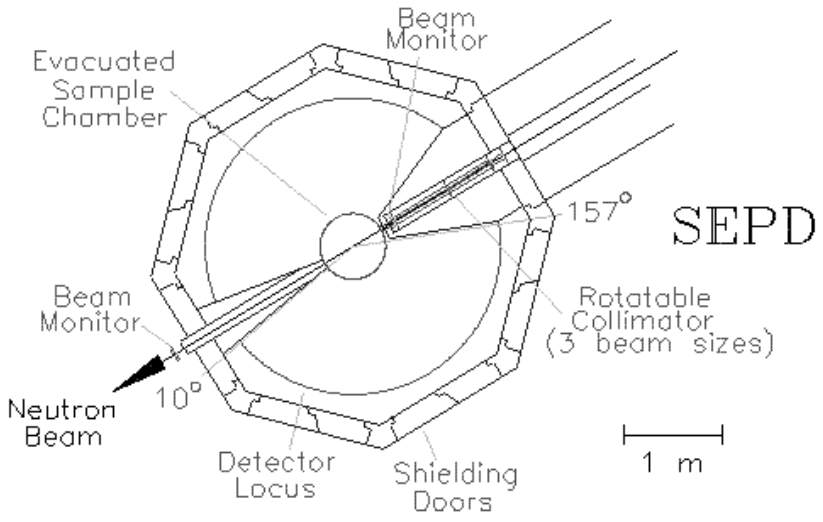

Figure 2.8: Schematic of the Special Environment Powder Diffractometer at IPNS.[8]

2.3.1 Analysis of diffraction data

2.3.1.1 Image plate data analysis

The use of two-dimensional detectors to record x-ray diffraction from solids is a standard practice both in the laboratory and at synchrotron facilities. Due to a large detector area, good x-ray sensitivity and a linear response over a large dynamic range, image plates are considered to be among the best detectors to record powder x-ray diffraction from small amounts of sample at ambient conditions or at very high pressure.[9] In an angle-dispersive x-ray diffraction experiment, such as the ones we carried out at CHESS, the diffracted x-rays from a powder sample in a diamond anvil cell at high pressure are recorded by a two-dimensional phosphor imaging plate detector. If the incoming x-ray beam is perpendicular to the plane of the image plate, Debye rings are recorded as circles (see Figure 2.9).

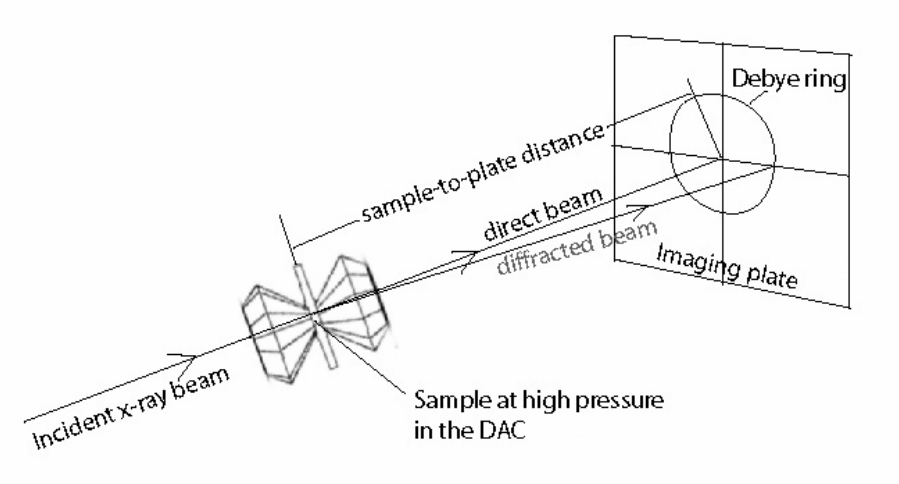

Figure 2.9: Schematic of angle-dispersive x-ray diffraction using imaging plate detection.

The image plates used to detect diffracted x-rays in the synchrotron experiments carried out at CHESS were read by a BAS 2000 scanner and integrated to give intensity versus 2θ values using the program SIMPA (Simplified Image Plate Analysis).[10]

2.3.1.2 Powder pattern analysis with the program JADE

The program JADE[11] was used to visualize the diffraction patterns after integration by SIMPA and to determine the positions of the NaCl peaks that were used for calculating the pressure in the diamond anvil cell in out high-pressure diffraction experiments. After background fitting, and selection of the peaks to be fitted, JADE can be used to refine the position and intensity of the individual peaks. JADE was also used for extraction of peak areas for the estimation of the amount of orthorhombic phase present in cubic ZrW_2O_8 under pressure in Chapter 4. Finally, JADE was used throughout this thesis work for the identification of phases present in powder samples.

2.3.1.3 Analysis of diffraction data: Rietveld refinement and Le Bail fittting

The General Structure Analysis System (GSAS) program[12] with the EXPGUI graphical user interface[13] was used for Rietveld analysis and Le Bail fitting of the x-ray and neutron diffraction data. High quality powder diffraction data in combination with the Rietveld method allows refinement of a structural model (atomic coordinates, site occupancies and atomic displacement parameters) as well as profile parameters (lattice constants, peak shape, sample height, instrument parameters, background). Changes in unit cell size (e.g. due to thermal expansion), in bond lengths and angles (e.g. due to compression) and other structural information can be extracted. Using the Le Bail method, one can perform fits with no structural model. In the present work, the lattice parameters for samples under high pressures were extracted by Le Bail fitting. This allowed us to obtain precise unit cell information without a good structural model.

2.4 X-ray absorption spectroscopy

X-rays are absorbed by matter through the photoelectric effect. An incident x-ray photon of sufficient energy can promote a core-level electron out of the atom and into the continuum. The atom is left in an excited state with an empty electronic level (a core hole). The electron that is ejected from the atom is called the photoelectron. The intensity of an x-ray beam passing through a material of thickness t is determined by the absorption coefficient μ:

$$\mu \cdot t = \ln \frac{I_0}{I} \qquad (1)$$

where I_0 is the intensity of the incident beam hitting the material and I is the intensity transmitted through the material. The absorption coefficient primarily depends on x-ray

energy and atomic number as well as on the density of the material. The absorption coefficient μ has sharp absorption edges corresponding to the characteristic core-level energies of the atom. Typical x-ray absorption spectra showing absorption edges for different elements are shown in Figure 2.10. In compounds, the absorption spectrum of each element is influenced by its local environment. All elements with atomic number Z > 18 have at least one absorption edge (either a K- or L-edge) between 3 and 35 keV, which can be accessed at many synchrotron sources.

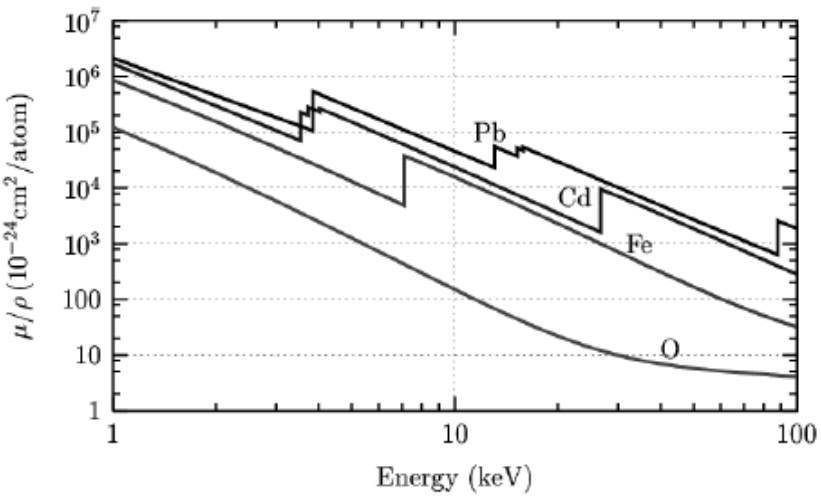

Figure 2.10: X-ray absorption spectrum of Pb, Cd, Fe and O showing the absorption edges for the metals. Taken from Newville.[14]

When x-rays are absorbed by the photoelectric effect, the excited core-hole will relax back to a lower energy state of the atom. A higher-level core electron drops into the core-hole, and a fluorescent x-ray or an Auger-electron is emitted. The energy of the fluorescent x-ray equals the difference between the core-levels. In the Auger effect, an electron is promoted to the continuum from another core-level. X-ray fluorescence and Auger emission occurs at discrete energies that are characteristic of the absorbing atom and thus can be used to identify the absorbing atom.

The energy-dependence of the x-ray absorption coefficient can consequently be measured in two ways; in transmission, when the absorption is measured directly by measuring what is transmitted through the sample, and in fluorescence, when the re-filling of the deep core-hole is detected and usually the fluorescence x-ray is measured. X-ray absorption spectroscopy (XAS) makes use of polychromatic x-rays produced by synchrotrons. The desired energy range corresponding to the absorption edge of the element under study is selected by diffraction from a double-crystal monochromator. XAS experiments focus either on a smaller energy region, within about 50 eV, around an absorption edge (X-ray Absorption Near Edge Spectroscopy, XANES) or on a larger energy range extending to far above an absorption edge (Extended X-ray Absorption Fine Structure, EXAFS). The corresponding XAS regions are shown in Figure 2.11.

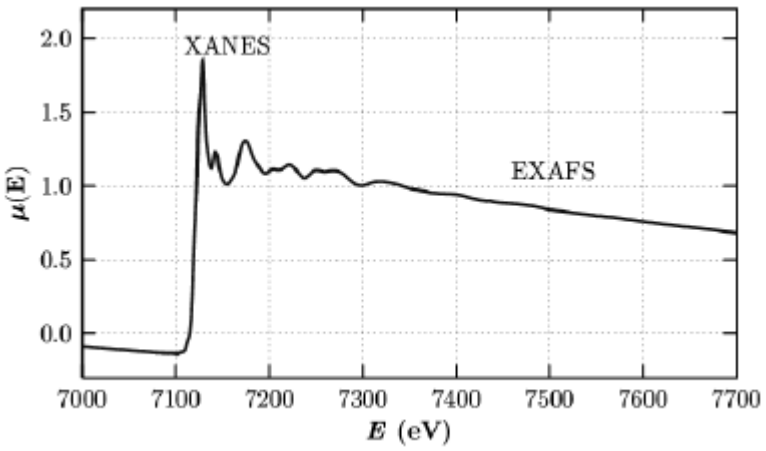

Figure 2.11: The XANES and EXAFS regions of the x-ray absorption spectrum. Taken from Newville.[14]

XAS is element specific and can yield information about the local environment of the atom of interest for both amorphous and crystalline materials. The XANES region contains information about the absorber atom, as the exact energy of the absorption edge and the presence of pre-edge features depend on its oxidation state and site symmetry.

EXAFS is an interference phenomenon. It carries information on the surrounding atoms: their type, number and distance from the absorber atom. The electron ejected from the "central" atom can be considered as an outgoing spherical wave. It will be backscattered by neighboring atoms, which results in an incoming wave that can interfere constructively and destructively with the outgoing wave. Interatomic distances extending out to several shells (up to ~6 Å for crystalline solids and good-quality data) and coordination numbers can be obtained from an EXAFS experiment. Atoms that differ by more than 3 in atomic number can be distinguished from each other.

XAS experiments for this thesis fall into two categories: high-pressure XAS studies carried out at CHESS, and variable temperature XAS measurements done at the National Synchrotron Light Source (NSLS) of Brookhaven National Laboratory (BNL). Both experiment types were complemented by measurements on reference samples at ambient conditions.

2.4.1 CHESS experiments

The high-pressure XAS measurements of Chapter 4 were carried out at beamline B-2 of CHESS in parallel with the diffraction measurements using the same double crystal monochromator and collimator. The transmission XAS measurements were carried out using two or three ion chambers. The two ion chamber arrangement is shown in Figure 2.12. In the three ion chamber setup, the DAC was between the first and second detector and a reference metal foil between the second and third detector. Conversion from the diffraction experimental setup (shown in Figure 2.5) to the XAS setup was straightforward: the beam stop and the image plate holder were removed from the optical

bench and replaced by the transmission and reference ion chambers, and the energy was changed to that of the appropriate absorption edge.

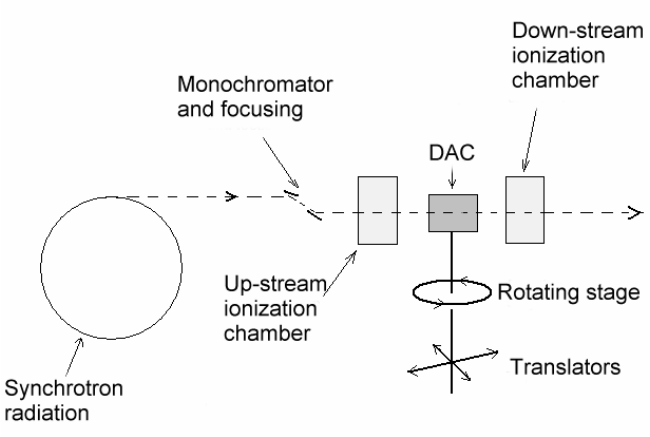

Figure 2.12: Experimental scheme for high-pressure XAS measurements at CHESS.

Diffraction of the x-rays from the single crystal diamond anvils can significantly contribute to the measured absorption, thus degrading data quality. Therefore, XAS data in the DAC were collected at several different orientations of the DAC so that the glitches due to diffraction from the diamonds occurred at different energies.

XAS data were also collected for a series of model compounds with different metal coordination environments at ambient pressure and temperature using samples that were diluted and ground with boron nitride and then packed into aluminum sample holders with Kapton tape windows so that the maximum value of μt was ~1.5 - 2. EXAFS and XANES scans were performed using appropriate monochromator detuning for harmonic rejection.

2.4.2 Variable temperature experiments at NSLS

The variable temperature XAS measurements discussed in Chapter 5 were carried out at beamline X11A of the National Synchrotron Light Source (NSLS), Brookhaven National Laboratory (BNL), Upton, NY. Data were collected under ambient pressure conditions, at several temperatures. A Displex refrigerator was used for measurements at low temperatures (as low as 55-65 K). The EXAFS and XANES data collection was done in transmission mode using a three ion chamber arrangement with a reference metal foil between the second and third detector. The samples were diluted and ground with boron nitride so that the maximum value of μt was ~1.5 - 2. Energy scans were performed around the corresponding metal absorption edges. The monochromator was detuned by a certain amount, depending on the absorption edge energy, for rejection of the higher harmonics.

2.5 High-pressure experiments

High-pressure experiments in this thesis work involved both *in-situ* studies using diamond anvil cells (DAC) and a He gas pressure cell, as well as high-pressure syntheses in a large multi-anvil press. In the latter case the samples were recovered to ambient conditions and used later for *ex-situ* studies. *In-situ* studies of samples under high pressure utilizing radiation require an appropriate container, a pressure cell. The pressure cell has two main roles: (1) it produces the pressure conditions to which we want to expose our samples and (2) it allows the radiation to reach the sample and exit out to the detector through appropriate "windows". High-pressure experiments also require highly penetrating radiation, as the sample is contained inside the pressure container.

Synchrotrons or neutron sources are usually used as radiation sources for diffraction. In some cases tube x-ray sources are also applied successfully, for example for high-pressure studies on large single crystals. There are many possible designs of pressure cells.[15] For high-pressure x-ray diffraction studies DACs,[16] for neutron studies the Paris-Edinburgh cell[17] and the He gas pressure cell[18] are most commonly used.

There are certain requirements for the sample studied and the pressure-transmitting medium used within a pressure cell as well. The sample, if a powder, should be completely dry, homogeneous and finely ground. Moisture may lead to chemical reactions under the conditions of the experiment or it can change the hydrostaticity of the pressure-transmitting medium. If the sample is a mixture of two or more components, e.g. sample and an internal pressure standard, inhomogeneity can lead to different pressure behavior as well as errors in the pressure calibration. Coarse samples generally cause the appearance of spots rather than smooth Debye rings in the diffraction image.

The pressure-transmitting medium should be chemically inert so that it does not react with the sample even under elevated pressure and temperature conditions. The degree of hydrostaticity within the pressure cell is also of great importance.[19] In high-pressure experiments it is often critical to ensure that the pressure applied to the sample crystal is homogeneous and free of any differential stress or shear strain. Only pressure-transmitting media that display hydrostatic behavior like a liquid or gas can provide homogeneous pressure conditions. However, all liquid and gas pressure-transmitting media solidify if exposed to high enough pressures. As the pressure medium into which the sample is immersed solidifies, it gives rise to nonhydrostatic pressure distribution around the sample. Nonhydrostaticity further increases as pressure rises. It may lead to

many kinds of problems, such as incorrect lattice constant determinations, undesired phase transitions, etc. Chapter 8 discusses a study of hydrostaticity in different grades of the pressure-transmitting medium fluorinert.

The high-pressure diffraction experiments discussed in this thesis were carried out at the B2 beamline of CHESS, Cornell University, Ithaca, NY (x-ray) and at the SEPD instrument of IPNS at Argonne National Laboratory, IL (neutron).

2.5.1 Diamond anvil cells

Diamond anvil cells are probably the most common pressure cells for *in-situ* diffraction studies. The generic types of DACs are the NBS cell, the Bassett cell, the Mao-Bell, the Syassen-Holzapfel and the Merril-Bassett cells,[15] but nowadays more options are available.

In a DAC, a small amount of sample, either powder or single-crystal is compressed between two, opposed diamond anvils typically less than a millimeter across. The sample is sitting in a gasket hole and is typically immersed in a pressure-transmitting medium. A material used for pressure-determination (e.g. ruby chips, NaCl) is also mixed into the sample. Compression force is often applied on the diamonds using screws in the steel casing. The gasket may be pre-indented for a certain amount of pressure depending on the experiment by compressing the gaskets (without sample) between the diamonds. The x-rays or neutrons enter the DAC through the table face of one anvil and the diffracted beam exits the cell through the opposed anvil. The schematic of a diamond anvil cell for diffraction is shown in Figure 2.13. The downstream cone opening of the DAC determines the usable 2θ-range of the diffraction data. Some DACs can be used up to

very high pressures, even to pressures of several hundred gigapascals (1 GPa = 10,000 atm).[20, 21]

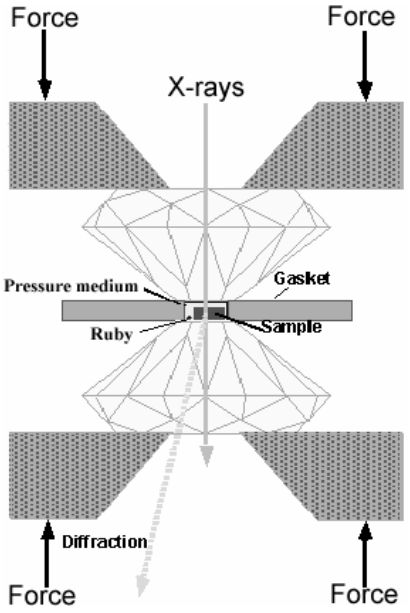

Figure 2.13: The principle of diamond anvil cell x-ray diffraction. The setup shown includes ruby chips mixed with the sample for purposes of pressure calibration (see section 2.5.4). Taken from Zha.[22]

In-situ high-pressure x-ray diffraction experiments in the present thesis utilized four different DAC designs: a hydrothermal DAC (HDAC) designed by the research group of Bassett,[23] a "BGI" (Bayerisches Geoinstitut, Bayreuth, Germany) design[19] and "ETH" (Swiss Federal Institute of Technology, Zurich, Switzerland) design[24] as well as a four-post DAC[25] were used. Images of the different designs are shown in the experimental part of the corresponding chapters.

2.5.2 He gas pressure cell

Our high-pressure neutron diffraction studies of Chapter 3 were carried out in a He gas pressure cell.[18] As neutron diffraction requires rather large sample volumes (up to

several cm^3), He gas cells are limited to relatively low pressures, around 0.65 PGa in our case, for safety reasons. Helium is claimed to provide hydrostatic pressure conditions up to 60-70 GPa.[19] It retains low shear strength to provide a quasi-hydrostatic environment even when it is a solid (~ >10 GPa).[26]

2.5.3 Multi-anvil press

Our high-pressure studies described in Chapters 4 and 5 involved the use of a Walker-type high-pressure multi-anvil press at the Mineral Physics Institute of SUNY Stony Brook, NY. This apparatus uses an octahedral arrangement of eight WC anvils to compress the octahedral sample cell. The size of the WC anvils and the edge length of the octahedral sample cell determine the maximum pressure that can be achieved. The press we used (shown in Figure 2.14) works with ~55 mm edge length cubes, and can reach pressures over 10 GPa. Heating of the sample under pressure is also possible using a graphite heater and a thermocouple. Details of the pressure cell used and the experimental conditions are discussed in the individual chapters.

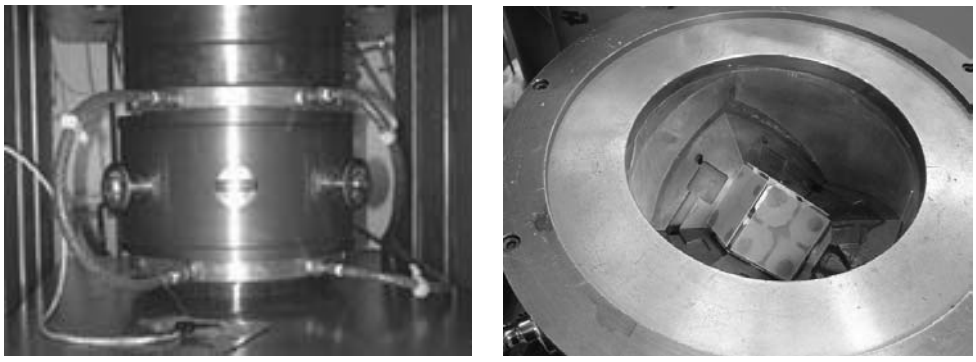

Figure 2.14: The Walker-type multi-anvil press at SUNY Stony Brook, NY: the hydraulic press (left) and the open multi-anvil apparatus with the octahedral pressure cell (right).

2.5.4 Determination of pressure

Two different pressure calibration techniques were applied in this work. One utilized the known variation of the unit cell parameters versus pressure (equation of state) of an internal pressure standard, or the sample itself, and the other method utilized the known shift of the ruby fluorescence lines with pressure (ruby fluorescence method).

In our high-pressure synchrotron powder diffraction experiments in an HDAC, NaCl was used as an internal pressure calibrant. It was mixed with the sample to give an approximate 4:1 = NaCl:sample weight ratio. NaCl is relatively soft, its bulk modulus (~25 GPa)[27, 28] is much less then those of the samples we studied, thus it provides near quasi-hydrostatic conditions at lower pressures. The pressure inside the HDAC was calculated using the program CALIBRATION,[29] which uses the Birch equation of state for NaCl.[27] The diffraction angle of a selected NaCl reflection was determined by fitting the pattern and then used in the calculation by the program.

Our high-pressure single crystal x-ray diffraction studies in Chapter 8 made use of the known variation of the cell parameters of quartz with pressure.[2]

The high-pressure synchrotron powder diffraction experiments carried out in a four-post DAC relied on the ruby fluorescence technique for pressure determination. This is an optical method for rapid routine measurement of pressure, which utilizes a pressure shift in the sharp R-line fluorescence spectrum of ruby (see Figure 2.15). The wavelength of the ruby R_1 fluorescent line shows a linear dependence with pressure. The precision of the pressure measurement in a hydrostatic environment up to 10 GPa is about 0.05 GPa.[30]

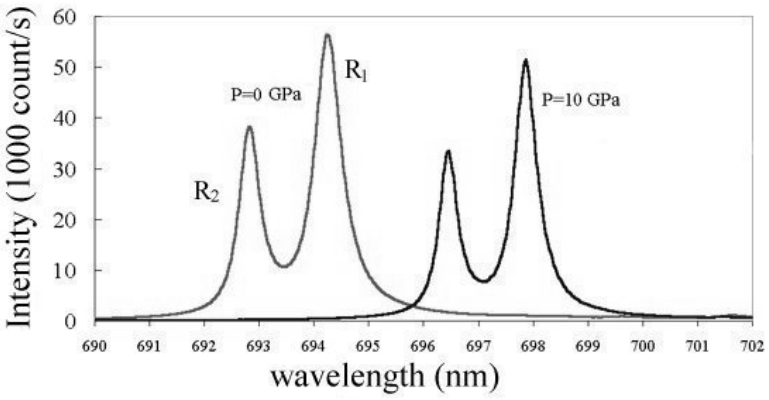

Figure 2.15: Example of the pressure dependence of ruby fluorescence lines. The frequency shifts of the R_1 and R_2 lines can be used for pressure determination based on equation 2.

The optical system for fluorescence calibration consists of a laser light source to excite the fluorescent radiation, an optics system for both the incident laser light and the fluorescent light, and a spectrometer for the spectral analysis of the fluorescence signal. The essential elements of the optics are a long working-length microscope and a dichroic mirror. A schematic diagram of the optical system is shown in Figure 2.16. Ruby fluorescence can be excited by the 441.6-nm line of a helium-cadmium laser or the 488.0 and 514.5-nm lines of an argon-ion laser. The process of pressure determination requires at least two measurements, one of the fluorescence spectrum from a reference sample at ambient pressure, and one of the equivalent material within the sample chamber at high pressure. The correlation of the measured wavelength shift $\Delta\lambda$ with applied pressure is the basis for the pressure determination inside the cell using the following formula:[19]

$$P(GPa) = 1904\ [(\Delta\lambda/\lambda_0)^B - 1] / B \qquad (2)$$

where $\Delta\lambda$ and λ_0 are the wavelength change under pressure and the wavelength at ambient pressure (in nm), respectively, and B is a parameter that corresponds to the

hydrostaticity within the pressure cell (non-hydrostatic: B = 5; quasi-hydrostatic: B = 7.665).[25]

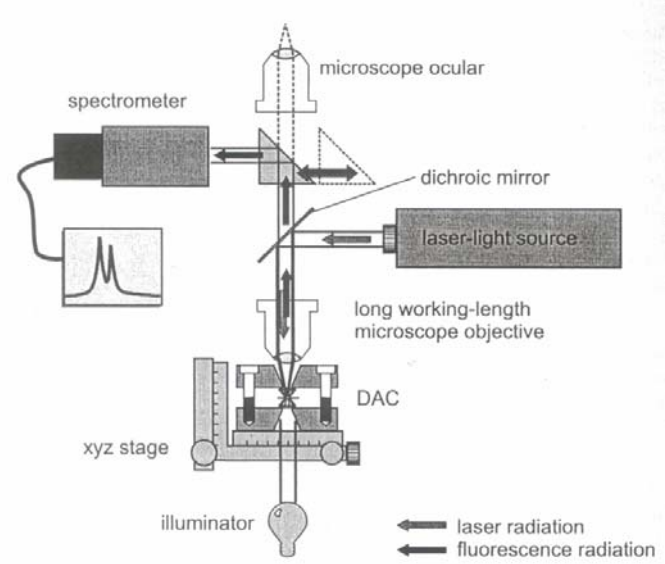

Figure 2.16: Schematic diagram of a fluorescence pressure calibration system. Taken from Miletich *et al*.[19]

2.5.5 Challenges of high-pressure XAS experiments

There are some difficulties associated with doing XAS in a DAC. We want to measure x-ray absorption by the sample but diffraction by the diamonds can make a strong contribution to the measured attenuation of the sample plus cell assembly at certain energies. In Figure 2.17, a section of the reciprocal lattice for diamond is shown along with Ewald spheres corresponding to the limits of the energy scan used in one of the absorption measurements. As the diamonds are single crystals, diffraction only occurs when the X-ray energy is such that a reciprocal lattice point for one of the diamonds lies on the Ewald sphere. The Ewald sphere will clearly move through several reciprocal lattice points as the x-ray energy is changed.

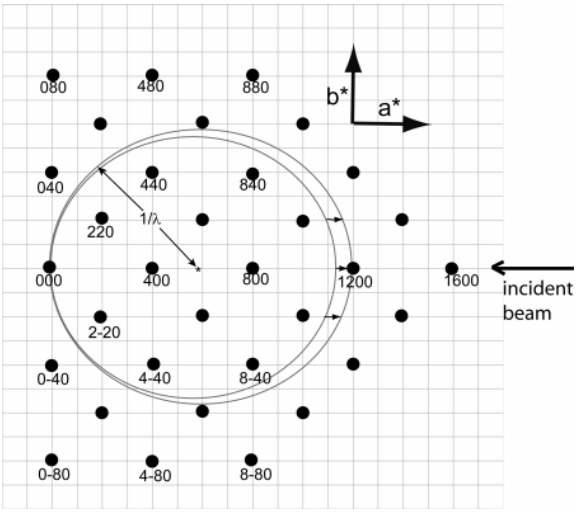

Figure 2.17: A section of the reciprocal lattice of diamond along with Ewald spheres corresponding to different energies. The spheres touch lattice points at certain energies.

In practice, for certain orientations of the diamond cell and at certain energies, attenuation will occur mainly due to diamond diffraction resulting in sharp peaks (glitches) in the absorption spectra. Those glitches degrade the quality of the data. Their effect was minimized by taking data at several cell orientations and producing composite spectra as described in Chapter 4. A "glitchy" spectrum versus an unglitched spectrum is shown in Figure 2.18. Two different methods were applied to eliminate the glitch problem and they are discussed in Chapter 4.

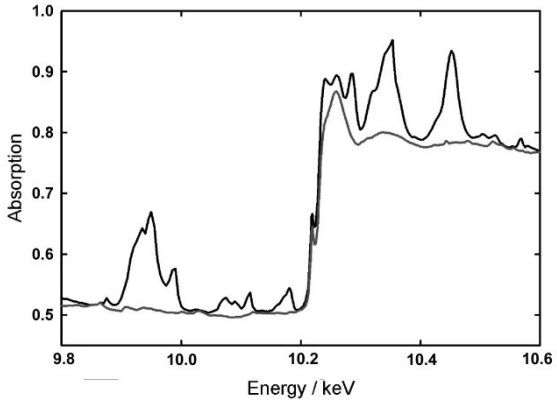

Figure 2.18: Comparison of an x-ray absorption spectrum affected by glitches due to diamond diffraction (upper, darker line) and a largely glitch-free spectrum (bottom, lighter line).

2.6 Thermal analysis

Thermal analysis methods are powerful techniques for the observation of phase transitions using small amounts of solid samples. Most crystallizations or crystal structure changes are accompanied by changes in the heat content of the sample, which can be measured by either Differential Scanning Calorimetry (DSC) or Differential Thermal Analysis (DTA). For the studies on pyrophosphates in Chapters 6 and 7, DSC was used. The measurements were made with a Seiko 220C DSC instrument at the School of Polymer, Textile & Fiber Engineering, Georgia Tech. The instrument can be used for experiments up to 600 °C both in nitrogen and in air.

In a typical DSC experiment, the sample and the reference are in separate furnaces and they are heated up so that they are always at the same temperature. The difference in heat required by the sample and the reference is measured. If the thermal event studied, such as a change in crystal structure, requires heat input to the sample (endothermic change), then a negative peak (endotherm) appears in the DSC (see Figure 2.19).

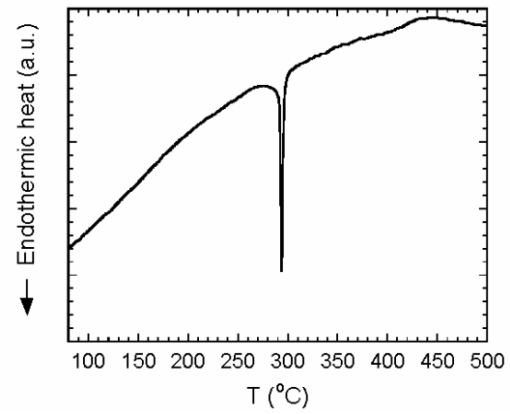

Figure 2.19: Endothermic peak in the DSC of ZrP_2O_7 showing the order-disorder phase transition in the material around 300 ^oC.

2.7 References

[1] C. Lind, Negative Thermal Expansion Materials Related to Cubic Zirconium Tungstate, PhD Thesis, Georgia Institute of Technology, Atlanta, GA, (2001).

[2] R. J. Angel, D. R. Allan, R. Miletich, et al.: The Use of Quartz as an Internal Pressure Standard in High-Pressure Crystallography. *J. Appl. Crystallogr.* **30**, 461 (1997).

[3] R. J. Angel, R. T. Downs, and L. W. Finger: High-Temperature - High-Pressure Diffractometry. *Rev. Mineral. Geochem.* **41**, 559 (2001).

[4] S. D. Shastri, R. J. Dejus, D. R. Haeffner, et al.: Performance of Advanced Photon Source insertion devices at high photon energies (50-300 keV). *Rev. Sci. Instrum.* **67**, 3346 (1996).

[5] D. S. R. Source, http://detserv1.dl.ac.uk/Herald/xray_review_propertiesofsr.htm (2005).

[6] C. G. Windsor, *Pulsed neutron scattering*, Taylor & Francis Ltd., London (1981).

[7] B. H. Toby, http://www.ncnr.nist.gov/instruments/bt1/ (2005).

[8] J. D. Jorgensen, J. J. Faber, J. M. Carpenter, et al.: Electronically focused time-of-flight powder diffractometers at the Intense Pulsed Neutron Source. *J. Appl. Crystallogr.* **22**, 321 (1989).

[9] R. J. Nelmes, P. D. Hatton, M. I. McMahon, et al.: Angle-dispersive powder-diffraction techniques for crystal structure refinement at high pressure. *Rev. Sci. Instrum.* **63**, 1039 (1992).

[10] K. Largarec and S. Desgreniers, computer code Simplified Image Plate Analysis, University of Ottawa, Ottawa, ON, Canada (1994-97).

[11] M. D. Inc., computer code JADE, XRD Pattern Processing, Materials Data, Inc., Livermore, CA (1995-2005).

[12] A. C. Larson and R. B. Von Dreele, computer code General Structural Analysis System, Los Alamos National Laboratory, Los Alamos, NM (2000).

[13] B. H. Toby: EXPGUI, a graphical user interface for GSAS. *J. Appl. Crystallogr.* **34**, 210 (2001).

[14] M. Newville, talk XAFS: X-ray Absorption Fine Structure, Brookhaven National Laboratory, Upton, NY (2003).

[15] A. Jayaraman: Diamond anvil cell and high-pressure physical investigations. *Rev. Modern Phys.* **55**, 65 (1983).

[16] G. J. Piermarini: High Pressure X-ray Crystallography With the Diamond Cell at NIST/NBS. *J. Res. NIST* **6**, 889 (2001).

[17] S. Klotz, J. M. Besson, G. Hamel, et al., Crystal structure studies to 10 GPa with the Paris-Edinburgh cell: high pressure aspects, *AIP Conf. Proc.*, **309**, 1577 (1993).

[18] J. D. Jorgensen, S. Pei, P. Lightfoot, et al.: Pressure-induced charge transfer and dT_c/dP in $YBa_2Cu_3O_{7-x}$. *Physica C* **171**, 93 (1990).

[19] R. Miletich, D. Allan, R., and W. Kuhs, F.: High-Pressure Single-Crystal Techniques. *Rev. Mineral. Geochem.* **41**, 445 (2001).

[20] J. M. Jackson, W. Sturhahn, G. Shen, et al.: A synchrotron Moessbauer spectroscopy study of $(Mg,Fe)SiO_3$ perovskite up to 120 GPa. *Am. Mineral.* **90**, 199 (2005).

[21] L. Sun, A. L. Ruoff, and G. Stupian: Convenient optical pressure gauge for multimegabar pressures calibrated to 300 GPa. *Appl. Phys. Lett.* **86**, 14103 (2005).

[22] C.-S. Zha, High Pressure Facilities at CHESS, *CHESS Newsletter*, CHESS, Cornell University, Ithaca, NY (2000)

[23] W. A. Bassett, A. J. Anderson, R. A. Mayanovic, et al.: Hydrothermal diamond anvil cell for XAFS studies of first-row transition elements in aqueous solution up to supercritical conditions. *Chem. Geol.* **167**, 3 (2000).

[24] D. R. Allan, R. Miletich, and R. J. Angel: A diamond-anvil cell for single-crystal X-ray diffraction studies to pressures in excess of 10 GPa. *Rev. Sci. Instrum.* **67**, 840 (1996).

[25] H. P. D. Optics, http://www.hpdo.com/br.html (2003).

[26] P. M. Bell and H.-k. Mao, in *Carnegie Institute of Washington Yearbook*, Vol. 80, p. 404, Carnegie Institute of Washington, Washington, D.C. (1981).

[27] F. Birch: Equation of state and thermodynamic parameters of sodium chloride to 300 kbar in the high-temperature domain. *J. Geophys. Res. B* **91**, 4949 (1986).

[28] D. L. Decker: High-Pressure Equation of State for NaCl, KCl, and CsCl. *J. Appl. Phys.* **42**, 3239 (1971).

[29] J. Zhao, computer code Calibration, University of Witwatersrand, Johannesburg-Gauteng, South Africa (1998).

[30] J. D. Barnett, S. Block, and G. J. Piermarini: An Optical Fluorescence System for Quantitative Pressure Measurement in the Diamond-Anvil Cell. *Rev. Sci. Instrum.* **44**, 1 (1973).

CHAPTER 3

PRESSURE-INDUCED PHASE TRANSITIONS AND AMORPHIZATION IN $A_2M_3O_{12}$-TYPE COMPOUNDS

Abstract

Compounds with the $A_2M_3O_{12}$ formula and with the $Sc_2W_3O_{12}$ structure are known to display negative thermal expansion and, many of them also show significant A^{3+} conductivity. Monochromatic synchrotron x-ray as well as neutron powder diffraction was used to study several $A_2M_3O_{12}$ materials at high pressures. A phase transition from orthorhombic (Pnca) to monoclinic ($P2_1/a$) symmetry was observed at pressures between 0.1-0.3 GPa for compounds $Sc_2W_3O_{12}$, $Sc_2Mo_3O_{12}$ and $Al_2W_3O_{12}$. A second crystalline to crystalline phase transition was also seen at ~ 3 GPa in the first two compounds. Almost complete amorphization occurred for several materials in the pressure range studied. For $Sc_2W_3O_{12}$ and $Sc_2Mo_3O_{12}$ it has been shown that the orthorhombic phase displays highly anisotropic compressibility, while that of the monoclinic phase is almost isotropic. These materials are very soft even when compared to most other NTE phases. The reduction in bulk modulus at the phase transition and the reduction in volume per formula unit is almost entirely associated with changes in the orthorhombic *a* and *c* directions. It has been shown that the mechanism of volume-reduction is different from what is seen on heating these materials. Our in-situ neutron diffraction study of $Sc_2W_3O_{12}$ confirms this: the volume reduction seems to be accommodated by structural changes that are different from those seen on heating.

3.1 Introduction

Oxide materials exhibiting negative thermal expansion (NTE) have received considerable recent attention[1-6] due to a combination of fundamental scientific interest and their potential for use in composites with tailored thermal expansion characteristics.[7-9] The majority of this work has focused on members of the AM_2O_8 (A - Zr, Hf and M - W or Mo), $A_2M_3O_{12}$ (A - variety of +3 ions, M - Mo or W) and AX_2O_7 (A - variety of + ions, X - P or V) families of materials, although other low density framework materials such as zeolites[10-14] and $NbOPO_4$[15, 16] have also been examined closely.

NTE materials typically show quite complex behavior upon application of modest pressures including pressure induced amorphization[17-19] as well as phase transitions in which the crystallinity is retained.[17, 20-23] While the detailed mechanisms behind phenomena such as amorphization are not always clear, the occurrence of these transformations at low pressure is related to the low densities and flexible frameworks of most NTE materials, and the existence of phonon modes that soften on volume reduction;[24-31] such modes are necessarily present as they are responsible for the NTE. Some authors have suggested an intimate relationship between NTE and pressure-induced amorphization.[32] The occurrence of phase transitions at low pressure in NTE materials is not purely of academic interest. They can be induced while fabricating or using composites of these materials and are a hindrance to their application in composites, as they lead to a loss or reduction in the negative thermal expansion.[9, 33, 34]

Early high pressure experiments on NTE materials examined ZrW_2O_8, $ZrMo_2O_8$ and ZrV_2O_7.[21, 35, 36] While there have been several high pressure studies of $A_2(MO_4)_3$ phases, much of this work has focused on compositions such as $Tb_2(MoO_4)_3$, $Gd_2(MoO_4)_3$,

$Eu_2(MoO_4)_3$,[37, 38] which do not adopt structures displaying NTE. Recently, high pressure work has started to appear on $A_2(MO_4)_3$ phases that display NTE under ambient conditions,[39-43] but this area is still relatively unexplored with no *in-situ* diffraction studies addressing the compressibility and symmetry of the phases that appear on compression.

Many different crystal structures are known for compounds of the type $A_2(MO_4)_3$ (A - variety of +3 ions, M - Mo or W).[44-47] The orthorhombic $Sc_2(WO_4)_3$-structure (space group Pnca) is found for A = Al, Sc, Cr, Fe, Y, In or the smaller rare earths from Lu to Ho and M = Mo, W. These orthorhombic materials show volume negative thermal expansion.[3-6, 48-52] $Sc_2W_3O_{12}$ consists of corner-sharing ScO_6 octahedra and WO_4 tetrahedra[46] (see Figure 1.6) and it displays anisotropic thermal expansion with two axes contracting and one expanding on heating as shown in Figure 3.1 for $Sc_2W_3O_{12}$. The contraction can be viewed as arising from a dynamic cooperative tilting of the quasi-rigid polyhedral units that make up the framework.[48]

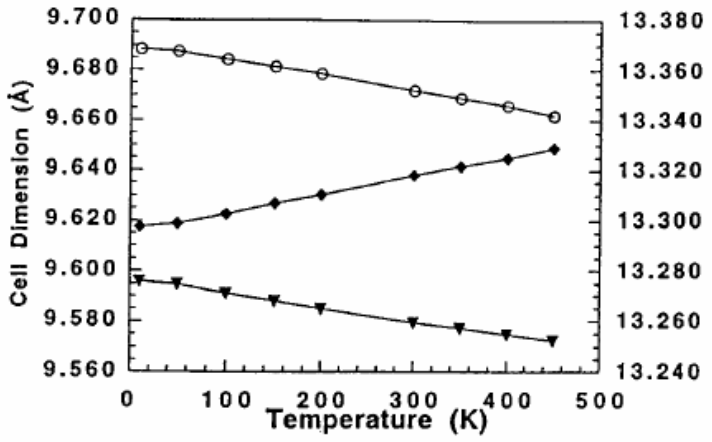

Figure 3.1: Unit cell dimensional changes as a function of temperature for orthorhombic $Sc_2W_3O_{12}$: open circles are *a*, closed diamonds are *b*, and closed triangles are *c*. Vertical axis scale on the left is for *a* and *c*, on the right for *b*. Taken from Evans *et al*.[49]

$Sc_2Mo_3O_{12}$ and $Al_2W_3O_{12}$ consist of corner-sharing ScO_6 and AlO_6 octahedra and MoO_4 and WO_4 tetrahedra, respectively, and they also display anisotropic thermal expansion with two axes contracting and one expanding on heating.[51, 53] While NTE in $Sc_2Mo_3O_{12}$ was clearly observed both by diffraction and dilatometry,[49, 53] the expansion characteristics $Al_2W_3O_{12}$ appear to depend on the method of measurement. NTE was seen by dilatometry, but low positive expansion was seen by x-ray diffraction.[49] This difference may be due to extrinsic effects associated with microstructure changes as a function of temperature.[54]

$Yb_2W_3O_{12}$ is also a member of the orthorhombic $Sc_2W_3O_{12}$-family (Yb is one of the smaller rare earths).[44, 45] Similar to other tungstates and molybdates containing lanthanides with this structure, it is hygroscopic and forms the trihydrate $Yb_2W_3O_{12}\cdot 3H_2O$ on contact with air.[45] The effect of hygroscopicity on the bulk thermal expansion of $Y_2W_3O_{12}$ has been studied.[55] Hydration causes the unit cell to shrink and suppresses the transverse vibrations responsible for NTE. Removal of the water molecules results in the initial expansion of the framework. Indeed, NTE in $Yb_2W_3O_{12}$ was only found after the complete removal of water molecules at 120 ^oC.[56]

Several members of the $Sc_2(WO_4)_3$ family have been shown to undergo a volume-reducing ferroelastic phase transition[57] to a monoclinic structure on cooling.[44, 45, 47, 53, 58] This structure does not show negative volume expansion,[53] as is illustrated for $Sc_2Mo_3O_{12}$ in Figure 3.2.

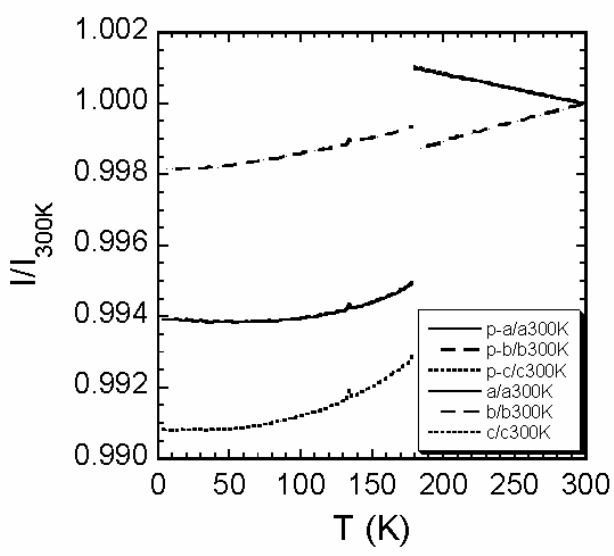

Figure 3.2: Thermal expansion of $Sc_2Mo_3O_{12}$: the change of normalized lattice constants with temperature is plotted. The monoclinic phase (<180 K) exhibits normal positive expansion and its parameters are expressed in pseudo-orthorhombic form. Above 180 K, the structure is orthorhombic and shows NTE in the direction of the *a*- and *c*-axes. Note that the data for *a* and *c* overlap in the orthorhombic range. Data kindly provided by John S. O. Evans.

$A_2(MO_4)_3$ materials are also known for their trivalent cation conductivity.[59-62] $Sc_2(WO_4)_3$ was the first material in which trivalent cation conduction has been unambiguously established for a solid.[63] Studies of trivalent conduction in a variety of $A_2(MO_4)_3$ compositions showed that $Sc_2(MoO_4)_3$ and $Sc_2(WO_4)_3$ possessed the highest conductivity among the molybdates and tungstates.[59, 62]

There have been high-pressure studies of $Sc_2W_3O_{12}$, $Sc_2Mo_3O_{12}$, $Al_2W_3O_{12}$ and $Lu_2W_3O_{12}$.[39-43, 64-68] Samples of $Sc_2W_3O_{12}$ recovered from room temperature and high pressure using a large volume press were examined by diffraction, and an irreversible pressure induced amorphization was observed to start at ~ 5 GPa and to be complete by ~8 GPa.[39] No intermediate pressure phase transformations were reported. Measurements

on $Sc_2(WO_4)_3$ at 400 ºC showed an initial decrease in ionic conductivity with increasing pressure followed by an increase above 2.9 GPa.[64-66] This change in the pressure dependence of conductivity was coincident with the pressure induced amorphization of the material, as seen by synchrotron energy dispersive x-ray diffraction (EDXRD) on samples in a multi-anvil apparatus at 400 ºC. In a room temperature Raman spectroscopy and EDXRD study of $Sc_2(MoO_4)_3$, using DACs with methanol-ethanol or methanol-ethanol-water as pressure transmitting media, reversible phase transitions were observed at 0.3 GPa and 2.7 GPa followed by the onset of amorphization at about 3.7 GPa.[42] This amorphization was initially reversible but became irreversible at higher pressures. The Raman data were interpreted as indicating that the MoO_4 tetrahedra persisted in the amorphous phase. The phase existing between 0.3 and 2.7 GPa was identified as monoclinic by comparison of the high pressure Raman spectra with those of the low temperature ambient pressure monoclinic form of $Sc_2Mo_3O_{12}$.[42] In a combined Raman – laboratory XRD – synchrotron XRD study of $Sc_2(MoO_4)_3$ conducted by Arora et al.[67] pressure induced amorphization was reported to occur in two stages beginning at 4 GPa with some disordering and ending at 12 GPa (DACs with methanol-ethanol pressure media). None of the $Sc_2(MoO_4)_3$ studies report the variation of the lattice constants on compression. A study examining samples of $Al_2W_3O_{12}$ that had been recovered from high temperature/pressure concluded that this compound undergoes no irreversible phase transitions below 8 GPa at room temperature and that at high pressure and temperature the material decomposes to form $AlWO_4$.[68] *In-situ* measurements of AC resistivity and compressibility at room temperature in large volume presses were interpreted as indicating a reversible phase transition at 5 kbar.[41] In a room temperature Raman study of

$Al_2(WO_4)_3$, reversible phase transitions were observed at 0.28 and 2.8 GPa.[43] The intermediate phase was identified as monoclinic and it was noted that the phase existing above 2.8 GPa probably contained WO_4 tetrahedra with smaller distortions than the MoO_4 tetrahedra in $Sc_2Mo_3O_{12}$ at pressures above 2.7 GPa. The room temperature high-pressure behaviour of $Lu_2(WO_4)_3$ has been investigated by examining samples recovered from high pressure using a Walker-type multi-anvil device. Pressure induced amorphization began at 5 GPa and was complete by 8 GPa, and no evidence was seen for any other transformation.[40]

$Sc_2W_3O_{12}$, $Sc_2Mo_3O_{12}$ and $Al_2W_3O_{12}$ are good model compounds to carry out a comparative study as they are expected to undergo similar changes under compression and with the presence of different cations, Mo versus W and Al versus Sc, the effect of chemistry on the high-pressure behaviour can be studied. No high-pressure study has been reported for $Yb_2W_3O_{12}$ and no monoclinic polymorph is known for the material.

In this chapter, we present high pressure *in-situ* synchrotron powder diffraction studies of $Sc_2(WO_4)_3$, $Sc_2Mo_3O_{12}$, $Al_2(WO_4)_3$ and $Yb_2(WO_4)_3$ under (quasi)-hydrostatic conditions in diamond-anvil cells as well as a high-pressure neutron diffraction study of $Sc_2(WO_4)_3$ in a He gas pressure cell.

3.2 Experimental

3.2.1 Sample preparation

$Sc_2W_3O_{12}$ powder was prepared from Sc_2O_3 (Strem Chemicals, Newburyport, MA) and WO_3 (Aldrich, Milwaukee, WI). Stoichiometric amounts of the two oxides were

thoroughly mixed and ground. The mixture was initially heated at 1000 ^{o}C for 5 hours and after regrinding it was heated at 1200 ^{o}C for an additional 12 hours in air.

$Sc_2(MoO_4)_3$ powder was prepared from Sc_2O_3 (Strem Chemicals, Newburyport, MA) and MoO_3 (J. T. Baker, Phillipsburg, NJ). Stoichiometric amounts of the two oxides were thoroughly mixed and ground. The mixture was initially heated at 700 ^{o}C for 5 hours and after regrinding it was heated at 1100 ^{o}C for an additional 12 hours in air.

$Al_2(WO_4)_3$ powder was synthesized from $Al_2O_3{\cdot}2H_2O$ (Catapal® β-Alumina, Vista Chemical Company, Houston, TX) and WO_3 (Aldrich, Milwaukee, WI). Stoichiometric amounts of the two oxides were thoroughly mixed and ground. The mixture was heated at 900, 1000 and 1100 ^{o}C for 20-hour periods with intermittent grinding steps.

$Yb_2(WO_4)_3$ powder was prepared from Yb_2O_3 (Strem Chemicals, Newburyport, MA) and WO_3 (Aldrich, Milwaukee, WI). The two oxides were thoroughly mixed in stoichiometric amounts and ground. The mixture was heated to 1000 ^{o}C for 5-hour, the 1150 ^{o}C for 22- and 38.5-hour periods with intermittent quenching in ice water and drying at 130 ^{o}C.

3.2.2 Diamond anvil cells

Two different diamond anvil cell (DAC) designs and pressure-transmitting media were used; a four-post DAC with nitrogen as pressure medium (only for $Sc_2W_3O_{12}$ and $Yb_2W_3O_{12}$), and a hydrothermal DAC (HDAC)[69] (see Figure 3.3) with anhydrous isopropanol. The two media were chosen to give good pressure control at low pressures (isopropanol) and hydrostatic conditions to > 10 GPa (nitrogen). The limit of (quasi)hydrostaticity for nitrogen has been reported to be 13 GPa.[70] However, the loading

method that we employed, sealing while immersed in liquid nitrogen, gave us poor control over our starting pressure. Isopropyl alcohol is claimed to provide hydrostatic pressure conditions up to 4.3 GPa.[70] Typically for high-pressure studies of the type that we report, methanol:ethanol:water = 16:3:1 and methanol:ethanol = 4:1 with hydrostatic limits of 14.5 and 10.4 GPa, respectively are used.[70] Water is known to react with the open-framework NTE phase cubic ZrW_2O_8, resulting in a volume contraction,[71] and we have seen similar phenomena with ZrW_2O_8 in methanol.[72] Additionally, it is well established that many $A_2M_3O_{12}$ phases react with water to give hydrates.[45, 55, 73, 74] While we have no evidence for the reaction of $Sc_2W_3O_{12}$ with water or any alcohol, we avoided water and small alcohols in our pressure-transmitting media so that reaction between the medium and the sample would not be a concern. Pressure inside the four-post DAC was measured using the ruby fluorescence technique[75] where pressure calibration errors of 0.05 - 0.1 GPa are possible.[70] The four-post DAC was equipped with 2.4 mm thick diamonds with 600 μm culet faces. A 23.3 mm OD, 200 μm thick stainless steel gasket with a 250 μm hole diameter was used with this DAC. This cell was only used for $Sc_2W_3O_{12}$. In the HDAC, NaCl was used as pressure calibrant. The diamonds were 1.7 mm thick with 500 μm culet faces. A rhenium gasket with a 300 μm hole diameter and 125 μm thickness was used. In both cases the gaskets were pre-indented between the diamonds. The downstream cone opening of the cells was 44 degrees resulting in a $2\theta_{max}$ of 22 degrees with ~15 degrees of usable data.

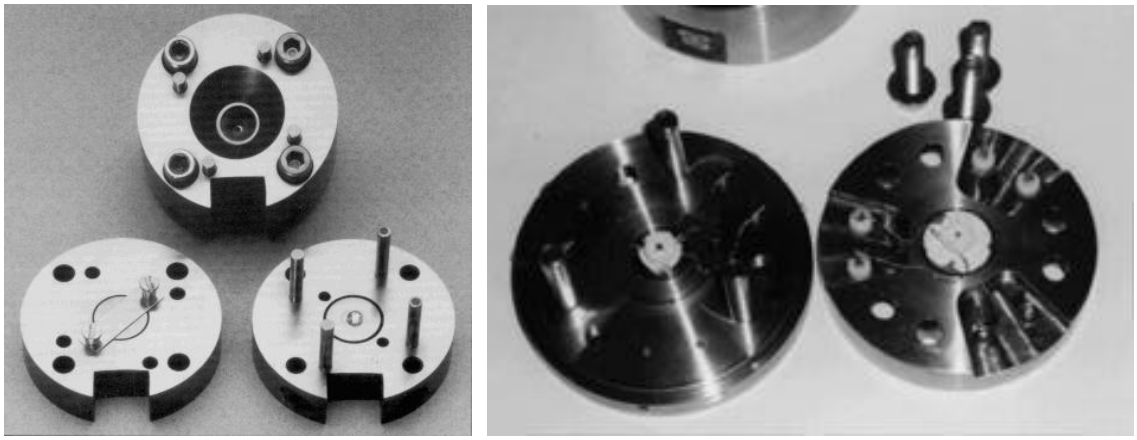

Figure 3.3: Assembly of the four-post DAC (left) and the HDAC (right). Taken from http://www.geo.arizona.edu/xtal/group/dac.html and http://www.esc.cam.ac.uk/astaff/shen/dac.htm.

3.2.3 He-gas pressure cell

The He-gas pressure cell shown in Figure 3.4 offers the advantages of perfectly hydrostatic conditions (helium is claimed to remain hydrostatic up to 60-70 GPa[70]), precise control and measurement of pressure, and, due to the use of the TOF technique where all of the data can be collected at a fixed scattering angle, diffraction data that are completely free from Bragg scattering from the cell.[76]

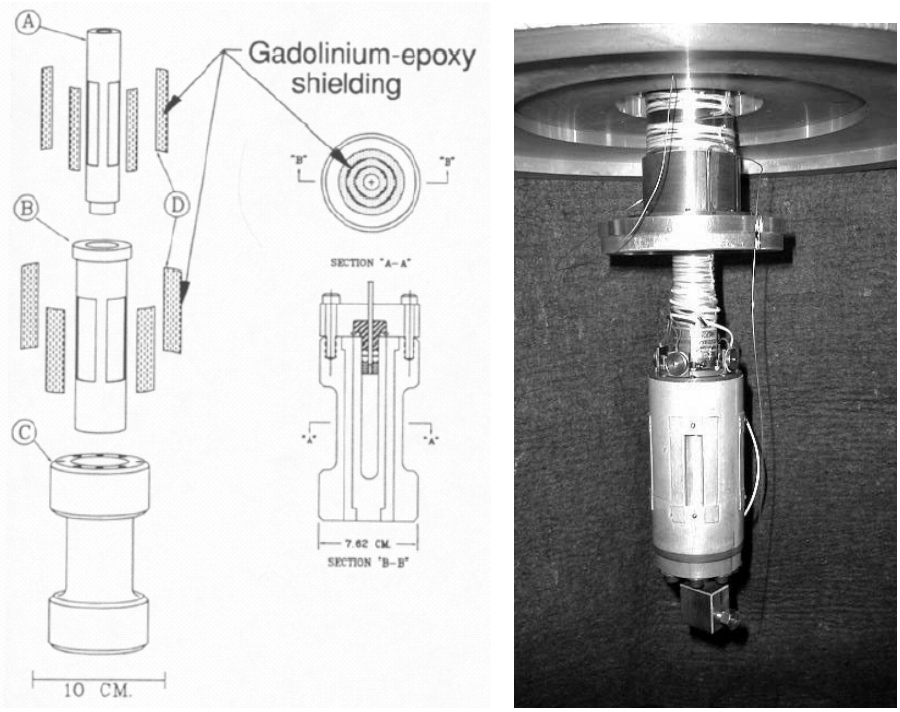

Figure 3.4: Exploded drawing and picture of the He-gas pressure cell. Taken from Jorgensen[76] and http://www.pns.anl.gov/instruments/sepd/subsepd/hp2.htm, respectively.

The cell is made of three concentric cylinders of 7075-T6 alloy aluminum. Its design is such that it avoids scattering from the cell while maximizing the effective volume of the sample illuminated by the incident neutron beam. The unique feature of the cell is its incorporated internal gadolinium-epoxy shielding, which serves two functions. Firstly, it collimates the incident and scattered neutron beams at the sample. Secondly, it minimizes the background from multiple scattering of neutrons in the aluminum. The active sample volume illuminated by neutrons is ~5 cm^3. The He-gas cell we used was limited to a pressure of 0.65 GPa for safety reasons.

3.2.4 Synchrotron x-ray diffraction data collection

Data were collected at room temperature and up to ~10 GPa pressure in the four-post DAC for $Sc_2W_3O_{12}$ and up to ~6.5 GPa for $Yb_2W_3O_{12}$, as well as up to 6.6 GPa in the HDAC for $Sc_2W_3O_{12}$, up to ~8 GPa pressure for $Sc_2(MoO_4)_3$ and up to 7.0 GPa for $Al_2(WO_4)_3$ using the B-2 line of the Cornell High Energy Synchrotron Source (CHESS), Wilson Lab, Cornell University, Ithaca, NY. The experimental setup is shown in Figure 3.5 and was schematically shown in Figure 2.5. 25 keV (λ = 0.496 Å) x-rays were selected using a Ge(111) double-crystal monochromator. Diffraction patterns were recorded on image plates. The sample-to-plate distance was calibrated using ambient pressure diffraction from NaCl. For the HDAC, the salt was packed in the cell with the sample ($A_2(MO_4)_3$:NaCl = 1:2-1:4 ratio by weight) and it was assumed that the pressure inside the cell was zero for the purposes of this calibration. For the four-post DAC, a small amount of NaCl was placed onto an external diamond face and the resulting sample-to-plate distance corrected for the thickness of the diamond.

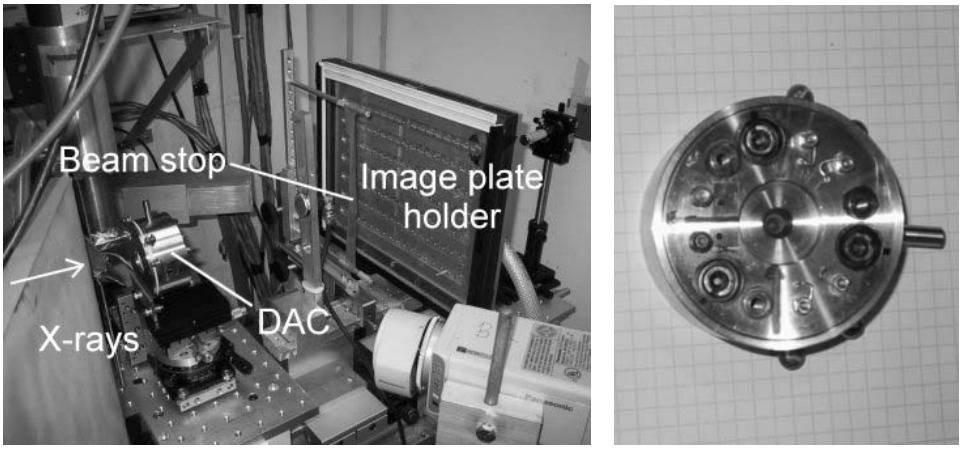

Figure 3.5: Experimental setup for synchrotron diffraction using the HDAC (left). Top view of the HDAC (right).

3.2.5 Neutron diffraction data collection

Neutron data collection on $Sc_2W_3O_{12}$ was performed using the Special Environment Powder Diffractometer (SEPD),[77] at the Intense Pulsed Neutron Source (IPNS) of Argonne National Laboratory, Argonne, IL (see Figures 3.6 and 2.7). The SEPD is a time-of-flight powder diffractometer that is optimized for diffraction in special environments, where a 90° scattering angle can be used to allow optimum collimation in order to eliminate scattering from the sample environment. When a large amount of sample is available, the high count rate of the instrument makes collection of usable quality data possible within minutes. Typical collection times for data for precision Rietveld refinements are about 5 hours for 5 grams of sample. The instrument uses 10 atm ^{3}He-gas proportional counters as detectors. The pressure within the sample cell is produced and controlled by a two-stage gas compressor.

a)  b) 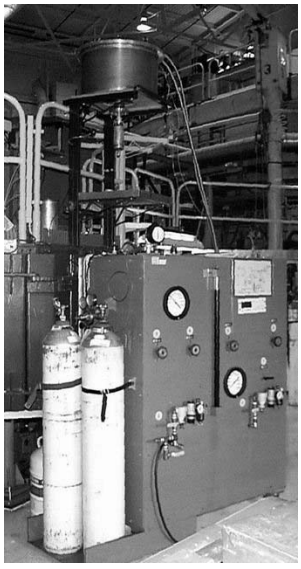

Figure 3.6: The SEPD instrument at IPNS: a) main deck (experimental floor); b) two-stage compressor

In our experiment, about 13.7 g finely ground and dried $Sc_2W_3O_{12}$ was loaded into the sample can of the He-gas pressure cell. The sample was compressed to 0.6 GPa in 8 small steps and then decompressed in 4 steps. Data were collected at each step for about 5 hours and converted into a format usable for further analysis. There are five detector banks for the SEPD instrument; at ±145 ° (80 detectors), ±90 ° (40 detectors), ±60 ° (24 detectors), +30 ° (7 detectors) and -15 ° (7 detectors). The data that can be collected with each detector bank differs both in d-spacing range and resolution. Only data from Bank 2 were used for Rietveld analysis, as that is the detector bank located at 90^o with a view through the pressure cell window (see above).

3.2.6 Data analysis

The image plates were read using a BAS 2000 scanner and integrated to give intensity vs. 2θ using SIMPA (v1.3).[78] The patterns were initially processed in JADE[79] and then further analyzed by a combination of the Rietveld and Le Bail methods using GSAS[80] with the EXPGUI interface.[81] Pressure was estimated for the HDAC experiments using the NaCl peak positions determined using JADE and the program Calibration.[82, 83] Pressure determination with the program Calibration made use of the Birch equation of state for NaCl.[83] This pressure scale is reported to be accurate to better than 1% in the range of our experiments.[84, 85] Le Bail fits were carried out to extract the lattice parameters at each pressure. In these fits, only the lattice parameters and profile parameters were varied. For the pressures where there was evidence for the coexistence of orthorhombic and monoclinic phases, the Rietveld method was used to obtain an estimate of the amount of each phase that was present. In these fits, the lattice parameters

for each phase, the background terms, the scale factors and the peak profile parameters were optimized, but the structural models were not refined due to the limited amount of data (low Q_{max}) that was available. Structural models for these fits were obtained from Abrahams and Bernstein[46] (orthorhombic $Sc_2W_3O_{12}$ model) as well as Evans and Mary[53] (monoclinic $Sc_2Mo_3O_{12}$ model with the replacement of the Sc or Mo atoms as needed; see Appendix A). The calculated unit cell volumes were fitted to the Birch-Murnaghan equation of state (EOS)[86] using the EOS-FIT program (v5.2).[87] The third-order Birch-Murnaghan EOS was used for both the orthorhombic and monoclinic phases.

The $Sc_2W_3O_{12}$ neutron data were also analyzed with the GSAS and EXPGUI programs using the same structural models as above.

3.3 $Sc_2W_3O_{12}$ – High-pressure *in-situ* synchrotron x-ray diffraction studies

3.3.1 Results

Subsets of the powder diffraction patterns obtained as a function of pressure using isopropanol and nitrogen as pressure-transmitting media are shown in Figure 3.7; those measured in nitrogen and isopropanol are qualitatively in excellent agreement with one another. Below ~0.3 GPa, $Sc_2(WO_4)_3$ remains orthorhombic and the diffraction data can be fitted well in space group Pnca using the atomic positions of Abrahams and Bernstein.[46] Above ~0.3 GPa (0.32 GPa in isopropanol and 0.28 GPa in nitrogen) a transformation to a monoclinic phase began. This was almost complete at 0.44 GPa. We estimated from Rietveld fits that at 0.28 GPa in nitrogen we had a 4:1 ratio of orthorhombic to monoclinic material by weight, at 0.32 GPa in isopropanol there was a

2:3 ratio of orthorhombic to monoclinic material, and at 0.44 GPa in isopropanol a trace of the orthorhombic phase could be detected.

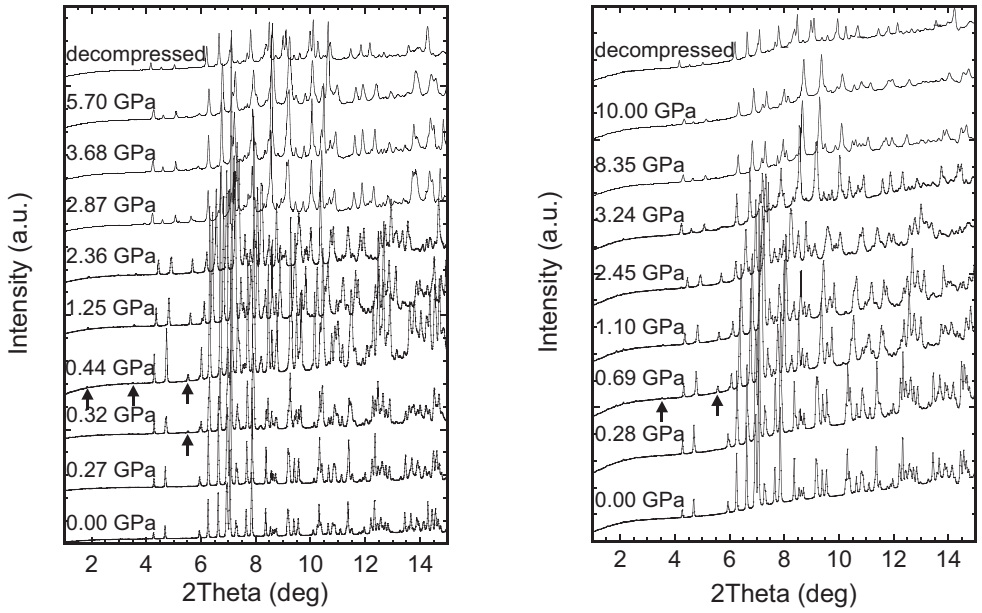

Figure 3.7: $Sc_2W_3O_{12}$ powder diffraction patterns as a function of pressure in isopropanol (left) and in nitrogen (right). Arrows indicate the location of peaks that are characteristic of the monoclinic phase. The data were collected at 25 keV (λ = 0.496 Å).

The monoclinic phase was indexed in space group $P2_1/a$ using as a starting point the lattice parameters of monoclinic $Sc_2(MoO_4)_3$.[53] It was stable on further compression to almost 3 GPa. A second phase transition was seen at 2.87 GPa in isopropanol, but the first signs were apparent at 2.45 GPa in nitrogen. This phase has not yet been indexed and it does not appear to be closely related to known $A_2M_3O_{12}$ structures such as tetragonal $Gd_2Mo_3O_{12}$[88] or monoclinic $Eu_2W_3O_{12}$.[89] Amorphization did not occur in the pressure range studied (< 10 GPa) although some broadening of the diffraction peaks was noticeable. The phase change at ~3 GPa did not reverse upon decompression indicating

that recovery from pressure for further high resolution structural studies might be possible.

Lattice constants obtained by Le Bail fitting are reported in Tables 3.1 and 3.2 for the isopropanol and nitrogen experiments respectively. The values obtained in the different media are in good agreement at low pressure but there are small systematic differences at higher pressures. The trends with pressure are the same for both experiments. The systematic differences are probably due to the different pressure determination methods in the two experiments and in particular our assumption of zero pressure in the as closed DAC containing isopropanol. We have also conducted a neutron diffraction study of $Sc_2W_3O_{12}$ in a helium gas cell at pressures of up to 0.6 GPa (see section 3.4).[90] The normalized lattice constants from the neutron experiments lie between the values obtained using nitrogen and isopropanol media, but closer to those in the nitrogen experiment.

As the structures of monoclinic and orthorhombic $Sc_2(WO_4)_3$ are very closely related to one another[53] it is possible to transform the primitive monoclinic lattice constants to a new A centred monoclinic lattice that is pseudo orthorhombic with $a_m \sim a_o$, $b_m \sim 2c_o$, $c_m \sim 2b_o$ and $\alpha_m \sim 90^o$ using the matrix (0 1 0; 0 0 -1; -2 0 -1) so that changes in linear compressibility through the phase transformation can be examined. Pseudo orthorhombic lattice constants are given in Tables 3.1 and 3.2 along with primitive monoclinic ones.

Table 3.1: $Sc_2(WO_4)_3$ lattice constants as of a function of pressure in an isopropanol pressure-transmitting medium. Derived pseudo-orthorhombic values are given for the monoclinic phase along with the primitive monoclinic lattice constants that were directly determined from the diffraction data. At 0.32 GPa lattice constants for both the monoclinic and orthorhombic phases are given as both were present in significant amounts. At 2.87 GPa, the second phase transition had begun, therefore it was difficult to obtain reliable lattice parameters from the fit.

Pressure, GPa	**Symmetry**	**a, Å**	**b, Å**	**C, Å**	**β or α, deg**	**Volume, Å^3**
0.00	orthorhombic	9.6694(2)	13.3255(2)	9.5792(2)	90.000	1234.28(4)
0.13	orthorhombic	9.6620(1)	13.3050(2)	9.5713(2)	90.000	1230.41(2)
0.18	orthorhombic	9.6591(2)	13.2912(2)	9.5687(2)	90.000	1228.45(3)
0.27	orthorhombic	9.6529(2)	13.2729(2)	9.5624(2)	90.000	1225.16(5)
0.32	orthorhombic Monoclinic Pseudo-orth	9.6501(2) 16.2556(4) 9.5783	13.2477(4) 9.5783(2) 13.2502	9.5579(2) 18.9383(4) 9.4692	90.000 125.402(2) 89.77	1221.90(4) 2403.54(4)
0.44	Monoclinic Pseudo-orth	16.2350(8) 9.5657	9.5657(3) 13.2364	18.9100(6) 9.4550	125.384(3) 89.77	2394.26(7)
0.49	Monoclinic Pseudo-orth	16.2050(2) 9.5504	9.5504(1) 13.2182	18.8714(2) 9.4357	125.346(1) 89.74	2382.26(3)
0.65	Monoclinic Pseudo-orth	16.1491(2) 9.5207	9.5207(1) 13.1803	18.8045(2) 9.4023	125.299(1) 89.69	2359.66(3)
0.72	Monoclinic Pseudo-orth	16.1157(3) 9.5043	9.5043(1) 13.1582	18.7648(3) 9.3824	125.267(1) 89.66	2346.67(4)
0.94	Monoclinic Pseudo-orth	16.0422(3) 9.4654	9.4654(1) 13.1036	18.6863(3) 9.3432	125.234(1) 89.61	2317.62(3)
1.06	Monoclinic Pseudo-orth	15.9966(2) 9.4425	9.4425(1) 13.0710	18.6395(3) 9.3198	125.206(1) 89.57	2300.48(6)
1.25	Monoclinic Pseudo-orth	15.9319(3) 9.4096	9.4096(1) 13.0217	18.5762(3) 9.2881	125.184(1) 89.52	2276.04(6)
1.81	Monoclinic Pseudo-orth	15.7795(2) 9.3277	9.3277(1) 12.9077	18.4314(3) 9.2157	125.119(1) 89.39	2219.03(3)
2.36	Monoclinic Pseudo-orth	15.6334(5) 9.2210	9.2210(3) 12.7856	18.3075(7) 9.1538	125.137(3) 89.30	2158.20(6)
(2.87)	*monoclinic*	*15.5506(16)*	*9.1919(12)*	*18.2706(26)*	*124.171(6)*	*2160.74(18)*

Table 3.2: $Sc_2(WO_4)_3$ lattice constants as of a function of pressure in a nitrogen pressure transmitting medium. Derived pseudo-orthorhombic values are given for the monoclinic phase along with the primitive monoclinic lattice constants that were directly determined from the diffraction data. At 0.28 GPa both phases were present in significant amounts.

Pressure (GPa)	**Symmetry**	**a, Å**	**b, Å**	**C, Å**	**β or α, deg**	**Volume, Å^3**
0.05	orthorhombic	9.6738(3)	13.3146(5)	9.5812(3)	90.000	1234.09(10)
0.28	orthorhombic monoclinic *Pseudo-ortho*	9.6654(2) 16.2765(12) *9.5952*	13.2716(3) 9.5952(7) *13.2780*	9.5720(2) 18.9613(16) *9.4807*	90.000 125.337(4) *89.71*	1227.86(3) 2415.72(33)
0.69	Monoclinic *Pseudo-ortho*	16.0810(9) 9.4893	9.4893(4) 13.1378	18.7328(10) 9.3664	125.219(2) 89.60	2335.33(22)
1.10	Monoclinic *Pseudo-ortho*	15.9182(7) 9.4062	9.4062(3) *13.0208*	18.5737(8) 9.2869	125.121(2) 89.43	2274.72(17)
1.62	Monoclinic *Pseudo-ortho*	15.7768(12) 9.3192	9.3192(7) 12.9249	18.4372(15) 9.2186	124.999(4) 89.25	2220.55(33)
2.04	Monoclinic *Pseudo-ortho*	15.6737(18) 9.2347	9.2347(10) 12.8386	18.3551(23) 9.1776	125.012(6) 89.18	2175.98(48)
2.45	Monoclinic *Pseudo-ortho*	15.5715(22) 9.1684	9.1684(14) 12.7539	18.2731(27) 9.1366	125.020(9) 89.10	2136.49(64)

In Figure 3.8 we present normalized orthorhombic and pseudo-orthorhombic lattice constants as a function of pressure. It is clear that the orthorhombic *b*-axis is much more compressible than the *a*- and *c*-axes and that there is essentially no change in length for the *b*-axis at the orthorhombic to monoclinic transition, unlike the other axes. There is an abrupt change in the pseudo-orthorhombic angle α at the phase transition pressure (see Figure 3.9).

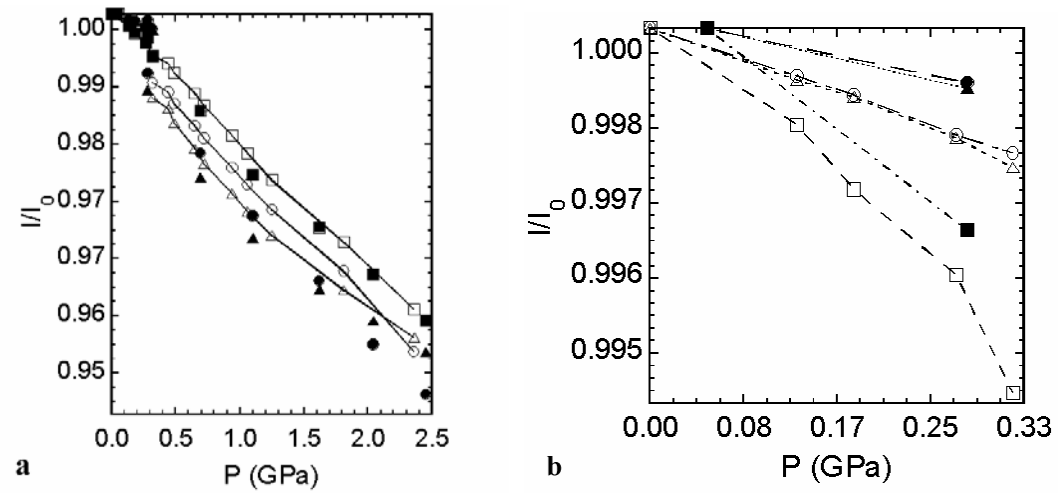

Figure 3.8: Normalized lattice constants as a function of pressure for experiments in isopropanol and nitrogen: a) 0 – 2.5 GPa. Open circles with line: a/a_0 monoclinic, open squares with line: b/b_0 monoclinic, open triangles with line: c/c_0 monoclinic in isopropanol; solid circles: a/a_0, solid squares: b/b_0, solid triangles: c/c_0 in nitrogen; b) A blow-up of the orthorhombic region (0 – 0.32 GPa). Open circles: a/a_0, open squares: b/b_0, open triangles: c/c_0 in isopropanol; solid circles: a/a_0, solid squares: b/b_0, solid triangles: c/c_0 in nitrogen. The monoclinic lattice constants for the phase existing above ~ 0.3 GPa have been converted to pseudo-orthorhombic values. Normalization of the lattice constants was done using the values from the first measured pressure point, which was not exactly zero pressure, rather than the zero pressure extrapolated values. The lines are only a guide to the eye.

Linear compressibilities were estimated for both phases in both media: for the orthorhombic phase $\beta_a = 6.32(16)\times10^{-3}$ GPa^{-1}, $\beta_b = 1.76(21)\times10^{-2}$ GPa^{-1}, $\beta_c = 6.84(32)\times10^{-3}$ GPa^{-1}, monoclinic phase $\beta_a = 1.85(3)\times10^{-2}$ GPa^{-1}, $\beta_b = 1.78(3)\times10^{-2}$ GPa^{-1}, $\beta_c = 1.69(9)\times10^{-2}$ GPa^{-1} (in isopropanol) and for the orthorhombic phase $\beta_a = 3.78\times10^{-3}$ GPa^{-1}, $\beta_b = 1.41\times10^{-2}$ GPa^{-1}, $\beta_c = 4.18\times10^{-3}$ GPa^{-1}, monoclinic phase $\beta_a = 2.06(7)\times10^{-2}$ GPa^{-1}, $\beta_b = 1.80(11)\times10^{-2}$ GPa^{-1}, $\beta_c = 1.64(18)\times10^{-2}$ GPa^{-1} (in nitrogen). For the orthorhombic values in nitrogen no standard deviation was estimated as only two data points were available.

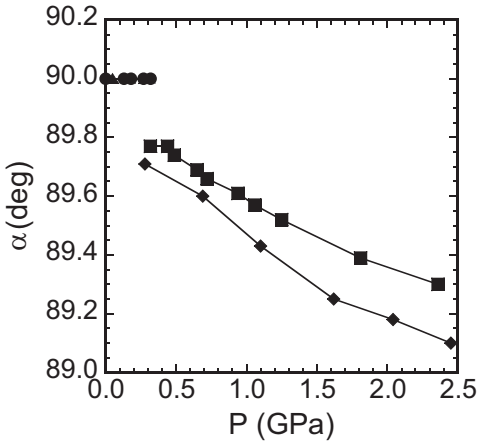

Figure 3.9: Orthorhombic and pseudo-orthorhombic angles α as a function of pressure. The lines are only a guide to the eye. Circles: orthorhombic, squares: monoclinic in isopropanol; triangles: orthorhombic, diamonds: monoclinic in nitrogen.

Figure 3.10 shows the volume/formula unit as a function of pressure derived from the measurements in isopropanol and nitrogen. From the isopropanol data, there is a 1 % decrease in volume prior to the orthorhombic-monoclinic transformation, a further 1.7 % decrease at the transition itself and a total decrease in volume of ~12.5% on going to 2.4 GPa. Fitting a third-order Birch-Murnaghan equation of state (EOS) to the P-V data for the sample in isopropanol data gave a bulk modulus, K_0, of 31(3) GPa for the orthorhombic and 14(1) GPa for the monoclinic phase. The zero pressure volume/formula unit (V_0) values were 308.75(17) $Å^3$ and 307.70(73) $Å^3$ for the orthorhombic and the monoclinic phase, respectively. The pressure derivative of the bulk modulus was fixed at 4.0 while fitting the data for the orthorhombic phase and determined by fitting to be 4.0(9) for the monoclinic phase. Fitting the same EOS to P-V data obtained from the diffraction patterns collected with a nitrogen medium resulted in a K_0 of 45 for the orthorhombic and 13.3(5) for the monoclinic phase. The zero pressure volumes (per

formula unit) were 309 and 307(1) Å^3. The pressure derivative was fixed at 4.0 for these fits due to the limited number of data points. No standard deviation for the bulk modulus and zero pressure volume of the orthorhombic phases is given as only two data points were available for the fitting.

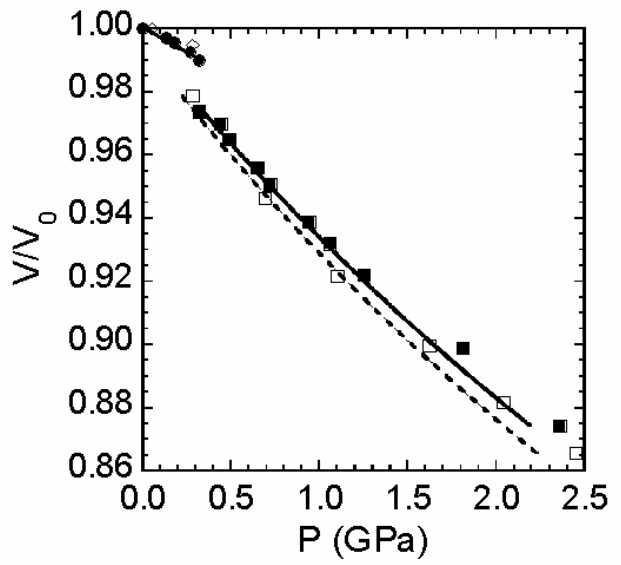

Figure 3.10: Normalized unit cell volume as a function of pressure. Closed symbols are for the sample in isopropanol, and open symbols are for the sample in nitrogen. The solid line shows a fit to the data for the monoclinic phase from the experiment in isopropanol using a third order Birch-Murnaghan equation of state: K_0 = 14(1) GPa, K' =4.0(9) , V_0 = 307.7(7)Å^3. The dashed line shows a fit to the data for the monoclinic phase from the experiment in nitrogen using a third order Birch-Murnaghan equation of state: K_0 = 13.3(5) GPa, K' fixed at 4 , V_0 = 307(1)Å^3.

3.3.2 Discussion

The pressure range over which monoclinic $Sc_2(WO_4)_3$ exists at room temperature is in surprisingly close agreement with Raman measurements for $Sc_2(MoO_4)_3$ and $Al_2(WO_4)_3$.[42, 43] At ambient pressure there is considerable variation in the temperature of the orthorhombic-monoclinic phase transition temperature amongst $A_2(WO_4)_3$ and $A_2(MoO_4)_3$ phases; $Al_2(MoO_4)_3$ (200 ^{o}C or 200-250 ^{o}C),[47, 58] $Al_2(WO_4)_3$ (-6 ^{o}C),[47]

$Cr_2(MoO_4)_3$ (385 °C or 380 °C),[47, 58] $Fe_2(MoO_4)_3$ (499 °C or 500-550 °C)[47, 58], $Sc_2(MoO_4)_3$ (9 °C, -94 °C or -153 °C) [47, 49, 53], $In_2(WO_4)_3$ (335 °C)[47] and $In_2(MoO_4)_3$ (252 °C).[47] However, $Sc_2W_3O_{12}$ remains orthorhombic down to 10 K.[48] The different transition temperatures that have been reported for some of these compounds are probably a consequence of differences in experimental methodology rather than true sample to sample variation or transition hysteresis.

The composition dependence of the transition temperature within a series of molybdates or tungstates has been rationalized by Sleight *et al.*:[47, 49] as the electronegativity of the A^{3+} cation increases, there is less negative charge on the oxide ions and consequently less repulsion between oxide ions resisting a volume collapse giving the monoclinic structure at higher temperatures. This reasoning suggests that $Sc_2W_3O_{12}$, with a very low cation electronegativity, and an orthorhombic form that is stable down to at least 10 K at ambient pressure, should transform to the monoclinic form at higher pressure than $Al_2W_3O_{12}$, but the observed transformation pressures are essentially the same, 0.28 GPa for $Al_2W_3O_{12}$[43] and 0.28 - 0.44 GPa for $Sc_2W_3O_{12}$. As the true thermodynamic transition pressures are not accurately known for these compounds, due to a combination of pressure calibration errors, phase coexistence over a range of pressures rather than sharp transformation, and a limited number of measurements in the relevant pressure range, it is not possible from these data to know if the thermodynamic transition pressures are in accordance with Sleight's arguments.[47, 49] However, it is clear that compounds with very different phase transition temperatures at ambient pressure can have very similar transition pressures at ambient temperature. From the perspective of possible applications in designed thermal expansion composites, the low transformation

pressure and the apparent insensitivity of the transformation pressure to chemical substitution may be troublesome.

The highly anisotropic nature of the orthorhombic phase's compressibility (Figure 3.8) is not trivially related to its anisotropic thermal expansion. Anisotropic thermal expansion in $Sc_2(WO_4)_3$ has been explained in terms of a coupled rotation of polyhedra.[48] If this mechanism for volume contraction were in operation on the application of pressure, the *a*- and *c*-axes would contract and the *b*-axis would expand on compression. However, all of the axes are observed to contract on compression and the *b*-axis is considerably softer than both the *a*- and *c*-axes. Compression of the b-axis is essentially continuous through the phase transition, but there is an abrupt decrease in the lattice constants for both the orthorhombic *a* and *c* directions at the phase transition that is associated with a significant softening of the lattice in these directions. Interestingly, this is quite similar to what is seen for the thermally induced transition in $Sc_2Mo_3O_{12}$; there is only a small discontinuity in the *b*-axis (~0.05%), but major discontinuities in both the *a* and *c* directions (>0.5%) at the transition temperature.[91] The monoclinic phase displays essentially isotropic compressibility.

Both the orthorhombic and monoclinic phases are very soft (bulk moduli of 31(3) and 14(1) GPa, respectively, based on isopropanol data) by comparison with most dense simple oxides[92] but similar values are seen for some simple framework structures, for example cubic NbO_2F[93] (K_o = 24.8(11) GPa). Low bulk moduli are common amongst NTE and related materials, for example cubic ZrW_2O_8 (72.5 GPa by neutron diffraction),[23] cubic $ZrMo_2O_8$ (44.6 GPa),[94] cubic ZrP_2O_7 (39 GPa),[36] cubic HfV_2O_7 (14 GPa)[95] and cubic ZrV_2O_7 (18 GPa),[36] presumably arising from the low density and

framework flexibility that is characteristic of them. The marked decrease in bulk modulus at the phase transition in $Sc_2W_3O_{12}$ is reminiscent of the compressibility collapse seen in ReO_3 as the O-Re-O-Re-O chains start to kink,[96, 97] and similar to that seen at the cubic to rhombohedral transition in NbO_2F.[93, 98] While ReO_3 and Nb_2OF do not show NTE, they have structural characteristics typical of NTE materials and the close structural relative TaO_2F has an expansion coefficient very close to zero, and perhaps slightly negative, over a wide temperature range.[99]

Our observation that $Sc_2(WO_4)_3$ does not undergo pressure induced amorphization below 10 GPa, contrasts with a previous report of amorphization in the 4-8 GPa range when using a Walker-type pressure device with a MgO pressure medium.[39] The amorphization is clearly sensitive to the sample's stress state and while our DAC experiments provide a pseudo hydrostatic environment, the amorphization observed by Secco et al.[39] was probably mediated by the nonhydrostatic conditions of their experiment.

3.4 $Sc_2W_3O_{12}$ – An *in-situ* neutron diffraction study under pressure

3.4.1 Results

The goal of the *in-situ* neutron experiment was to collect good-quality structural data under truly hydrostatic conditions in the pressure range where the orthorhombic to monoclinic phase transition occurs in the material. As we have already seen, this phase transition happens around 0.3 GPa on compression, thus the 0 – 0.65 GPa range given by the He-gas pressure cell was suitable for this study. By careful Rietveld analysis of the data, in addition to the lattice constants, we extracted bond lengths and bond angles so

that we could examine how the structure accommodates the decrease in volume on compression. We already pointed out in the previous section that the mechanism of volume reduction on compression is different from that on heating. By comparing the finite structural changes that occur on compression with those occurring on heating, we can learn about the difference in the volume reduction mechanisms for the two cases.

The structure of $Sc_2W_3O_{12}$ was refined at twelve pressures, including three pressure points on decompression, using the atomic positions of Abrahams and Bernstein[46] (orthorhombic phase, space group Pnca), as well as Evans and Mary[53] (monoclinic phase, $P2_1/a$) as starting points (see Appendix A). Since we were interested in the minor changes in bond distances and angles that occur as a function of pressure, care was taken to adopt a consistent refinement strategy throughout the analysis. For each of the refinements discussed below, an addition to the fractional atomic coordinates and isotropic thermal parameters, 12 background terms, 3 peak profile variables, all cell parameters, the diffractometer constants ZERO and DIFA, and an overall scale factor (two in the case of phase coexistence) were refined. Figure 3.11 shows observed, calculated and difference profiles of typical refinements for the orthorhombic and the monoclinic phase, respectively.

D-spacing ranges for the analyses were 0.45-5.28 Å for the 0-0.25 GPa pressure range and 0.70-5.28 Å for the 0.30-0.61 GPa range. The isotropic thermal parameters were constrained to be the same within the same atom type (Sc, O and W, respectively) in the refinements of both phases. The lattice constants obtained at different pressures by Rietveld refinement are tabulated in Table 3.3. Similarly to our x-ray study, pseudo-orthorhombic lattice constants were also calculated and are given along with primitive

monoclinic ones. The orthorhombic and monoclinic phase seemed to coexist at 0.25 GPa (on compression; 99.0 % orthorhombic + 1.0 % monoclinic), 0.3 GPa (on compression; 4.0 % and 96.0 %, resp.) as well as 0.25 GPa on decompression (1.3 % and 98.7 %, resp.). The weight percent amount (phase fractions) of the two phases was also estimated from the Rietveld fits. While no data with considerable amounts of both phases was recorded, considerable hysteresis was observed; on compression at 0.25 GPa the sample was almost entirely orthorhombic, but on decompression it was almost all monoclinic. At 0.25 GPa on compression, the amount of monoclinic phase was apparently too small for a reliable lattice constant determination. Therefore, a two-histogram refinement was also carried out for the 0.25 GPa datasets using both the data collected on compression and on decompression. The lattice parameters from this combined refinement (bottom row in Table 3.3) seemed very reasonable and thus the results form this refinement were used for further comparisons.

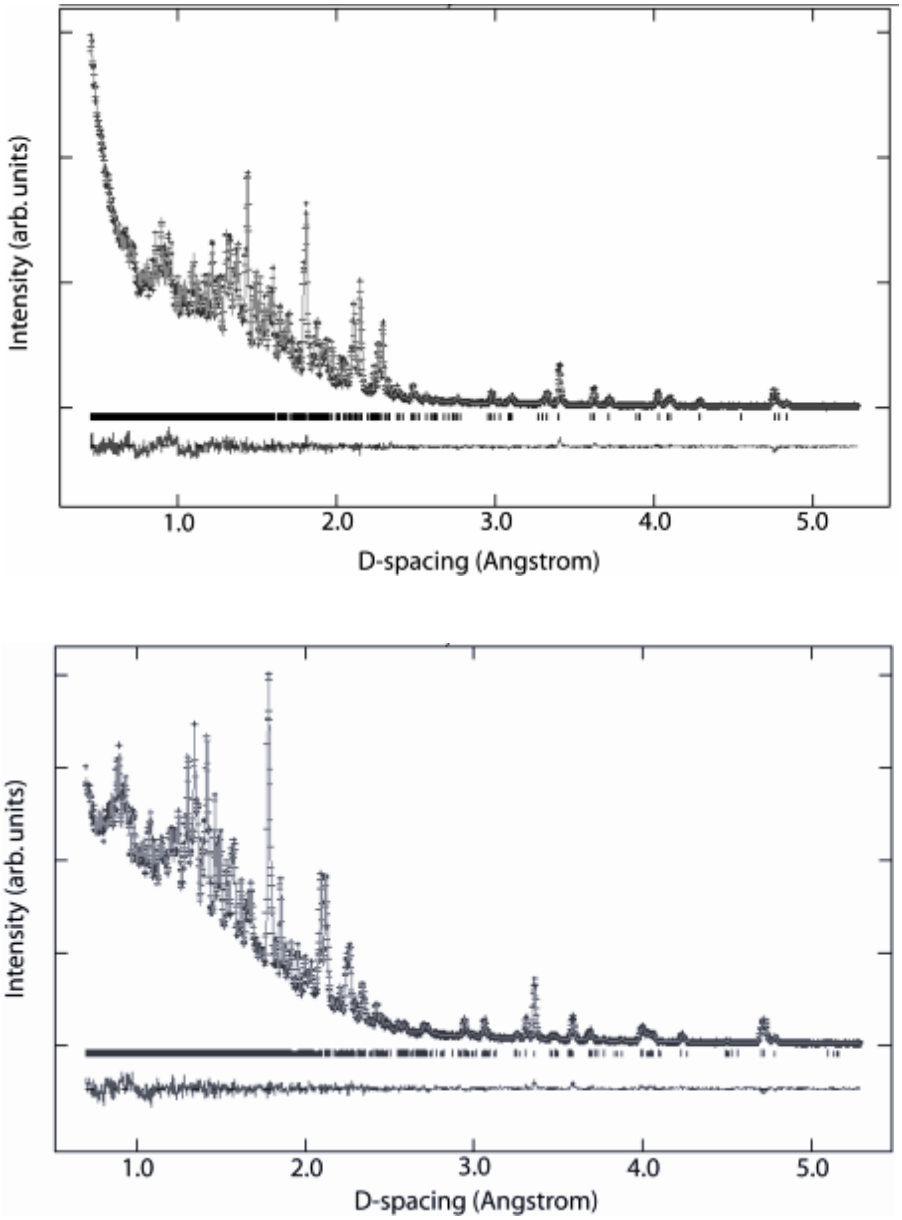

Figure 3.11: Observed (+), calculated (line) and difference (lower line) neutron diffraction patterns for typical Rietveld refinements of orthorhombic (top; 0.1 GPa) and monoclinic $Sc_2W_3O_{12}$ (bottom; 0.4 GPa). The tick marks between the pattern and the difference curve represent peak positions predicted by the model.

Table 3.3: $Sc_2(WO_4)_3$ lattice constants as a function of pressure in helium pressure-transmitting medium. Derived pseudo-orthorhombic values are given for the monoclinic phase along with the primitive monoclinic lattice constants that were directly determined from the diffraction data. At 0.30 GPa on compression and 0.25 GPa on decompression, both phases were present in significant amounts.

Pressure (GPa)	Symmetry	a, Å	b, Å	c, Å	β or α, deg	Volume, Å^3
0.00*	Orthorhombic	9.6872(8)	13.3406(12)	9.5952(8)	90.000	1240.00(31)
0.00	Orthorhombic	9.6755(30)	13.3299(42)	9.5848(29)	90.000	1236(1)
0.10	Orthorhombic	9.6687(13)	13.3021(17)	9.5778(12)	90.000	1231.84(46)
0.20	Orthorhombic	9.6653(11)	13.2792(15)	9.5724(10)	90.000	1228.58(39)
0.25	Orthorhombic Monoclinic	9.6629(11) -	13.2689(15) -	9.5710(11) -	90.000 -	1227.16(41)
0.30	Orthorhombic *Pseudo-ortho* Monoclinic	9.5881(33) 9.5776 16.2513(25)	13.2515(41) 13.2541 9.5776(15)	9.4638(27) 9.4656 18.9313(29)	90.000 89.73 125.357(4)	1202.45(67) 2403(1)
0.35	Monoclinic *Pseudo-ortho*	16.2286(27) 9.5638	9.5638(16) 13.2376	18.8958(32) 9.4479	125.345(3) 89.74	2392(1)
0.40	Monoclinic *Pseudo-ortho*	16.2086(25) 9.5546	9.5546(15) 13.2254	18.8688(30) 9.4344	125.320(3) 89.72	2384(1)
0.50	Monoclinic *Pseudo-ortho*	16.1676(30) 9.5326	9.5326(18) 13.1974	18.8199(35) 9.4100	125.286(3) 89.69	2368(1)
0.61	Monoclinic *Pseudo-ortho*	16.1338(28) 9.5172	9.5172(17) 13.1746	18.7826(33) 9.3913	125.257(3) 89.66	2355(1)
0.45 decompr.	Monoclinic *Pseudo-ortho*	16.1841(25) 9.5415	9.5415(15) 13.2084	18.8397(29) 9.4198	125.301(3) 89.71	2374(1)
0.35 decompr.	Monoclinic *Pseudo-ortho*	16.2289(28) 9.5653	9.5653(17) 13.2384	18.8955(33) 9.4478	125.341(3) 89.74	2393(1)
0.25 decompr.	Orthorhombic *Pseudo-ortho* Monoclinic	9.6620(58) 9.6004 16.2893(25)	13.3616(71) 13.2762 9.6004(14)	9.5741(56) 9.4636 18.9792(28)	90.000 89.89 125.410(3)	1236(1) 2419(1)
0.25 combined refinement	Orthorhombic *Pseudo-ortho* Monoclinic	9.6631(11) 9.5954 16.2882(26)	13.2692(15) 13.2724 9.5954(15)	9.5712(11) 9.4879 18.9758(30)	90.000 89.80 125.428(4)	1227.22(41) 2416.64(90)

*Out of the pressure cell data obtained in a separate experiment using the same instrument.

In Figure 3.12 we present normalized orthorhombic and pseudo-orthorhombic lattice constants as a function of pressure. In accordance with the results from our in-situ synchrotron x-ray study, the orthorhombic *b*-axis appears to be much more compressible than the *a*- and *c*-axes and that there is essentially no change in length for the *b*-axis at the orthorhombic to monoclinic transition, unlike the other axes. The comparison with x-ray data in isopropanol medium shows reasonably good agreement (see Figure 3.13).

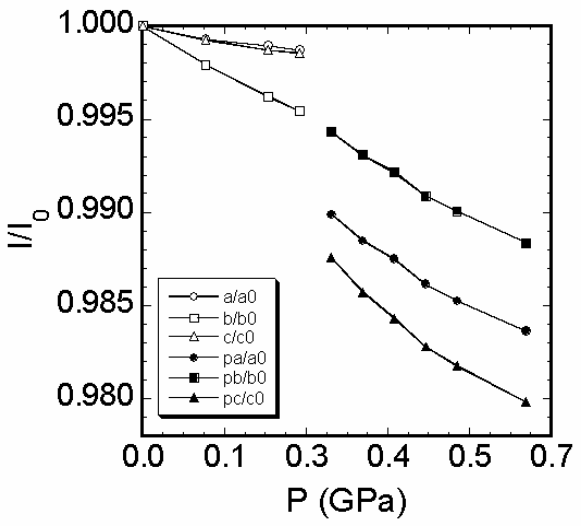

Figure 3.12: Normalized lattice constants as a function of pressure for $Sc_2W_3O_{12}$ in helium. Open symbols are for the orthorhombic, closed symbols are for the monoclinic phase. The monoclinic lattice constants for the phase existing above ~ 0.3 GPa have been converted to pseudo-orthorhombic values. Normalization of the lattice constants was done using the zero pressure values. The lines are only a guide to the eye.

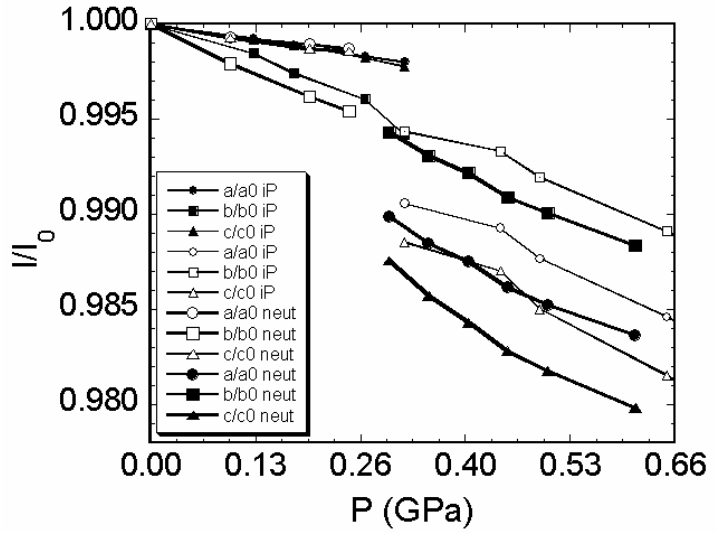

Figure 3.13: Comparison of the normalized lattice constants as a function of pressure for $Sc_2W_3O_{12}$ in helium (denoted as "neut") and isopropanol ("iP"). The monoclinic lattice constants for the phase existing above ~ 0.3 GPa have been converted to pseudo-orthorhombic values. Normalization of the lattice constants was done using the zero pressure values. The lines are only a guide to the eye.

Linear compressibilities were estimated for both phases from the change in the lattice constants: for the orthorhombic phase $\beta_a = 5.05(56)\times10^{-3}$ GPa^{-1}, $\beta_b = 1.83(8)\times10^{-2}$ GPa^{-1}, $\beta_c = 5.85(54)\times10^{-3}$ GPa^{-1}; monoclinic phase $\beta_a = 2.05(14)\times10^{-2}$ GPa^{-1}, $\beta_b = 1.95(10)\times10^{-2}$ GPa^{-1}, $\beta_c = 2.53(20)\times10^{-2}$ GPa^{-1}. Fitting a third-order Birch-Murnaghan equation of state (EOS) to the P-V data gave a bulk modulus, K_0, of 34(2) GPa for the orthorhombic and 13.5(10) GPa for the monoclinic phase. The zero pressure volume/formula unit (V_0) values were 308.95(8) Å^3 and 306.56(61) Å^3 for the orthorhombic and the monoclinic phase, respectively. The pressure derivative of the bulk modulus was fixed at 4.0 while fitting the data for both phases due to the limited number of data points. Table 3.4 compares the above linear compressibility and bulk modulus data with those obtained from the x-ray experiment.

Table 3.4: Comparison of the linear compressibilities (β), zero pressure volumes/formula unit (V_0), bulk moduli (K_0) and pressure derivatives (K_p) for orthorhombic and monoclinic $Sc_2W_3O_{12}$ obtained from P-V data of high-pressure x-ray and neutron diffraction experiments using different pressure media.

	X-ray diffraction (CHESS) in isopropanol		**X-ray diffraction (CHESS) in nitrogen**		**Neutron diffraction (IPNS) in helium**	
Parameter	*Orthorhombic*	*Monoclinic*	*Orthorhombic*	*Monoclinic*	*Orthorhombic*	*Monoclinic*
β_a (GPa^{-1})	$6.32(16)\times10^{-3}$	$1.85(3)\times10^{-2}$	$3.78(*)\times10^{-3}$	$2.06(7)\times10^{-2}$	$5.05(56)\times10^{-3}$	$2.05(14)\times10^{-2}$
β_b (GPa^{-1})	$1.76(21)\times10^{-2}$	$1.78(3)\times10^{-2}$	$1.41(*)\times10^{-2}$	$1.80(11)\times10^{-2}$	$1.83(8)\times10^{-2}$	$1.95(10)\times10^{-2}$
β_c (GPa^{-1})	$6.84(32)\times10^{-3}$	$1.69(9)\times10^{-2}$	$4.18(*)\times10^{-3}$	$1.64(18)\times10^{-2}$	$5.85(54)\times10^{-3}$	$2.53(20)\times10^{-2}$
V_0 (Å^3)	308.75(17)	307.70(73)	309*	307(1)	308.95(8)	306.56(61)
K_0 (GPa)	31(3)	14(1)	45*	13.3(5)	34(2)	13.5(10)
K_p	4.0(implied)	4.0(9)	4.0(implied)	4.0(implied	4.0(implied)	4.0(implied)

*No standard deviation was estimated as only two data points were available.

The linear compressibilities and the parameters obtained by EOS fitting from the neutron experiment show reasonably good agreement with the data from our high-

pressure synchrotron studies. The relative differences between the x-ray and neutron data seem to largest in the case of the linear compressibilites along the *a* and *c* axes of the orthorhombic structure. These differences may be due to the different pressure-transmitting media used (He is supposedly similar to nitrogen),[100] pressure calibration problems as well as a possible non-zero pressure in the as-closed DAC in the isopropanol experiment.

In order to examine the structural distortions that occur on compression, the Sc – O, W – O bond lengths, the O – Sc – O octahedral and the O – Mo – O tetrahedral angles, as well as the Sc – O – W bridging angles obtained from the refinements were examined. The variation in these parameters has been looked at before in thermal expansion studies targeted at determining the mechanism of the structural changes in e.g. $Sc_2W_3O_{12}$[48, 101] and $Sc_2Mo_3O_{12}$[53] on heating. Changes in the Sc – O and W - O bond lengths, as well as the 90^o O – Sc – O octahedral and the O – Mo – O tetrahedral angles, if they occur, would reflect distortions of the polyhedra. They are not expected to change significantly up to the pressure of the phase transition in $Sc_2W_3O_{12}$, as the ScO_6 and WO_4 polyhedra are typically considered as rigid units (strongly bonded group of atoms with highly correlated thermal vibrations).[48] The octahedral and tetrahedral angles were reported to show only minor changes on heating in orthorhombic $Sc_2W_3O_{12}$ (in the 10-450 K range),[48] and changes in the O – Mo – O tetrahedral bond angles in $Sc_2Mo_3O_{12}$ were found only at the monoclinic to orthorhombic phase transition (at 180 K) in a variable temperature study carried out in the 4–300 K range.[53] Therefore, for this comparison, the O – Sc – O octahedral and the O – Mo – O tetrahedral angles were not examined. However, changes in the bond lengths were not insignificant in variable temperature

studies of $Sc_2W_3O_{12}$ (50-823 K),[101] and the previously mentioned study of $Sc_2Mo_3O_{12}$. Variation in the Sc – O – W bridging angles that connect the ScO_6 octahedra and the WO_4 tetrahedra indicate tilting of the structural units. The bridging angles were expected to show changes on compression, as they varied on heating in both the tungstate and the molybdate in the above mentioned studies. There are six different bridging angles in the orthorhombic structure, one for each oxygen in the unit cell. The Sc – W nonbonded distances associated with the bridging angles were also extracted for the orthorhombic phase, as in case of a change in any of the bridging angles, the corresponding metal-metal distances would also change. The above bond lengths, metal-metal distances and bond angles at different pressures for the orthorhombic phase are given in Table 3.5. The volume per formula unit values were used for a comparison discussed later. The Sc – O and W – O bond distances were derived from six independent distances at each pressure by taking their mean. Errors on the mean Sc – O and W – O bond distances are given as the standard deviation amongst the independent metal-oxygen distances divided by the square root of the number of independent distances. For the bridging angles and the Sc – W distances, which are unique for all six oxygens, the standard deviations from the Rietveld refinements are given.

Table 3.5: Derived Sc – O, W – O bond lengths, Sc – W nonbonded distances (at the six different oxygen atoms; top table) and O – W bridging angles (bottom table) as a function of pressure and volume per formula unit for orthorhombic $Sc_2W_3O_{12}$.

P (GPa)	V/form. unit (Å^3)	Sc – O bond (Å)	W – O bond (Å)	Sc – W at O1 (Å)	Sc – W at O2 (Å)	Sc – W at O3 (Å)	Sc – W at O4 (Å)	Sc – W at O5 (Å)	Sc – W at O6 (Å)
0.00	309.00	2.0850(33)	1.7640(30)	3.737(5)	3.818(4)	3.764(4)	3.734(5)	3.835(4)	3.672(4)
0.10	307.96	2.0900(60)	1.7620(60)	3.739(8)	3.817(6)	3.737(7)	3.727(7)	3.849(7)	3.653(7)
0.20	307.14	2.0912(80)	1.7580(80)	3.729(7)	3.810(5)	3.729(6)	3.742(6)	3.851(6)	3.651(6)
0.25	306.80	2.0910(70)	1.7590(70)	3.742(6)	3.823(5)	3.740(6)	3.720(6)	3.839(5)	3.633(5)

P (GPa)	V/form. unit (Å^3)	Sc1-**O1**-W2 angle (deg)	Sc1-**O2**-W1 angle (deg)	Sc1-**O3**-W2 angle (deg)	Sc1-**O4**-W1 angle (deg)	Sc1-**O5**-W2 angle (deg)	Sc1-**O6**-W2 angle (deg)
0.00	309.00	150.40(22)	169.60(20)	157.70(22)	148.00(20)	171.90(23)	145.30(21)
0.10	307.96	149.80(40)	171.14(33)	154.40(40)	148.45(32)	173.50(40)	144.06(34)
0.20	307.14	149.75(33)	172.06(27)	154.94(31)	148.34(28)	173.88(31)	144.13(30)
0.25	306.80	149.84(30)	171.22(29)	154.20(31)	147.88(27)	173.89(31)	142.65(28)

The mean Sc – O and W – O bond distances for the monoclinic phase were derived from 24 independent values at each pressure by taking their mean. There are 24 different bridging angles for the monoclinic structure, four for each of the six oxygens in the original orthorhombic structure. The bond lengths and the bridging angles for the monoclinic structure at different pressures are given in Table 3.6. The errors on the numbers are given as for Table 3.5.

Table 3.6: Mean Sc – O, W – O bond lengths (top table) and Sc – O – W bridging angles (next three tables) as a function of pressure for monoclinic $Sc_2W_3O_{12}$.

P (GPa)	Sc – O bond (Å)	W – O bond (Å)
0.25	2.1000(30)	1.7578(7)
0.30	2.0956(70)	1.7593(25)
0.35	2.0988(120)	1.7610(100)
0.40	2.0905(120)	1.7671(97)
0.45	2.0942(120)	1.7595(92)
0.50	2.0941(120)	1.7608(100)
0.61	2.0939(120)	1.7582(95)

P (GPa)	Sc1-**O11**-W1 angle (deg)	Sc4-**O12**-W1 angle (deg)	Sc1-**O13**-W1 angle (deg)	Sc4-**O14**-W1 angle (deg)	Sc3-**O21**-W2 angle (deg)	Sc2-**O22**-W2 angle (deg)	Sc2-**O23**-W2 angle (deg)	Sc1-**O24**-W2 angle (deg)
0.25	160.3(14)	163.0(15)	145.5(12)	146.9(13)	175.8(14)	150.3(14)	147.5(13)	134.2(12)
0.30	155.6(13)	162.0(14)	144.1(12)	148.1(13)	173.1(14)	145.7)14)	147.1(12)	137.6(13)
0.35	151.7(13)	168.9(15)	141.8(13)	149.2(14)	169.1(14)	145.0(14)	142.4(12)	136.3(13)
0.40	154.8(13)	163.3(14)	145.5(13)	146.9(13)	172.2(13)	149.3(13)	143.4(13)	133.8(12)
0.45	153.2(12)	163.3(14)	143.1(12)	147.3(12)	171.6(12)	147.2(12)	143.9(12)	134.8(13)
0.50	154.2(14)	160.2(16)	142.2(14)	146.3(13)	169.1(14)	147.7(14)	144.9(13)	134.1(12)
0.61	152.4(13)	161.4(14)	140.8(12)	145.6(12)	169.4(13)	147.0(13)	144.8(12)	136.5(12)

P (GPa)	Sc4-**O31**-W3 angle (deg)	Sc1-**O32**-W3 angle (deg)	Sc2-**O33**-W3 angle (deg)	Sc3-**O34**-W3 angle (deg)	Sc4-**O41**-W4 angle (deg)	Sc3-**O42**-W4 angle (deg)	Sc1-**O43**-W4 angle (deg)	Sc4-**O44**-W4 angle (deg)
0.25	154.4(14)	146.5(13)	159.9(13)	138.4(13)	157.8(13)	153.3(13)	162.3(14)	144.9(13)
0.30	155.6(14)	145.2(13)	159.9(13)	137.5(13)	159.0(13)	152.4(13)	161.5(14)	146.1(13)
0.35	149.1(14)	151.7(14)	156.1(14)	136.4(14)	152.0(13)	158.9(14)	160.0(14)	145.1(14)
0.40	150.2(13)	147.9(13)	159.3(13)	133.5(12)	151.1(12)	156.3(13)	158.1(13)	144.5(12)
0.45	151.0(13)	153.8(12)	161.6(12)	135.4(12)	154.2(12)	153.8(13)	161.6(13)	144.8(12)
0.50	152.1(15)	146.0(14)	156.1(14)	133.2(14)	154.5(15)	152.5(15)	161.4(15)	144.1(14)
0.61	153.3(14)	143.4(13)	157.0(13)	132.8(13)	153.4(13)	153.6(14)	162.6(14)	144.1(13)

P (GPa)	Sc4-**O51**-W5 angle (deg)	Sc2-**O52**-W5 angle (deg)	Sc3-**O53**-W5 angle (deg)	Sc1-**O54**-W5 angle (deg)	Sc3-**O61**-W6 angle (deg)	Sc2-**O62**-W6 angle (deg)	Sc3-**O63**-W6 angle (deg)	Sc2-**O64**-W6 angle (deg)
0.25	170.1(14)	152.6(12)	162.5(13)	137.5(12)	148.0(13)	137.6(10)	157.0(12)	159.1(13)
0.30	168.1(14)	148.3(12)	161.8(13)	140.0(13)	148.0(13)	135.8(11)	156.3(12)	156.4(12)
0.35	166.6(13)	149.8(12)	164.0(13)	142.2(12)	144.4(15)	132.3(13)	159.3(13)	160.1(13)
0.40	169.6(12)	150.6(11)	163.6(11)	138.9(11)	146.2(12)	132.6(12)	156.7(12)	160.1(12)
0.45	166.9(12)	150.0(11)	165.1(11)	140.6(11)	144.8(11)	130.8(11)	158.5(12)	158.8(11)
0.50	166.4(14)	151.4(13)	166.7(13)	141.0(13)	143.3(13)	128.8(14)	155.3(14)	159.1(14)
0.61	167.3(13)	149.6(12)	166.0(12)	141.5(12)	140.5(13)	130.0(12)	155.9(12)	158.8(13)

Figure 3.14 plots average the metal-oxygen bonded distances for the entire pressure range that was studied. The Sc – O distance remains unchanged within our error limits on compression. The W – O distance may show some very small decrease over the 0-0.25

GPa region, and perhaps over the entire pressure range, but the errors on the individual data points are unfortunately too large to be sure of this.

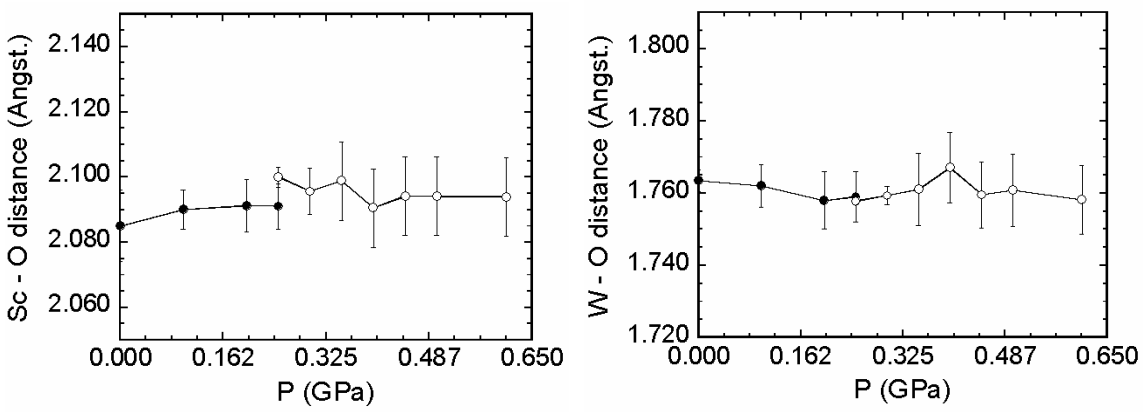

Figure 3.14: Variation of the mean Sc – O (left) and W – O bond lengths (right) as a function of pressure. Closed symbols: orthorhombic phase; open symbols: monoclinic phase.

The pressure dependence of the bridging angles for the orthorhombic region is shown graphically in Figure 3.15. Most angles remain unchanged in the 0-0.25 GPa range, but the two large angles Sc1-O2-W1 and Sc1-O5-W2 seem to show a slight increase. These are the same angles that showed a marked decrease with temperature in a study by Weller et al.,[101] and agree with the corresponding Sc-O-Mo angles that have been seen to decrease on heating in $Sc_2Mo_3O_{12}$.[53] The values for the 0.25 GPa pressure points seem to be systematically smaller for all six angles. This can probably be attributed to problems with the refinement due to correlations between the lattice parameters of the two coexisting phases rather than due to true bond angle changes. The errors on the derived angles are rather small, the error bars in the graph are barely visible even upon reducing the symbols to a very small size

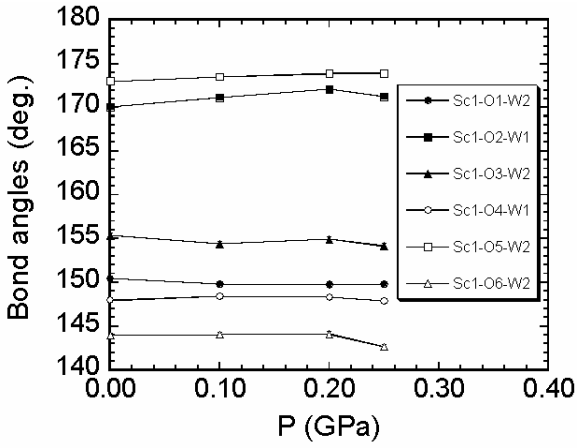

Figure 3.15: Sc – O – W bond angles (bridging angles) as a function of pressure for orthorhombic $Sc_2W_3O_{12}$. The size of the error bars is comparable to the size of the symbols.

The pressure dependence of the bridging angles for both the orthorhombic and monoclinic phase is shown in Figure 3.16. Each of the six crystallographically unique bond angles of the orthorhombic structure corresponds to four bond angles in the monoclinic form. These four angles (open symbols) are plotted along with corresponding orthorhombic angle for each unique oxygen. Due to the large error bars on most of the monoclinic bridging angles, it is difficult to draw any conclusions based on the variations. Nevertheless, there seems to be a decreasing trend in some of the monoclinic bridging angles at O1 (graph a), O3 (graph c) and O6 (graph f). In the case of some of the angles at O3 (see Sc3-O34-W3) and O6 (Sc3-O61-W6 and Sc2-O62-W6) the decrease is significant.

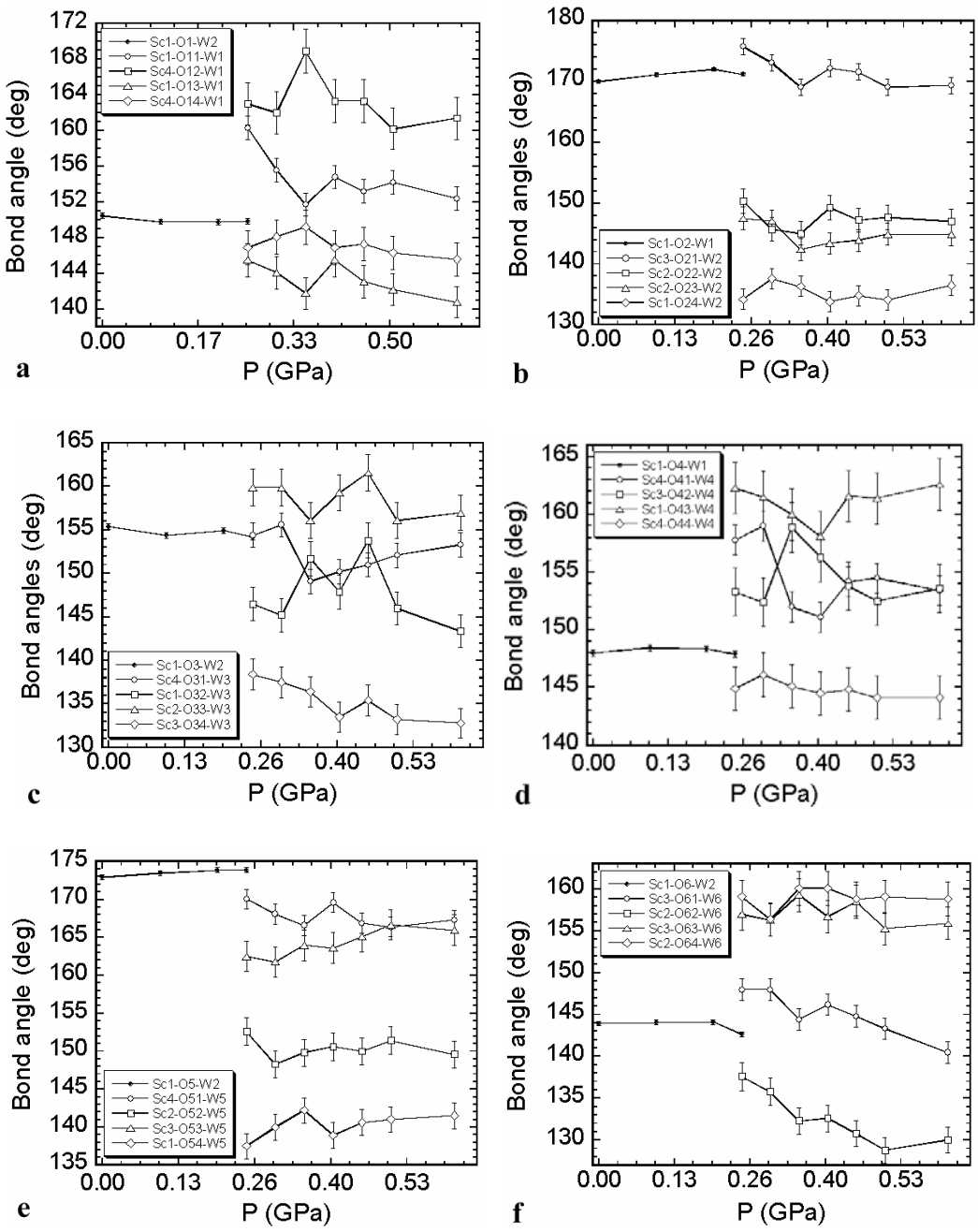

Figure 3.16: Sc – W – O bridging bond angles for orthorhombic (closed symbols) and the four equivalent angles for monoclinic $Sc_2W_3O_{12}$ (open symbols). The angles for oxygens O1 (a), O2 (b), O3 (c); O4 (d), O5 (e) O6 (f) are shown.

The nonbonded Sc – W distances at the bridging angles were also examined for the orthorhombic structure and are plotted along with the corresponding Sc-O-W angles in Figure 3.17. The data for the bridging angles and nonbonded Sc – W distances should correlate well with one another as any changes in the metal-metal distances arise as a result of changes in the bridging angle, that is, tilting of the polyhedra. However, due to the accuracy of the experiment in determining these values the correlation is not well reflected. With the too large errors on the nonbonded distances (open symbols) no conclusion can be made other than that the increase in the Sc1-O2-W1 and Sc1-O5-W2 angles did not result in any decrease (and it should not, based on a previous report[48]) in the corresponding Sc – W distances. The increase in the Sc – W distance at the Sc1-O5-W2 angle suggested by the data may be the result of an increase in the bridging angle.

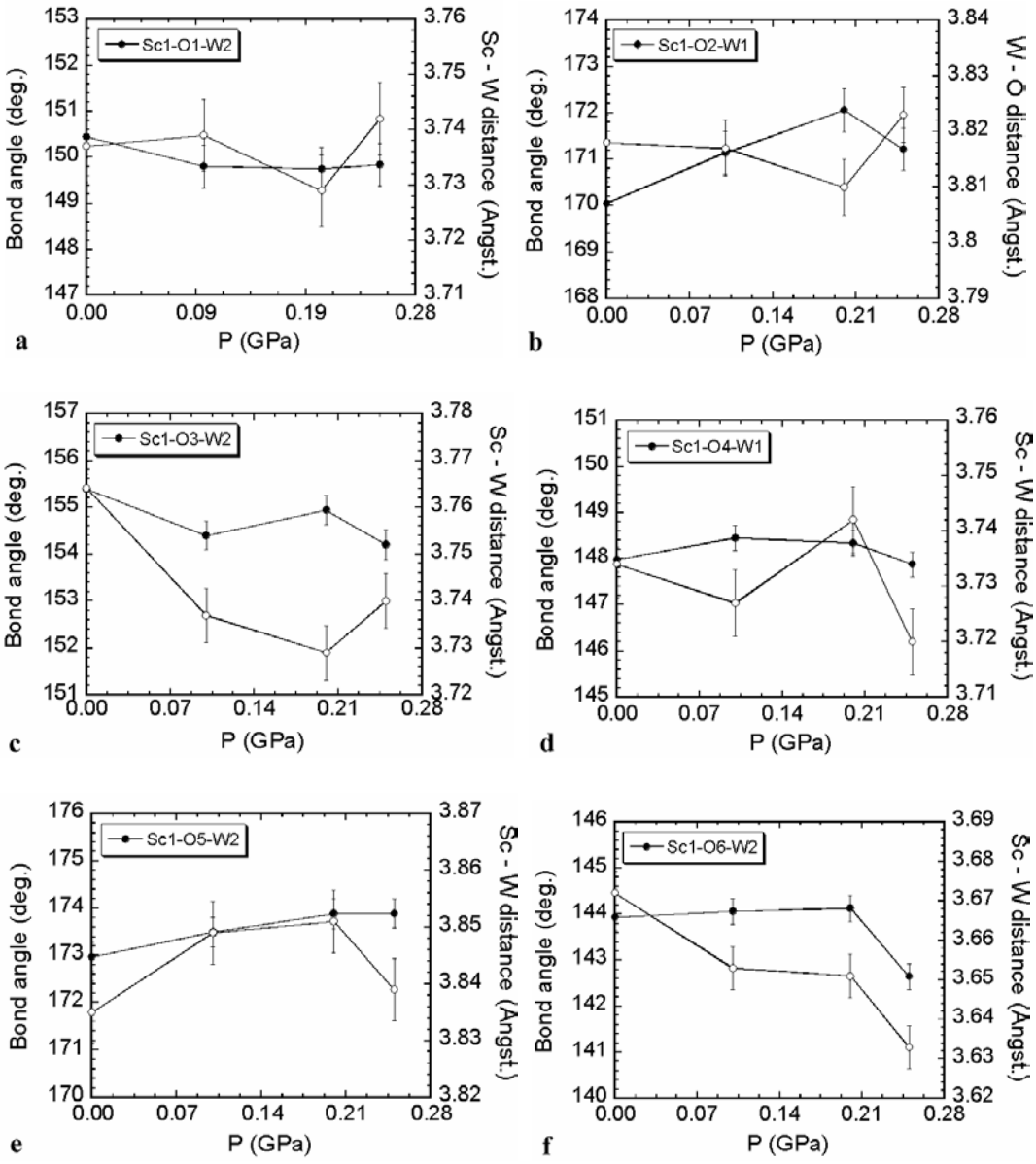

Figure 3.17: Sc – W nonbonded distances (open symbols) and corresponding Sc-O-W bond angles as a function of pressure for orthorhombic $Sc_2W_3O_{12}$.

The negative thermal expansion in $Sc_2W_3O_{12}$ is viewed as being a result of complex coupled twisting of the framework polyhedra in three dimensions.[48] In an attempt to compare the mechanism of volume reduction in $Sc_2W_3O_{12}$ on compression with the mechanism of volume contraction on heating, we contrasted the results from our high-

pressure measurements with the results of Weller *et al.*[101] obtained at ambient pressure over the 50-823 K temperature range. The data from the two experiments were brought to a common scale by examining the data as a function of volume per formula unit normalized to ambient conditions; zero pressure and 298 K. The overall changes in bond distances and angles as a function of temperature in this and other NTE materials are small. In addition, it is well known that apparent changes in bond distances as a function of temperature can occur due to correlated thermal vibrations. This was seen by Weller *et al.*,[101] the apparent bond lengths obtained directly from their refinements decreased with increasing sample temperature, while bond lengths should increase with temperature (see section 1.1). Therefore they applied a correction to their bond length data to account for the effects of correlated thermal motion.[101] Deficiencies in this correction may be the reason for their values being different from ours in the normalized volume region where they overlap (see Figure 3.18). The metal-oxygen distances and the bridging angles reported by Weller *et al.*,[101] and used for our comparison, are tabulated in Table 3.7. The errors on the average bond distances were calculated the same way as for our high-pressure data. For the bridging angles, the deviation is given as reported by Weller.

Table 3.7: Mean Sc – O, W – O bond lengths (top table) and Sc – O – W bridging angles (top and bottom table) as a function of temperature and volume per formula unit for orthorhombic $Sc_2W_3O_{12}$ as reported by Weller *et al.*[101] For all of the bridging angles the standard deviation is 0.30.

Temperature (K)	V/form. unit (Å^3)	Sc – O bond (Å)	W – O bond (Å)	Sc1-**O1**-W2 angle (deg)	Sc1-**O2**-W1 angle (deg)	Sc1-**O3**-W2 angle (deg)
50.0	309.41	2.0832(56)	1.7761(22)	151.09	173.34	155.19
100	309.25	2.0813(56)	1.7769(16)	151.34	172.60	155.40
150	309.09	2.0794(53)	1.7749(20)	151.25	171.84	155.47
200	308.97	2.0782(57)	1.7740(18)	151.62	170.78	155.38
250	308.83	2.0771(40)	1.7726(29)	151.28	169.79	155.63
298	308.69	2.0757(51)	1.7720(35)	151.41	168.96	155.79
373	308.43	2.0682(120)	1.7766(49)	152.40	168.10	154.90
423	308.30	2.0772(89)	1.7711(37)	150.70	167.80	154.40
473	308.27	2.0717(110)	1.7722(69)	151.50	167.80	154.30
523	308.06	2.0763(130)	1.7685(56)	150.60	167.30	155.20
573	307.88	2.0688(110)	1.7722(60)	152.40	166.70	154.00
623	307.75	2.0740(140)	1.7679(110)	151.70	167.20	155.20
673	307.68	2.0672(120)	1.7726(140)	149.60	166.20	154.00
723	307.49	2.0660(130)	1.7698(73)	150.40	165.90	154.20
773	307.30	2.0717(140)	1.7635(110)	151.20	166.90	155.00
823	307.23	2.0693(140)	1.7662(130)	151.00	167.30	153.20

Temperature (K)	V/form. unit (Å^3)	Sc1-**O1**-W2 angle (deg)	Sc1-**O2**-W1 angle (deg)	Sc1-**O3**-W2 angle (deg)
50.0	309.41	146.82	175.34	141.63
100	309.25	147.04	174.74	141.80
150	309.09	147.71	174.40	142.38
200	308.97	148.05	174.17	142.96
250	308.83	149.12	173.52	143.30
298	308.69	149.21	173.26	143.41
373	308.43	149.80	173.10	144.30
423	308.30	149.60	172.40	144.30
473	308.27	150.80	172.30	144.70
523	308.06	149.10	172.80	145.90
573	307.88	150.70	172.10	144.70
623	307.75	150.20	171.40	144.70
673	307.68	150.90	172.30	146.70
723	307.49	150.90	171.70	146.20
773	307.30	150.50	170.90	146.90
823	307.23	151.30	171.80	146.60

A comparison of the variation of the Sc – O and W – O bond distances on compression with that seen on heating is shown in Figure 3.18. The errors on the data are large. There does not seem to be a trend in the variation of the Sc – O distances. However, the overall trend in the W – O distances suggest that both compression and heating results in a slight contraction of the W - O bonds (pressure and temperature increase to the left). The bond length being reduced on heating is unrealistic, thus the

observation is probably associated with an inadequate correction for correlated thermal motion.

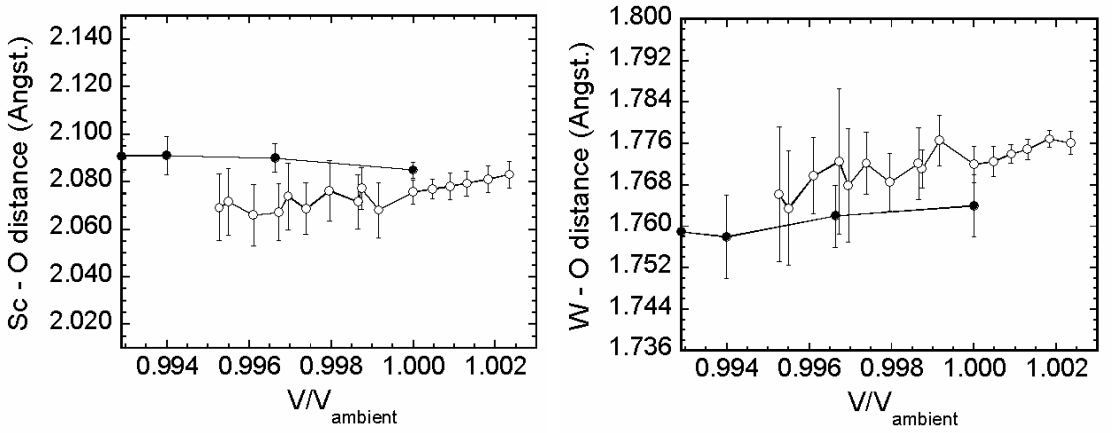

Figure 3.18: Variation of the average Sc – O (left) and average W – O bond length (right) for orthorhombic $Sc_2W_3O_{12}$ as a function of volume per formula unit normalized to 0.00 GPa (our pressure data; closed symbols), and normalized to 298 K (Weller's temperature data; open symbols).

A similar comparison for variation of the six bridging angles of the orthorhombic structure is plotted in Figure 3.19. The trend already seen in the Sc-O2-W and Sc-O5-W angles as a function of pressure is apparent from the graphs (graphs b and e, resp.). The trend of increasing bridging angle versus pressure in these two cases and the corresponding decrease of the same angle with increasing temperature are convincing even with the error bars on the data points. No other trend can be seen in the pressure data, but the bridging angles for oxygens O4 and O6 (graphs d and f, resp.) clearly increase with temperature. The variations of all six the bridging angles with temperature from the study of Weller et al. are in agreement with the report of Evans et al.[48]

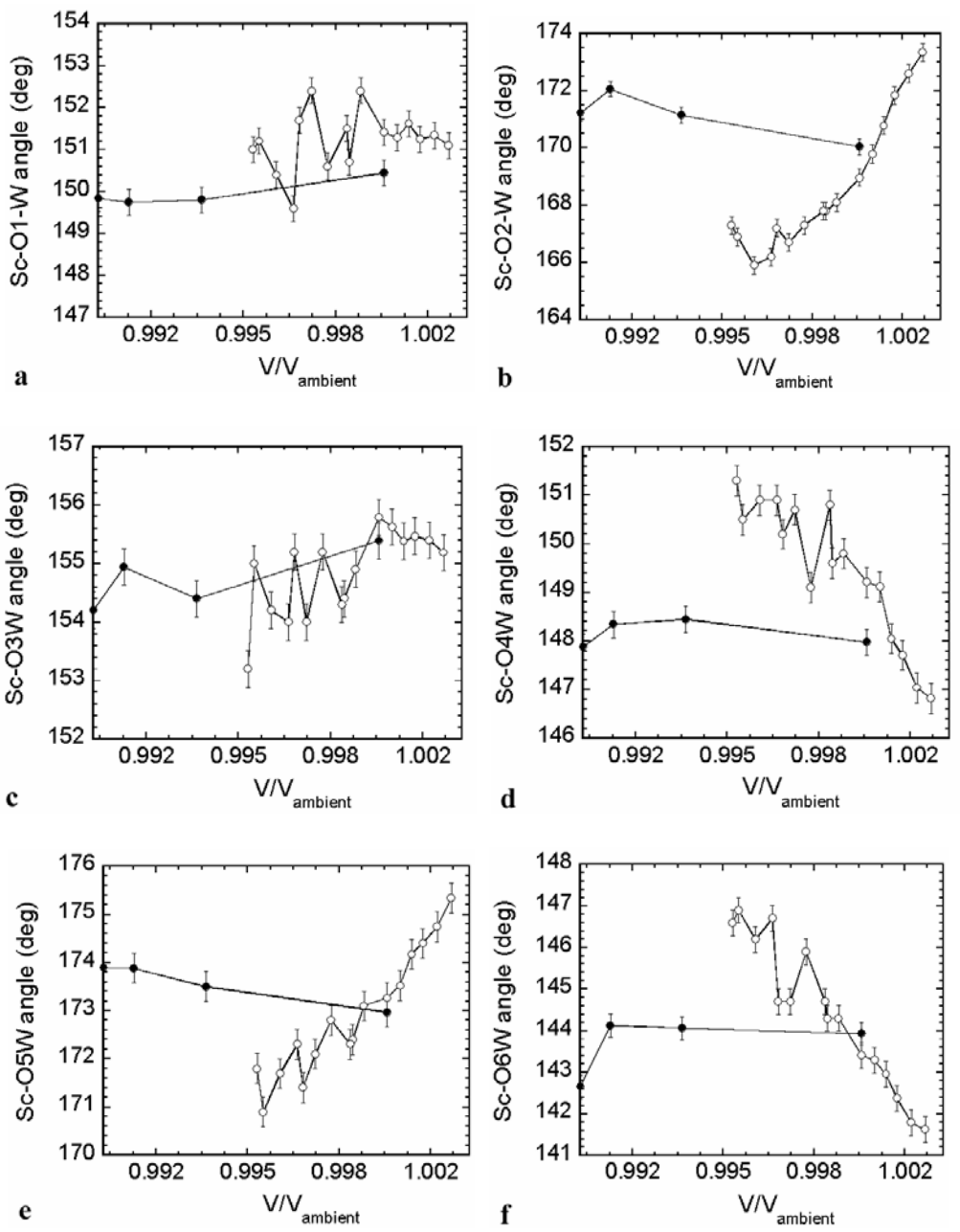

Figure 3.19: Variation of the bridging angles for orthorhombic $Sc_2W_3O_{12}$ as a function of volume per formula unit normalized to 0.00 GPa (our pressure data; closed symbols), and normalized to 298 K (Weller's temperature data; open symbols): Sc-O1-W (a), Sc-O2-W (b), Sc-O3-W (c), Sc-O4-W (d), Sc-O5-W (e) and Sc-O6-W (f).

3.4.2 Discussion

The structure of $Sc_2W_3O_{12}$ consists of a corner-sharing network of ScO_6 octahedra and WO_4 tetrahedra. In the orthorhombic form (space group Pnca), there is a single Sc site in the asymmetric unit and two crystallographically distinct W atoms, one (W1) on the twofold axis, and the other (W2) on a general position. There are six unique oxygen atoms. Each ScO_6 octahedron corner shares with six WO_4 tetrahedra, and each WO_4 corner shares with four ScO_6 octahedra. This results in a relatively open framework structure of metal atoms linked by two-coordinate oxygens. The structure of monoclinic $Sc_2W_3O_{12}$ (space group $P2_1/a$) is far more complex: the unit cell can be described by four Sc atoms, six W atoms and 24 O atoms. Due to the complexity of its structure as well as the very large error bars on our derived bond angles and as it does not display NTE, a more detailed analysis of interatomic distances (such as Sc – W nonbonded distances) and a comparison of thermal versus pressure behaviour for the monoclinic material is beyond the scope of this thesis.

The large errors on our data are due to instrumental limitations. Although we used the best He-gas pressure cell – neutron powder diffractometer combination currently available in the U.S., the large error bars on our bond distances and bond angles suggest that still better instrumental resolution is needed for this kind of study. The instrumental resolution ($\Delta d/d$) for the SEPD instrument is 0.0054 FWHM at 90^o.[77] Better data could be collected using the high resolution powder diffractometer at ISIS, UK ($\Delta d/d = 0.002$),[102] and in the future using an instrument at the Spallation Neutron Source that is being built in Oak Ridge National Laboratory, Oak Ridge, TN.

3.4.2.1 Variation in bond distances

We saw a very small decrease in the average W – O bond length with pressure in the orthorhombic region (see Figures 3.14 and 3.18). However, with the large errors on the data, it is not possible to draw a definitive conclusion.

3.4.2.2 Variation of bridging angles

To put our observations in the context of the mechanism of negative thermal expansion, let us consider some earlier findings about the bridging angles. The low-energy vibrations of the relatively rigid polyhedral groups, which is considered the basis of NTE in many framework materials require a certain degree of structural flexibility.[103-105] The orthorhombic to monoclinic phase transition is evidence of structural flexibility in these materials, given that it may be described as a static rotation of the polyhedral units.[53] From the examination of changes in Sc-O-W bond angles, insight can be gained into how and to what extent the observed structural changes are related to rocking motion of polyhedra. For $Sc_2Mo_3O_{12}$, it was found that the bridging bond angles at O1, O3, O4 and O6 showed essentially no change between their average values in the monoclinic form and the single value in the orthorhombic form. The average bond angles each showed a smooth trend, gradually increasing with temperature with essentially no discontinuity at the phase transition. However, angles at O2 and O5 showed a sharp increase in value at the monoclinic to orthorhombic phase transition.[53] The same two angles (Sc1-O2-W1 and Sc1-O5-W2) showed a significant decrease with temperature in the two variable temperature studies on $Sc_2W_3O_{12}$, while Sc1-O4-W1 and Sc1-O6-W2

both increased monotonically. Sc1-O1-W2 and Sc1-O3-W2 did not change significantly.[48, 101]

However, on compression the behavior of the orthorhombic bridging angles Sc1-O2-W1 and Sc1-O5-W2 seems to be different. We already pointed out based on our high-pressure x-ray results that the mechanism for volume reduction on compression is apparently different from what is seen on heating (see section 3.3.2). The *b*-axis, which displays normal positive thermal expansion, was found to show the greatest compressibility. The observation that both the Sc1-O2-W1 and Sc1-O5-W2 bridging angles increase (see Figures 3.15 through 3.17), while they decrease on heating, also supports the point about the difference in volume reduction mechanism. The difference in the behavior of the above two bridging angles on compression and heating, respectively, is the most apparent in the b and e parts of Figure 3.19. The observation that the changes seen in the bridging angles are very small suggests that volume reduction on compression is not accompanied with significant polyhedral tilting as was found for volume reduction on heating.

One more thing can be stated based on the comparison of the temperature and pressure behavior of $Sc_2W_3O_{12}$ (and $Sc_2Mo_3O_{12}$): this is the difference in anisotropy of the volume reduction. This high-pressure neutron study confirmed our high-pressure x-ray diffraction results: while the NTE (volume reduction) in the orthorhombic material is highly anisotropic, on compression it is much more isotropic. All three axes contract on compression, as a matter of fact, the *b* axis contracts even more than *a* and *c*, indicating that the anisotropy, in a sense, reversed. The very small variation in the bond distances and angles is consistent with a more isotropic behavior on compression.

3.5 $Sc_2Mo_3O_{12}$ and $Al_2W_3O_{12}$ – A high-pressure synchrotron x-ray diffraction study

3.5.1 Results for $Sc_2Mo_3O_{12}$

A selection of the recorded diffraction patterns for $Sc_2Mo_3O_{12}$ is shown in Figure 3.20. The diffraction data are consistent with a transition from the ambient pressure and temperature orthorhombic structure (Space group: Pnca) to a monoclinic structure (Space group: $P2_1/a$) at around 0.3 GPa. At ambient pressure this monoclinic structure is only seen for $Sc_2Mo_3O_{12}$ at low temperatures (< 180K).[47, 49, 53] Rietveld fits to the diffraction patterns indicate the onset of this transition is at ~0.24 GPa , with an approximate 50:50 mix of orthorhombic and monoclinic material in the 0.3-0.35 GPa range and almost complete transformation to monoclinic material by 0.6 GPa. A second transition giving a phase with unidentified symmetry was observed in the range 2.2-2.5 GPa. Further compression to ~7.9 GPa resulted in considerable peak broadening and a very weak diffraction pattern, but not complete amorphization. Decompression at ambient temperature did not lead to recovery of the starting orthorhombic phase; some weak Bragg peaks were seen from the decompressed material, but they were not readily assignable as arising from any of the crystalline phases that were observed on compression.

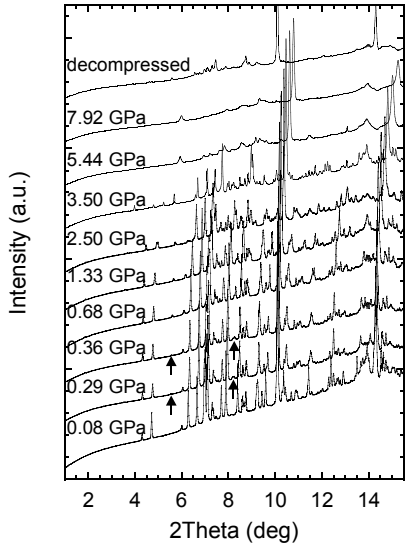

Figure 3.20: Powder diffraction patterns as a function of pressure for $Sc_2Mo_3O_{12}$. Arrows indicate the location of peaks that are characteristic of the monoclinic phase. The data were collected at 25 keV ($\lambda = 0.496$ Å).

Lattice constants for the orthorhombic and monoclinic phases, derived from LeBail fits to the data using GSAS, are shown as a function of pressure in Table 3.8. In order to examine the changes in linear compressibility through the phase transformation, the primitive monoclinic lattice constants were transformed to a new A-centered monoclinic lattice that is pseudo orthorhombic with $a_m \sim a_o$, $b_m \sim 2c_o$, $c_m \sim 2b_o$ and $\alpha_m \sim 90^o$. This can be done because the structures of the monoclinic and orthorhombic phases are very closely related to one another,[53] and it was carried out using the transformation matrix (0 1 0; 0 0 -1; -2 0 -1) as in section 3.3.1. The transformed pseudo-orthorhombic lattice constants for the monoclinic phase are also shown in Table 3.8.

Table 3.8: $Sc_2(MoO_4)_3$ lattice constants as of a function of pressure in isopropanol pressure- transmitting medium. Derived pseudo-orthorhombic values are given for the monoclinic phase along with the primitive monoclinic lattice constants that were directly determined from the diffraction data. At 0.29 and 0.36 GPa, both phases were present in significant amounts. Percentages of the first column indicate the weight percentage of the two coexisting phases as estimated from Rietveld fits to the data (the balance is the pressure calibrant NaCl).

Pressure (GPa)	Symmetry	a, Å	b, Å	c, Å	β or α, deg	Volume, Å^3
0.08	Orthorhombic	9.6305(4)	13.2271(6)	9.5368(4)	90.000	1214.83(12)
0.12	Orthorhombic	9.6262(3)	13.2252(4)	9.5345(3)	90.000	1213.82(8)
0.18	Orthorhombic	9.6254(3)	13.2078(5)	9.5303(3)	90.000	1211.58(9)
0.24 39.7 %	Orthorhombic	9.6199(5)	13.1928(7)	9.5267(5)	90.000	1209.07(14)
3.6 %	Monoclinic	-	-	-	-	
0.29 24.3 %	Orthorhombic	9.5468(7)	13.1777(10)	9.4240(7)	90.000	1185.58(11)
	Pseudo-ortho	9.5405	13.1734	9.4219	89.67	
21.1 %	Monoclinic	16.1513(3)	9.5405(4)	18.8438(6)	125.352(2)	2368.26(7)
0.36 21.4 %	Orthorhombic	9.5261(15)	13.1718(16)	9.4025(14)	90.000	1179.79(20)
	Pseudo-ortho	9.5191	13.1540	9.3950	89.71	
23.3 %	Monoclinic	16.1263(7)	9.5191(4)	18.7900(9)	125.346(2)	2352.76(11)
0.60 4.4 %	Orthorhombic	-	-	-	-	2320.48(13)
	Pseudo-ortho	9.4752	13.0984	9.3486	89.65	
39.3 %	Monoclinic	16.0460(6)	9.4752(3)	18.6973(6)	125.285(1)	
0.68	Monoclinic	16.0141(6)	9.4602(3)	18.6586(6)	125.266(1)	2307.96(13)
	Pseudo-ortho	9.4602	13.0754	9.3293	89.64	
0.86	Monoclinic	15.9587(8)	9.4306(3)	18.5977(8)	125.219(2)	2286.63(18)
	Pseudo-ortho	9.4306	13.0378	9.2988	89.58	
1.15	Monoclinic	15.8750(7)	9.3877(4)	18.5124(8)	125.184(2)	2254.86(18)
	Pseudo-ortho	9.3877	12.9752	9.2562	89.52	
1.33	Monoclinic	15.8175(12)	9.3588(5)	18.4553(15)	125.153(3)	2233.71(30)
	Pseudo-ortho	9.3588	12.9332	9.2276	89.47	
1.63	Monoclinic	15.7475(6)	9.3193(3)	18.3893(8)	125.130(2)	2207.16(16)
	Pseudo-ortho	9.3193	12.8798	9.1946	89.41	
1.84	Monoclinic	15.6948(7)	9.2906(3)	18.3435(9)	125.108(2)	2188.15(19)
	Pseudo-ortho	9.2906	12.8402	9.1718	89.35	
2.20	Monoclinic	15.5944(7)	9.2094(4)	18.2611(9)	125.106(3)	2145.50(9)
	Pseudo-ortho	9.2094	12.7586	9.1306	89.27	
2.50	Monoclinic	15.4668(13)	9.1104(7)	18.1547(14)	124.743(3)	2102.08(32)
	Pseudo-ortho	9.1104	12.7120	9.0774	88.82	

The variation of both the orthorhombic and pseudo-orthorhombic lattice parameters is plotted in Figures 3.21 and 3.22. The orthorhombic phase displays highly anisotropic compressibility, with the b axis much softer (β_b = 1.7(2)x10^{-2} GPa^{-1}) than the *a*- and *c*-axes (β_a = 6(1)x10^{-3} GPa^{-1} and β_c = 6.7(2)x10^{-3} GPa^{-1}, respectively). The *b*-axis varies

almost continuously through the phase transition, but there is a sharp discontinuity in the *a*- and *c*-axes associated with a pronounced softening in these directions at the phase transition. The monoclinic phase displays almost isotropic compressibility. The corresponding linear compressibilities are: $\beta_a = 1.73(4)\text{x}10^{-2}$ GPa^{-1}, $\beta_b = 1.65(3)\text{x}10^{-2}$ GPa^{-1} and $\beta_c = 1.60(8)\text{x}10^{-2}$ GPa^{-1}.

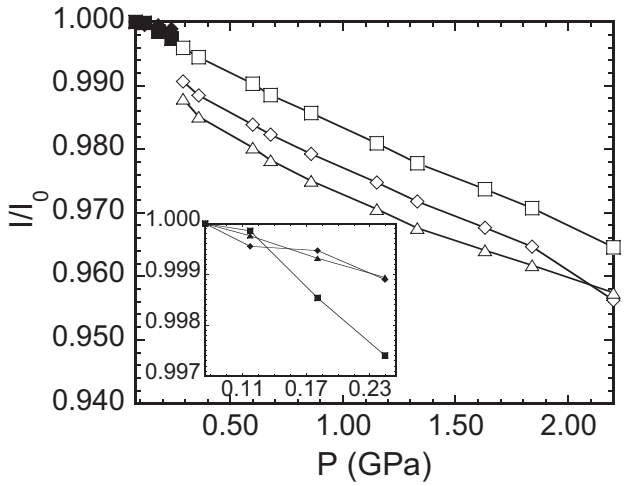

Figure 3.21: Normalized lattice constants of $Sc_2Mo_3O_{12}$ as a function of pressure. The monoclinic lattice constants for the phase existing between 0.29-2.50 GPa have been converted to pseudo-orthorhombic values. The inset shows the orthorhombic region (0 – 0.24 GPa). The lines are only a guide to the eye. Solid circles: a/a_0 orthorhombic, solid squares: b/b_0 orthorhombic, solid triangles: c/c_0 orthorhombic, open circles: a/a_0 monoclinic, open squares: b/b_0 monoclinic, open triangles: c/c_0 monoclinic.

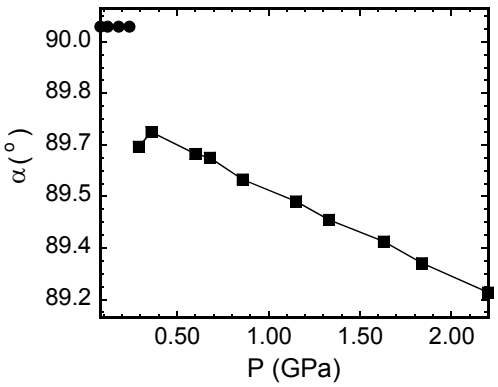

Figure 3.22: Orthorhombic and pseudo-orthorhombic angles α as a function of pressure for $Sc_2Mo_3O_{12}$. The lines are only a guide to the eye. Circles: orthorhombic, squares: monoclinic.

The variation of normalized volume with pressure is shown in Figure 3.23. There is a <1% decrease in volume prior to the phase transition and an ~2% decrease at the transition itself. Fitting an EOS to the volume data gave bulk a modulus (K_0) of 32(2) GPa for the orthorhombic and 16(1) GPa for the monoclinic phase, indicating that, like $Sc_2W_3O_{12}$, $Sc_2Mo_3O_{12}$ displays an unusual compressibility collapse on going through the phase transition. The pressure derivatives were 4.0 (implied value) and 4(1), the zero pressure volumes were 304.43(10) $Å^3$ and 300.71(77) $Å^3$ (per formula unit), respectively.

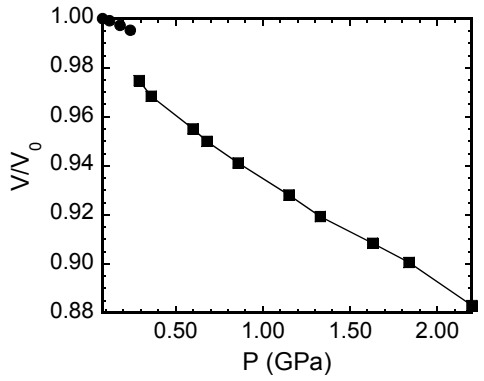

Figure 3.23: Normalized unit cell volume as a function of pressure for $Sc_2Mo_3O_{12}$. Circles: orthorhombic, squares: monoclinic.

3.5.2 Results for $Al_2W_3O_{12}$

A selection of the diffraction patterns recorded for $Al_2W_3O_{12}$ is shown in Figure 3.24. The data are consistent with a transition from the ambient pressure and temperature orthorhombic structure (Pnca) to a monoclinic structure ($P2_1/a$) at ~0.1 GPa. At ambient pressure this monoclinic structure forms on cooling to < 267K.[47] Rietveld fits to the diffraction patterns indicate the onset of this transition is at < 0.08 GPa, our first pressure point with an approximate 3:2 mix of orthorhombic and monoclinic material by 0.14 GPa, and complete transformation to monoclinic material at < 0.24 GPa. Unlike $Sc_2Mo_3O_{12}$, the diffraction data do not clearly indicate any further crystalline to crystalline phase transitions, although above 4 GPa the peak broadening is sufficiently great that subtle changes could easily be missed. By 7.0 GPa the diffraction data showed only weak broad peaks, but on decompression the quality of the diffraction pattern improved dramatically and showed well defined Bragg peaks, with some broadening over and above that seen during the initial stages of compression, consistent with the recovery

of the monoclinic, not the starting orthorhombic structure. NaCl peak positions for this sample indicate a residual "pressure" of ~ 0.18 GPa.

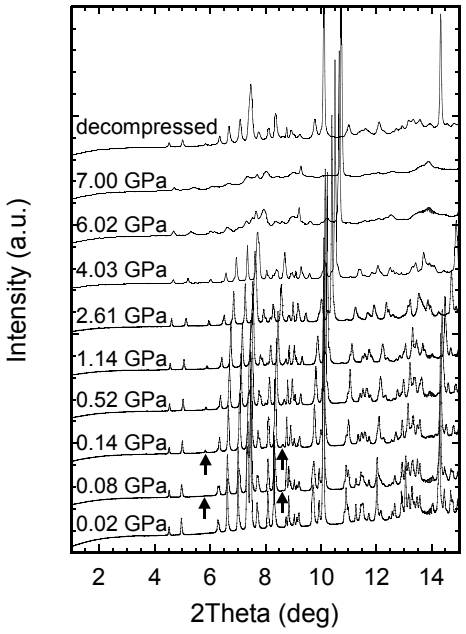

Figure 3.24: Powder diffraction patterns as a function of pressure for $Al_2W_3O_{12}$. Arrows indicate the location of peaks that are characteristic of the monoclinic phase. The data were collected at 25 keV (λ = 0.496 Å).

Lattice constants for the orthorhombic and monoclinic phases, derived from LeBail fits to the data using GSAS, are shown as a function of pressure in Table 3.9 along with pseudo-orthorhombic values for the monoclinic phase that were derived by transformation as described for $Sc_2Mo_3O_{12}$ in the previous section.

Table 3.9: $Al_2(WO_4)_3$ lattice constants as of a function of pressure in isopropanol pressure-transmitting medium. The values were determined the same way as those of Table 3.4. At 0.08 and 0.14 GPa, both phases were present in significant amounts. In the first column weight percentage for the two coexisting phases are given. These were estimated from Rietveld fits to the data.

Pressure (GPa)	**Symmetry**	**a, Å**	**b, Å**	**c, Å**	**β or α, deg**	**Volume, Å^3**
0.02	Orthorhombic	9.1367(3)	12.5940(4)	9.0553(3)	90.000	1041.97(5)
0.08 24.7 %	Orthorhombic	9.1325(4)	12.5877(6)	9.0505(4)	90.000	1040.42(10)
	Pseudo-ortho	9.0722	12.5949	8.9787	89.79	
10.8 %	Monoclinic	15.4406(15)	9.0722(6)	17.9574(17)	125.344(6)	2051.85(22)
0.14 19.4 %	Orthorhombic	9.0710(5)	12.5872(7)	8.9736(5)	90.000	1024.59(6)
	Pseudo-ortho	9.0710	12.5864	8.9749	89.73	
13.0 %	Monoclinic	15.4244(15)	9.0710(7)	17.9498(15)	125.314(7)	2049.33(16)
0.24	Monoclinic	15.4098(16)	9.0533(5)	17.9093(12)	125.346(5)	2037.97(26)
	Pseudo-ortho	9.0533	12.5694	8.9546	89.82	
0.45	Monoclinic	15.3884(13)	9.0370(5)	17.8756(12)	125.318(4)	2028.35(23)
	Pseudo-ortho	9.0370	12.5564	8.9378	89.81	
0.52	Monoclinic	15.3719(12)	9.0218(6)	17.8454(13)	125.272(5)	2020.51(24)
	Pseudo-ortho	9.0218	12.5500	8.9227	89.79	
0.69	Monoclinic	15.3401(11)	9.0013(5)	17.8050(11)	125.245(4)	2007.85(21)
	Pseudo-ortho	9.0013	12.5282	8.9025	89.77	
0.76	Monoclinic	15.3368(11)	8.9957(5)	17.7943(12)	125.211(4)	2005.79(22)
	Pseudo-ortho	8.9957	12.5308	8.8972	89.75	
0.90	Monoclinic	15.3013(12)	8.9767(5)	17.7522(13)	125.191(4)	1992.71(24)
	Pseudo-ortho	8.9767	12.5049	8.8761	89.73	
1.14	Monoclinic	15.2728(10)	8.9561(5)	17.7120(11)	125.152(4)	1980.90(21)
	Pseudo-ortho	8.9561	12.4876	8.8560	89.71	
1.30	Monoclinic	15.2350(9)	8.9367(4)	17.6732(11)	125.122(3)	1968.10(20)
	Pseudo-ortho	8.9367	12.4614	8.8366	89.67	
1.59	Monoclinic	15.2027(10)	8.9072(5)	17.6210(11)	125.088(3)	1952.48(21)
	Pseudo-ortho	8.9072	12.4401	8.8105	89.67	
2.02	Monoclinic	15.1416(11)	8.8669(6)	17.5549(14)	125.017(4)	1930.26(25)
	Pseudo-ortho	8.8669	12.4010	8.7774	89.59	
2.61	Monoclinic	15.0555(9)	8.8153(5)	17.4710(10)	124.952(4)	1900.50(11)
	Pseudo-ortho	8.8153	12.3404	8.7355	89.49	
3.69	Monoclinic	14.9174(9)	8.7292(5)	17.3516(8)	124.998(4)	1850.90(9)
	Pseudo-ortho	8.7292	12.2205	8.6758	89.44	
4.03	Monoclinic	14.8572(11)	8.6925(5)	17.2936(12)	125.027(6)	1828.87(10)
	Pseudo-ortho	8.6925	12.1668	8.6468	89.44	
4.85	Monoclinic	14.7525(39)	8.6048(28)	17.1855(52)	124.672(15)	1794(1)
	Pseudo-ortho	8.6048	12.1344	8.5928	89.05	
6.02	Monoclinic	14.5129(56)	8.1907(46)	17.0367(89)	123.370(23)	1691(1)
	Pseudo-ortho	8.1907	12.1320	8.5184	87.47	
7.00	Monoclinic	14.220(17)	8.1768(81)	17.167(20)	121.785(86)	1697(2)
	Pseudo-ortho	8.1768	12.1368	8.5835	84.83	
Decompr.	Monoclinic	15.420(15)	9.0444(10)	17.9205(23)	125.288(67)	2039.99
0.18	*Pseudo-ortho*	9.0444	12.5868	8.9602	89.76	

As we have only one dataset at pressures where only the orthorhombic phase was present (0.02 GPa) and a further dataset at a pressure where the orthorhombic phase is dominant (0.08 GPa) there is insufficient data for a reliable determination of linear compressibilities for the orthorhombic phase. (The linear compressibilities obtained for the orthorhombic phase based on only the 2 data points are: $\beta_a = 7.66 \times 10^{-3}$ GPa^{-1}, $\beta_b = 8.34 \times 10^{-3}$ GPa^{-1} and $\beta_c = 8.84 \times 10^{-3}$ GPa^{-1}.) The orthorhombic lattice constants from the 0.14 GPa data appear to be in error, probably due to correlations between the lattice constants of the closely related monoclinic and orthorhombic structures. However, based on the limited data that is available, the anisotropy in the compressibility seems to be less than that for $Sc_2Mo_3O_{12}$. The orthorhombic and pseudo-orthorhombic lattice parameters are plotted in Figures 3.25 and 3.26. In Figure 3.25, we can see that the *b*-axis varies in an almost continuous fashion through the phase transition, but there is a sharp discontinuity in both the *a*- and *c*-axes associated with the phase transition. The monoclinic phase displays almost isotropic compressibility (with linear compressibilities of: $\beta_a = 1.07(2) \times 10^{-2}$ GPa^{-1}, $\beta_b = 8.4(1) \times 10^{-3}$ GPa^{-1} and $\beta_c = 9.3(4) \times 10^{-3}$ GPa^{-1}), there is an apparent softening at > 3.7 GPa that may indicate a phase transition that is not clearly seen in the diffraction data.

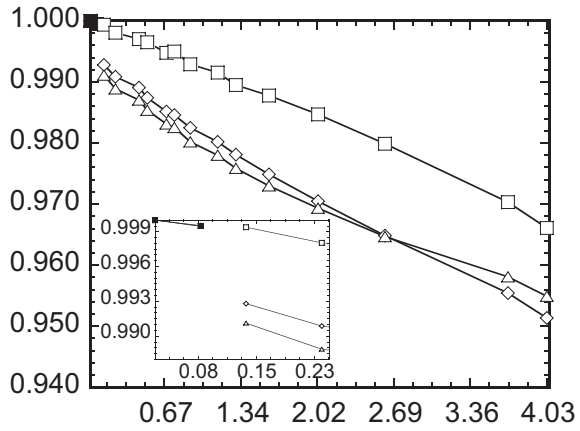

Figure 3.25: Normalized lattice constants for $Al_2W_3O_{12}$ as a function of pressure. The monoclinic lattice constants for the phase existing between 0.14-4.03 GPa have been converted to pseudo-orthorhombic values. The inset shows the orthorhombic region (0 – 0.08 GPa). The lines are only a guide to the eye. Solid circles: a/a_0 orthorhombic, solid squares: b/b_0 orthorhombic, solid triangles: c/c_0 orthorhombic, open circles: a/a_0 monoclinic, open squares: b/b_0 monoclinic, open triangles: c/c_0 monoclinic.

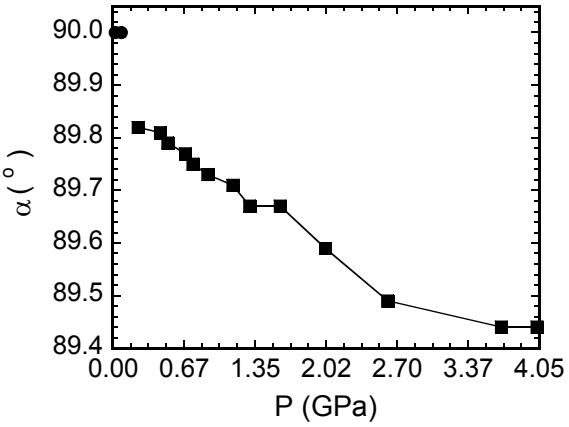

Figure 3.26: Orthorhombic and pseudo-orthorhombic angles α as a function of pressure for $Al_2W_3O_{12}$. The line is only a guide to the eye. Circles: orthorhombic, squares: monoclinic.

The variation of normalized volume with pressure is shown in Figure 3.27. There is a volume decrease at the phase transition of ~ 2%. Fitting an EOS to the volume data gave

bulk a modulus (K_0) of 48 GPa for the orthorhombic, based on only two points, and 28(1) GPa for the monoclinic phase. The pressure derivatives were 4.0 (implied value) and 3.7(7), the zero pressure volumes were 260.61 $Å^3$ and 257.14(28) $Å^3$ per formula unit, respectively, suggesting that, like $Sc_2W_3O_{12}$ and $Sc_2Mo_3O_{12}$, $Al_2W_3O_{12}$ may also display a compressibility collapse on going through the phase transition.

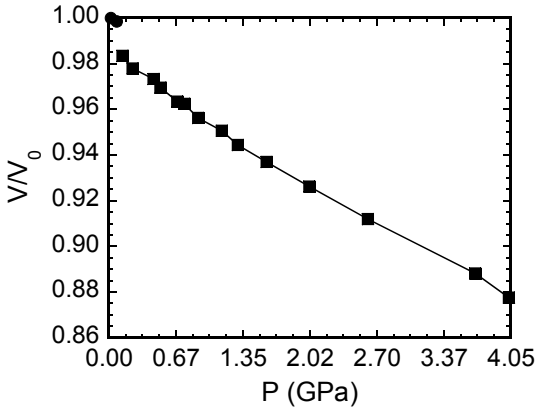

Figure 3.27: Normalized unit cell volume as a function of pressure for $Al_2W_3O_{12}$. Circles: orthorhombic, squares: monoclinic.

3.5.3 Discussion

The phase transition pressures seen for $Sc_2Mo_3O_{12}$ in our monochromatic diffraction study (~0.3 GPa and ~2.4 GPa) are in reasonable agreement with those previously reported for this compound based on Raman and EDXRD data (0.3 GPa and 2.7 GPa),[42] and they are close to those observed in our previous study of $Sc_2W_3O_{12}$ (0.3 and 2.8 GPa).[100] Comparison of the diffraction data for the phase formed at > 2.4 GPa with the corresponding data for $Sc_2W_3O_{12}$[100] suggests that this, as yet unidentified phase, has the same structure as the corresponding tungstate. The bulk moduli for the orthorhombic and monoclinic forms of $Sc_2Mo_3O_{12}$ (32(2) and 16(1) GPa, respectively) are also very close

to those that we previously determined for $Sc_2W_3O_{12}$ (31(3) and 14(1) GPa, respectively). The anisotropy of the compressibility that is seen in orthorhombic $Sc_2Mo_3O_{12}$ is also seen in the corresponding tungstate.[100] Clearly, the replacement of tungsten by molybdenum in $Sc_2W_3O_{12}$ leads to little change in the high-pressure properties of the material, even though at ambient pressure the two compounds have markedly different temperatures for their ferroelastic orthorhombic to monoclinic phase transitions;[47] the tungstate does not undergo this transition above 10 K,[48] but the molybdate undergoes this transition at 180 K.[53] The behaviour of the orthorhombic/pseudo-orthorhombic lattice constants on compression for the two scandium compounds is also very similar with sharp discontinuities in the *a* and *c* lattice constants, but an almost continuous variation of the *b*-axis through the transition (Figures 3.8 and 3.21, Tables 3.1, 3.2 and 3.8). Interestingly, similar behaviour is seen for $Sc_2Mo_3O_{12}$ at ambient pressure as the temperature is varied (see Figure 3.2).[53] There is a 0.15 % increase in the *b*-axis length on cooling through the transition to get monoclinic material, but decreases of nearly 1 % for the *a*- and *c*-axes. The overall volume decrease (1.5 %) associated with the thermally induced transition is similar to that seen for the pressure-induced transition. As previously pointed out for the tungstate,[100] the structural changes accompanying volume reduction on compression of the orthorhombic phase must be different from those involved in the volume reduction that occurs on heating at ambient pressure as the *a*- and *c*-axes have negative coefficients of thermal expansion (CTE), but the b-axis has a positive CTE, [53] whereas all axis lengths decrease on compression.

The behaviour of $Al_2W_3O_{12}$ on compression is different from that of both $Sc_2W_3O_{12}$ and $Sc_2Mo_3O_{12}$. The orthorhombic to monoclinic transformation is seen at lower pressure

(onset <0.08 GPa) for the aluminum compound than for the tungsten compounds, although in a previous Raman study it was reported to occur at 0.28 GPa,[43] and a second crystalline to crystalline phase transition, analogous to those seen at ~ 2.6 GPa in the two scandium compounds is not observed; there are no major changes in the powder diffraction patterns of $Al_2W_3O_{12}$ in the pressure range 0.15 to 4.0 GPa. However, a prior Raman study of this compound indicated that there was a second transition at 2.8 GPa.[43] Careful inspection of the lattice constants and unit cell volumes derived from our study (see Figures 3.25 and 3.27) seems to show a slight softening above 2.6 GPa that is coincident with a change in the pressure dependence of the monoclinic angle (see Figure 3.26). These changes may be an indication of a transition that has only subtle effects on the diffraction pattern. In the prior high pressure Raman study of $Al_2(WO_4)_3$,[43] it was stated that the phase existing above 2.8 GPa probably contained WO_4 tetrahedra with smaller distortions than those in the MoO_4 tetrahedra of $Sc_2Mo_3O_{12}$ at pressures above 2.7 GPa; this is consistent with our observation of an obvious structural change in the molybdate but no obvious change in the case of $Al_2W_3O_{12}$.

The phase coexistence that is associated with the pressure induced orthorhombic to monoclinic transitions in both $Sc_2Mo_3O_{12}$ and $Al_2W_3O_{12}$, suggests that there is hysteresis associated with the transition. This introduces uncertainty into the estimation of the true thermodynamic phase transition pressure from our data. However, the onset pressures for the transitions observed in our measurements (< 0.08 GPa for $Al_2W_3O_{12}$, < 0.24 GPa for $Sc_2Mo_3O_{12}$ and < 0.28 GPa for $Sc_2W_3O_{12}$[100]) are consistent with the rationalization that was put forward by Sleight[47, 49] for the composition dependence of the orthorhombic-monoclinic phase transition temperature at ambient pressure within the series of

molybdates or tungstates. He argued that as the electronegativity of the A^{3+} cation increases (aluminum is more electronegative than scandium), there is less negative charge on the oxide ions and consequently less repulsion between oxide ions resisting a volume collapse giving the monoclinic structure at higher temperatures. Based on this argument we would expect a lower phase transition pressure for $Al_2W_3O_{12}$ than for $Sc_2W_3O_{12}$.

The available, somewhat limited, diffraction data suggest that orthorhombic $Al_2W_3O_{12}$ does not have a strongly anisotropic compressibility in contrast to what is seen for the scandium compounds and to the large anisotropy of the thermal expansion seen for $Al_2W_3O_{12}$; by dilatometry the thermal expansion coefficients determined from a single crystal were $\alpha_a = -1.69 \times 10^{-6}\ ^oC^{-1}$, $\alpha_b = 8.31 \times 10^{-6}\ ^oC^{-1}$ and $\alpha_c = -0.15 \times 10^{-6}\ ^oC^{-1}$.[51] The volume thermal expansion implied by these numbers corresponds to an intermediate thermal expansion material ($\alpha_V \cong 6.5 \times 10^{-6}\ ^oC^{-1}$), which is not in agreement with dilatometry results reported by Evans *et al*.[49] The difference may be due to both extrinsic effects associated with microstructure changes as a function of temperature as well as differences from the experimental conditions, such as instruments used, single crystal versus powder sample (or ceramic bar) and measurement errors.[54] While the estimated bulk modulus for orthorhombic $Al_2W_3O_{12}$ (~48 GPa) is somewhat uncertain due to the limited amount of data that was available at very low pressure (only two data points), it is considerably larger than that for $Sc_2Mo_3O_{12}$ and $Sc_2W_3O_{12}$ (32(2) and 31(3) GPa, respectively). Additionally, the bulk modulus of the monoclinic aluminum tungstate, 28(1) GPa, is also much larger than those for the two scandium compounds (16(1) GPa for the molybdate and 14(1) GPa for the tungstate). The considerable increase in bulk modulus on going from the scandium compounds to aluminum tungstate can be

rationalized by considering the packing densities of the different compounds; at ambient temperature and pressure, each oxygen in the orthorhombic scandium molybdate occupies a volume of ~ 25.5 $Å^3$,[53] but for $Al_2W_3O_{12}$, the volume per oxygen is only ~21.6 $Å^3$.[68] The greater oxygen packing density in the aluminum compound will lead to more oxygen-oxygen repulsion on compression and a higher bulk modulus. The packing density in the monoclinic aluminum compound is also much higher than that in monoclinic scandium molybdate, so a similar rationalization of their relative bulk moduli can be used. However, this simplistic rationalization does not seem to be fully consistent with Sleight's explanation[47, 49] for the composition dependence of the orthorhombic-monoclinic phase transition temperature at ambient pressure within the series of molybdates or tungstates that was mentioned in the previous paragraph. A comprehensive understanding of how changes in A^{3+} influence the phase transition temperatures and pressures, and the compressibility's of both the orthorhombic and monoclinic phases can probably only be achieved by considering entropic as well as enthalpic factors. There is presumably a significant loss of vibrational entropy on going from the orthorhombic to the monoclinic phase and this entropy change will be dependent on the identity of A^{3+}, as the nature of this cation can affect the unit cell volume quite dramatically and hence change the phonon density of states.

3.6 $Yb_2W_3O_{12}$ – A high-pressure synchrotron x-ray diffraction experiment

High-pressure x-ray diffraction measurements on $Yb_2W_3O_{12}$ in a nitrogen pressure medium did not unambiguously confirm an orthorhombic to monoclinic phase transition in the material. Due to the difficulties in controlling the pressure upon closing the four-

post DAC under liquid nitrogen, the starting pressure of the experiment was very high (1 GPa). This and the poor quality of the data, which in part may be due to the hygroscopicity of $Yb_2W_3O_{12}$, made phase identification difficult, but the pattern of the material at 1 GPa shows great similarity to those of monoclinic $Sc_2W_3O_{12}$ and $Al_2W_3O_{12}$. Although no pressure for a possible crystalline to crystalline phase transition or compressibility could be determined, the experiment revealed a pressure-induced amorphization in $Yb_2W_3O_{12}$ starting slightly below 5 GPa, leading to complete loss of long-range order by 6.46 GPa (see Figure 3.28). No crystalline phase was recovered upon pressure-release.

The amorphization of $Yb_2W_3O_{12}$ at lower pressure relative to $Sc_2W_3O_{12}$ (no PIA up to 10 GPa), $Sc_2Mo_3O_{12}$ (PIA not complete at 8 GPa) and $Al_2W_3O_{12}$ (PIA not complete at 7 GPa) may indicate a decreasing amorphization pressure with an increasing size of the A^{3+} cation. The hygroscopic nature of this rare earth tungstate presents a limitation to the applicability of this rare earth tungstate in composites with controlled thermal expansion.

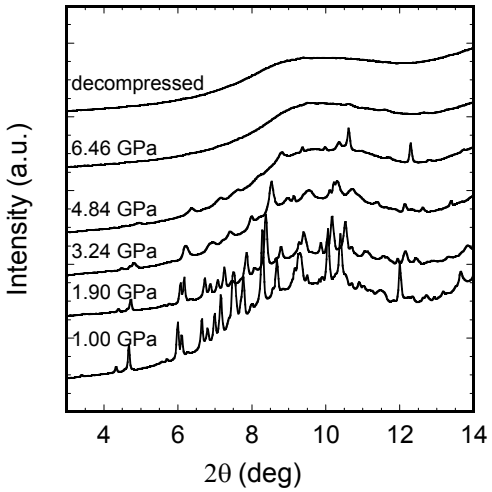

Figure 3.28: Powder diffraction patterns as a function of pressure for $Yb_2W_3O_{12}$. Complete, irreversible amorphization was seen by 6.46 GPa. The data were collected at 25 keV (λ = 0.496 Å).

3.7 Conclusions

Orthorhombic $Sc_2(WO_4)_3$ displays highly anisotropic compressibility with a volume reduction mechanism that is different for that observed on heating this negative thermal expansion material. At ~ 0.28 GPa it transforms to an isotropically compressible monoclinic structure that is much softer than the orthorhombic phase. The orthorhombic-monoclinic phase transition pressure in $A_2W_3O_{12}$ compounds apparently does not display a strong dependence on the nature of A even though the temperature of this transition at ambient pressure is strongly dependent on A. At ~ 2.8 GPa the monoclinic phase transforms to an as yet unidentified crystal structure. This transition is not reversible on decompression. In contrast to prior work in a multi-anvil apparatus, pressure induced amorphization was not observed at < 10 GPa.[39]

The replacement of tungsten in $Sc_2W_3O_{12}$ by molybdenum to give $Sc_2Mo_3O_{12}$ leads to no major changes in the high pressure behavior of the material. The nature of the high pressure phases that occur, the transition pressures and their compressibilities are almost the same. However, $Al_2W_3O_{12}$ displays quite different high pressure behavior. The phase that appears on compression of either of the scandium compounds to ~ 2.7 GPa is not formed on compression of the aluminum compound, and the bulk moduli for monoclinic $Al_2W_3O_{12}$, and probably the orthorhombic phase as well, are much higher than those for the corresponding scandium tungstate and molybdate phases. $Sc_2Mo_3O_{12}$, $Sc_2W_3O_{12}$ and, probably, $Al_2W_3O_{12}$ all show a compressibility collapse at their orthorhombic to monoclinic transition pressures; the bulk modulus of the high pressure phase is lower than that of the high-pressure phase.

$Yb_2W_3O_{12}$ shows pressure-induced amorphization at lower pressures than the above three materials. Similar high-pressure studies on several rare earth tungstates and molybdates would be necessary to find out whether this is common to the other rare earth containing members of the $A_2M_3O_{12}$ family. In addition to their hygroscopic nature and their cost, this can be another limitation to their usability as NTE components in composites.

Our high-pressure neutron diffraction study further proved that the mechanism of volume reduction must be different on compression than on heating. The data, in accordance with our synchrotron x-ray results suggest a difference in the anisotropy of the volume reduction on compression versus on heating: the volume reduction in $Sc_2W_3O_{12}$ and $Sc_2Mo_3O_{12}$ is much more isotropic on compression than on heating. The apparently very small variation in the bond distances and angles on compression seem to

be in accordance with a more isotropic behavior. It was not possible to draw more definitive conclusions based on the small changes seen in the orthorhombic $Sc_2W_3O_{12}$ bond distances and angles due to the large errors on our data other than that the small changes in the Sc-O-W bridging angles are not consistent with the volume reduction mechanism responsible for the NTE because they do not reflect a similar polyhedral tilting that is clearly detectable during volume reduction on heating.

Data of higher quality would be needed for a better picture of the finite changes we looked for. A more sophisticated refinement strategy called “rigid body refinement”, which treats the polyhedra as individual structural units during the analysis could also help in getting more information out of the data.

3.8 References

[1] A. W. Sleight: Thermal Contraction. *Endeavour* **19**, 64 (1995).

[2] A. W. Sleight: Compounds that Contract on Heating. *Inorg. Chem.* **37**, 2854 (1998).

[3] A. W. Sleight: Isotropic Negative Thermal Expansion. *Annu. Rev. Mater. Sci.* **28**, 29 (1998).

[4] A. W. Sleight: Negative thermal expansion materials. *Curr. Opin. Solid State Mater. Sci.* **3**, 128 (1998).

[5] J. S. O. Evans, T. A. Mary, and A. W. Sleight: Negative thermal expansion materials. *Physica B* **241-243**, 311 (1998).

[6] J. S. O. Evans: Negative Thermal Expansion Materials. *J. Chem. Soc. Dalton Trans.*, 3317 (1999).

[7] R. C. Wetherfold and J. Wang: Tailoring thermal deformation by using layered beams. *Compos. Sci. Technol.* **53**, 1 (1995).

[8] D. A. Fleming, D. W. Johnson, and P. J. Lemaire, Article Comprising a Temperature Compensated Optical Fiber Refractive Index Grating, US Patent 5,694,503, Lucent Technologies, USA (1997).

[9] D. K. Balch and D. Dunand, C.: Copper-Zirconium Tungstate Composites Exhibiting Low and Negative Thermal Expansion Influenced by Reinforcement Phase Transformations. *Metall. Mater. Trans. A* **35A**, 1159 (2004).

[10] P. Tschaufeser and S. C. Parker: Thermal Expansion Behavior of Zeolites and $AlPO_4$s. *J. Phys. Chem.* **99**, 10609 (1995).

[11] M. P. Attfield and A. W. Sleight: Strong negative thermal expansion in siliceous faujasite. *Chem. Commun.*, 601 (1998).

[12] M. P. Attfield and A. W. Sleight: Exceptional Negative Thermal Expansion in $AlPO_4$-17. *Chem. Mater.* **10**, 2013 (1998).

[13] D. A. Woodcock, P. Lightfoot, L. A. Villaescusa, et al.: Negative Thermal Expansion in the Siliceous Zeolites Chabazite and ITQ-4: A Neutron Powder Diffraction Study. *Chem. Mater.* **11**, 2508 (1999).

[14] D. A. Woodcock, P. Lightfoot, P. A. Wright, et al.: Strong negative thermal expansion in the siliceous zeolites ITQ-1, ITQ-3 and SSZ-23. *J. Mater. Chem.* **9**, 349 (1999).

[15] T. G. Amos, A. Yokochi, and A. W. Sleight: Phase transition and negative thermal expansion in tetragonal $NbOPO_4$. *J. Solid State Chem.* **141**, 303 (1998).

[16] T. G. Amos and A. W. Sleight: Negative thermal expansion in orthorhombic $NbOPO_4$. *J. Solid State Chem.* **160**, 230 (2001).

[17] A. Grzechnik and W. A. Crichton: Structural transformations in cubic $ZrMo_2O_8$ at high pressures and high temperatures. *Solid State Sci.* **4**, 1137 (2002).

[18] C. A. Perottoni and J. A. H. de Jornada: Pressure-Induced Amorphization and Negative Thermal Expansion in ZrW_2O_8. *Science* **280**, 886 (1998).

[19] B. Chen, High-pressure study on borides, nanocrystals and negative thermal expansion materials, PhD Thesis, University of Missouri, Kansas City, Missouri, (2001).

[20] D. V. S. Muthu, B. Chen, J. M. Wrobel, et al.: Pressure-induced phase transitions in α–$ZrMo_2O_8$. *Phys. Rev. B* **65**, 064101 (2002).

[21] J. S. O. Evans, Z. Hu, J. D. Jorgensen, et al.: Compressibility, Phase Transitions, and Oxygen Migration in Zirconium Tungstate, ZrW_2O_8. *Science* **275**, 61 (1997).

[22] J. D. Jorgensen, Z. Hu, S. Short, et al.: Pressure-induced cubic-to-orthorhombic phase transfromation in the negative thermal expansion material HfW_2O_8. *J. Appl. Phys.* **89**, 3184 (2001).

[23] J. D. Jorgensen, Z. Hu, S. Teslic, et al.: Pressure -induced cubic-to-orthorhombic phase transition in ZrW_2O_8. *Phys. Rev. B* **59**, 215 (1999).

[24] R. Mittal, S. L. Chaplot, H. Schober, et al.: Origin of Negative Thermal Expansion in Cubic ZrW_2O_8 Revealed by High Pressure Inelastic Neutron Scattering. *Phys. Rev. Lett.* **86**, 4692 (2001).

[25] R. Mittal, S. L. Chaplot, H. Schober, et al.: Origin of negative thermal expansion in cubic ZrW_2O_8 and $ZrMo_2O_8$: High pressure inelastic neutron scattering study. *Solid State Phys. (India)* **44**, 656 (2001).

[26] T. R. Ravindran, A. K. Arora, and T. A. Mary: High Pressure Behavior of ZrW_2O_8: Gruneisen Parameter and Thermal Properties. *Phys. Rev. Lett.* **84**, 3879 (2000).

[27] T. R. Ravindran, A. K. Arora, and T. A. Mary: High-pressure Raman spectroscopic study of zirconium tungstate. *J. Phys.: Condens. Matter* **13**, 11573 (2001).

[28] Y. Yamamura, N. Nakajima, T. Tsuji, et al.: Low-temperature heat capacities and Raman spectra of negative thermal expansion compounds ZrW_2O_8 and HfW_2O_8. *Phys. Rev. B* **66**, 014301 (2002).

[29] S. M. Bennington, J. Li, M. J. Harris, et al.: Phonon softening in ice Ih. *Physica B* **263-264**, 396 (1999).

[30] B. Chen, D. V. S. Muthu, Z. X. Liu, et al.: High-pressure Raman and infrared study of HfW_2O_8. *Phys. Rev. B* **64**, 214111 (2001).

[31] R. Mittal, S. L. Chaplot, A. I. Kolesnikov, et al.: Inelastic neutron scattering and lattice dynamical calculation of negative thermal expansion in HfW_2O_8. *Phys. Rev. B* **68**, 054302 (2003).

[32] R. J. Speedy: Models for the amorphization of compressed crystals. *J. Phys.: Condens. Matter* **8**, 10907 (1996).

[33] C. Verdon and D. C. Dunand: High-Temperature Reactivity in the ZrW_2O_8-Cu System. *Scr. Mater.* **36**, 1075 (1997).

[34] H. Holzer and D. C. Dunand: Phase transformation and thermal expansion of Cu/ZrW_2O_8 metal matrix composites. *J. Mater. Res.* **14**, 780 (1999).

[35] C. Lind, D. G. VanDerveer, A. P. Wilkinson, et al.: New high pressure form of the negative thermal expansion materials zirconium molybdate and hafnium molybdate. *Chem. Mater.* **13**, 487 (2001).

[36] S. Carlson and A. M. Krogh Andersen: High-pressure properties of TiP_2O_7, ZrP_2O_7 and ZrV_2O_7. *J. Appl. Crystallogr.* **34**, 7 (2000).

[37] A. Jayaraman, S. K. Sharma, Z. Wang, et al.: Pressure-induced amorphization of $Tb_2(MoO_4)_3$: a high pressure Raman and x-ray diffraction study. *J. Phys. Chem. Solids* **54**, 827 (1993).

[38] V. Dmitriev, V. Sinitsyn, R. Dilanian, et al.: In situ pressure-induced solid-state amorphization in $Sm_2(MoO_4)_3$, $Eu_2(MoO_4)_3$ and $Gd_2(MoO_4)_3$ crystals: chemical decomposition scenario. *J. Phys. Chem. Solids* **64**, 307 (2003).

[39] R. A. Secco, H. Liu, N. Imanaka, et al.: Pressure-induced amorphization in negative thermal expansion $Sc_2(WO_4)_3$. *J. Mater. Sci. Lett.* **20**, 1339 (2001).

[40] H. Liu, R. A. Secco, N. Imanaka, et al.: X-ray diffraction study of pressure induced amorphization in $Lu_2(WO_4)_3$. *Solid State Commun.* **121**, 177 (2002).

[41] G. D. Mukherjee, S. N. Achary, A. K. Tyagi, et al.: High pressure AC resistivity and compressibility study on $Al_2(WO_4)_3$. *J. Phys. Chem. Solids* **64**, 611 (2003).

[42] W. Paraguassu, M. Maczka, A. G. Souza Filho, et al.: Pressure-induced structural transformations in the molybdate $Sc_2(MoO_4)_3$. *Phys. Rev. B* **69**, 094111(1 (2004).

[43] M. Maczka, W. Paraguassu, A. G. Souza Filho, et al.: High-pressure Raman study of $Al_2(WO_4)_3$. *J. Solid State Chem.* **177**, 2002 (2004).

[44] K. Nassau, H. J. Levinstein, and G. M. Loiacono: Trivalent Rare-Earth Tungstates of the Type $M_2(WO_4)_3$. *J. Am. Ceram. Soc.* **47**, 363 (1964).

[45] K. Nassau, H. J. Levinstein, and G. M. Loiacono: A comprehensive study of trivalent tungstates and molybdates of the type $L_2(MO_4)_3$. *J. Phys. Chem. Solids* **26**, 1805 (1965).

[46] S. C. Abrahams and J. L. Bernstein: Crystal Structure of the Transition-Metal Molybdates and Tungstates. II. Diamagnetic $Sc_2(WO_4)_3$. *J. Chem. Phys.* **45**, 2745 (1966).

[47] A. W. Sleight and L. H. Brixner: A New Ferroelastic Transition in Some $A_2(MO_4)_3$ Molybdates and Tungstates. *J. Solid State Chem.* **7**, 172 (1973).

[48] J. S. O. Evans, T. A. Mary, and A. W. Sleight: Negative Thermal Expansion in $Sc_2(WO_4)_3$. *J. Solid State Chem.* **137**, 148 (1998).

[49] J. S. O. Evans, T. A. Mary, and A. W. Sleight: Negative Thermal Expansion in a Large Molybdate and Tungstate Family. *J. Solid State Chem.* **133**, 580 (1997).

[50] P. M. Forster, A. Yokochi, and A. W. Sleight: Enhanced Negative Thermal Expansion in $Lu_2W_3O_{12}$. *J. Solid State Chem.* **140**, 157 (1998).

[51] N. Imanaka, M. Hiraiwa, G. Adachi, et al.: Thermal contraction in $Al_2(WO_4)_3$ single crystal. *J. Cryst. Growth* **220**, 176 (2000).

[52] D. A. Woodcock, P. Lightfoot, and C. Ritter: Negative thermal expansion in $Y_2(WO_4)_3$. *J. Solid State Chem.* **149**, 92 (2000).

[53] J. S. O. Evans and T. A. Mary: Structural phase transitions and negative thermal expansion in $Sc_2(MoO_4)_3$. *Int. J. Inorg. Mater.* **2**, 143 (2000).

[54] W. R. Buessem, in *Mechanical Properties of Engineering Ceramics*, Vol., p. 127, edited by W. W. Kriegel and H. Palmour, Interscience, New York, NY (1961).

[55] S. Sumithra and A. M. Umarji: Hygroscopicity and bulk thermal expansion in $Y_2W_3O_{12}$. *Mater. Res. Bull.* **40**, 167 (2005).

[56] S. Sumithra, A. K. Tyagi, and A. M. Umarji: Negative thermal expansion in $Er_2W_3O_{12}$ and $Yb_2W_3O_{12}$ by high temperature X-ray diffraction. *Mater. Sci. Eng., B* **116**, 14 (2005).

[57] K. Aizu: Possible Species of Ferromagnetic, Ferroelectric, and Ferroelastic Crystals. *Phys. Rev. B* **2**, 754 (1970).

[58] A. K. Tyagi, S. N. Achary, and M. D. Mathews: Phase transition and negative thermal expansion in $A_2(MoO_4)_3$ system (A = Fe^{3+}, Cr^{3+} and Al^{3+}). *J. Alloys Compd.* **339**, 207 (2002).

[59] G. Adachi, N. Imanaka, and S. Tamura: Rare earth ion conduction in solids. *J. Alloys Compd.* **323-324**, 534 (2001).

[60] N. Imanaka and G.-y. Adachi: Rare earth contribution in solid state electrolytes, especially in the chemical sensor field. *J. Alloys Compd.* **250**, 492 (1997).

[61] N. Imanaka and G.-Y. Adachi: Rare earth ion conduction in tungstate and phosphate solids. *J. Alloys Compd.* **344**, 137 (2002).

[62] Y. Okazaki, T. Ueda, S. Tamura, et al.: Trivalent Sc^{3+} ion conduction in the $Sc_2(WO_4)_3$-$Sc_2(MoO_4)_3$ solid solution. *Solid State Ionics* **136-137**, 437 (2000).

[63] N. Imanaka, Y. Kobayashi, and G.-y. Adachi: A Direct Evidence for Trivalent Ion Conduction in Solids. *Chem. Lett.*, 433 (1995).

[64] R. A. Secco: Ionic conduction in pressure-amorphized solids. *Recent Res. Dev. Non-Cryst. Solids* **2**, 171 (2002).

[65] R. A. Secco, H. Liu, N. Imanaka, et al.: Anomalous ionic conductivity of $Sc_2(WO_4)_3$ mediated by structural changes at high pressures and temperatures. *J. Phys.: Condens. Matter* **14**, 11285 (2002).

[66] R. A. Secco, H. Liu, N. Imanaka, et al.: Electrical conductivity and amorphization of $Sc_2(WO_4)_3$ at high pressures and temperatures. *J. Phys. Chem. Solids* **63**, 425 (2002).

[67] A. K. Arora, R. Nithya, T. Yagi, et al.: Two-stage amorphziation of scandium molybdate at high pressure. *Solid State Commun.* **129**, 9 (2004).

[68] S. N. Achary, G. D. Mukherjee, A. K. Tyagi, et al.: Preparation, thermal expansion, high pressure and high temperature behavior of $Al_2(WO_4)_3$. *J. Mater. Sci.* **37**, 2501 (2002).

[69] W. A. Bassett, A. J. Anderson, R. A. Mayanovic, et al.: Hydrothermal diamond anvil cell for XAFS studies of first-row transition elements in aqueous solution up to supercritical conditions. *Chem. Geol.* **167**, 3 (2000).

[70] R. Miletich, D. Allan, R., and W. Kuhs, F.: High-Pressure Single-Crystal Techniques. *Rev. Mineral. Geochem.* **41**, 445 (2001).

[71] N. Duan, U. Kamerwari, and A. W. Sleight: Further contraction of ZrW_2O_8. *J. Am. Chem. Soc.* **121**, 10432 (1999).

[72] T. Varga: Uptake of small polar molecules by ZrW_2O_8 frameworks. *(unpublished)*.

[73] E. M. Avzhieva, I. V. Shakhno, V. E. Plyushchev, et al.: Preparation and Properties of the Crystalline Hydrated Normal Molybdates of the Rare Earth Elements of the Yttrium Sub-group. *Russ.J. Inorg. Chem.* **20**, 874 (1975).

[74] T. N. Kol'tsova: X-ray Diffraction Study of $Y_2W_3O_{12}.3H_2O$. *Inorg. Mater.* **37**, 1175 (2001).

[75] J. D. Barnett, S. Block, and G. J. Piermarini: An Optical Fluorescence System for Quantitative Pressure Measurement in the Diamond-Anvil Cell. *Rev. Sci. Instrum.* **44**, 1 (1973).

[76] J. D. Jorgensen, S. Pei, P. Lightfoot, et al.: Pressure-induced charge transfer and dT_c/dP in $YBa_2Cu_3O_{7-x}$. *Physica C* **171**, 93 (1990).

[77] J. D. Jorgensen, J. J. Faber, J. M. Carpenter, et al.: Electronically focused time-of-flight powder diffractometers at the Intense Pulsed Neutron Source. *J. Appl. Crystallogr.* **22**, 321 (1989).

[78] K. Largarec and S. Desgreniers, computer code Simplified Image Plate Analysis, University of Ottawa, Ottawa, ON, Canada (1994-97).

[79] JADE, computer code for XRD Pattern Processing, Materials Data, Inc., Livermore, CA (1995-2005).

[80] A. C. Larson and R. B. Von Dreele, computer code General Structural Analysis System, Los Alamos National Laboratory, Los Alamos, NM (2000).

[81] B. H. Toby: EXPGUI, a graphical user interface for GSAS. *J. Appl. Crystallogr.* **34**, 210 (2001).

[82] J. M. Jackson, W. Sturhahn, G. Shen, et al.: A synchrotron Moessbauer spectroscopy study of (Mg,Fe)SiO_3 perovskite up to 120 GPa. *Am. Mineral.* **90**, 199 (2005).

[83] F. Birch: Equation of state and thermodynamic parameters of sodium chloride to 300 kbar in the high-temperature domain. *J. Geophys. Res. B* **91**, 4949 (1986).

[84] J. M. Brown: The NaCl pressure standard. *J. Appl. Phys.* **86**, 5801 (1999).

[85] H. J. Mueller, F. R. Schilling, J. Lauterjung, et al.: A standard-free pressure calibration using simultaneous XRD and elastic property measurements in a multi-anvil device. *Eur. J. Mineral.* **15**, 865 (2003).

[86] F. Birch: Finite elastic strain of cubic crystals. *Phys. Rev.* **71**, 809 (1947).

[87] R. J. Angel, computer code EOS-FIT, Virginia Tech, Blacksburg, VA (2001).

[88] W. Jeitschko: Comprehensive x-ray study of the ferroelectric-ferroelastic and paraelectric-paraelastic phases of gadolinium molybdate. *Acta Crystallogr., Sect. B* **28**, 60 (1972).

[89] D. H. Templeton and A. Zalkin: Crystal structure of europium tungstate. *Acta Crystallogr.* **16**, 762 (1963).

[90] T. Varga, A. P. Wilkinson, S. Short, et al.: In-situ high pressure neutron difftaction study of the orthorhombic-to-monoclinic phase transition in $Sc_2W_3O_{12}$. *(manuscript in preparation)*, (2005).

[91] J. Z. Tao and A. W. Sleight: The role of rigid unit modes in negative thermal expansion. *J. Solid State Chem.* **173**, 442 (2003).

[92] J. R. Smyth, S. D. Jacobsen, and R. M. Hazen, in *High Temperature and High Pressure Crystal Chemistry*, Vol. 41, p. 157, edited by R. M. Hazen, Downs, R. T., Mineralogical Society of America, Washington, D.C. (2000).

[93] S. Carlson: High-pressure studies of the cubic to rhombohedral transformation in NbO_2F. *J. Appl. Crystallogr.* **33**, 1175 (2000).

[94] C. Lind, A. P. Wilkinson, Z. Hu, et al.: Synthesis and Properties of the Negative Thermal Expansion Material Cubic Zirconium Molybdate. *Chem. Mater.* **10**, 2335 (1998).

[95] U. L. C. Hemamala, F. El-Ghussein, A. M. Goedken, et al.: High-pressure x-ray diffraction and Raman spectroscopy of HfV_2O_7. *Phys. Rev. B* **70**, 214114 (2004).

[96] B. Batlogg, R. G. Maines, M. Greenblatt, et al.: Novel p-V relationship in ReO_3 under pressure. *Phys. Rev. B* **29**, 3762 (1984).

[97] J.-E. Jorgensen, J. D. Jorgensen, B. Batlogg, et al.: Order parameter and critical exponent for the pressure-induced phase transitions in ReO_3. *Phys. Rev. B* **33**, 4793 (1986).

[98] S. Carlson, A.-K. Larsson, and F. E. Rohrer: High-pressure transformations of NbO_2F. *Acta Crystallogr., Sect. B* **56**, 189 (2000).

[99] J. Z. Tao and A. W. Sleight: Very low thermal expansion in TaO_2F. *J. Solid State Chem.* **173**, 45 (2003).

[100] T. Varga, A. P. Wilkinson, C. Lind, et al.: In-situ high pressure synchrotron x-ray diffraction study of $Sc_2W_3O_{12}$ at up to 10 GPa. *accepted for publication in Phys. Rev. B*, (2005).

[101] M. T. Weller, P. F. Henry, and C. C. Wilson: An Analysis of the Thermal Motion in the Negative Thermal Expansion Material $Sc_2(WO_4)_3$ Using Isotopes in Neutron Diffraction. *J. Phys. Chem. B* **104**, 12224 (2000).

[102] ISIS, http://www.isis.rl.ac.uk/crystallography/hrpd/ (2001).

[103] A. K. A. Pryde, K. D. Hammonds, M. T. Dove, et al.: Origin of the Negative Thermal Expansion in ZrW_2O_8 and ZrV_2O_7. *J. Phys. Condens. Matter* **8**, 10973 (1996).

[104] A. K. A. Pryde, K. D. Hammonds, M. T. Dove, et al.: Rigid Unit Modes and the Negative Thermal Expansion in ZrW_2O_8. *Phase Transit.* **61**, 141 (1997).

[105] P. R. L. Welche, V. Heine, and M. T. Dove: Negative thermal expansion in beta-quartz. *Phys. Chem. Minerals* **26**, 63 (1998).

CHAPTER 4

IN-SITU STUDIES OF PRESSURE-INDUCED AMORPHIZATION IN AM_2O_8-TYPE COMPOUNDS

Abstract

The behavior of cubic ZrW_2O_8 and $ZrMo_2O_8$ on compression in a DAC was examined *in-situ* by a combination of synchrotron XRD and XAS. The data for ZrW_2O_8 were compared with x-ray absorption measurements on an amorphous sample recovered from 7.5 GPa in a multi-anvil apparatus. The *in-situ* data for ZrW_2O_8 show amorphization onset at > 2.4 GPa with completion at < 7.6 GPa. For $ZrMo_2O_8$, the onset was at 1.7 with completion at 4.1 GPa. The local structure in ZrW_2O_8 as indicated by the W L_I pre-edge and the average W-O distance from EXAFS continues to evolve as the material is compressed into an amorphous state. The data are consistent with a move towards a more centrosymmetric tungsten coordination environment as the pressure is increased. These observations are inconsistent with a model for the amorphization that simply involves a loss of orientational order amongst existing coordination polyhedra. The XANES data for the amorphous sample recovered from the multi-anvil apparatus are unlike any of the XANES seen in the *in-situ* measurements indicating that either the local structure in the glassy material relaxes on decompression or that the differing stress states that the samples have experienced result in different local structures. The XANES for the recovered sample are very similar to those for ammonium paratungstate, a material that contains tungsten in a variety of heavily distorted octahedral environments. XANES

results on $ZrMo_2O_8$ reflect a less pronounced change in Mo coordination on amorphization, but still a move towards a more centrosymmetric local environment.

4.1 Introduction

Since the amorphization of hexagonal ice was discovered under compression,[1] pressure-induced amorphization (PIA) has been observed for many different materials.[2-11] The phenomenon is not uncommon for framework structures and it has been observed at unusually low pressures in several negative thermal expansion (NTE) materials.[12-15] A possible theoretical link between NTE and PIA has been suggested by some authors.[16]

Negative thermal expansion materials have received considerable attention in the last decade,[17-19] driven by a combination of scientific curiosity and technological interest, as they are of potential value in composites with tailored thermal expansion. The relatively low density and highly flexible framework structures found for many NTE materials combined with the necessary presence of lattice modes that soften on volume reduction[20-27] predisposes them to a rich behavior at high pressures. Pressure-induced crystalline to crystalline phase transitions have been reported for cubic ZrW_2O_8,[23, 24, 28-31] cubic HfW_2O_8,[25, 32] cubic $ZrMo_2O_8$,[33, 34] cubic $HfMo_2O_8$,[33] ZrV_2O_7,[35] $Sc_2W_3O_{12}$,[36] $Sc_2Mo_3O_{12}$[37] and $Al_2W_3O_{12}$[38, 39] as well as PIA at low pressures in $ZrMo_2O_8$[12], ZrW_2O_8[14], $Sc_2W_3O_{12}$,[40] $Sc_2Mo_3O_{12}$[41] and $Lu_2W_3O_{12}$.[42] Typically, the volume thermal expansion coefficient of the high-pressure phase is significantly larger (more positive) than for the original material. For example in ZrW_2O_8, NTE is changed by about an order of magnitude on transforming to an orthorhombic phase.[28, 29] This increase in expansion coefficient on

phase transformation is detrimental to some possible applications, as composites containing NTE materials may be subjected to high pressures during processing.[43-45]

Cubic ZrW_2O_8 has been the subject of many studies as it displays isotropic NTE over a very wide temperature range.[46, 47] Its structure,[46, 48, 49] thermal expansion mechanism[26, 47, 50-54] and high-pressure behavior have been examined.[14, 21-24, 28, 30, 55] Work on controlled thermal expansion composites for use in precision optical devices has also been conducted.[56] The framework consists of corner-sharing ZrO_6 octahedra and WO_4 tetrahedra with all of the oxygens of the ZrO_6 octahedra bridging to tungsten but one oxygen in each tetrahedron in a terminal position, giving rise to considerable structural flexibility (see Figure 1.5).[48] This flexibility plays an important role in the unusual properties of cubic ZrW_2O_8.[46, 47] There is an order-disorder phase transition at around 430 K going from space group $P2_13$ to $Pa\bar{3}$, leading to an increase in the thermal expansion coefficient at this temperature (see Figure 1.12).[46] The material displays isotropic NTE with (see Figure 1.4) a linear coefficient of thermal expansion (CTE) of -8.8×10^{-6} K^{-1} below the temperature of the phase transition (0.3 - 430 K range) and -4.9×10^{-6} K^{-1} above the phase transition (430 - 690 K) resulting in an average CTE of -8.7×10^{-6} K^{-1} over the range of 0.3 – 690 K.[47] From a local structure perspective, the negative thermal expansion can be viewed as originating in the transverse thermal vibrations of bridging oxygen atoms (see Figure 1.10).[47] From the perspective of lattice dynamics, the NTE apparently primarily originates from low-energy vibrations in which the WO_4 and ZrO_6 polyhedra are essentially rigid.[21, 54, 57-60] In a high-pressure inelastic neutron diffraction study of cubic ZrW_2O_8 the negative thermal expansion was attributed to modes below 8 meV that showed significant softening on compression and hence had large negative

Grüneisen parameters.[21] However, some high-pressure Raman spectroscopic studies have indicated that in addition to the low-frequency rigid unit modes, several other modes also have negative Grüneisen parameters and hence contribute to the NTE.[23, 61]

Cubic $ZrMo_2O_8$ shows isotropic NTE between 11 K and 573 K with a linear thermal expansion coefficient of ~ -4.9 x 10^{-6} K^{-1} (see Figure 4.1).[62] It adopts the disordered β-ZrW_2O_8 structure and thus consist of a flexible network of corner-sharing ZrO_6 octahedra and MoO_4 tetrahedra. Unlike cubic ZrW_2O_8 it undergoes no reversible structural phase transitions at atmospheric pressure. The lack of structural phase transition within its range of stability is potentially beneficial from the applications point of view as the thermal expansion coefficient displays no discontinuity. Cubic $ZrMo_2O_8$ irreversibly transforms to the trigonal polymorph at 390 ^oC.[63]

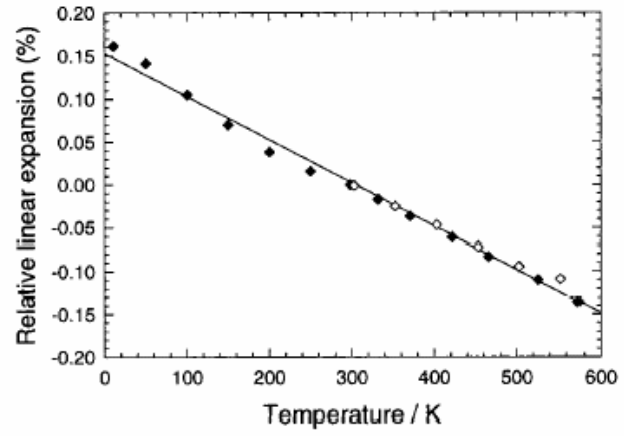

Figure 4.1: Thermal expansion of cubic $ZrMo_2O_8$ determined by both neutron (solid symbols) and x-ray diffraction data (open symbols). Taken from Lind *et al.*[62]

High-pressure studies of cubic ZrW_2O_8 have uncovered a transition to orthorhombic γ-ZrW_2O_8 starting at ~ 0.2 GPa,[28, 29] followed by progressive PIA in the range 1.5 to 3.5 GPa.[14, 23, 24] The glassy phases resulting from pressure-induced amorphization are often considered to be metastable intermediates between a crystalline starting material and one or more crystalline products. The glass forms as a result of kinetic hindrance to the equilibrium transformation. As was discussed in section 1.3.1, numerous structural mechanisms have been proposed for pressure-induced amorphization, some of which are related and can be simultaneously in operation. Based on *ex-situ* high-pressure x-ray diffraction and Raman spectroscopic studies on cubic ZrW_2O_8, it has been proposed that above 1.5 GPa, tilting and deformation of the ZrO_6 and WO_4 polyhedra leads to a loss of crystallinity as the material becomes denser.[14] *In-situ* high pressure neutron diffraction experiments were interpreted in terms of tungsten with 4-, 4+1- and 4+2-coordination in the orthorhombic γ-phase.[28] On the basis of high-pressure simulations, it has been argued that these extra tungsten-oxygen "short" contacts do not play a big role in bonding and that the structure of the orthorhombic (γ) phase should really be viewed as consisting of WO_4 tetrahedra with some oxygens that are close to the tetrahedra and impede large amplitude vibrations involving their motion.[60] This same simulation study proposed that, at high pressure, major coordination changes involving the zirconium were more likely than those involving tungsten.[60] Raman studies of ZrW_2O_8 were interpreted as indicating amorphization at 2.2 GPa due to a kinetically hindered pressure-induced decomposition into its constituent oxides.[23, 24] The preparation of a new ZrW_2O_8 polymorph with a cation-disordered α-U_3O_8-type structure by heating a pressure-amorphized sample under pressure suggests that the amorphization process may involve an increase in coordination

number.[55] The Zr and W cations in this structure display 6+1 coordination,[55] indicating that the tetrahedral coordination of tungsten in cubic ZrW_2O_8 and the predominantly 4+1 coordination of tungsten in orthorhombic ZrW_2O_8[28] is unstable at high pressure.

Cubic $ZrMo_2O_8$ does not undergo any phase transformations under hydrostatic conditions at pressures below 0.6 GPa,[62] but it was reported to undergo a fully reversible 1st order phase transition between 0.7 and 2.0 GPa at room temperature under quasi-hydrostatic conditions.[33] At higher pressure or under non-hydrostatic conditions, $ZrMo_2O_8$ becomes amorphous. As recently reported by Grzechnik et al., on the simultaneous application of temperature and pressure, up to the onset of amorphization at 1.3 GPa, the recovered products from temperatures up to about 400 ^oC are a mixture of the thermodynamically stable monoclinic polymorph and the trigonal phase. At pressures between 1.3 and 4 GPa and up to 790 ^oC (even at 1.3 GPa above 545 ^oC), the material adopts the monoclinic structure. Quenching from temperatures in the range 740-825 ^oC and above 4 GPa, the recovered crystalline phases consist of a mixture of several phases in the ZrO_2-MoO_3 system, including a high-temperature high-pressure phase of MoO_3.[34] The materials that crystallized from amorphous $ZrMo_2O_8$ at higher pressures were found to be phases with five- and six-fold coordinated Mo atoms.[34] From pressures of up to 4.0 GPa, the obtained sample is monoclinic $ZrMo_2O_8$ with infinite ribbons of edge-sharing ZrO_8 polyhedra and MoO_5 tetragonal pyramids or highly distorted MoO_6 octahedra.[64] The recovered crystalline phases from above 4.0 GPa, in addition to several phases in the ZrO_2-MoO_3 system (not explicitly mentioned), include the layered high-pressure, high-temperature form of MoO_3 ($P2_1/m$) with all the Mo atoms in octahedral coordination.[65, 66] The formation of these products suggests that a kinetically hindered transformation to the

denser polymorph might be responsible for PIA at lower pressures (< 4 GPa), but a kinetically hindered decomposition may play a role in PIA at higher pressures.

The high-pressure behavior of trigonal $ZrMo_2O_8$ has also been investigated. Reversible phase transitions were observed to monoclinic (at 1.1 GPa) and triclinic phases (at 2-2.5 GPa).[67, 68] The new polymorphs formed on compressing the trigonal phase were different from the material obtained on compressing the cubic material.[33]

In order to directly probe the mechanism of amorphization in ZrW_2O_8 and $ZrMo_2O_8$, *in-situ* high-pressure measurements examining local structure are desirable. An *in-situ* experiment avoids structural relaxation on pressure release, a phenomenon that is well known in high-pressure studies of glasses,[69, 70] and facilitates the study of changes in the structure during compression and decompression. The local structure of glasses can be probed directly by total scattering using x-rays[71-73] or neutrons,[74] x-ray absorption spectroscopy (XAS)[72] and other spectroscopic probes such as NMR,[75, 76] but the use of these techniques at high pressure is nontrivial. Pair distribution function (PDF) analysis using x-ray total scattering data recorded from samples in diamond anvil cells (DACs) has been employed to study local structure under pressure,[77, 78] but the methodology is still under development.[78] High-pressure XAS (EXAFS and XANES)[79] has been practiced for many years[80] and is somewhat better developed, but still experimentally very challenging. Systems studied by high pressure XAS include iron,[81] copper,[82] gallium,[83] germanium,[84-86] krypton,[87, 88] metal halides,[84, 89] a wide variety of III-V,[90-92] III-VI[93] and II-VI[92, 94] semiconductors, the framework oxides ReO_3[95] and $KNbO_3$,[96] rare earth oxides,[97, 98] GeO_2,[99] germanium oxide glasses,[100] germanium nitrides,[101] and transition metal ions in aqueous solutions.[102] The main difficulty associated with XAS

measurements at high pressure is diffraction from diamonds if a DAC is employed. This diffraction can make a strong contribution to the measured attenuation of the sample and cell assembly at certain x-ray energies and orientations of the diamonds.[84, 103, 104] This leads to unwanted and potentially quite broad peaks (glitches) in the absorption spectra. There are a number of methods for avoiding these glitches. Energy dispersive EXAFS with a DAC facilitates the rapid screening of cell orientations for one that has no or very few glitches.[105, 106] The use of polycrystalline B_4C for both anvils eliminates the problem at the expense of complicating pressure calibration as the optically opaque anvils preclude the use of the ruby fluorescence method;[80] some workers have opted to use one diamond and one polycrystalline anvil to get around this issue.[80, 94] Data can be taken using a DAC by employing a low atomic number gasket and recording spectra through the gasket rather than the diamonds.[97, 98] A multi-anvil apparatus can be employed.[85] If transmission data is recorded through the diamonds of a DAC, the glitches can in principle be eliminated by measuring spectra at several different orientations of the cell, so that the glitches appear at different energies, and producing a composite spectrum.[79]

Here we report an *in-situ* high-pressure, combined XAS and diffraction study of cubic ZrW_2O_8 and cubic $ZrMo_2O_8$. Diffraction probes the loss of long range order on compression and XAS probes the corresponding changes in local environment. Changes in the local coordination environment provide insight into the mechanism by which the material becomes amorphous under pressure. Single crystal diamond anvils were used for these studies as the diffraction background from polycrystalline anvils would have been unacceptable. XAS data on an amorphous ZrW_2O_8 sample recovered from high pressure are also reported.

4.2 Experimental

4.2.1 Syntheses

Cubic ZrW_2O_8: A stoichiometric amount of $ZrO(NO_3)_2 \cdot xH_2O$ (Aldrich, Milwaukee, WI) was thoroughly mixed and ground with 2 weight % excess of H_2WO_4 (Strem Chemicals, Newburyport, MA). The powder was heated at 1150 ^oC for 5 hour, 24 hour and 36 hour periods with intermittent ice-water quenching, drying (at 130 ^oC) and regrinding steps.

Amorphous ZrW_2O_8: Cubic ZrW_2O_8 was compressed using a Walker-type high-pressure multi-anvil press at the Mineral Physics Institute, SUNY Stony Brook, NY (see section 2.5.3). The pressure cell consisted of a platinum sample capsule in a 14 mm magnesia octahedron surrounded by eight one-inch tungsten carbide cubes, all truncated on the corner facing the magnesia. Pyrophyllite and teflon gaskets as well as balsa spacers were used between the cubes. ~140 mg cubic ZrW_2O_8 was placed into the Pt capsule and the sample was exposed to a pressure of about 7.5 GPa at room temperature for 2 hours prior to slow decompression.

Ba_2NiWO_6: $BaCO_3$, $NiCO_3$ and WO_3 were thoroughly mixed and ground. The mixture was heated at 1100 ^oC for 20 hours and, after regrinding, heated at 1400 ^oC for an additional 2 hours.

$Sc_2W_3O_{12}$: Sc_2O_3 and WO_3 were mixed, ground and heated together at 1000 ^oC for 5 hours, then, after regrinding, heated at 1200 ^oC for 12 hours.

The reference compounds $Na_2WO_4 \cdot 2H_2O$, $(NH_4)_{10}W_{12}O_{41} \cdot 5H_2O$ (Alfa Aesar, Ward Hill, MA) and WO_3 (Aldrich, Milwaukee, WI) were used as received.

Cubic $ZrMo_2O_8$: $ZrMo_2O_7(OH)_2 \cdot 2H_2O$ was produced by the reaction of aqueous solutions of $ZrO(ClO_4)_2 \cdot 5H_2O$ and $(NH_4)_6Mo_7O_{24} \cdot 4H_2O$ in acid medium by 3 days of refluxing. Then $ZrMo_2O_7(OH)_2 \cdot 2H_2O$ was dehydrated by a series of low-T heat treatment steps (350 ^oC for 12 hours, 375 ^oC for 15 minutes, 400 ^oC for 15 minutes, 425 ^oC for 30 minutes and finally 450 ^oC for 30 minutes).

$Sc_2Mo_3O_{12}$: stoichiometric quantities of Sc_2O_3 (Strem Chemicals, Newburyport, MA) and MoO_3 (J. T. Baker, Phillipsburg, NJ) were thoroughly mixed, ground and heated together at 700 ^oC for 5 hours and then, after regrinding, at 1100 ^oC for 12 hours.

All other Mo-containing reference compounds were commercial products and used as received: $Na_2MoO_4 \cdot 2H_2O$ (Fisher Scientific, Fair Lawn, NJ), MoO_3 (J. T. Baker, Phillipsburg, NJ) and $MoO_2(acac)_2$ (Strem Chemicals, Newburyport, MA).

4.2.2 Diamond anvil cell

A so called "hydrothermal diamond anvil cell" (HDAC, see Figure 4.2)[107] was used with NaCl as both a pressure calibrant and pressure transmitting medium. 1.7 mm thick diamonds with 500 μm culet faces were employed along with a 125 μm thick rhenium gasket that had a 3 mm outside diameter and 300 μm hole. The gasket was pre-indented to a pressure of about 10 GPa. The downstream cone opening of the cell was ~44 degrees. The samples were uniformly mixed and ground with NaCl and packed into the HDAC with a ratio (AM_2O_8:NaCl) of ~1:4.

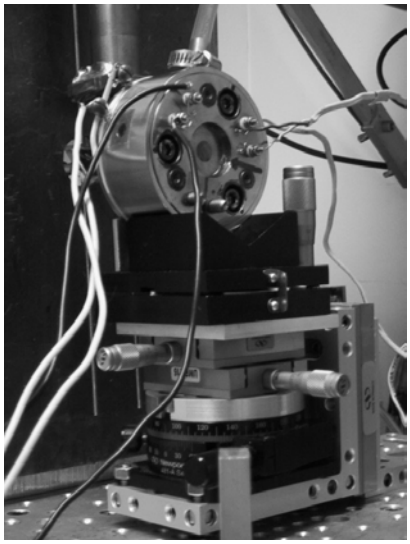

Figure 4.2: The hydrothermal diamond anvil cell placed on a translation-rotation stage and wired for heating ($ZrMo_2O_8$ case).

4.2.3 Diffraction data collection

Diffraction data on ZrW_2O_8 were collected at room temperature and up to 7.6 GPa pressure using the B-2 line of the Cornell High Energy Synchrotron Source (CHESS), Wilson Lab, Cornell University, Ithaca, NY. An x-ray energy of 17.968 keV (λ = 0.6901 Å) was selected using a Ge(111) double-crystal monochromator. The beam was collimated to ~130 μm diameter, and centered onto the sample cavity of the DAC. The diffraction patterns were recorded on image plates using ~5 minute exposures. The sample-to-plate distance was calibrated using diffraction from NaCl in the initially closed HDAC. As the initial pressure will have been slightly above ambient, our subsequent pressure calibrations were slightly in error (see results and discussion, section 4.3). The image plates were read using a BAS 2000 scanner and integrated to give intensity *vs*. 2θ values using the SIMPA software.[108] The integrated patterns were then processed in JADE[109] for pressure calibration and visualization purposes. Further analysis

(identification of the orthorhombic phase) was performed using the program package GSAS.[110] NaCl diffraction angles obtained by fitting in JADE were used along with the program CALIBRATION[111] for pressure determination. CALIBRATION makes use of the Birch equation of state for NaCl.[112] As the pressure was increased, diffraction data were collected at each pressure point. At selected pressures (0.0, 0.7, 2.3, 3.6 and 7.6 GPa) the experimental arrangement was adjusted so that XANES and EXAFS data could be collected.

For $ZrMo_2O_8$, data were collected in the 0 – 4.1 GPa pressure range. An x-ray energy of 19.95 keV (λ = 0.62148 Å) was selected using a Si(220) double-crystal monochromator for the diffraction measurement. A ~130 μm size collimator was used for diffraction and spectroscopy in the DAC. Data were collected at 0.0, 0.24, 0.5, 0.71, 0.99, 1.28, 1.67 and 4.10 GPa. The amorphous material at 4.1 GPa was heated to 600 ^oC within the DAC, and then cooled to room temperature. Diffraction and spectroscopic data were also collected on this material. The experimental setup for diffraction data collection is similar to what was described in the previous chapter (see Figure 3.5) and was also shown schematically in Figure 2.5. The program JADE was also used to attempt to identify the phases present in the sample recovered from high pressure and temperature (see later in Figure 4.12).

Diffraction data were collected on $ZrMo_2O_8$ during another series of experiments at the same beamline using anhydrous isopropanol as a pressure-transmitting medium. Isopropanol was used for reasons already discussed in section 3.2.2 of the previous chapter. These measurements were carried out at room temperature and up to 1.15 GPa in the HDAC. 25 keV (λ = 0.496 Å) x-rays were selected using a Ge(111) double-crystal

monochromator. The method of detection and pressure determination was as described above.

4.2.4 EXAFS and XANES data collection

The XAS measurements were carried out at the same beamline (B-2 line at CHESS) in parallel with the diffraction measurements using the same double crystal monochromators and collimators. For ZrW_2O_8, data were collected at room temperature in the 0 – 7.6 GPa pressure range. The transmission XAS measurements made use of three ion chambers with the DAC between the first and second detector and a reference metal foil between the second and third detector. The reference foil data were used to ensure that the sample spectra were on a common energy scale. Swapping between diffraction and XAS measurements involved removing the beam stop and the image plate holder from the optical bench and replacing them by the transmission and reference ion chambers, and then changing the energy from ~18 keV to that of the appropriate tungsten absorption edge.

XAS data were collected for cubic ZrW_2O_8, $Sc_2W_3O_{12}$, Ba_2NiWO_6, $Na_2WO_4{\cdot}2H_2O$, $(NH_4)_{10}W_{12}O_{41}{\cdot}5H_2O$ and WO_3 (see Table 4.2 for tungsten coordination geometries) at ambient pressure and temperature using samples that were diluted and ground with boron nitride and then packed into aluminum sample holders with Kapton tape windows so that the maximum value of μt was ~1.5 - 2. EXAFS scans were performed at the W L_{III}-edge (9.85-10.90 keV) and XANES data were recorded at the W L_I-edge (12.025-12.200 keV) using 50 % monochromator detuning for harmonic rejection. For the L_{III}-edge EXAFS, a three region scan was employed with 10 eV steps in the pre-edge region (9.85 - 10.19

keV), 0.5 eV steps in the near-edge region (10.19 - 10.22 keV) and 2 eV steps in the post-edge region (10.22 - 10.90 keV). XANES data at the L_I edge were recorded using three regions scans with 5 eV steps in the pre-edge region (12.025 - 12.060 keV), 1.0 eV steps in the near-edge region (12.060 - 12.150 keV) and 2 eV steps in the post-edge region (12.150 - 12.200 keV). Data at each point were recorded until a preset number of monitor counts was achieved, taking approximately 4 seconds per point, and three scans were performed for each sample.

XAS data for the ZrW_2O_8 sample in the DAC were collected at several different orientations of the DAC so that the glitches due to diffraction from the diamonds occurred at different energies. The DAC was mounted on a "V" block above a rotation stage so that it could be reoriented around a vertical, ω, axis. As the DAC casing was smooth and cylindrical, the DAC body could be manually rotated in the V-block about the cylinders axis providing for a χ-type rotation (ω and χ are used here in the sense of a Eulerian cradle diffractometer, see section 8.2.1). 8 to 10 different cell orientations were used at each pressure, with one scan in each orientation. While widely different values of χ were used (~ ±30º), ω was only varied by ~±1.5º amongst these scans.

XAS data for $ZrMo_2O_8$ were collected at the Mo K-edge (20.00 keV) using three scan regions with 5.0 eV steps in the pre-edge region (19.50 - 19.94 keV), 1.0 eV steps in the near-edge region (19.94 - 20.06 keV) and 3.0 eV steps in the post-edge region (20.06 – 20.80 keV). The pre-edge region for the standards was from 19.80 keV to 19.94 keV. Data at each point were recorded until a preset number of monitor counts was achieved. Only one scan was performed for each sample.

Similarly to the case of ZrW_2O_8, spectroscopy data for $ZrMo_2O_8$ in the DAC were collected at several different orientations of the DAC in order to be able to account for the glitches due to diamond diffraction. 8-10 different cell orientations were used at each pressure, with one scan in each orientation. χ was typically varied in a 15º-range, ω was varied by ~±1.5º in these scans.

4.2.5 Processing of XAS data

Data processing was performed using the program ATHENA.[113, 114] For ZrW_2O_8, at least 3 energy scans were averaged for each sample. All data were put on a common energy scale using the reference foil absorption spectra. For $ZrMo_2O_8$, only one dataset was available per sample and no reference foil was used.

Glitches arising from diamond diffraction severely contaminated the recorded XAS at each orientation of the DAC. In general, this problem is a function of the edge energy that is being examined and the energy range over which data is required. The number of diamond glitches appearing in an absorption spectrum recorded in a DAC depends upon the energy of the measurement, with the glitch density increasing as the energy goes up (approximately with the square of the edge energy).[79] For tungsten, in practice, it was not possible to find a single diamond cell orientation that will not give glitches in the energy range of a useful XANES or EXAFS energy scan. This problem is compounded by the presence of two diamonds in the beam with different crystallographic orientations and by the strains that are introduced into the diamonds as the cell pressure increases. The strain gradients that arise from loading the diamonds effectively increase their mosaic spread and broaden the range or energies/orientations over which they give rise to glitches.

Rather than attempting to obtain glitch-free data directly, we have instead carried out multiple data collections with different orientations of the DAC with respect to the incident beam and then processed these data to obtain composite spectra that are largely free from glitches.

Initially, in each raw energy scan, regions containing glitches were selected by eye and the glitch replaced by an interpolated straight line. The locations of these regions were tracked so that they could be excluded from the final summation. We insured that each scan was on a common energy scale by determining the apparent absorption edge energy for the scan using the simultaneously collected reference foil data. This procedure made use of the program ATHENA.[113] ATHENA was then used to background subtract and normalize the individual energy scans giving $\chi(k)$ for each scan. Comparing these scans, the estimated absorption edge energies were mostly within 1 eV of the mean value in each data cluster. In each case the apparent absorption edge energy was noted so that the end points of the original glitched segments could be found in k space. A composite $\chi(k)$ was created by summing the available individual energy scans (excluding the interpolated regions) and dividing by the number of contributing scans at each point. Typically, 2-4 scans at different orientations contributed to each point in the composite $\chi(k)$. However, for the higher pressure data, where strain in the diamonds led to a worse glitch problem, it was not possible to construct complete composite spectra without glitches. The composite spectra for ZrW_2O_8 will be shown in section 4.3.1.5.

In the case of the $ZrMo_2O_8$ data, which were collected at higher energy, the glitch problem was even more serious. In a similar fashion to the measurements on ZrW_2O_8, XAS spectra for the sample in the DAC were collected at several slightly different

orientations of the cell so that a composite spectrum free from glitches due to diamond diffraction could be subsequently constructed. 8-10 different cell orientations were used at each pressure with one scan in each orientation. In the case of $ZrMo_2O_8$, the glitch density was so high that we were unable to produce a useable reconstruction of the EXAFS part of the XAS spectrum, but we were able to produce usable data in the XANES region as described in the next paragraph.

Spectra recorded at different orientations of the DAC were compared to one another point by point in energy space, and the lowest absorption value that was seen for all of the orientations at a given energy was taken to be the true absorption. This procedure works because the presence of a diamond glitch at some energy/DAC orientation always leads to an increase in the measured attenuation. In the event that all the scans have a contribution from a diamond glitch at some energy, the composite spectrum will contain a residual artifact from the diamond glitches.

4.2.6 Analysis of the XANES and EXAFS data

The raw XANES spectra were background subtracted, normalized and plotted for comparison. All EXAFS data fits were performed using the program ARTEMIS.[114, 115] As the data obtained in the DAC was of low quality due to a combination of poor signal to noise ratio and the glitch problem, a very simple model was adopted as a base line for the analysis of all the EXAFS data. In EXAFS analyses there are often problems with correlations between estimated path lengths and E_0, and Debye-Waller factors and the amplitude reduction factor. We chose to estimate E_0 and S_0 (the amplitude reduction factor) using the data for $Na_2WO_4 \cdot 2H_2O$ and then use these values in all of our

subsequent fits. The first shell for $Na_2WO_4 \cdot 2H_2O$ was fit, in both q-space (Fourier filtered k-space) and R-space, using the crystallographic model for this compound with the Debye-Waller factor for all paths fixed at 0.002 $Å^2$, based on an inspection of literature values for W-O bonds, and E_0, S_0 and Δr (deviation of bond lengths from their initial values) as variable parameters. The first shell in the ambient pressure data for all the model compounds, amorphous ZrW_2O_8 and the DAC data was then fit in both q and R-space using fixed values of E_0 and S_0. The base line model for all of the first shell data was a single W-O scattering path with Δr and σ^2, a Debye-Waller factor, as variables. Fits were once again performed in both R- and q-space. Additionally, a model for the amorphous ZrW_2O_8 based on the known crystal structure of orthorhombic ZrW_2O_8[28] was used to fit the *ex-situ* data for this compound and the in DAC data. All the fits were performed using the same q- (2.5-11 $Å^{-1}$) and R-ranges (0.85-1.80 Å). The results are shown in Table 4.1. No EXAFS fitting could be carried out for $ZrMo_2O_8$ due to the low quality of the data.

4.3 Results and discussion

4.3.1 ZrW_2O_8

4.3.1.1 High-pressure diffraction

The diffraction data from our DAC measurements is shown in Figure 4.3. Our closed cell diffraction pattern, marked as 0.00 GPa, shows the presence of a small quantity of orthorhombic ZrW_2O_8 (~ 9 % from the Bragg peak areas) along with the expected cubic ZrW_2O_8 and NaCl. The orthorhombic γ–phase is known to first form at ~ 0.21 GPa, with complete transformation at ~0.32 GPa,[28] indicating that the pressure in some parts of the

sample must be slightly above ambient. As our calibration procedure assumed that this closed cell data was at ambient pressure, all of our subsequent pressure estimates are likely to be slightly too low. However, an error of ~0.2 GPa is of little significance in the context of the amorphization of ZrW_2O_8.

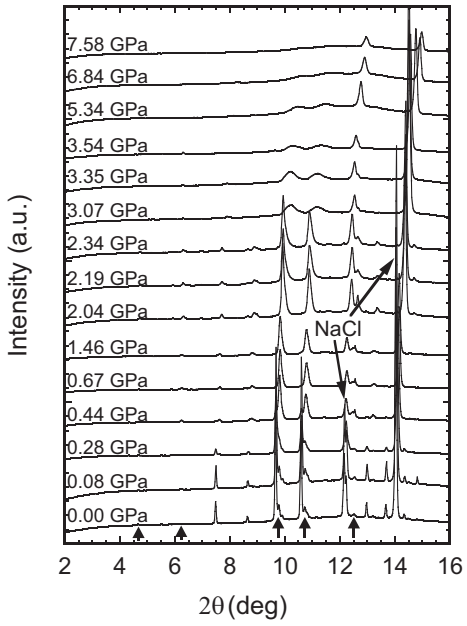

Figure 4.3: Powder diffraction patterns for ZrW_2O_8 as a function of pressure. Arrows indicate the location of peaks characteristic of the orthorhombic phase. The NaCl calibrant peaks are also marked. The data were collected at 17.968 keV (λ = 0.6901 Å).

The transformation of the cubic phase to the orthorhombic phase appears to be well advanced at 0.28 GPa and complete by 0.44 GPa. There is substantial line broadening in the diffraction pattern of the ZrW_2O_8 at pressures higher than 3 GPa and by 7.5 GPa there is little evidence of any Bragg peaks from the ZrW_2O_8, suggesting the formation of a glassy product. The NaCl (200) peak broadened from an initial FWHM of 0.06º 2θ in the as closed cell to 0.09º 2θ by 0.5 GPa, but there was little further increase in its width on

going to 7 GPa (~ 0.10º FWHM, see Figure 4.4). This line broadening indicates non-hydrostatic conditions even at low pressures, but little deterioration as the average pressure was raised above 0.5 GPa. It should be noted that non-hydrostatic conditions are known to promote pressure-induced phase transformations[116-120] including amorphization.[119] Our data indicate the onset of amorphization above ~ 2.5 GPa, with completion of the process at > 5 GPa. This onset pressure is higher than that reported by some (but not all) other workers (1.5 GPa),[14, 55] and the discrepancy may be related to differing stress states for the samples.

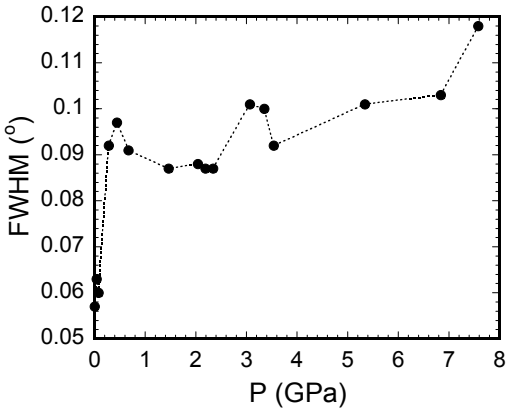

Figure 4.4: Change of the full peak width at half maximum (FWHM) of the NaCl (200) reflection with pressure in the DAC. After the initial broadening, there is very little change.

4.3.1.2 *Ex-situ* XANES

XANES is sensitive to both the oxidation state and site symmetry of an absorbing atom, see for example the early work of Wong.[121] For 3d-metals, sensitivity to site symmetry is typically achieved by examining the behavior of a pre-edge feature in the K-edge spectra that arises primarily from a 1s to 3d transition that is dipole forbidden in a

centrosymmetric coordination environment, but is observed in non-centrosymmetric environments. If only L-edge spectra can be recorded, similar sensitivity can be obtained at the L_I-edge (2s to nd transitions). There have been several studies using W L_I-XANES to probe absorber oxidation state and site symmetry.[122-124]

In Figure 4.5, we show W L_I-XANES spectra for a series of model compounds containing tungsten in different coordination environments along with a XANES spectrum for the amorphous ZrW_2O_8 recovered from 7.5 GPa in a Walker press. The XANES from cubic ZrW_2O_8, $Na_2WO_4{\cdot}2H_2O$ and $Sc_2W_3O_{12}$ are very similar to one another, showing a pronounced pre-edge peak consistent with a coordination environment that is far from centrosymmetric. In all of these compounds, the tungsten is tetrahedrally coordinated. This pre-edge feature is much weaker in the XANES from ammonium paratungstate ($(NH_4)_{10}W_{12}O_{41}{\cdot}5H_2O$), a compound that contains tungsten in heavily distorted octahedral coordination environments (W-O ranges from ~ 1.75 - 2.25 Å for many of the tungsten sites).[125] In ambient pressure WO_3 the pre-edge feature is weaker still, indicative of a more regular coordination, although there is still considerable distortion in the pseduo-octahedral tungsten coordination environment.[126] The data for Ba_2NiWO_6 has almost no pre-edge feature, consistent with the regular octahedral coordination that is expected for this perovskite.[127] The pre-edge feature for the amorphous ZrW_2O_8 is very similar to that observed for the paratungstate. This indicates that compression has destroyed the original tetrahedral symmetry for tungsten, ruling out a simple polyhedral tilting model for the amorphization. However, it also suggests that the final product does not predominantly contain tungsten in an octahedral or slightly distorted octahedral coordination environment, but it may contain tungsten in heavily

distorted octahedral or perhaps five-coordinate environments. The loss of predominantly tetrahedral coordination is expected on compression as orthorhombic ZrW_2O_8 is known to form at 0.2-0.4 GPa and this phase contains a mixture of 4-, 4+1- and 4+2-coordinate tungsten, with predominantly 4+1 coordination.[28] The XANES data seem to be inconsistent with a simple-minded view of a kinetically frustrated pressure-induced demixing driving the amorphization, as the pre-edge in the amorphous material is more pronounced than that of ambient pressure WO_3. However, tungsten in WO_3 is known to undergo significant coordination changes on compression[126] and at ambient temperature a kinetically frustrated demixing could not proceed very far, perhaps, leading to more distorted coordination than that in ambient pressure WO_3. ZrW_2O_8 has been reported to transform to a dense phase with a structure related to that of α-U_3O_8.[55] The highly irregular 6+1 coordination reported for the metals in this phase may be compatible with the XANES data.

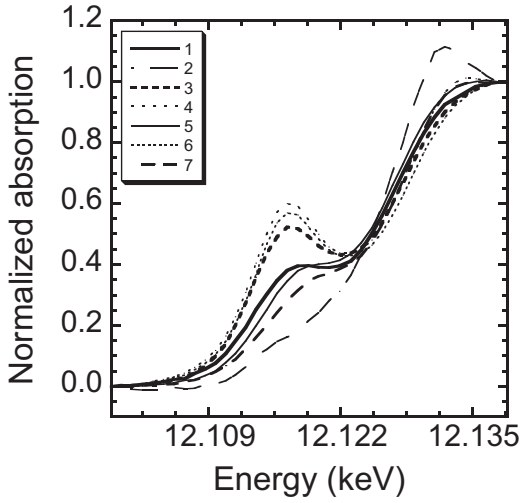

Figure 4.5: W L_I XANES for a series of reference compounds with different tungsten coordination environments: (1) amorphous ZrW_2O_8 recovered from 7.5 GPa, (2) Ba_2NiWO_6 – octahedral, (3) cubic ZrW_2O_8 – tetrahedral, (4) $Na_2WO_4{\cdot}2H_2O$ - tetrahedral, (5) $(NH_4)_{10}W_{12}O_{41}{\cdot}5H_2O$ – heavily distorted 6-coordinate, (6) $Sc_2W_3O_{12}$ - tetrahedral, and (7) WO_3 - distorted octahedral.

4.3.1.3 *In-situ* XANES

XANES data for ZrW_2O_8 as it is compressed in the DAC are shown in Figure 4.6, as a function of pressure. In general, the intensity of the pre-edge feature drops as the pressure is increased. Although the data is of low quality due to the imperfect nature of the deglitching, it appears that there is an initial drop in the size of this feature on going from ambient pressure to 0.7 GPa and a further decrease above 2.3 GPa. The diffraction patterns for the sample at 0.7 and 2.3 GPa both indicate the presence of single phase orthorhombic ZrW_2O_8, so the initial change in the pre-edge feature is presumably associated with transformation of cubic ZrW_2O_8, containing only tetrahedral tungsten (1+3 coordination), to orthorhombic ZrW_2O_8, with primarily 4+1 coordination for the tungsten. At 3.6 GPa, the diffraction data still show very broad weak Bragg peaks in the

positions expected for the orthorhombic phase, suggesting incomplete disordering or considerable strain broadening, but as the FHWM for NaCl (200) at this pressure is similar to that at lower pressures (see Figure 4.4), it seems likely that the origin of the peak broadening in the ZrW_2O_8 is a disordering rather than just strain broadening. The pre-edge feature in the XANES at 3.6 GPa is only slightly less pronounced than that at 2.3 GPa, suggesting that the disordering is not associated with large changes in coordination environment. Further compression to 7.6 GPa leads to a dramatic decrease in the magnitude of the pre-edge feature, suggesting a move towards a coordination environment that is much closer to centrosymmetric. The 7.6 GPa XANES do not appear to be consistent with distorted six-fold coordination such as that seen in the ambient pressure ammonium paratungstate or WO_3 (see Figure 4.5), but they could be viewed as indicating residual 4+1 coordination in a matrix that contains almost centrosymmetric tungsten. The diffraction data recorded at this pressure show that the sample is glass-like.

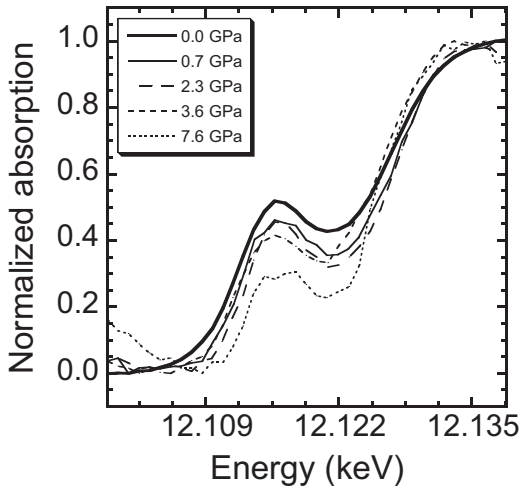

Figure 4.6: W L_I XANES for ZrW_2O_8 under pressure in the DAC.

It is notable that none of the XANES spectra recorded in the DAC under pressure resembles the XANES for the amorphous sample recovered from the Walker cell (see

Figure 4.5). The DAC data always show a pre-edge peak that is well separated from the edge, whereas the *ex-situ* data show a pre-edge feature that is starting to merge into the edge. The differences between the *in-situ* and *ex-situ* measurements could arise from structural relaxation on decompression of the material that was prepared in a multi-anvil device, or the different stress states in the DAC and multi-anvil device or some combination of these effects. It might be expected that the DAC would be closer to hydrostatic than the multi-anvil apparatus due to the presence of large amounts of relatively soft NaCl mixed in with the DAC sample. The ambient pressure bulk modulus, K_0, for NaCl is ~25 GPa[112, 128] and for orthorhombic ZrW_2O_8 it is ~65 GPa.[30]

4.3.1.4 *Ex-situ* EXAFS

In analyzing the EXAFS data collected for our set of reference compounds and the amorphous ZrW_2O_8 recovered from high pressure, several different models were used. The models and the results from the fits are shown in Table 4.1. For all of the samples two very simple models consisting of a single W-O path with a multiplicity of 4 and 6 were explored, even though for samples with irregular coordination the fits are inevitably quite poor. This approach was adopted as, in general, the average M-O bond length for a coordination polyhedron increases as the coordination number of the metal increases and this variation is big enough for us to use the refined W-O distance from our EXAFS analyses as an indicator of the coordination number for the tungsten. Average M-O distance has been used as a metric by other workers looking for changes in coordination under pressure.[129, 130] In Table 4.2 we present the average W-O bond lengths from our fits; a clear relationship between average W-O bond length and coordination number is

observed. This relationship can also be seen by visual inspection of the Fourier filtered EXAFS data (see Figure 4.8). The two compounds with tetrahedral coordination gave average distances of 1.77 Å, but ammonium paratungstate, containing tungsten with heavily distorted octahedral coordination, gave a value of 1.83 Å, WO_3 which also has distorted octahedral coordination gave a value of 1.83 Å, and Ba_2NiWO_6, which is believed to contain tungsten in a regular octahedral environment,[131] gave a distance of 1.87 Å. The difference between the values for the paratungstate and the perovksite are to be expected as EXAFS analyses do not give a simple average of the W-O distances around the tungsten because the fits are more sensitive to the short W-O distances in a coordination polyhedron. The average W-O distance obtained from the single path length fits to the amorphous ZrW_2O_8 sample, ~ 1.81 Å, is much shorter than that seen for the reference compound Ba_2NiWO_6, effectively ruling out anything approaching regular octahedral coordination for tungsten in the amorphous sample. However, it is close to, but slightly smaller than, the value obtained for the paratungstate, suggesting that tungsten could have, on average, very irregular six coordination or perhaps five coordination. This interpretation is consistent with that for the XANES data. We performed fits to the data for amorphous zirconium tungstate using models derived from cubic ZrW_2O_8 (1+3 coordination) and orthorhombic ZrW_2O_8 (irregular five coordination). The 1+3 model offered no improvement over the single-path model, but the five-coordinate model gave better fits again supporting an irregular average coordination environment for the tungsten. However, the XANES data are not consistent with this sample having local environments identical to those in orthorhombic ZrW_2O_8.

Table 4.1: Details of the EXAFS fits. The structural models that were used along with the resulting quality of fit indicator (*R*-factor), Debye-Waller factor (σ^2) and change in half-path length (Δr) are presented. Fixed values of S_0 and E_0 were used unless otherwise indicated: S_0: 0.80 (R-space), 0.83 (q-space); E_0: 7.53 eV (R-space), 8.87 eV (q-space). For all the fits a k-range of 2.5 – 11 $Å^{-1}$ and an R-range of 0.85-1.80 Å were employed. Values in the shaded cells were used to calculate the average W – O bond lengths shown in Table 4.2.

Sample	**Starting model / W-O path lengths (Å)**	**R space fit**		**q space fit**	
		4-coord.	**6-coord.**	**4-coord.**	**6-coord.**
$Na_2WO_4{\cdot}2H_2O$	1.775, 1.776, 1.781 x2	*R*: 0.028 S_0: 0.80(10) E_0: 7.53 ± 3.25 Δr: -0.016(27)	-	*R*: 0.010 S_0: 0.83(7) E_0: 8.87 ± 2.34 Δr: -0.009(17)	-
$Na_2WO_4{\cdot}2H_2O$	1.798	*R*: 0.022 σ^2: 0.0006(13) Δr: -0.038(8)	*R*: 0.093 σ^2: 0.007(3) Δr: -0.029(18)	*R*: 0.006 σ^2: 0.0008(6) Δr: -0.030(4)	*R*: 0.062 σ^2: 0.007(2) Δr: -0.026(14)
$Sc_2W_3O_{12}$	1.798	*R*: 0.025 σ^2: 0.0004(14) Δr: -0.045(9)	*R*: 0.101 σ^2: 0.007(3) Δr: -0.035(18)	*R*: 0.006 σ^2: 0.0007(6) Δr: -0.037(4)	*R*: 0.062 σ^2: 0.007(2) Δr: -0.033(14)
cubic ZrW_2O_8	1.798	*R*: 0.051 σ^2: 0.002(2) Δr: -0.039(13)	*R*: 0.167 σ^2: 0.010(5) Δr: -0.029(24)	*R*: 0.025 σ^2: 0.002(1) Δr: -0.033(8)	*R*: 0.113 σ^2: 0.009(4) Δr: -0.029(19)
amorphous ZrW_2O_8	cubic model, 1.707 x1, 1.798 x3	*R*: 0.112 σ^2: 0.007(4) Δr: 0.023(20)	-	*R*: 0.094 σ^2: 0.008(3) Δr: 0.025(18)	-
amorphous ZrW_2O_8	orth. model, 1.712 (σ^2_1), 1.743-2.300 (σ^2) (5 paths)	*R*: 0.031 σ^2_1: -0.005(2) σ^2: 0.012(7) Δr: 0.032(14)		*R*: 0.007 σ^2_1: -0.005(1) σ^2: 0.013(3) Δr: 0.041(7)	
amorphous ZrW_2O_8	1.798	*R*: 0.109 σ^2: 0.009(4) Δr: 0.003(19)	*R*: 0.242 σ^2: 0.020(7) Δr: 0.022(33)	*R*: 0.093 σ^2: 0.009(3) Δr: 0.005(18)	*R*: 0.198 σ^2: 0.019(6) Δr: 0.017(29)

Table 4.1 (Continued)

Sample	Starting model / W-O path lengths (Å)	R space fit		q space fit	
		4-coord.	6-coord.	4-coord.	6-coord.
WO_3	1.798	*R*: 0.121 σ^2: 0.011(4) Δr: 0.023(22)	*R*: 0.211 σ^2: 0.022(7) Δr: 0.046(32)	*R*: 0.147 σ^2: 0.013(5) Δr: 0.024(24)	*R*: 0.229 σ^2: 0.024(7) Δr: 0.041(34)
$(NH_4)_{10}W_{12}O_{41}\cdot 5H_2O$	1.798	*R*: 0.093 σ^2: 0.015(4) Δr: 0.028(18)	*R*: 0.188 σ^2: 0.027(7) Δr: 0.043(30)	*R*: 0.053 σ^2: 0.015(3) Δr: 0.035(15)	*R*: 0.115 σ^2: 0.025(5) Δr: 0.042(23)
Ba_2NiWO_6	1.798	*R*: 0.057 σ^2: -0.003(2) Δr: 0.061(14)	*R*: 0.008 σ^2: 0.0016(9) Δr: 0.067(5)	*R*: 0.033 σ^2: -0.003(1) Δr: 0.073(10)	*R*: 0.003 σ^2: 0.0021(5) Δr: 0.077(3)
cubic ZrW_2O_8 0.0 GPa	1.798	*R*: 0.044 σ^2: 0.003(2) Δr: -0.026(12)	*R*: 0.163 σ^2: 0.012(5) Δr: -0.012(25)	*R*: 0.031 σ^2: 0.004(2) Δr: -0.022(9)	*R*: 0.129 σ^2: 0.012(4) Δr: -0.014(21)
cubic ZrW_2O_8 0.7 GPa	1.798	*R*: 0.069 σ^2: 0.006(3) Δr: -0.025(15)	*R*: 0.177 σ^2: 0.015(6) Δr: -0.008(27)	*R*: 0.040 σ^2: 0.007(2) Δr: -0.022(11)	*R*: 0.121 σ^2: 0.015(4) Δr: -0.013(21)
orth. ZrW_2O_8 2.3 GPa	1.798	*R*: 0.087 σ^2: 0.005(3) Δr: -0.007(16)	*R*: 0.239 σ^2: 0.015(7) Δr: 0.010(31)	*R*: 0.065 σ^2: 0.006(2) Δr: -0.005(14)	*R*: 0.187 σ^2: 0.015(5) Δr: 0.004(26)
orth. ZrW_2O_8 3.6 GPa	1.798	*R*: 0.085 σ^2: 0.006(3) Δr: 0.010(17)	*R*: 0.200 σ^2: 0.016(6) Δr: 0.027(28)	*R*: 0.062 σ^2: 0007(2) Δr: 0.012(14)	*R*: 0.061 σ^2: 0.016(5) Δr: 0.022(25)
amorphous ZrW_2O_8 7.6 GPa	1.798	*R*: 0.210 σ^2: 0.014(7) Δr: 0.053(31)	*R*: 0.278 σ^2: 0.027(10) Δr: 0.066(40)	*R*: 0.176 σ^2: 0.014(5) Δr: 0.064(27)	*R*: 0.258 σ^2: 0.025(8) Δr: 0.074(37)

Table 4.2: The first-shell W – O average bond lengths obtained from the EXAFS data for a series of reference compounds, with different W coordination, and compressed ZrW_2O_8 at different pressures. The fits were carried out in Fourier-filtered k-space using only 1 scattering path (k-range: 2.5 – 11 $Å^{-1}$, R-range: 0.85-1.80 Å).

	Sample / Pressure	Aver. W-O bond length (Å)	
		4-coord.	6-coord.
Ex-situ (out-side DAC)	$Sc_2W_3O_{12}$ (tetrahedral)[132]	1.760(4)	1.765(14)
	Cubic ZrW_2O_8 (tetrahedral)[133]	1.765(8)	1.769(19)
	$Na_2WO_4 \cdot 2H_2O$ (tetrahedral)[134]	1.767(4)	1.771(14)
	Amorphous ZrW_2O_8	1.803(18)	1.815(29)
	WO_3 (distort. octahedr.)[135]	1.822(24)	1.838(34)
	$(NH_4)_{10}W_{12}O_{41} \cdot 5H_2O$ (irregular 6-coord.)[136]	1.832(15)	1.839(23)
	Ba_2NiWO_6 (octahedral)[137]	1.871(10)	1.875(3)
In-situ (in-DAC)	ZrW_2O_8 / 0.0 GPa	1.776(9)	1.783(21)
	ZrW_2O_8 / 0.7 GPa	1.775(11)	1.783(21)
	ZrW_2O_8 / 2.3 GPa	1.793(14)	1.802(26)
	ZrW_2O_8 / 3.6 GPa	1.810(14)	1.820(25)
	ZrW_2O_8 / 7.6 GPa	1.861(27)	1.871(37)

4.3.1.5 *In-situ* EXAFS

In Figure 4.7, we show $\chi(k)$ as a function of pressure for ZrW_2O_8 as it is compressed in the DAC along with $\chi(k)$ for cubic ZrW_2O_8 and amorphous ZrW_2O_8 recovered from high pressure. The EXAFS evolve in an apparently continuous fashion from something resembling the starting cubic ZrW_2O_8 at low pressure through to a curve at 7.6 GPa that, at low *k,* looks very similar to that for the material recovered from high pressure. Qualitatively the low *k* EXAFS for the sample at 3.6 GPa (showing only weak very broad Bragg peaks by diffraction) are clearly different from those of the 2.3 GPa sample

(orthorhombic by diffraction) indicating a significant change in local structure between these pressures.

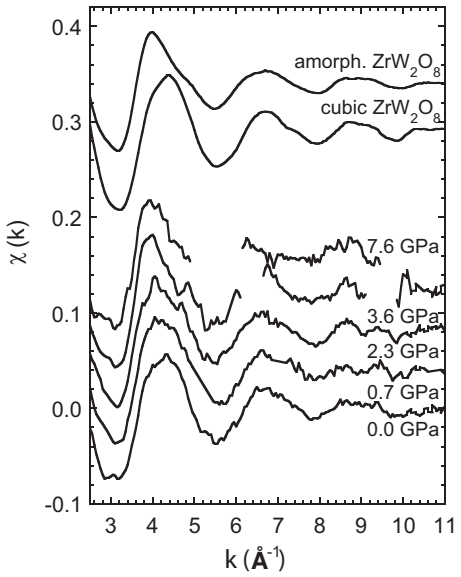

Figure 4.7: W L_{III} $\chi(k)$ for ZrW_2O_8 as a function of pressure along with those for cubic (outside the pressure cell) and pre-amorphized ZrW_2O_8 samples. The missing sections of the 3.6 and 7.6 GPa data arise because we were unable to eliminate the glitches from these regions using the available data.

Although the *in-situ* EXAFS data are noisy and the $\chi(k)$ at 3.6 and 7.6 GPa are incomplete, we performed a fit to these data using a single W-O path model so that we could look for changes in the average W-O bond length as a function of pressure that are indicative of changes in coordination environment. The results from these fits are shown in detail in Table 4.1, the W-O distances are summarized in Table 4.2 and the Fourier-filtered EXAFS data are shown in Figure 4.8. There is no apparent change in average W-O distance on going to 0.7 GPa, perhaps because the coordination changes that occur on going from the cubic to the orthorhombic phase primarily involve the introduction of long W-O contacts that do not contribute strongly to the EXAFS average W-O value. On

compression to 2.3 GPa, where the sample is still orthorhombic by diffraction, the average W-O distance increases slightly, suggesting that some of the longer W-O contacts are shortening and in response the shorter W-O contacts are getting longer; effectively the coordination polyhedron is becoming less irregular and hence more compact. At 3.6 GPa, where the sample shows signs of severe structural disorder by diffraction, the average W-O distance increases to a value close to that seen in the sample recovered from 7.5 GPa, again suggesting a further increase in coordination number or regularization of the coordination polyhedra so that some of the longer contacts that contributed weakly to the average W-O distance contribute more strongly. The average W-O distance from the fit to the data for 7.6 GPa is ~ 1.86Å, close to the value seen for octahedral tungsten in Ba_2NiWO_6. However, the data are so poor that this value is not reliable.

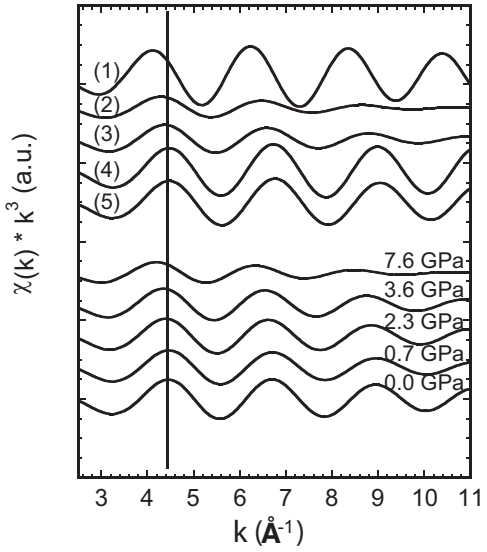

Figure 4.8: Comparison of Fourier-filtered first-shell EXAFS data at ambient pressure for: (1) Ba_2NiWO_6, (2) $(NH_4)_{10}W_{12}O_{41}\cdot 5H_2O$, (3) recovered amorphous ZrW_2O_8, (4) $Na_2WO_4\cdot 2H_2O$ (5) cubic ZrW_2O_8 with those of a ZrW_2O_8 sample at different pressures in a DAC. The vertical line serves as a guide to the eye.

4.3.2 $ZrMo_2O_8$

4.3.2.1 High-pressure diffraction

The integrated high pressure diffraction patterns are shown in Figure 4.9. On compression to 1.7 GPa there is progressive peak broadening and the appearance of significant tailing on the high angle side of the $ZrMo_2O_8$ Bragg peaks. The broadening probably indicates the onset of amorphization that has previously been reported to occur at > 1.3 GPa.[33, 34] Alternatively, it could be a consequence of pressure inhomogeneity / non-hydrostatic conditions within the DAC. However, as the NaCl peaks do not show a pronounced broadening like that seen for the $ZrMo_2O_8$, and NaCl has a lower bulk modulous (~25 GPa[138, 139]) than cubic $ZrMo_2O_8$ (~45 GPa[62]), it is likely that the broadening is not just a consequence of non-hydrostatic conditions. The high-angle asymmetry seen on the $ZrMo_2O_8$ peaks is most likely due to a non-uniform pressure distribution within the illuminated sample volume, where some relatively small fraction of the sample experiences higher pressure than the majority of the material, perhaps due to grain to grain contacts. Alternatively, it could indicate the onset of a phase transformation where the second phase has slightly smaller lattice constants than the original material, but the current data provide no clear evidence of the previously reported crystalline to crystalline phase transition.[33] On further compression to 4.1 GPa, all traces of Bragg peaks from the $ZrMo_2O_8$ are gone and the sample is glass-like.

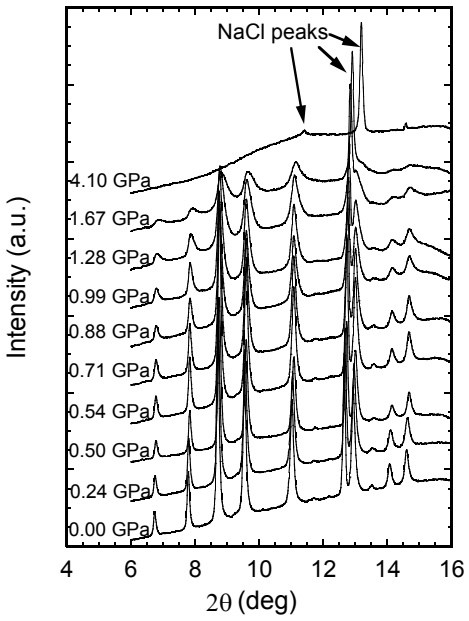

Figure 4.9: Diffraction patterns of $ZrMo_2O_8$ at room temperature under different pressure conditions. Data collected at 19.95 keV (λ = 0.6215 Å).

Heating the amorphous material to 600 ^{o}C for 1 hour at 4.1 GPa led to re-crystallization. The crystalline sample could be recovered to ambient temperature and pressure. The diffraction data for $ZrMo_2O_8$ at ambient pressure, at 4.1 GPa as well as after heating to 600 ºC at 4.1 GPa followed by decompression at ambient temperature are shown in Figure 4.10. The diffraction pattern of this material after cooling and decompression (labeled "decompressed") suggested that there were some binary oxide decomposition products present. One of the binary oxides found as a match is the high-pressure, high-temperature form of MoO_3 (monoclinic space group $P2_1/m$).[66] However, this assignment was not fully satisfactory and there were additional peaks that could not be accounted for by any known binary oxides or $ZrMo_2O_8$ polymorphs. In particular, there was no evidence of any monoclinic $ZrMo_2O_8$[140] in the recovered sample. These

observations are generally in agreement with previous work where $ZrMo_2O_8$ was recovered from high pressure and temperature in a multi-anvil device.[34]

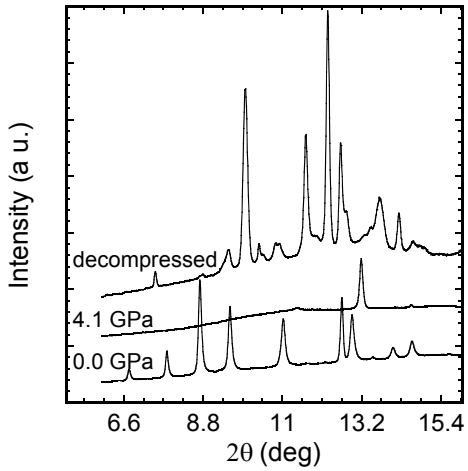

Figure 4.10: Diffraction data for $ZrMo_2O_8$ at ambient pressure (0.0 GPa), at 4.1 GPa and after heating to 600 ^oC at 4.1 GPa followed by decompression at ambient temperature (decompressed). Data collected at 19.95 keV (λ = 0.6215 Å).

We associated the lack of phase transition between 0.7 and 2.0 GPa with the nonhydrostatic pressure conditions imposed by the solid medium (NaCl) in the cell. Therefore another experiment was carried out with isopropanol pressure medium, which provides more hydrostatic pressure conditions (up to 4.3 GPa).[141] Unfortunately, the highest pressure we could reach in the isopropanol experiment was 1.15 GPa. At that pressure our gasket failed and it was no longer possible to control the pressure. No phase transition was observed up to 1.15 GPa (see Figure 4.11). As the end pressure of the experiment was so low, this still leaves open the question whether the previously reported phase transition can be reproduced. In the experiment where this phase transition was originally found,[33] fluorinert was used as pressure-transmitting medium. It is now known

from a recent study by Varga et al.[142] (also discussed in Chapter 8), that fluorinerts provide quasi-hydrostatic pressure conditions only up to about 1 GPa.

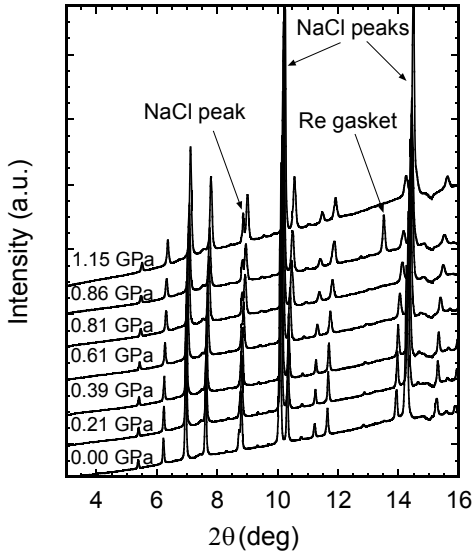

Figure 4.11: Diffraction patterns of $ZrMo_2O_8$ compressed in a DAC using isopropanol pressure medium. The data were collected at 25 keV (λ = 0.496 Å).

The variation of the unit cell volume with pressure is illustrated in Figure 4.12. The results from the present study (CHESS - NaCl) are compared with a previous neutron diffraction study carried out in a He-gas pressure cell (ANL neutron - He)[62] and with the results of the experiment where fluorinert medium was employed (NSLS - fluorinert).[33] The current unit cell volume data agree well with the neutron measurements performed at $P < 0.6$ GPa under perfectly hydrostatic conditions. However, there is a significant deviation from the fluorinert data above 0.8 GPa, which can be due to the different pressure media that were used in the different experiments.

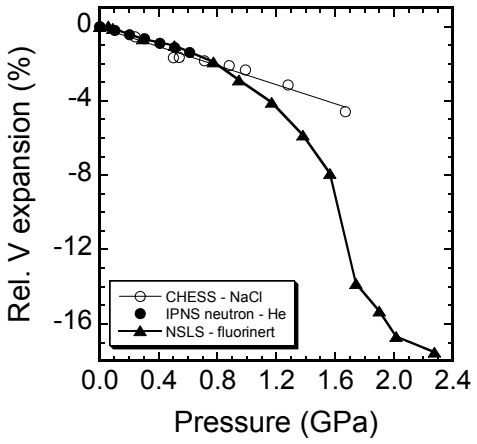

Figure 4.12: Percentage change in the unit cell volume with pressure for cubic $ZrMo_2O_8$: this experiment (CHESS - NaCl with open symbols), a previous neutron study (ANL neutron - He with solid circles) and a previous x-ray study in fluorinert (labeled NSLS - fluorinert with solid triangles).

4.3.2.2 High-pressure XANES

A XANES study similar to that on ZrW_2O_8 was carried out for $ZrMo_2O_8$. The sensitivity of the pre-edge feature in the Mo K-edge spectra can be utilized in studying the oxidation state and site symmetry of the Mo atom.[143, 144]

In Figure 4.13, Mo K-edge XANES spectra are shown for a series of model compounds containing molybdenum in different coordination environments. The XANES spectra of the compounds with tetrahedrally coordinated molybdenum, cubic $ZrMo_2O_8$, $Na_2MoO_4{\cdot}2H_2O$ and $Sc_2Mo_3O_{12}$, show great similarities, they all have a pronounced pre-edge peak (at ~20.02 keV) consistent with a non-centrosymmetric coordination environment. This pre-edge feature is very weak for MoO_3 and is almost non-existent in the spectrum of molybdenum oxide bis-acetylacetonate ($MoO_2(C_5H_7O_2)_2$ or $MoO_2(acac)_2$). This is consistent with the distorted octahedral coordination in MoO_3,[145,

[146] and the more regular, but still distorted octahedral coordination in $MoO_2(acac)_2$;[147] the oxygenyl groups on this later compound are *cis* to one another.[147] In α-MoO_3, the Mo-O bond lengths range from 1.67 - 2.33 Å for the MoO_6 octahedra.[145] In $MoO_2(acac)_2$, these bond lengths fall into the 1.66-2.21 Å range,[147] giving a bit more regular MoO_6 octahedra.

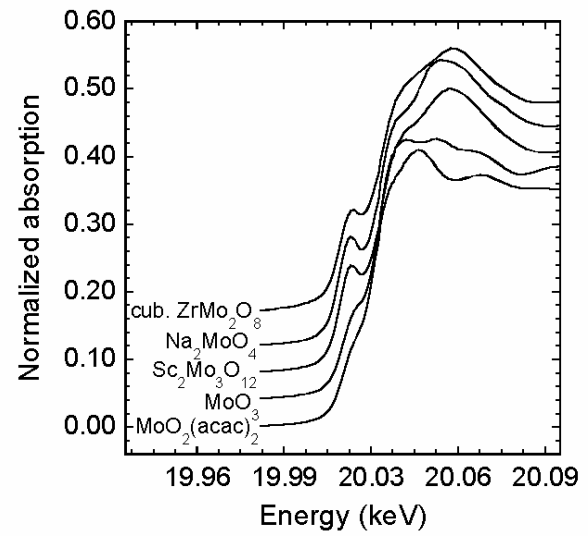

Figure 4.13: Mo K-edge XANES for a series of reference compounds with different Mo coordination environments: cubic ZrW_2O_8 – tetrahedral, $Na_2MoO_4 \cdot 2H_2O$ - tetrahedral, $Sc_2Mo_3O_{12}$ - tetrahedral, MoO_3 - distorted octahedral and $MoO_2(acac)_2$ – distorted octahedral coordination.

In-situ XANES data for $ZrMo_2O_8$ as it is compressed in the DAC are shown in Figure 4.14, as a function of pressure. As we were unable to remove all traces of diamond glitches from these spectra, there are still some spurious features present, most notably the attenuation at ~20.00 keV in the 0.71 GPa data, as well as the feature between the pre-edge peak at 20.02 keV and the main edge in the decompressed sample, almost certainly arise from residual diamond glitches. The apparent shift in the 0.50 and 0.72 GPa data is probably an artifact of the experiment, it may be due to monochromator

instabilities. However, the data are sufficiently good to draw reliable qualitative conclusions. Over the pressure range where the sample is still crystalline (0 - 1.7 GPa), the intensity of the pre-edge feature and its separation from the absorption edge does not change very much, although there may be a slight drop in magnitude of this feature at 1.67 GPa. Additionally, the shape of the absorption maximum itself (20.04-20.07 keV) is almost constant over this pressure range. However, on compressing to 4.1 GPa, where the sample is x-ray amorphous, the shape of the absorption maximum itself changes and the pre-edge peak becomes noticeably less pronounced. The heated and decompressed sample (top curve labeled "decompressed") shows a similar pre-edge peak to the amorphous 4.1 GPa sample, but the shape of the absorption maxima are very different.

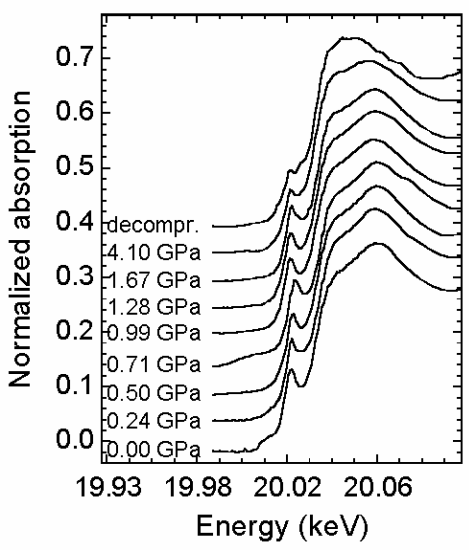

Figure 4.14: Mo K-edge XANES for cubic $ZrMo_2O_8$ under pressure in the DAC.

The presence of a pronounced pre-edge peak in the XANES for the amorphous sample at 4.1 GPa conclusively demonstrates that the molybdenum does not transform from 4 coordination, in cubic $ZrMo_2O_8$, to approximately octahedral coordination on

amorphization. This strongly suggests that the amorphous material should not be viewed as a metastable intermediate on the pathway from crystalline cubic $ZrMo_2O_8$ to a simple mixture of the binary oxide decomposition products ZrO_2 and MoO_3. MoO_3, even the known high pressure form of this compound, would be expected to have a XANES signature similar to that shown for α-MoO_3 in Figure 4.13, with a very weak pre-edge peak, as the molybdenum coordination environments in these two forms of MoO_3 are almost identical.[66] The XANES indicate that this sample contains Mo in an environment that is far from centrosymmetric, perhaps similar to that found in monoclinic $ZrMo_2O_8$,[140, 148] and suggest to us that the amorphous material might be an intermediate on the pathway to a higher density zirconium molybdate, although not necessarily one with a 1:2 metal ratio. The XANES data for the sample that was recovered to room temperature after heating at 600 ºC and 4.1 GPa for one hour still show a well defined pre-edge peak. This is inconsistent with the recrystallized sample only containing molybdenum as the known high pressure form of MoO_3, as the XANES spectrum would be similar to that of the α-MoO_3 sample shown in Figure 4.13. The data suggests that the recovered sample contained a zirconium molybdate that we were unable to identify; the formation of a new high pressure MoO_3 polymorph with coordination that is not close to octahedral seems unlikely. It should be noted that the change in shape of the absorption maximum after recrystallization tells us that the molybdenum in this sample is in a different coordination environment from that in the starting amorphous material. These observations also suggest that the amorphous phase should be viewed as a metastable intermediate on the way to a denser zirconium molybdate, not as an intermediate on the pathway to binary oxide decomposition products.

4.4 Conclusions

Our in-situ measurements show the expected formation of orthorhombic ZrW_2O_8 at low pressure followed by the onset of amorphization above 2.3 GPa with completion by ~7.6 GPa. The XAS data support a continuous evolution of the local tungsten coordination environment on compression after forming the orthorhombic phase, with the average W-O bond length increasing, indicating an increase in average coordination number, and the W L_I pre-edge peak decreasing in magnitude, indicating a movement towards tungsten coordination that is closer to centrosymmetric. While the 7.6 GPa XAS data is consistent with the presence of some tungsten with octahedral coordination, the data is of insufficient quality to be sure of this. These observations are perhaps not fully consistent with the conclusions of a high pressure simulation study,[60] where it was suggested that changes in zirconium coordination as the pressure increased were more likely than changes in the tungsten coordination. The *in-situ* XANES measurements on ZrW_2O_8 clearly differ from the *ex-situ* measurements made on an amorphous sample recovered from 7.6 GPa in a multi-anvil press. This indicates that either structural relaxation occurs on decompression or the sample stress states in the DAC and multi-anvil apparatus were sufficiently different that glasses with different local structures were formed. It is unfortunate that we did not obtain data on the sample in the DAC after decompression, as this would have directly addressed the origin of the observed differences.

No apparent pressure-induced crystalline to crystalline phase transition was observed in cubic $ZrMo_2O_8$ in contrast to earlier results.[33] The material was observed to amorphize starting at ~ 1.7 GPa, and by 4.1 GPa there was no evidence for any residual crystalline

component in the sample. Heating the amorphous sample at 4.1 GPa and 600 ^{o}C led to crystalline products that included some binary oxide decomposition products. The combination of *in-situ* high pressure diffraction and XANES clearly demonstrates that the pressure-induced amorphization of cubic $ZrMo_2O_8$ does not involve a change of molybdenum coordination from tetrahedral, in the starting phase, to approximately octahedral as would be expected if the amorphous material where a metastable intermediate well along the pathway towards decomposition into a mixture of binary oxides. The recrystallized amorphous material is not a simple mixture of known binary oxides, it probably contains a zirconium molybdate phase that we were unable to identify. The amorphous material at 4.1 GPa might best be viewed as a metastable intermediate on the pathway to another crystalline zirconium molybdate.

Our measurements on cubic ZrW_2O_8 are not consistent with a mechanism for amorphization that primarily involves reorienting existing coordination polyhedra in a disordered fashion. From the perspective of tungsten coordination, the *in-situ* data are consistent with initial transformation to the orthorhombic phase, containing 4-, 4+1- and 4+2- coordinated tungsten, followed by a shortening of the long W-O contacts that exist in this structure as the sample is further compressed. This regularization of the coordination environments seems to continue into the pressure regime where the sample becomes amorphous.

Measurements showing changes in longer range local structure (M-M distances) and the zirconium coordination environment would be helpful in providing a better picture of the amorphization process. Ideally these should be made *in-situ*, as our current data suggest that structural relaxation on decompression may be a problem. However, our *ex-*

situ XAS studies discussed in the next chapter further contributed to our understanding of the process.

The issue of low-pressure phase transition in cubic $ZrMo_2O_8$ before amorphization takes place could be addressed in the future by carrying out an in-situ high-pressure XRD study using a hydrostatic pressure-transmitting medium (preferably a gas, such as nitrogen).

4.5 References

[1] O. Mishima, L. D. Calvert, and E. Whalley: 'Melting ice' I at 77 K and 10 kbar: a new method of making amorphous solids. *Nature* **310**, 393 (1984).

[2] R. J. Hemley, A. P. Jephcoat, H. K. Mao, et al.: Pressure-induced amorphization of crystalline silica. *Nature* **334**, 52 (1988).

[3] M. B. Kruger and R. Jeanloz: Memory Glass: An Amorphous Material Formed from $AlPO_4$. *Science* **249**, 647 (1990).

[4] E. G. Ponyatovsky and O. I. Barkalov: Pressure-induced amorphous phases. *Mater. Sci. Rep.* **8**, 147 (1992).

[5] A. Jayaraman, S. K. Sharma, Z. Wang, et al.: Pressure-induced amorphization of $Tb_2(MoO_4)_3$: a high pressure Raman and x-ray diffraction study. *J. Phys. Chem. Solids* **54**, 827 (1993).

[6] S. M. Sharma and S. K. Sikka: Pressure Induced Amorphization of Materials. *Prog. Mater. Sci.* **40**, 1 (1996).

[7] P. Richet and P. Gillet: Pressure-induced amorphization of minerals: a review. *Eur. J. Mineral.* **9**, 907 (1997).

[8] J. Badro, P. Gillet, and J.-L. Barrat: Melting and pressure-induced amorphization of quartz. *Europhys. Lett.* **42**, 643 (1998).

[9] T. Sakuntala, A. K. Arora, N. V. Chandra Shekar, et al.: Pressure-induced amorphization and orientational disorder in potash alum. *J. Phys.: Condens. Matter* **12**, 4417 (2000).

[10] H. Liu, R. A. Secco, N. Imanaka, et al.: X-ray diffraction study of pressure-induced amorphization in Lu2(WO4)3. *Solid State Commun.* **121**, 177 (2002).

[11] V. Dmitriev, V. Sinitsyn, R. Dilanian, et al.: In situ pressure-induced solid-state amorphization in $Sm_2(MoO_4)_3$, $Eu_2(MoO_4)_3$ and $Gd_2(MoO_4)_3$ crystals: chemical decomposition scenario. *J. Phys. Chem. Solids* **64**, 307 (2003).

[12] A. Grzechnik and W. A. Crichton: Structural transformations in cubic $ZrMo_2O_8$ at high pressures and high temperatures. *Solid State Sci.* **4**, 1137 (2002).

[13] H. Liu, R. A. Secco, N. Imanaka, et al.: X-ray diffraction study of pressure induced amorphization in $Lu_2(WO_4)_3$. *Solid State Commun.* **121**, 177 (2002).

[14] C. A. Perottoni and J. A. H. de Jornada: Pressure-Induced Amorphization and Negative Thermal Expansion in ZrW_2O_8. *Science* **280**, 886 (1998).

[15] R. A. Secco, H. Liu, N. Imanaka, et al.: Pressure-induced amorphization in negative thermal expansion $Sc_2(WO_4)_3$. *J. Mater. Sci. Lett.* **20**, 1339 (2001).

[16] R. J. Speedy: Models for the amorphization of compressed crystals. *J. Phys. Condens. Matter* **8**, 10907 (1996).

[17] A. W. Sleight: Compounds that Contract on Heating. *Inorg. Chem.* **37**, 2854 (1998).

[18] A. W. Sleight: Isotropic Negative Thermal Expansion. *Annu. Rev. Mater. Sci.* **28**, 29 (1998).

[19] J. S. O. Evans: Negative Thermal Expansion Materials. *J. Chem. Soc. Dalton Trans.*, 3317 (1999).

[20] S. M. Bennington, J. Li, M. J. Harris, et al.: Phonon softening in ice Ih. *Physica B* **263-264**, 396 (1999).

[21] R. Mittal, S. L. Chaplot, H. Schober, et al.: Origin of Negative Thermal Expansion in Cubic ZrW_2O_8 Revealed by High Pressure Inelastic Neutron Scattering. *Phys. Rev. Lett.* **86**, 4692 (2001).

[22] R. Mittal, S. L. Chaplot, H. Schober, et al.: Origin of negative thermal expansion in cubic ZrW_2O_8 and $ZrMo_2O_8$: High pressure inelastic neutron scattering study. *Solid State Phys. (India)* **44**, 656 (2001).

[23] T. R. Ravindran, A. K. Arora, and T. A. Mary: High Pressure Behavior of ZrW_2O_8: Gruneisen Parameter and Thermal Properties. *Phys. Rev. Lett.* **84**, 3879 (2000).

[24] T. R. Ravindran, A. K. Arora, and T. A. Mary: High-pressure Raman spectroscopic study of zirconium tungstate. *J. Phys.: Condens. Matter* **13**, 11573 (2001).

[25] B. Chen, D. V. S. Muthu, Z. X. Liu, et al.: High-pressure Raman and infrared study of HfW_2O_8. *Phys. Rev. B* **64**, 214111 (2001).

[26] Y. Yamamura, N. Nakajima, T. Tsuji, et al.: Low-temperature heat capacities and Raman spectra of negative thermal expansion compounds ZrW_2O_8 and HfW_2O_8. *Phys. Rev. B* **66**, 014301 (2002).

[27] R. Mittal, S. L. Chaplot, A. I. Kolesnikov, et al.: Inelastic neutron scattering and lattice dynamical calculation of negatie thermal expansion in HfW_2O_8. *Phys. Rev. B* **68**, 054302 (2003).

[28] J. S. O. Evans, Z. Hu, J. D. Jorgensen, et al.: Compressibility, Phase Transitions, and Oxygen Migration in Zirconium Tungstate, ZrW_2O_8. *Science* **275**, 61 (1997).

[29] Z. Hu, J. D. Jorgensen, S. Teslic, et al.: Pressure-induced phase transformation in ZrW_2O_8 - Compressibility and thermal expansion of the orthorhombic phase. *Physica B* **241-243**, 370 (1998).

[30] J. D. Jorgensen, Z. Hu, S. Teslic, et al.: Pressure -induced cubic-to-orthorhombic phase transition in ZrW_2O_8. *Phys. Rev. B* **59**, 215 (1999).

[31] J. M. Gallardo-Amores, U. Amador, E. Moran, et al.: XRD study of ZrW_2O_8 versus temperature and pressure. *Int. J. Inorg. Mater.* **2**, 123 (2000).

[32] J. D. Jorgensen, Z. Hu, S. Short, et al.: Pressure-induced cubic-to-orthorhombic phase transfromation in the negative thermal expansion material HfW_2O_8. *J. Appl. Phys.* **89**, 3184 (2001).

[33] C. Lind, D. G. VanDerveer, A. P. Wilkinson, et al.: New high pressure form of the negative thermal expansion materials zirconium molybdate and hafnium molybdate. *Chem. Mater.* **13**, 487 (2001).

[34] A. Grzechnik and W. A. Crichton: Structural transformations in cubic $ZrMo_2O_8$ at high pressures and high temperatures. *Solid State Sci.* **4**, 1137 (2002).

[35] S. Carlson and A. M. Krogh Andersen: High-pressure properties of TiP_2O_7, ZrP_2O_7 and ZrV_2O_7. *J. Appl. Cryst.* **34**, 7 (2000).

[36] T. Varga, A. P. Wilkinson, C. Lind, et al.: In-situ high pressure synchrotron x-ray diffraction study of $Sc_2W_3O_{12}$ at up to 10 GPa. *accepted for publication in Phys. Rev. B*, (2005).

[37] W. Paraguassu, M. Maczka, A. G. Souza Filho, et al.: Pressure-induced structural transformations in the molybdate $Sc_2(MoO_4)_3$. *Phys. Rev. B* **69**, 094111(1 (2004).

[38] M. Maczka, W. Paraguassu, A. G. Souza Filho, et al.: High-pressure Raman study of $Al_2(WO_4)_3$. *J. Solid State Chem.* **177**, 2002 (2004).

[39] G. D. Mukherjee, S. N. Achary, A. K. Tyagi, et al.: High pressure AC resistivity and compressibility study on $Al_2(WO_4)_3$. *J. Phys. Chem. Solids* **64**, 611 (2003).

[40] R. A. Secco, H. Liu, N. Imanaka, et al.: Pressure-induced amorphization in negative thermal expansion $Sc_2(WO_4)_3$. *J. Mater. Sci. Lett.* **20**, 1339 (2001).

[41] A. K. Arora, R. Nithya, T. Yagi, et al.: Two-stage amorphziation of scandium molybdate at high pressure. *Solid State Commun.* **129**, 9 (2004).

[42] H. Liu, R. A. Secco, N. Imanaka, et al.: X-ray diffraction study of pressure induced amorphization in $Lu_2(WO_4)_3$. *Solid State Commun.* **121**, 177 (2002).

[43] C. Verdon and D. C. Dunand: High-Temperature Reactivity in the ZrW_2O_8-Cu System. *Script. Mater.* **36**, 1075 (1997).

[44] H. Holzer and D. C. Dunand: Phase transformation and thermal expansion of Cu/ZrW_2O_8 metal matrix composites. *J. Mater. Res.* **14**, 780 (1999).

[45] D. K. Balch and D. Dunand, C.: Copper-Zirconium Tungstate Composites Exhibiting Low and Negative Thermal Expansion Influenced by Reinforcement Phase Transformations. *Metallurg. Mater. Trans. A* **35A**, 1159 (2004).

[46] T. A. Mary, J. S. O. Evans, T. Vogt, et al.: Negative Thermal Expansion from 0.3 to 1050 Kelvin in ZrW_2O_8. *Science* **272**, 90 (1996).

[47] J. S. O. Evans, T. A. Mary, T. Vogt, et al.: Negative Thermal Expansion in ZrW_2O_8 and HfW_2O_8. *Chem. Mater.* **8**, 2809 (1996).

[48] M. Auray and M. Quarton: Zirconium Tungstate. *Acta Crystallogr., Section C* **51**, 2210 (1995).

[49] L. Ouyang, Y.-N. Xu, and W. Y. Ching: Electronic structure of cubic and orthorhombic phases of ZrW_2O_8. *Phys. Rev. B* **65**, 113110 (2002).

[50] N. Duan, U. Kamerwari, and A. W. Sleight: Further contraction of ZrW_2O_8. *J. Am. Chem. Soc.* **121**, 10432 (1999).

[51] J. S. O. Evans, J. D. Jorgensen, S. Short, et al.: Thermal expansion in the orthorhombic γ-phase of ZrW_2O_8. *Phys. Rev. B* **60**, 14643 (1999).

[52] K. Wang and R. R. Reeber: Mode Gruneisen parameters and negative thermal expansion of cubic ZrW_2O_8 and $ZrMo_2O_8$. *Appl. Phys. Lett.* **76**, 2203 (2000).

[53] R. Stevens, J. Linford, B. F. Woodfield, et al.: Heat Capacities, Third-Law Entropies and Thermodynamic Functions of the Negative Thermal Expansion Materials, Cubic α-ZrW_2O_8 and β-$ZrMo_2O_8$ From T = 0 K to 400 K. *J. Chem. Thermodyn.* **35**, 919 (2003).

[54] W. I. F. David, J. S. O. Evans, and A. W. Sleight: Direct evidence for a low-frequency phonon mode mechanism in the negative thermal expansion compound ZrW_2O_8. *Europhys. Lett.* **46**, 661 (1999).

[55] A. Grzechnik, W. A. Crichton, K. Syassen, et al.: A New Polymorph of ZrW_2O_8 Synthesized at High Pressures and High Temperatures. *Chem. Mater.* **13**, 4255 (2001).

[56] D. A. Fleming, D. W. Johnson, and P. J. Lemaire, Article Comprising a Temperature Compensated Optical Fiber Refractive Index Grating, Lucent Technologies, USA (1997).

[57] G. Ernst, C. Broholm, G. R. Kowach, et al.: Phonon Density of States and Negative Thermal Expansion in ZrW_2O_8. *Nature* **396**, 147 (1998).

[58] A. P. Ramirez and G. R. Kowach: Large Low Temperature Specific Heat in the Negative Thermal Expansion Compound ZrW_2O_8. *Phys. Rev. Lett.* **80**, 4903 (1998).

[59] Y. Yamamura, N. Nakajima, and T. Tsuji: Heat capacity anomaly due to the α-to-β structural phase transition in ZrW_2O_8. *Solid State Commun.* **114**, 453 (2000).

[60] A. K. A. Pryde, M. T. Dove, and V. Heine: Simulation studies of ZrW_2O_8 at high pressure. *J. Phys.: Condens. Matter.* **10**, 8417 (1998).

[61] T. R. Ravindran, A. K. Arora, and T. A. Mary: High-pressure Raman spectroscopic study of zirconium tungstate. *J. Phys.: Condens. Matter* **13**, 11573 (2001).

[62] C. Lind, A. P. Wilkinson, Z. Hu, et al.: Synthesis and Properties of the Negative Thermal Expansion Material Cubic Zirconium Molybdate. *Chem. Mater.* **10**, 2335 (1998).

[63] C. Lind, A. P. Wilkinson, C. J. Rawn, et al.: Kinetics of the cubic to trigonal transformation in $ZrMo_2O_8$ and their dependence on precursor chemistry. *J. Mater. Chem.* **12**, 990 (2002).

[64] M. Auray, M. Quarton, and P. Tarte: Crystal Data for Two Molybdates $M(MoO_4)_2$ with M = Zr, Hf. *Powder Diffr.* **2**, 36 (1987).

[65] B. Baker, T. P. Feist, and E. M. McCarron III: Soft Chemical Synthesis of a High-Pressure Phase of Molybdenum Trioxide: MoO_3-II. *J. Solid State Chem.* **119**, 199 (1995).

[66] E. M. McCarron III and J. C. Calabrese: The growth and single crystal structure of a high pressure phase of molybdenum trioxide: MoO_3-II. *J. Solid State Chem.* **91**, 121 (1991).

[67] S. Carlson and A. M. Krogh Andersen: High-pressure transitions of trigonal α-$ZrMo_2O_8$. *Phys. Rev. B* **61**, 11209 (2000).

[68] A. M. Krogh Andersen and S. Carlson: High-pressure structures of α- and δ-$ZrMo_2O_8$. *Acta Crystallogr., Sect. B* **57**, 20 (2001).

[69] R. J. Hemley, C. Meade, and H.-k. Mao: Comment on "Medium-Range Order in Permanently Densified SiO_2 and GeO_2 Glass". *Phys. Rev. Lett.* **79**, 1420 (1997).

[70] M. Guthrie, C. A. Tulk, C. J. Benmore, et al.: Formation and Structure of a Dense Octahedral Glass. *Phys. Rev. Lett.* **93**, 115502 (2004).

[71] S. J. L. Billinge and M. G. Kanatzidis: Beyond crystallography: the study of disorder, nanocrystallinity and crystallographically challenged materials with pair distribution functions. *Chem. Commun.* **7**, 749 (2004).

[72] S. Mobilio and C. Meneghini: Synchrotron radiation in the study of amorphous materials. *J. Non-Crsyt. Solids* **232-234**, 25 (1998).

[73] Y. Waseda: Structural characterization of noncrystalline materials by anomalous (resonance) x-ray scattering. *J. Phys.: Colloque* **C8**, 293 (1985).

[74] L. Cormier: Glass structure studied by neutron diffraction. *J. Phys. IV: Proc.* **111**, 187 (2003).

[75] J. W. Zwanziger, NMR as a probe of glass structure, *International Congress on Glass Vol. 19*, 182 (2001).

[76] J. W. Zwanziger, K. K. Olsen, S. L. Tagg, et al.: High resolution and multidimensional nuclear magnetic resonance probes of glass structure. *NATO ASI Ser., 3: High Technology* **23(Amorphous Insulators and Semiconductors)**, 245 (1997).

[77] C. Meade, R. J. Hemley, and H.-k. Mao: High-Pressure X-ray Diffraction of SiO_2 Glass. *Phys. Rev. Lett.* **69**, 1387 (1992).

[78] G. Shen, V. B. Prakapenka, M. L. Rivers, et al.: Structural investigation of amorphous materials at high pressures using the diamond anvil cell. *Rev. Sci. Instrum.* **74**, 3021 (2003).

[79] A. V. Sapelkin and S. C. Bayliss: X-ray Absorption Spectroscopy Under High Pressures in Diamond Anvil Cells. *High Pressure Res.* **21**, 315 (2001).

[80] R. Ingalls, G. A. Garcia, and E. A. Stern: X-Ray Absorption at High Pressure. *Phys. Rev. Lett.* **40**, 334 (1978).

[81] F. M. Wang and R. Ingalls: Iron bcc-hcp transition: Local structure from x-ray-asbsorption fine structure. *Phys. Rev. B* **57**, 5647 (1998).

[82] J. Freund, R. Ingalls, and E. D. Crozier: Extended X-Ray-Absorption Fine-Structure Study of Copper under High-Pressure. *Phys. Rev. B* **39**, 12537 (1989).

[83] L. Comez, A. DiCicco, J. P. Itie, et al.: High-pressure and high-temperature x-ray absorption study of liquid and solid gallium. *Phys. Rev. B* **65**, 014114 (2001).

[84] R. Ingalls, E. D. Crozier, J. E. Whitmore, et al.: Extended x-ray absorption fine structure of NaBr and Ge at high pressure. *J. Appl. Phys.* **51**, 3158 (1980).

[85] A. Yoshiasa, T. Nagai, O. Ohtaka, et al.: Pressure and temperature dependence of EXAFS Debye-Waller factors in diamond-type and white-tin type germanium. *J. Synchrotron Radiat.* **6**, 43 (1999).

[86] J. Freund, R. Ingalls, and E. D. Crozier: X-Ray Absorption Fine-Structure Study of Amorphous-Germanium under High-Pressure. *J. Phys. Chem.* **94**, 1087 (1990).

[87] A. Polian, J. P. Itie, E. Dartyge, et al.: X-ray absorption spectroscopy on solid krypton up to 20 GPa. *Phys. Rev. B* **39**, 3369 (1989).

[88] A. Di Cicco, A. Filipponi, J. P. Itie, et al.: High-pressure EXAFS measurements on solid and liquid Kr. *Phys. Rev. B* **54**, 9086 (1996).

[89] J. M. Tranquada and R. Ingalls: X-Ray-Absorption Study of CuBr at High-Pressure. *Phys. Rev. B* **34**, 4267 (1986).

[90] C. B. Vanpeteghem, R. J. Nelmes, D. R. Allan, et al.: High-pressure High-Temperature Studies of Structural Ordering in GaSb. *Phys. Status Solidi B* **223**, 405 (2001).

[91] J. P. Itie, A. Polian, C. Jauberthie-Carillon, et al.: High-pressure phase transition in gallium phosphide: an x-ray absorption spectroscopy study. *Phys. Rev. B* **40**, 9709 (1989).

[92] J. P. Itie, V. Briois, D. Martinez-Garcia, et al.: X-ray Absorption Spectroscopy Applied to Pressure-Induced Transformations of Semiconductors. *Phys. Status Solidi B* **211**, 323 (1999).

[93] J. Pellicer-Porres, A. Segura, V. Munoz, et al.: High-pressure x-ray absorption study of GaTe including polarization. *Phys. Rev. B* **61**, 125 (2000).

[94] S. H. Tolbert and A. P. Alivisatos: Se EXAFS study of the elevated wurtzite to rock salt structural phase transition in CdSe nanocrystals. *NATO ASI Ser., E: Applied Sciences* **260(Nanophase Materials)**, 471 (1994).

[95] B. Houser and R. Ingalls: X-ray-absorption fine structure determination of pressure-induced bond-angle changes in ReO_3. *Phys. Rev. B* **61**, 6515 (2000).

[96] A. I. Frenkel, F. M. Wang, S. Kelly, et al.: Local structural changes in KNbO3 under high pressure. *Phys. Rev. B* **56**, 10869 (1997).

[97] Z. Hu, S. Bertram, and G. Kaindl: X-ray-absorption study of PrO_2 at high pressure. *Phys. Rev. B* **49**, 39 (1994).

[98] G. Kaindl, G. Schmiester, E. V. Sampathkumaran, et al.: Pressure-induced changes in L_{III} x-ray-absorption near-edge structure of CeO_2 and CeF_4: Televance to 4f-electronic structure. *Phys. Rev. B* **38**, R10174 (1988).

[99] J. P. Itie, A. Polian, G. Calas, et al.: Pressure-Induced Coordination Changes in Crystalline and Vitreous GeO_2. *Phys. Rev. Lett.* **63**, 398 (1989).

[100] O. Majerus, L. Cormier, J.-P. Itie, et al.: Pressure-induced Ge coordination change and polyamorphism in SiO_2-GeO_2 glasses. *J. Non-Cryst. Solids* **345-346**, 34 (2004).

[101] C. L. Bull, P. F. McMillan, J. P. Itie, et al.: X-ray absorption and EXAFS studies of Ge coordination and bonding in high-pressure nitrides: β-Ge_3N_4 (phenacite) and γ-Ge_3N_4 (spinel). *Phys. Status Solidi A* **201**, 909 (2004).

[102] W. A. Bassett, A. J. Anderson, R. A. Mayanovic, et al.: Hydrothermal diamond anvil cell for XAFS studies of first-row transition elements in aqueous solution up to supercritical conditions. *Chem. Geol.* **167**, 3 (2000).

[103] K. Ohsumi, S. Sueno, I. Nakai, et al.: EXAFS Measurement under High-Pressure by Diamond Anvil Cell. *J. Phys.* **47**, 189 (1986).

[104] S. Sueno, I. Nakai, M. Imafuku, et al.: EXAFS measurements under high pressure conditions using a combination of a diamond anvil cell and synchrotron radiation. *Chem. Lett.* **10**, 1663 (1986).

[105] H. Tolentino, E. Dartyge, A. Fontaine, et al.: X-ray Absorption Spectroscopy in the Dispersive Mode with Synchrotron Radiation: Optical Considerations. *J. Appl. Crystallogr.* **21**, 15 (1988).

[106] S. Pascarelli, O. Mathon, and G. Aquilanti: New opportunities for high pressure X-ray absorption spectroscopy using dispersive optics. *J. Alloys Compd.* **362**, 33 (2004).

[107] W. A. Bassett, A. J. Anderson, R. A. Mayanovic, et al.: Hydrothermal diamond anvil cell for XAFS studies of first-row transition elements in aqueous solution up to supercritical conditions. *Chem. Geol.* **167**, 3 (2000).

[108] K. Largarec and S. Desgreniers, computer code Simplified Image Plate Analysis, University of Ottawa, Ottawa, ON, Canada (1994-97).

[109] I. Materials Data, computer code JADE, XRD Pattern Processing, Materials Data, Inc., Livermore, CA (1995-2005).

[110] A. C. Larson and R. B. Von Dreele, computer code General Structural Analysis Software, Los Alamos National Laboratory, Los Alamos (2000).

[111] J. Zhao, computer code Pressure calibration, University of Witwatersrand, Johannesburg-Gauteng.

[112] F. Birch: Equation of state and thermodynamic parameters of sodium chloride to 300 kbar in the high-temperature domain. *J. Geophys. Res. B* **91**, 4949 (1986).

[113] B. Ravel, computer code ATHENA - EXAFS Data Processing, (2001-2003).

[114] M. Newville: Interactive XAFS analysis and FEFF fitting. *J. Synchrotron Radiat.* **8**, 322 (2001).

[115] B. Ravel: ARTEMIS - EXAFS Data Analysis. (2001-2003).

[116] L. Dubrovinsky, N. Dubrovinskaia, S. Saxena, et al.: X-ray diffraction under non-hydrostatic conditions in experiments with diamond anvil cell: wüstite (FeO) as an example. *Mater. Sci. Eng.* **A288**, 187 (2000).

[117] N. Funamori, M. Funamori, R. Jeanloz, et al.: Broadening of x-ray powder diffraction lines under nonhydrostatic stress. *J. Appl. Phys.* **82**, 142 (1997).

[118] H. Libotte and J.-P. Gaspard: Pressure-induced distortion of the β-Sn phase in silicon: Effects of nonhydrostaticity. *Phys. Rev. B* **62**, 7110 (2000).

[119] T. Taniguchi, T. Sato, W. Utsumi, et al.: Effect of nonhydrostaticity on the pressure induced phase transformation of rhombohedral boron nitride. *Appl. Phys. Lett.* **70**, 2392 (1997).

[120] T.-C. Wu, W. A. Bassett, P. C. Burnley, et al.: Shear-Promoted Phase Transitions in Fe_2SiO_4 and Mg_2SiO_4 and the Mechanism of Deep Earthquakes. *J. Geophys. Res.* **98**, 19767 (1993).

[121] J. Wong, F. W. Lytle, R. P. Messmer, et al.: K-edge absorption spectra of selected vanadium compounds. *Phys. Rev. B* **30**, 5596 (1984).

[122] A. Balerna, E. Bernieri, E. Burattini, et al.: EXAFS studies of MeO_{3-x} (Me = W, Mo, Re, Ir) crystalline and amorphous oxides. *Nucl. Instrum. Methods Phys. Res.* **A308**, 234 (1991).

[123] J. A. Horsley, I. E. Wachs, J. M. Brown, et al.: Structure of Surface Tungsten Oxide Species in the WO_3/Al_2O_3 Supported Oxide System from X-ray Absorption Near-edge Spectroscopy and Raman Spectroscopy. *J. Phys. Chem.* **91**, 4014 (1987).

[124] F. Hilbrig, H. E. Gobel, H. Knozinger, et al.: X-ray Absorption Spectroscopy Study of the Titania- and Alumina-Supported Tungsten Oxide System. *J. Phys. Chem.* **95**, 6973 (1991).

[125] v. H. D'Amour and R. Allman: Die Kristallstruktur des Ammoniumparawulframat-tetrahydrats. *Z. Krist.* **136**, 23 (1972).

[126] Y. N. Xu, S. Carlson, and R. Norrestam: Single Crystal Diffraction Studies of WO_3 at High Pressures and the Structure of High-Pressure WO_3 Phase. *J. Solid State Chem.* **132**, 123 (1997).

[127] V. S. Filip'ev, G. E. Shatalova, and E. G. Fesenko: Determination of bond lengths in tungstates with the perovskite structure. *Kristallografiya* **19**, 386 (1974).

[128] D. L. Decker: High-Pressure Equation of State for NaCl, KCl, and CsCl. *J. Appl. Phys.* **42**, 3239 (1971).

[129] C. Meade, R. J. Hemley, and H. K. Mao: High-Pressure X-Ray Diffraction of SiO_2 Glass. *Phys. Rev. Lett.* **69**, 1387 (1992).

[130] J. P. Itie, A. Polian, C. Jauberthie-Carillon, et al.: High-pressure phase transition in gallium phosphide: an x-ray absorption spectroscopy study. *Phys. Rev. B* **40**, 9709 (1989).

[131] D. E. Cox, G. Shirane, and B. C. Frazer: Neutron-Diffraction Study of Antiferromagnetic Ba_2CoWO_6 and Ba_2NiWO_6. *J. Appl. Phys.* **38**, 1459 (1967).

[132] J. S. O. Evans, T. A. Mary, and A. W. Sleight: Negative Thermal Expansion in $Sc_2(WO_4)_3$. *J. Solid State Chem.* **137**, 148 (1998).

[133] T. A. Mary, J. S. O. Evans, T. Vogt, et al.: Negative Thermal Expansion from 0.3 to 1050 Kelvin in ZrW_2O_8. *Science* **272**, 90 (1996).

[134] K. Okada, H. Morikawa, F. Marumo, et al.: Crystal structure of $Na_2WO_4.2H_2O$. *Bull. Tokyo Inst. Technol.*, 7 (1974).

[135] P. M. Woodward, A. W. Sleight, and T. Vogt: Structure refinement of triclinic tungsten trioxide. *J. Phys. Chem. Solids* **56**, 1305 (1995).

[136] v. H. D'Amour and R. Allman: Die Kristallstruktur des Ammoniumparawulframat-tetrahydrats. *Z. Kristallogr.* **136**, 23 (1972).

[137] D. E. Cox, G. Shirane, and B. C. Frazer: Neutron-Diffraction Study of Antiferrromagnetic Ba_2CoWO_6 and Ba_2NiWO_6. *J. Appl. Phys.* **38**, 1459 (1967).

[138] D. L. Decker: High-Pressure Equation of State for NaCl, KCl, and CsCl. *J. Appl. Phys.* **42**, 3239 (1971).

[139] F. Birch: Equation of state and thermodynamic parameters of sodium chloride to 300 kbar in the high-temperature domain. *J. Geophys. Res. B* **91**, 4949 (1986).

[140] M. Auray and M. Quarton: Revised Crystal Data of $Zr(MoO_4)_2$, L.T. Form. *Powder Diffr.* **4**, 29 (1989).

[141] R. Miletich, D. Allan, R., and W. Kuhs, F.: High-Pressure Single-Crystal Techniques. *Rev. Mineral. Geochem.* **41**, 445 (2001).

[142] T. Varga, A. P. Wilkinson, and R. J. Angel: Fluorinert as a pressure-transmitting medium for high-pressure diffraction studies. *Rev. Sci. Instrum.* **74**, 4564 (2003).

[143] A. Balerna, E. Bernieri, E. Burattini, et al.: EXAFS studies of MeO_{3-x} (Me = W, Mo, Re, Ir) crystalline and amorphous oxides. *Nucl. Instrum. Methods Phys. Res.* **A308**, 234 (1991).

[144] L. M. R. Hill, G. N. George, A.-K. Duhme-Klair, et al.: Solution structural studies of molybdate-nucleotide polyanions. *J. Inorg. Biochem.* **88**, 274 (2002).

[145] L. Kihlborg: Least-squares refinement of the crystal structure of Mo trioxide. *Arkiv för Kemi* **21**, 357 (1963).

[146] J. B. Parise, E. M. McCarron, A. W. Sleight, et al.: Refinement of the structure of beta'-MoO_3. *Mater. Sci. Forum* **27-28**, 85 (1988).

[147] O. N. Krasochka, Y. A. Sokolova, and L. O. Atovmyan: Crystal and molecular structures of molybdenum bic-acetylacetonate, $MoO_2(C_5H_7O_2)_2$. *J. Struct. Chem.* **16**, 648 (1975).

[148] R. F. Klevtsova, L. A. Glinskaya, E. S. Zolotova, et al.: Crystal Structure of zirconium molybdate $Zr(MoO_4)_2$. *Dokl. Akad. Nauk SSSR* **305**, 91 (1989).

CHAPTER 5

EX-SITU STUDIES OF THE PRESSURE-INDUCED AMORPHIZATION IN ZrW_2O_8 AND $ZrMo_2O_8$

Abstract

The pressure-induced amorphization of cubic ZrW_2O_8 and cubic $ZrMo_2O_8$ was studied in samples previously amorphized in a multi-anvil press and recovered to ambient conditions by low-temperature EXAFS and XANES carried out at the W L_{III}-, L_I- and Mo K-edges, respectively as well as at the Zr K-edge. Both the EXAFS and XANES revealed an increase in the average coordination number of tungsten in ZrW_2O_8 and a less pronounced increase in that of molybdenum in $ZrMo_2O_8$. These observations are in accordance with our results from a combined *in-situ* – *ex-situ* high-pressure study performed separately. The Zr K-edge data indicated a pronounced change of about the same extent in the average Zr-coordination in both compounds. The results suggest that both the framework tetrahedra and octahedra distort on amorphization, and in the case of $ZrMo_2O_8$, the ZrO_6 octahedra are more prone to distortion at the amorphization pressure. A decrease in the photoelectron scattering magnitudes for the metal-metal correlations was seen in the amorphous materials indicating that those correlations started to become less significant. The pressure-induced amorphization in both ZrW_2O_8 and $ZrMo_2O_8$ is most likely driven by a kinetically frustrated phase transformation to a high-pressure phase with higher metal coordination numbers, but a kinetically hindered pressure-induced demixing may also play a role.

5.1 Introduction

In the previous chapter we discussed the changes in the local coordination environment of W in cubic ZrW_2O_8, and Mo in $ZrMo_2O_8$ on pressure-induced amorphization as seen by in-situ x-ray absorption spectroscopy (XAS). A change in local coordination (W and Mo, respectively) was observed in both compounds, which was much less pronounced in the case of the molybdenum compound. These findings are inconsistent with an amorphization mechanism that primarily involves a reorientation of the existing coordination polyhedra at least in the case of tungsten. Instead, the amorphous material may perhaps best be viewed as a metastable intermediate between the starting phase and another crystalline phase stable at high pressures, or alternatively, as a phase resulting from a kinetically hindered decomposition to the constituent binary oxides. We also pointed out that further measurements, showing changes in the local structure over a longer length scale and also in the zirconium coordination environment would help us get a better picture of the amorphization process. Therefore, to complement our *in-situ* spectroscopic studies, we carried out a series of XAS measurements on amorphous samples that had been prepared at high pressure and recovered to ambient pressure. Transmission XAS data were collected on cubic and amorphous ZrW_2O_8 at the W L_{III}-edge (EXAFS), the W L_I-edge (XANES) and at the Zr K-edge (EXAFS and XANES), on cubic and amorphous $ZrMo_2O_8$ at the Mo K- and Zr K–edges (EXAFS and XANES), and on a number of model compounds with different W, Mo and Zr coordination, respectively. Some of these measurements were carried at low temperature (down to 55-65 K) in order to minimize the effect of thermal vibrations of the atoms and thus maximize the signal at high wavenumber (k). Data were also collected

at 160 and 298 K temperatures so that when we performed the EXAFS analyses we could check if all of the extracted parameters behaved in a physically sensible fashion as a function of temperature, and modify our analysis as necessary to obtain meaningful results. An important point of this study is that changes in local metal environment could be followed from the perspective of both metals, W versus Zr and Mo versus Zr, as data was available at the different metal absorption edges for each compound. Changes in the Zr coordination can also be expected on compression. In their high-pressure simulation study on ZrW_2O_8, Pryde et al. argued that at high pressure, the ZrO_6 octahedra are more liable to distort than the WO_4 tetrahedra, and thus major coordination changes involving the zirconium were more likely than those involving tungsten.[1] In a high-pressure polymorph of ZrW_2O_8 with a cation-disordered α-U_3O_8–type structure obtained by heating a pressure-amorphized sample under pressure, both the Zr and W cations were reported to display 6+1 coordination.[2]

Although, in-situ studies would have been ideal due to possible structural relaxation on decompression as discussed in Chapter 4, such study was not an option at this time due to severe problems related to diffraction from the diamonds at the Zr K- and Mo K-edges. Both previously amorphized samples were re-confirmed to be x-ray amorphous prior to the experiments by laboratory XRD (see Figure 5.3).

5.2 Experimental

5.2.1 Syntheses

Cubic ZrW_2O_8: A stoichiometric amount of $ZrO(NO_3)_2 \cdot xH_2O$ (Aldrich, Milwaukee, WI) was thoroughly mixed and ground with 2 weight % excess of H_2WO_4 (Strem

Chemicals, Newburyport, MA). The powder was heated at 1150 ^{o}C for 5 hour, 24 hour and 36 hour periods with intermittent ice-water quenching, drying (at 130 ^{o}C) and regrinding steps.

Amorphous ZrW_2O_8: Cubic ZrW_2O_8 was compressed using a Walker-type high-pressure multi-anvil press at the Mineral Physics Institute, SUNY Stony Brook, NY. The pressure cell consisted of a platinum sample capsule in a 14 mm magnesia octahedron surrounded by eight one-inch tungsten carbide cubes, all truncated on the corner facing the magnesia. Pyrophyllite and teflon gaskets as well as balsa spacers were used between the cubes (see Figure 5.1). ~140 mg cubic ZrW_2O_8 was placed into the Pt capsule and the sample was exposed to a pressure of about 7.5 GPa at room temperature for 2 hours prior to slow decompression.

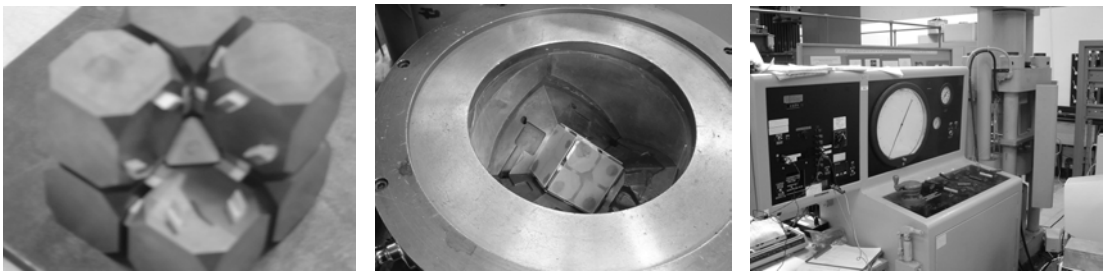

Figure 5.1: Picture of the octahedral sample cell before closing (left); the multi-anvil cell with the octahedral sample cell in place (middle); the main control console of the hydraulic press.

Ba_2NiWO_6: $BaCO_3$, $NiCO_3$ and WO_3 were thoroughly mixed and ground. The mixture was heated at 1100 ^{o}C for 20 hours and, after regrinding, heated at 1400 ^{o}C for an additional 2 hours.

$Sc_2W_3O_{12}$: Sc_2O_3 and WO_3 were mixed, ground and heated together at 1000 ^{o}C for 5 hours, then, after regrinding, heated at 1200 ^{o}C for 12 hours.

The reference compounds $Na_2WO_4 \cdot 2H_2O$, $(NH_4)_{10}W_{12}O_{41} \cdot 5H_2O$ (Alfa Aesar, Ward Hill, MA) and WO_3 (Aldrich, Milwaukee, WI) were used as received.

Cubic $ZrMo_2O_8$: $ZrMo_2O_7(OH)_2 \cdot 2H_2O$ was produced by the reaction of aqueous solutions of $ZrO(ClO_4)_2 \cdot 5H_2O$ and $(NH_4)_6Mo_7O_{24} \cdot 4H_2O$ in acid medium by 3 days of refluxing. Then $ZrMo_2O_7(OH)_2 \cdot 2H_2O$ was dehydrated by a series of low temperature heat treatment steps (350 ^oC for 12 hours, 375 ^oC for 15 minutes, 400 ^oC for 15 minutes, 425 ^oC for 30 minutes and finally 450 ^oC for 30 minutes).

Amorphous $ZrMo_2O_8$: Cubic $ZrMo_2O_8$ was compressed using the same Walker-type high-pressure multi-anvil press used for the preparation of amorphous ZrW_2O_8 using the same pressure cell assembly. ~100 mg cubic $ZrMo_2O_8$ was placed into the Pt capsule and the sample was exposed to a pressure of about 5 GPa at room temperature for 2 hours prior to slow decompression.

$Sc_2Mo_3O_{12}$: stoichiometric quantities of Sc_2O_3 (Strem Chemicals, Newburyport, MA) and MoO_3 (J. T. Baker, Phillipsburg, NJ) were thoroughly mixed, ground and heated together at 700 ^oC for 5 hours and then, after regrinding, at 1100 ^oC for 12 hours.

All other Mo-containing reference compounds were commercial products and used as received: $Na_2MoO_4 \cdot 2H_2O$ (Fisher Scientific, Fair Lawn, NJ), MoO_3 (J. T. Baker, Phillipsburg, NJ) and $MoO_2(acac)_2$ (Strem Chemicals, Newburyport, MA).

The Zr-containing reference phases ZrO_2 (Alfa Aesar, Ward Hill, MA) and $ZrSiO_4$ (Strem Chemicals, Newburyport, MA) were used as received.

Both amorphous samples were prepared at most a few weeks prior to the experiment (and their structure checked only a few days before the measurements, see Figure 5.3),

therefore possible sample relaxation (see section 4.3.1.3) was not considered as a problem.

5.2.2 X-ray diffraction

All samples were characterized after synthesis by x-ray diffraction using a Scintag X1 diffractometer with a Peltier-cooled solid state detector and a copper tube. The structure of the samples including the commercial ones was verified by XRD. For the scans typically a scan rate of 2.5°/min and a step size of 0.02° were employed along with a 251 mm diffractometer radius, 2/1 mm slits on the tube side and 0.5/0.3 mm slits on the detector side. For the scan on amorphous ZrW_2O_8, a scan rate of 0.03°/min, for amorphous $ZrMo_2O_8$ 1.0°/min was used.

5.2.3 Variable temperature XAS data collection

The XAS measurements were carried out at beamline X11A of NSLS in BNL, Upton, NY in June 2004. Data were collected at ambient pressure conditions, but at several temperatures. Low-temperature (55-65 as well as 160 K) data were collected using a Displex cryostat (see Figure 5.2). A Displex is a two-stage helium compressor with a copper cold finger. The cold finger is wrapped with a resistive heating element and is in contact with a temperature-sensing diode. Using the heating element and diode, a commercial temperature controller was used to control the temperature at the cold finger between ~50 K and 300 K with good stability.

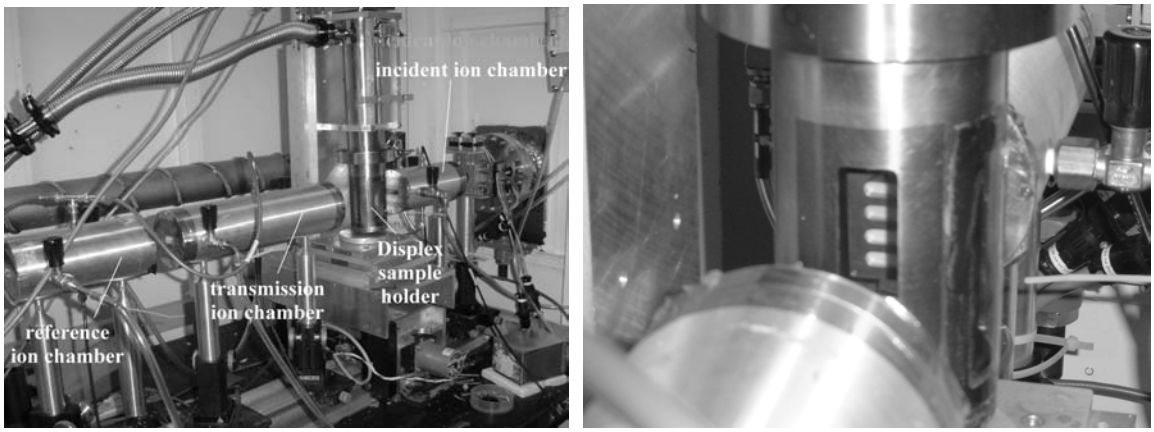

Figure 5.2: Picture of the Displex refrigerator in the beam (left); a close-up of the Displex with samples within (right).

The EXAFS and XANES data collection was done in transmission mode using a three ion chamber arrangement with a reference metal foil between the second and third detector (see Figure 5.2). Transmission XAS data were collected for cubic and amorphous ZrW_2O_8, cubic and amorphous $ZrMo_2O_8$ at ambient pressure and different temperatures, and a series of reference compounds with different metal coordination (see Table 5.1 for a list) at ambient pressure and temperature. The samples were diluted and ground with boron nitride so that the maximum value of μt was ~1.5 – 2, and then packed into the copper sample holder of the Displex cell and covered with Kapton tape on both sides (the white powder samples in four of the five slots of can be seen in the right picture of Figure 5.2). Tungsten XANES scans were performed around the W L_I-edge (12.100 keV) in the 11.900-12.170 keV range with 5 eV steps in the pre-edge region (11.900-12.050 keV), 0.75 eV steps in the near-edge region (12.050-12.150 keV) and 0.05k (~2.5 eV) steps in the post-edge region (12.150-12.170 keV) using 25 % monochromator detuning for rejection of the higher harmonics. Tungsten EXAFS data were recorded at the W L_{III}-edge (10.207 keV) in the 10.007-11.185 keV range with 5 eV steps in the pre-

edge region (10.007-10.157 keV), 0.75 eV steps in the near-edge region (10.157-10.257 keV) and 0.05 k (~6 eV) steps in the post-edge region (10.257-11.185 keV) with 30 % monochromator detuning. Molybdenum XANES and EXAFS scans were performed around the Mo K-edge (20.000 keV) in the 19.800-21.238 keV range with 5 eV steps in the pre-edge region (19.800- 19.950 keV), 1 eV steps in the near-edge region (19.950-20.050 keV) and 0.05k (~6.7 eV) steps in the post-edge region (20.050-21.238 keV) using 10-15 % monochromator detuning for harmonic rejection. Zr XANES and EXAFS data were recorded at the Zr K-edge (17.998 keV) in the 17.798-18.974 keV range with 5 eV steps in the pre-edge region (17.798-17.968 keV), 1 eV steps in the near-edge region (17.968-18.028 keV) and 0.05 k (~6 eV) steps in the post-edge region (18.028-18.974 keV) using 15 % monochromator detuning. Data at each point were recorded for 2 seconds and typically three scans were performed for each sample. A summary of the samples, absorption edges and temperature conditions is given in Table 5.1.

5.2.4 Data processing and analysis

Data processing was performed using the program ATHENA.[3, 4] For the ZrW_2O_8 and $ZrMo_2O_8$ samples at least 3 energy scans were averaged at each temperature. For the reference samples, generally 2 scans were performed at room temperature. All data were put on a common energy scale using the reference foil absorption spectra. The raw XANES spectra were background subtracted, normalized and plotted for comparison. All EXAFS data fits were performed using the program ARTEMIS.[4, 5] For the cubic and amorphous ZrW_2O_8 and $ZrMo_2O_8$ samples, detailed EXAFS fitting was attempted using many metal-oxygen and metal-metal scattering paths; for amorphous ZrW_2O_8 at the W

L_{III}- and Zr K-edges and for $ZrMo_2O_8$ at the Mo K- and Zr K-edges. Details of these fits are discussed in the corresponding section of the results. For the examination of the average first-shell metal-oxygen distances for possible coordination changes in the amorphous materials, a very simple model was adopted as a base line for the analysis of all the EXAFS data. In EXAFS analyses there are often problems with correlations between estimated path lengths and the shift of the energy reference, E_0, and Debye-Waller factors and the amplitude reduction factor. In a similar fashion to what is described in section 4.2.6 for the combined in-situ and ex-situ studies of ZrW_2O_8, in all three series of fits we estimated E_0 and the amplitude reduction factor S_0 using the data for $Na_2WO_4 \cdot 2H_2O$ (W L_{III}-edge), $Na_2MoO_4 \cdot 2H_2O$ (Mo K-edge) and ZrO_2 (Zr K-edge), and then used these values in all of our subsequent fits.

Table 5.1: Summary of the W-, Mo- and Zr-containing samples with their coordination geometries, as well as absorption edges and temperature conditions used in the low-temperature XAS study.

Sample	Coordination	Absorption edge	Temperature (K)
ZrO_2	7[6]	Zr K	298
$ZrSiO_4$	8[7]	Zr K	298
cubic $ZrMo_2O_8$	octahedral[8]	Zr K	298
amorph. $ZrMo_2O_8$	-	Zr K	298
cubic ZrW_2O_8	octahedral[9]	Zr K	298
amorph. ZrW_2O_8	-	Zr K	298
$Sc_2W_3O_{12}$	tetrahedral[10]	W L_I (XANES)	298
$Na_2WO_4.2H_2O$	tetrahedral[11, 12]	W L_I (XANES)	298
Ba_2NiWO_6	octahedral[12]	W L_I (XANES)	298
WO_3	distorted octahedral[13]	W L_I (XANES)	298
$(NH_4)_{10}W_{12}O_{41}.5H_2O$	irregular 6-coordinate[14]	W L_I (XANES)	298
cubic ZrW_2O_8	tetrahedral	W L_I (XANES)	298
amorph. ZrW_2O_8	-	W L_I (XANES)	298
$Sc_2W_3O_{12}$	tetrahedral	W L_{III} (EXAFS)	298
$Na_2WO_4.2H_2O$	tetrahedral	W L_{III} (EXAFS)	298
Ba_2NiWO_6	octahedral	W L_{III} (EXAFS)	298
WO_3	distorted octahedral	W L_{III} (EXAFS)	298
$(NH_4)_{10}W_{12}O_{41}.5H_2O$	irregular 6-coordinate	W L_{III} (EXAFS)	298
cubic ZrW_2O_8	tetrahedral	W L_{III} (EXAFS)	65, 160, 298
amorph. ZrW_2O_8	-	W L_{III} (EXAFS)	65, 160, 298
$Na_2MoO_4.2H_2O$	tetrahedral	Mo K	298
$Sc_2Mo_3O_{12}$	tetrahedral	Mo K	298
trigonal $ZrMo_2O_8$	tetrahedral[15]	Mo K	298
MoO_3	distorted octahedral[16]	Mo K	298
$MoO_2(acac)_2$	distorted octahedral[15, 17]	Mo K	298
cubic $ZrMo_2O_8$	tetrahedral	Mo K	55, 160, 298
amorph. $ZrMo_2O_8$	-	Mo K	55, 298

The first shell for the reference compound was fit, in both q-space (Fourier filtered k-space) and R-space, using the crystallographic model for this compound with the Debye-

Waller factor for all paths fixed at a value chosen based on an inspection of literature values for the corresponding metal-oxygen bonds. E_0, S_0 and Δr (change in scattering half-path length, also viewed as the deviation of bond lengths from their initial values) were used as variable parameters. The first shell in the room temperature data for all the model compounds and the amorphous ZrW_2O_8 and the $ZrMo_2O_8$ was then fit in both q and R-space using fixed values of E_0 and S_0 obtained from the latter fit. The base line model for all of the first shell data was a single metal-oxygen scattering path with Δr and σ^2, a Debye-Waller factor, as variables. Fits were once again performed in both R- and q-space. The known crystal structure of orthorhombic ZrW_2O_8[18] was used to fit the data for amorphous ZrW_2O_8 and the crystal structure of cubic $ZrMo_2O_8$ derived from the known structure for ordered α-ZrW_2O_8[9] was used for amorphous $ZrMo_2O_8$. All the fits were performed using the same q- and R-ranges within each of the three data series (see details in sections 5.3.1.2, 5.3.2.2 and 5.3.3.2).

5.3 Results

X-ray diffraction patterns for the cubic and amorphous ZrW_2O_8 and $ZrMo_2O_8$ samples are shown in Figure 5.3. No Bragg diffraction peaks are visible for any of the amorphous samples indicating that they are completely x-ray amorphous.

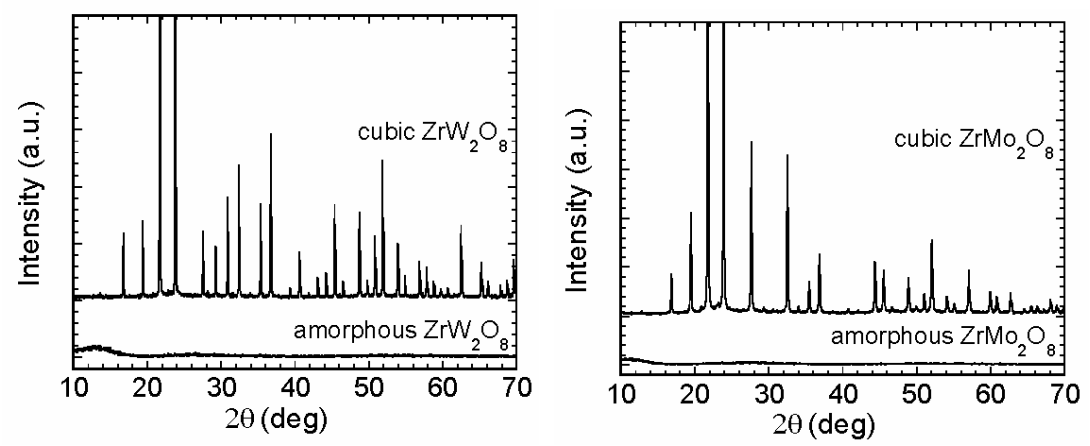

Figure 5.3: Comparison of the x-ray diffraction patterns for the cubic and amorphous phases of ZrW_2O_8 and $ZrMo_2O_8$. No Bragg peaks appear in the pattern for the amorphous materials. Data collected using Cu K_α radiation.

5.3.1 W L_I- and L_{III}-edge data

5.3.1.1 W L_I-edge XANES

XANES is sensitive to both the oxidation state and site symmetry of an absorbing atom and have been used for comparing species with different metal coordination geometries.[19] In the L_I-edge spectra for a tungsten-containing species, a pre-edge feature arises primarily from a 2s to nd transition that is dipole forbidden in a centrosymmetric coordination (such as octahedral) environment, but is observed in non-centrosymmetric (e.g. tetrahedral) environments. There have been several studies using W L_I-XANES to probe absorber oxidation state and site symmetry.[20-22]

In Figure 5.4 W L_I-XANES spectra are shown for a series of model compounds containing tungsten in different coordination environments along with a XANES spectrum for the amorphous ZrW_2O_8 recovered from the multi-anvil press (see Table 5.1 for coordination geometries). The XANES from cubic ZrW_2O_8, $Na_2WO_4{\cdot}2H_2O$ and $Sc_2W_3O_{12}$ are very similar to one another, showing a pronounced pre-edge peak

consistent with a tetrahedral coordination environment. This pre-edge feature is much weaker in the XANES from the amorphous ZrW_2O_8 sample, ammonium paratungstate ($(NH_4)_{10}W_{12}O_{41}.5H_2O$) and WO_3. The data for Ba_2NiWO_6 has almost no pre-edge feature, as expected for a perovskite with regular octahedral tungsten coordination.[23] Details on the coordination environment in these model compounds were already mentioned in the previous chapter (see section 4.3.1.2). The pre-edge feature for the amorphous ZrW_2O_8 is very similar to that observed for the paratungstate. This is in agreement with our XANES results reported in Chapter 4 from a similar ex-situ experiment related to our high-pressure in-situ studies and indicates an increase in the tungsten coordination from tetrahedral to a more regular coordination. As the XANES for the amorphous sample in nothing like that of Ba_2NiWO_6, this more regular coordination is probably far from centrosymmetric. The compression has destroyed the original tetrahedral coordination of the tungsten, resulting in heavily distorted octahedral or perhaps five-coordinate tungsten environments.

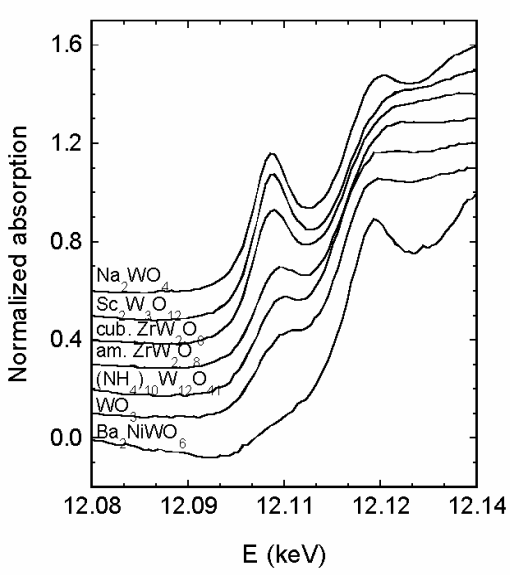

Figure 5.4: W L_I-edge XANES of compounds with different tungsten-coordination including an amorphous sample.

5.3.1.2 W L_{III}-edge EXAFS

Room temperature $k\chi(k)$ curves are shown for samples with different W coordination and for the amorphous material in Figure 5.5. The overall picture is consistent with the XANES data. The tetrahedral compounds $Sc_2W_3O_{12}$ and cubic ZrW_2O_8 have very similar curves, while the also tetrahedral Na_2WO_4 shows more well-resolved features. The curves for the amorphous sample and ammonium paratungstate are vaguely similar in accordance with the previous statement that the tetrahedral coordination of cubic ZrW_2O_8 shifts towards a more regular coordination on compression, which is probably close to irregular octahedral. The curve for the amorphous material seems to be intermediate between that of the cubic one and ammonium paratungstate. WO_3 shows more resemblance to the regular octahedral Ba_2NiWO_6, only with features that are less pronounced at lower k and almost no features above ~8 $Å^{-1}$.

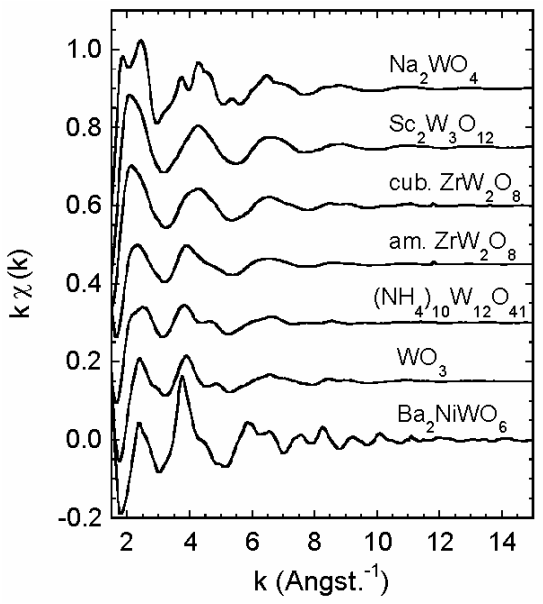

Figure 5.5: W L_{III} kχ(k)-k curves for compounds with different W-coordination along with that of the pre-amorphized ZrW_2O_8 sample.

The kχ(k)-k curves at different temperatures do not show any significant differencies in the case of the ZrW_2O_8 samples. Although the features in the 65 K data seem to be a slightly more pronounced, all features are clearly visible at room temperature, too (see Figure 5.6).

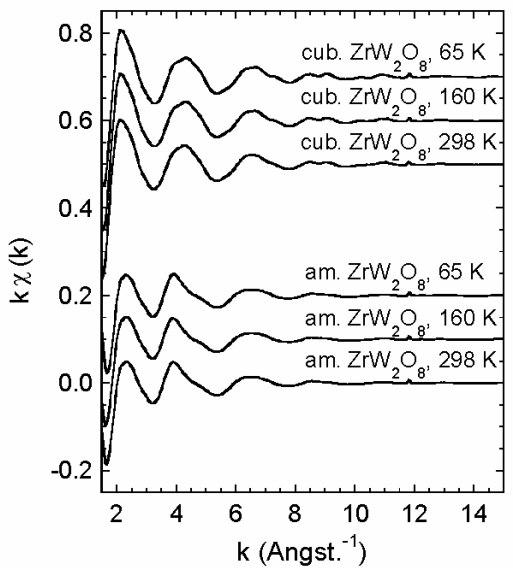

Figure 5.6: W L_{III} kχ(k)-k curves for cubic and amorphous ZrW_2O_8 at different temperatures.

The Fourier-transformed kχ(k) curves show the contribution of the different scattering paths to the EXAFS (see Figure 5.7). There is a dramatic change in amorphous ZrW_2O_8 compared to the cubic material. Also notable is the similarity of the data for the amorphous sample to those for with distorted octahedral coordination (WO_3 and the paratungstate).

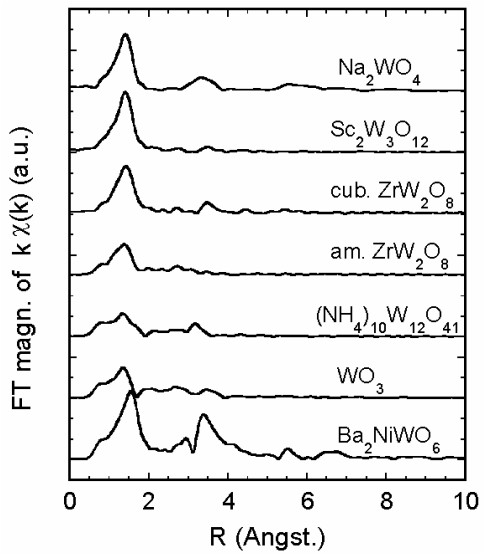

Figure 5.7: FT magnitudes for compounds with different W-coordination along with that of the amorphous ZrW_2O_8 sample.

The local structure of cubic ZrW_2O_8 has already been studied in detail by XAS.[24, 25] In Figure 5.8 we give an illustration of which scattering paths contribute to which peak in the Fourier-transformed magnitude plot based on simulations generated using the code FEFF within the IFEFFIT program package.[4] The graph shows only the 0-6 Å range, which covers all the interatomic distances of interest, and is arbitrarily divided into five sections. By a single scattering path we mean that the photoelectron wave is directly backscattered from another atom, while paths involving more than two atoms are considered as multiple scattering paths. We distinguish between the R-range as the x-axis of the plot and the scattering path lengths given by the FEFF calculation. The W-O single scattering paths that belong to the first section give rise to the first large peak between roughly 1 and 2 Å. These three paths are in the 1.707-2.386 Å range, the numbers indicating the path lenghts for the scattering effects. The scattering in the region between ~2.25-3.25 Å (second section) can be accounted for by several W-O-O multiple

scattering paths and a W-O single scattering path with lengths falling into the 3.111-4.093 Å range. The latter W-O path contributes over a relatively wide range. The peak in the third section between ~3.25-4.25 Å arises as a result of the contribution of paths related to W and Zr, both single scattering W-Zr and multiple scattering W-Zr-O and W-O-Zr paths. The shoulder of the peak that extends over 4 Å is a result from W-O single scattering. The path lengths contributing to the third region fall in the range 3.744-3.907 Å. The peak in the fourth region (~4.25-4.75 Å) can be described using tungsten-tungsten scattering effects that include contributions from W-W single scattering and W-W-O and W-O-W multiple scattering with path lengths in the 4.119-4.639 Å range. Finally, the last region between ~4.75 and 6 Å can be accounted for by many scattering paths involving metal-metal scattering effects with path lenghts between 5 and 6 Å. Particularly, the first peak of the three is partly due to W-Zr-O, W-O-Zr and W-O-W multiple scattering, the second peak seem to arise mostly due to two W-W single scattering paths and numerous W-O-Zr, W-Zr-O, W-O-O-Zr and W-O-Zr-O multiple scattering paths appear to contribute over the whole 5-6 Å range.

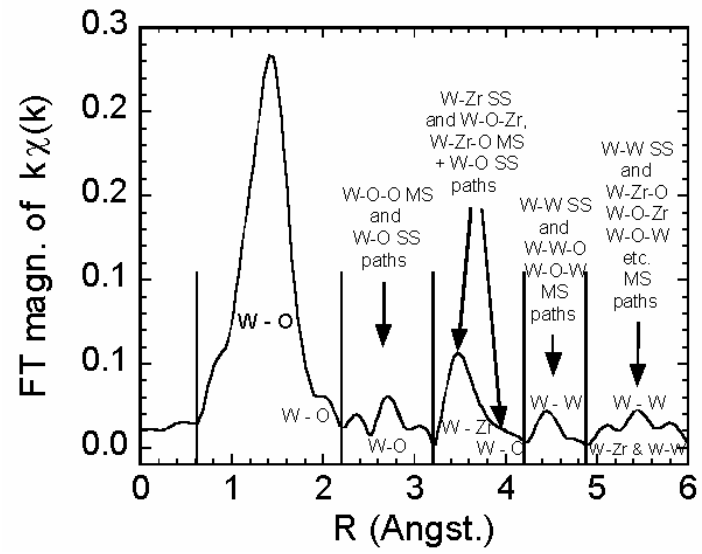

Figure 5.8: Contribution of the different metal-oxygen and metal-metal single (SS) and multiple scattering (MS) paths to the Fourier-transformed R-space spectrum of cubic ZrW_2O_8.

Looking at Figure 5.7 again, the first, largest peak (W-O) decreased dramatically in the amorphous material, but the multiple scattering contributions after the first peak in the 2.25-3.25 Å region are still visible and there are some weak peaks around the region where W-O single and multiple scattering contributions were noted for the cubic material. The peak between ~3 and 4 Å in the cubic material related to W-Zr paths seems to be washed out, and the same is true for the rest of the peaks at higher R. A detailed fit was carried out to the 65 K W L_{III}-edge data on the amorphous sample in the 3.5-15 $Å^{-1}$ k- and 0.9-4.4 Å R-range (no notable features are seen at R's greater than 4 Å) using a structural model derived from the known crystal structure of orthorhombic ZrW_2O_8. We used a similar structural model for fitting amorphous ZrW_2O_8 data in Chapter 4 (see section 4.2.6 and 4.3.1.4) as better fit results were obtained with it compared to the cubic model. In our model derived from the orthorhombic crystal structure, the scattering paths involving only W and O as well as W and Zr have approximately the same distances as in

the cubic model. However, the W-W scattering involves shorter scattering paths (~3.8-4.0 Å) than in the cubic model (~4.1-4.6 Å).

The goal of this EXAFS fitting was only qualitative: by comparing the fitting results and the FT magnitude for the amorphous sample, we tried to find out which types of scattering paths still contribute to the EXAFS of the amorphous sample. Therefore, no amplitude reduction factors, energy shifts, path distances and Debye-Waller factors are reported for the fits. We tried to fit the data for the amorphous sample by using W-O-, W-Zr- and W-W-containing scattering paths ("Full fit"), W-O- and W-W-containing paths ("No Zr"), W-O and W-Zr paths ("No W") and finally using only W-O paths ("No Zr, W"; see Figure 5.9). It is not possible to exclude the W-O single and multiple scattering paths as the largest peak between ~1 and 2 Å is still present in the amorphous sample. When all three groups were used, the fit described the data reasonably well. This suggests that the effect of W-Zr and/or W-W (single and multiple) scattering paths is not negligible in the amorphous sample, they have to be included in the fitting for a complete description. However, the fit was not significantly worse even when all metal-metal scattering paths were excluded. No difference was seen when only one of the metals were excluded ("No Zr" and "No W" plots). This suggests that the effect of metal-metal scattering has become largely suppressed and the EXAFS scattering of the amorphous material can be approximated by considering only W- and O- containing single and multiple scattering effects.

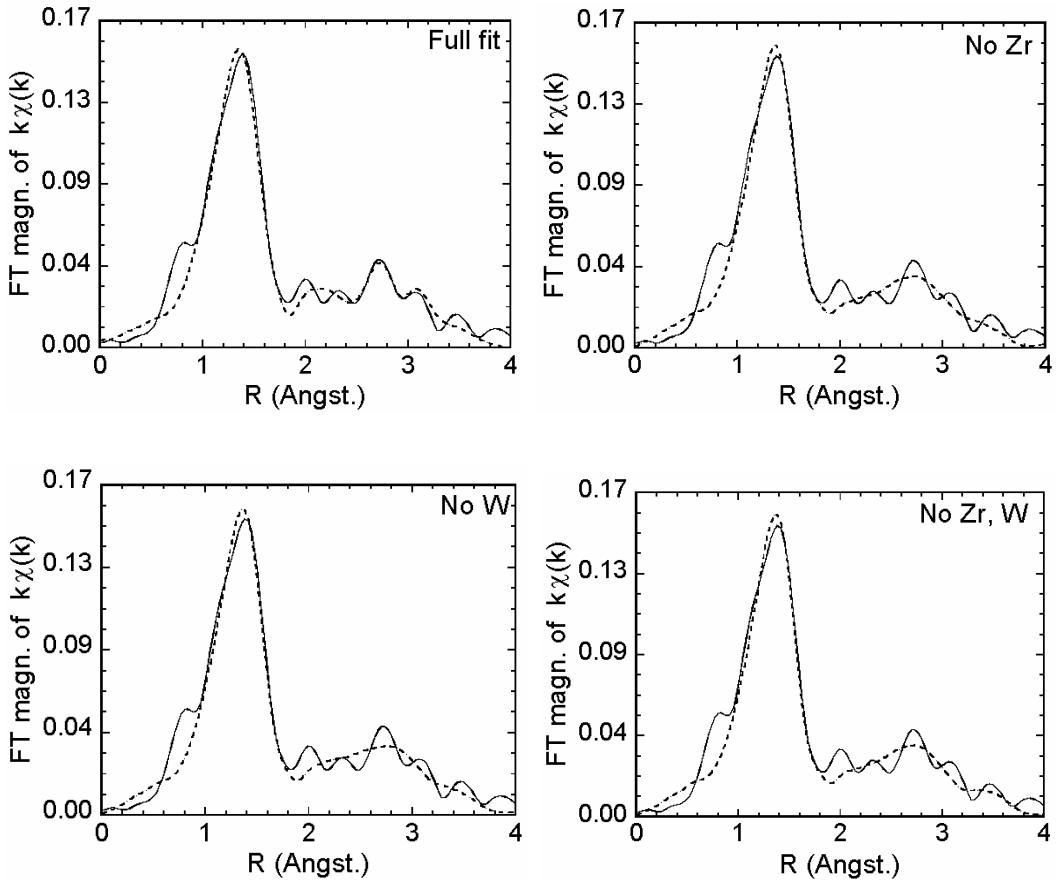

Figure 5.9: Results of EXAFS fitting for amorphous ZrW_2O_8 at the W L_{III}-edge at 65 K, considering contributions from different groups of scattering paths. Data: solid line, fit: dotted line.

The FT magnitude plots do not show a notable dependence on temperature, as expected based on the kχ(*k*)-k curves in Figure 5.6. Figure 5.10 is a comparison of the FT magnitude plots for cubic and amorphous ZrW_2O_8 at different temperatures

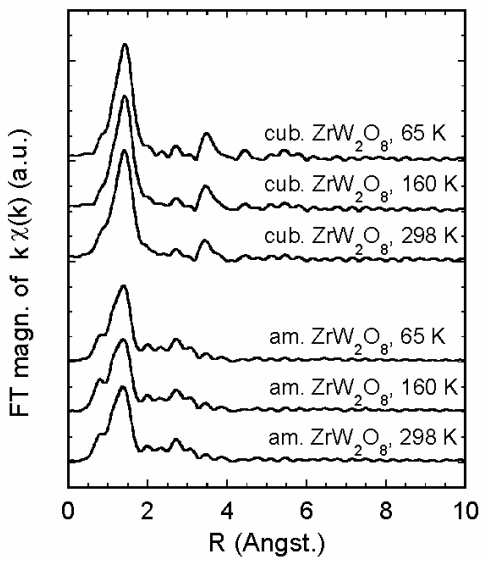

Figure 5.10: FT magnitude curves for cubic and amorphous ZrW_2O_8 at different temperatures.

In analyzing the EXAFS data collected for our set of reference compounds and the amorphous ZrW_2O_8 recovered from high pressure, very simple models were used. The models and the results from the fits are shown in Table 5.2. For all of the samples, fits were carried out using only scattering paths that contribute to the first (W-O) coordination shell and fits using an even simpler model consisting of a single W-O path (with a distance of 1.798 Å) with a multiplicity of both 4 and 6. Even though for samples with irregular coordination the fits are inevitably quite poor, this approach was adopted as, in general, the average M-O bond length for a coordination polyhedron increases as the coordination number of the metal increases. The average bond lengths were calculated as the sum of the starting path length value (1.798) and Δr from the fitting (values in the shaded cells of the table). The variation in the refined W-O distance from this analysis can be used as an indicator of the coordination environment for the tungsten. Average M-O distance has been used as a metric by others looking for changes in

coordination under pressure.[26, 27] More detail about this fitting procedure was given in section 5.2.4.

Table 5.2: Details of the EXAFS fits. The structural models that were used along with the resulting quality of fit indicator (*R*-factor), Debye-Waller factor (σ^2) and change in half-path length (Δr) are presented. Fixed values of S_0 and E_0 were used unless otherwise indicated: S_0: 0.74 (R-space), 0.80 (q-space); E_0: 7.38 eV (R-space), 7.94 eV (q-space). For all the fits a k-range of 3.5 – 15 $Å^{-1}$ and an R-range of 0.90-1.80 Å were employed. Values in the shaded cells were used to calculate the average W – O bond lengths shown in Table 5.3.

Sample	**Starting model / W-O path lengths (Å)**	**R space fit**		**q space fit**	
		4-coord.	**6-coord.**	**4-coord.**	**6-coord.**
$Na_2WO_4{\cdot}2H_2O$	1.775, 1.776, 1.781 x2 $\sigma^2 = 0.002$	*R*: 0.062 S_0: 0.74(10) E_0: 7.38 ± 4.24 Δr: 0.013(27)	-	*R*: 0.027 S_0: 0.80(8) E_0: 7.94 ± 2.87 Δr: 0.013(16)	-
$Na_2WO_4{\cdot}2H_2O$	1.798	*R*: 0.049 σ^2: 0.0006(11) Δr: -0.010(9)	*R*: 0.169 σ^2: 0.006(3) Δr: -0.003(17)	*R*: 0.018 σ^2: 0.001(1) Δr: -0.008(5)	*R*: 0.101 σ^2: 0.005(2) Δr: -0.005(12)
$Sc_2W_3O_{12}$	1.695 x2, 1.782 x2	*R*: 0.055 σ^2: -0.002(1) Δr: 0.037(9)	-	*R*: 0.019 σ^2: -0.0014(6) Δr: 0.039(5)	-
$Sc_2W_3O_{12}$	1.798	*R*: 0.054 σ^2: 0.0004(11) Δr: -0.021(9)	*R*: 0.170 σ^2: 0.005(3) Δr: -0.015(17)	*R*: 0.018 σ^2: 0.0007(6) Δr: -0.019(5)	*R*: 0.094 σ^2: 0.005(2) Δr: -0.016(12)
cubic ZrW_2O_8 @ RT	1.707, 1.798 x3	*R*: 0.084 σ^2: 0.0015(17) Δr: 0.009(12)	-	*R*: 0.030 σ^2: 0.002(1) Δr: 0.011(7)	-
cubic ZrW_2O_8	1.798	*R*: 0.082 σ^2: 0.003(2) Δr: -0.010(12)	*R*: 0.218 σ^2: 0.010(4) Δr: -0.002(22)	*R*: 0.031 σ^2: 0.003(1) Δr: -0.008(7)	*R*: 0.114 σ^2: 0.009(2) Δr: -0.005(14)
amorphous ZrW_2O_8 @ RT	cubic model, 1.707 x1, 1.798 x3	*R*: 0.195 σ^2: 0.007(3) Δr: 0.044(21)	-	*R*: 0.122 σ^2: 0.007(2) Δr: 0.037(15)	-
amorphous ZrW_2O_8 @ RT	orth. model, 1.712, 1.743: σ^2_1; 1.855, 1.870: σ^2_2; 2.300: σ^2_3, $\Delta r2$	*R*: 0.052 σ^2_1: 0.006(26) σ^2_2: 0.014(25) σ^2_3: -0.0016(15) $\Delta r1$: 0.060(34); $\Delta r2$: -0.077(120)		*R*: 0.016 σ^2_1: 0.001(1) σ^2_2: 0.009(13) σ^2_3: -0.002(7) $\Delta r1$: 0.053(28); $\Delta r2$: -0.113(85)	
amorphous ZrW_2O_8 @ RT	1.798	*R*: 0.190 σ^2: 0.009(3) Δr: 0.024(20)	*R*: 0.339 σ^2: 0.019(6) Δr: 0.042(33)	*R*: 0.118 σ^2: 0.009(2) Δr: 0.018(15)	*R*: 0.228 σ^2: 0.017(4) Δr: 0.028(23)

Table 5.2 (Continued)

Sample	Starting model / W-O path lengths (Å)	R space fit		q space fit	
		4-coord.	6-coord.	4-coord.	6-coord.
$(NH_4)_{10}W_{12}O_{41}$ ·$5H_2O$	1.721: σ^2_1; 1.813-2.302: σ^2_2 (6 paths)	-	*R*: 0.163 σ^2_1: -0.001(3) σ^2_2: 0.027(19) Δr: 0.064(28)	-	*R*: 0.075 σ^2_1: 0.096(680) σ^2_2: 0.007(3) Δr: -0.054(19)
$(NH_4)_{10}W_{12}O_{41}$ ·$5H_2O$	1.798	*R*: 0.278 σ^2: 0.015(5) Δr: 0.052(28)	*R*: 0.412 σ^2: 0.026(8) Δr: 0.073(43)	*R*: 0.128 σ^2: 0.014(3) Δr: 0.040(17)	*R*: 0.219 σ^2: 0.022(5) Δr: 0.051(25)
WO_3	1.841-2.017 (7 paths)	-	*R*: 0.257 σ^2: 0.009(4) Δr: -0.134(22)	-	*R*: 0.271 σ^2: 0.009(3) Δr: -0.146(23)
WO_3	1.798	*R*: 0.360 σ^2: 0.011(6) Δr: 0.042(32)	*R*: 0.481 σ^2: 0.023(9) Δr: 0.071(48)	*R*: 0.314 σ^2: 0.011(4) Δr: 0.026(26)	*R*: 0.430 σ^2: 0.021(7) Δr: 0.042(38)
Ba_2NiWO_6	1.992 x6	-	*R*: 0.041 σ^2: 0.002(1) Δr: -0.069(9)	-	*R*: 0.012 σ^2: 0.003(1) Δr: -0.067(5)
Ba_2NiWO_6	1.798	*R*: 0.090 σ^2: -0.001(2) Δr: 0.108(13)	*R*: 0.031 σ^2: 0.002(1) Δr: 0.113(8)	*R*: 0.055 σ^2: -0.001(1) Δr: 0.114(9)	*R*: 0.008 σ^2: 0.0021(5) Δr: 0.116(4)

In Table 5.3 we present the average W-O bond lengths from our fits. The derived average W – O bond lengths show the same increasing trend with coordination that we saw in Chapter 4 (see section 4.3.1.4) and consequently the same discussion applies. The average W-O distance in amorphous ZrW_2O_8 is closest to that in WO_3. This relationship can also be seen by visual inspection of the Fourier filtered EXAFS data (see Figure 5.7). The average W-O distance obtained for the amorphous ZrW_2O_8 sample, ~ 1.82 Å, is much shorter than that seen for the reference compound Ba_2NiWO_6, indicating that the coordination for tungsten in the amorphous sample is far from regular octahedral. However, it is close to the values obtained for WO_3 and ammonium paratungstate, suggesting that the average coordination in the amorphous material could be irregular/distorted 6-coordinate or perhaps five-coordinate. These results are consistent with the XANES data.

Table 5.3: The first-shell W – O average bond lengths obtained from room temperature EXAFS data for compounds with different W coordination. The fits were carried out in Fourier-filtered k-space using only 1 scattering path (k-range: 3.5 – 15 $Å^{-1}$, R-range: 0.90-1.80 Å).

Sample	**Average W-O bond length (Å)**	
	4-coord.	**6-coord.**
$Sc_2W_3O_{12}$ (tetrahedral)	1.779(5)	1.782(12)
Cubic ZrW_2O_8 (tetrahedral)	1.789(7)	1.792(14)
$Na_2WO_4 \cdot 2H_2O$ (tetrahedral)	1.790(5)	1.793(12)
Amorphous ZrW_2O_8	1.815(15)	1.825(23)
WO_3 (distort. octahedr.)	1.823(26)	1.839(38)
$(NH_4)_{10}W_{12}O_{41} \cdot 5H_2O$ (irregular 6-coord.)	1.838(17)	1.848(25)
Ba_2NiWO_6 (octahedral)	1.911(9)	1.914(4)

5.3.2 Mo K-edge data

5.3.2.1 Mo K-edge XANES

In Figure 5.11, Mo K-edge XANES spectra are shown for a series of model compounds containing molybdenum in different coordination environments and for amorphous $ZrMo_2O_8$. The XANES spectra of the compounds with tetrahedrally coordinated molybdenum, cubic $ZrMo_2O_8$, trigonal $ZrMo_2O_8$, $Na_2MoO_4 \cdot 2H_2O$ and $Sc_2Mo_3O_{12}$ show great similarities, they all have a pronounced pre-edge peak (slightly below 20 keV) consistent with a non-centrosymmetric coordination environment. This pre-edge feature is very weak for both MoO_3 and molybdenum oxide bis-acetylacetonate ($MoO_2(acac)_2$). The pre-edge peak for the amorphous sample is only a little smaller than for the tetrahedral compounds and the shape of the main edge differs slightly from that of the cubic material.

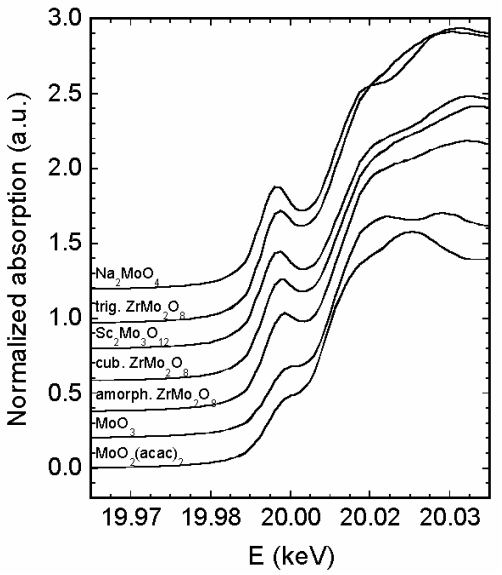

Figure 5.11: Mo K-edge XANES of compounds with different molybdenum-coordination including the amorphous sample.

5.3.2.2 Mo K-edge EXAFS

Room temperature $k\chi(k)$ curves are shown for samples with different Mo coordination and for the amorphous material in Figure 5.12. The overall picture is consistent with the XANES data. All tetrahedral compounds have very similar curves. The curves for the samples with distorted octahedral coordination are dramatically different from those for the tetrahedral ones. The amorphous sample has a very similar curve to that for the tetrahedral compounds and does not show any resemblance to the octahedral $k\chi(k)$'s. The only difference in the curve for the amorphous sample is that all the features in it are a bit weaker than in the curve for cubic $ZrMo_2O_8$. There does not appear to be a large shift from tetrahedral towards higher coordination on the amorphization of $ZrMo_2O_8$.

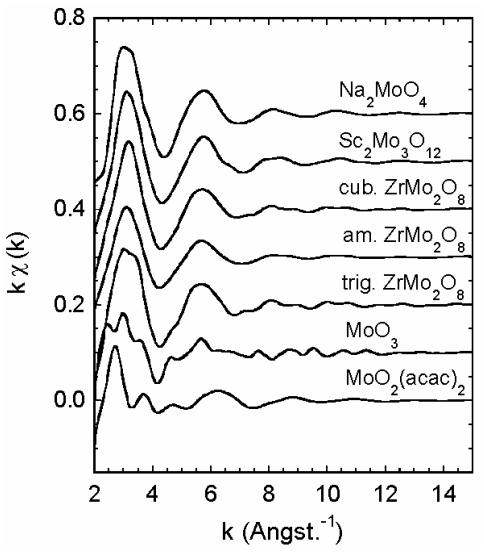

Figure 5.12: Mo K-edge$_I$ kχ(k)-k curves for compounds with different Mo-coordination along with that of the pre-amorphized $ZrMo_2O_8$ sample.

There are no large differencies between the kχ(k)-k curves at different temperatures (see Figure 5.13). However, the temperature dependence of the peak magnitudes seems to be slightly more significant here than in the case of ZrW_2O_8 (see Figure 5.6). Still, all the features are present at all temperatures. Another temperature dependence can be seen in Figure 5.13: the peaks for the cubic sample appear to shift towards smaller wavenumbers with increasing temperature. We are not sure whether this shift is real (could be an artifact of the measurement), but if it was, it could indicate a change in the crystal structure of cubic $ZrMo_2O_8$. Recently, by very precise measurements of the lattice constants of the material as a function of temperature, a subtle change from static to dynamic oxygen disorder has been detected on warming through 200 K.[28] This temperature falls in the region where we see a change, so our observation may be related to this phenomenon.

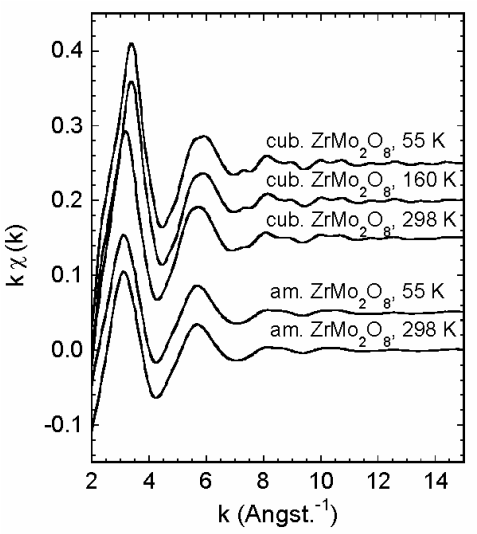

Figure 5.13: Mo K-edge kχ(*k*)-k curves for cubic and amorphous $ZrMo_2O_8$ at different temperatures.

The Fourier-transformed kχ(*k*) curves show that in the amorphous material, up to about 4 Å the same scattering contributions are present as in the cubic polymorph, only the amplitudes are reduced a bit. Above 4 Å, the peak that appears in cubic $ZrMo_2O_8$ is missing. This probably indicates a loss of well-defined Mo- to some other metal (Zr or Mo) correlations on amorphization (see Figure 5.14). In accordance with the dependence of the kχ(*k*) curves on local Mo coordination, the FT magnitudes for the compounds with distorted octahedral coordination is largely different from those for tetrahedral coordination and for the amorphous material.

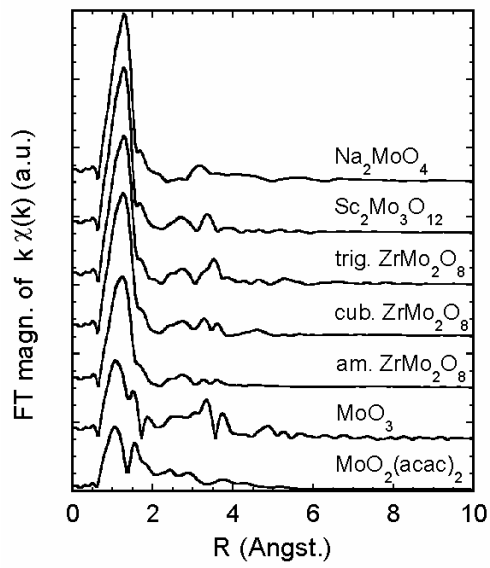

Figure 5.14: FT magnitudes for compounds with different Mo-coordination along with that of the amorphous $ZrMo_2O_8$ sample.

In order to know which scattering amplitudes made less of a contribution in the amorphous material, we have to look at the corresponding scattering effects in detail. Figure 5.16 illustrates which scattering paths contribute to the Fourier magnitude curve for cubic $ZrMo_2O_8$. The contributions were determined and are presented in a similar fashion as in section 5.3.1.2 for ZrW_2O_8. For a structural model, the ordered α-ZrW_2O_8 structure (space group $P2_13$)[9] with the W atoms replaced by Mo atoms was used for the FEFF calculation. Cubic $ZrMo_2O_8$ adopts the disordered β-ZrW_2O_8 structure (space group $Pa\bar{3}$), over its whole stability range,[8] but the use of the disordered structural model results in the generation unrealistic scattering path lengths upon running the FEFF calculation. Figure 5.15 shows our fit to the cubic $ZrMo_2O_8$ data and illustrates how well the scattering from cubic $ZrMo_2O_8$ can be described using a model based on the ordered ZrW_2O_8 structure. The fit was carried out over the k-range 2.5-15 $Å^{-1}$ and R-range 0.9-6.0 Å using basically all contributing scattering paths up to 6.4 Å path length. The 55 K Mo

K-edge data were used for the fit.

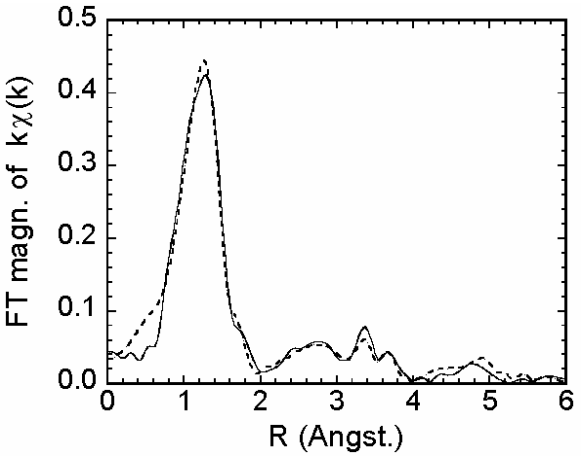

Figure 5.15: Agreement between data (solid line) and fit (dotted line) for the 55 K data for cubic $ZrMo_2O_8$ at the Mo K-edge using the structural model for α-ZrW_2O_8, and considering contributions from all important scattering paths in the 1-6 Å range.

Figure 5.16 gives the different scattering path types that are responsible for the EXAFS of cubic $ZrMo_2O_8$ in the 0-6 Å range. We divided the plot into four regions (1-4 in Figure 5.16). Again, we have to distinguish between the R-range corresponding to the regions on the plot and the true path lengths. The Mo-O single scattering paths that belong to the first region give rise to the first large peak between roughly 1 and 2 Å. These three paths are in the 1.7-2.4 Å range, just in the case of ZrW_2O_8. The scattering in region 2 (~2-3 Å) can be accounted for by several Mo-O-… multiple scattering paths with length in the 3.1-3.6 Å range as well as Mo-O single and multiple scattering paths with lengths between 3.9-4.1 Å. The latter paths contribute over a relatively wide range that includes region 3. The peak in the third region between ~3.2-3.6 Å arises as a result of Mo-Zr single and multiple scattering (distances 3.7-3.8 Å), while the second, smaller peak in the same region is mostly due to Mo-Mo single and multiple scattering with

lengths between 4.1 and 4.6 Å. In addition, several Mo-O single and multiple scattering paths contribute to regions 2 and 3 with scattering path lengths of 4.15-4.67 Å. The paths contributing to the fourth region are very diverse: a Mo-Zr-O multiple scattering path (5.4 Å length) can be associated with the largest peak, but it is combined with Mo-Mo single and multiple scattering effects (5.6-5.8 Å length). Numerous Mo-O-Zr multiple scattering paths (5.82-6.35 Å length) and two Mo-O-Mo paths (6.38-6.40 Å length) also contribute to the large R-range of ~3-5.5 Å covering regions 3 and 4.

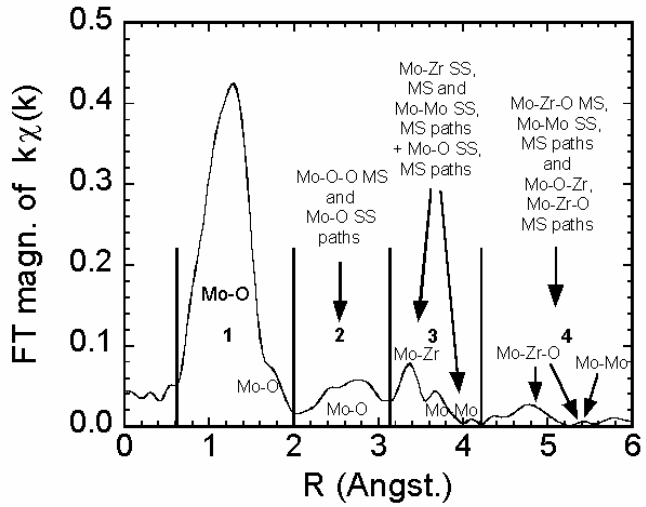

Figure 5.16: Contribution of the different metal-oxygen and metal-metal single (SS) and multiple scattering (MS) paths to the Fourier-transformed R-space spectrum of cubic $ZrMo_2O_8$.

In the light of the contributions from the different scattering paths, the changes that can be seen in Figure 5.14 are as follows: all peak amplitudes are reduced in the amorphous material relative to the cubic one, but this reduction is most significant for the metal-metal peaks, that is all scattering paths related to either Mo and Zr or Mo and Mo (and in addition, they may involve oxygen) are reduced (region 3). The scattering in region 4 seems to be washed out completely on amorphization. Detailed fitting of the

amorphous $ZrMo_2O_8$ data at the Mo K-edge was not carried out as for a good fit the same scattering contributions will still be needed as were used for the cubic sample.

The FT magnitude plots show a notable dependence on temperature, especially for the cubic material. All the peaks are noticeably more pronounced at 55 K (see Figure 5.17).

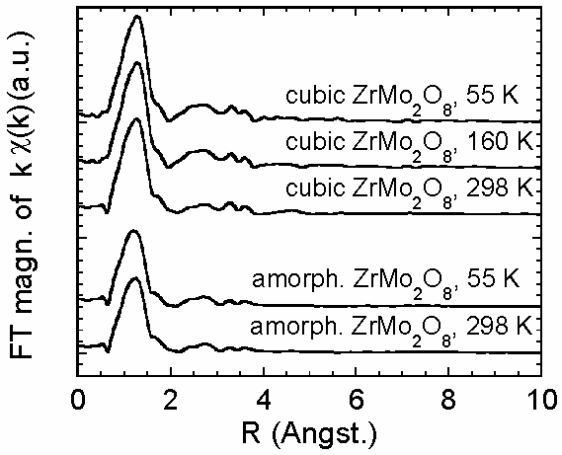

Figure 5.17: FT magnitude curves for cubic and amorphous $ZrMo_2O_8$ at different temperatures.

A similar EXAFS analysis procedure was performed for the Mo K-edge data as was for the W L_{III}-edge data in section 5.3.1.2. Data for the reference compounds and the amorphous $ZrMo_2O_8$ recovered from high pressure were fitted using very simple models. The models and the results from the fits are shown in Table 5.4. For all of the samples, fits were carried out using only scattering paths that contribute to the first (Mo-O) coordination shell as well as fits using an even simpler model consisting of a single Mo-O path (with a distance of 1.792 Å) with a degeneracy of both 4 and 6 (tetrahedral and octahedral extremes). The average bond lengths were calculated as the sum of the starting path length value (1.792) and Δr from the fitting (values in the shaded cells of the table

were used). The variation in the refined Mo-O distance from the analysis was used as an indicator of the Mo-coordination.

Table 5.4: Details of the EXAFS fits at the Mo K-edge. The structural models that were used along with the resulting quality of fit indicator (*R*-factor), Debye-Waller factor (σ^2) and change in half-path length (Δr) are presented. Fixed values of S_0 and E_0 were used unless otherwise indicated: S_0: 1.05 (R-space), 1.07 (q-space); E_0: 2.51 eV (R-space), 3.51 eV (q-space). For all the fits a k-range of 2.5 – 15 $Å^{-1}$ and an R-range of 0.9-2.0 Å were employed. Values in the shaded cells were used to calculate the average W – O bond lengths shown in Table 5.5.

Sample	Starting model / Mo - O path lengths (Å)	R space fit		Q space fit	
		4-coord.	6-coord.	4-coord.	6-coord.
$Na_2MoO_4.2H_2O$	1.753, 1.768, 1.781, 1.788 $\sigma^2 = 0.003$	*R*: 0.016 S_0: 1.05(6) E_0: 2.51 ± 1.48 Δr: -0.019(12)	-	*R*: 0.010 S_0: 1.07(5) E_0: 3.51 ± 1.22 Δr: -0.015(9)	-
$Na_2MoO_4.2H_2O$	1.792	*R*: 0.009 σ^2: 0.0018(5) Δr: -0.039(3)	*R*: 0.060 σ^2: 0.008(2) Δr: -0.030(10)	*R*: 0.003 σ^2: 0.0020(3) Δr: -0.033(2)	*R*: 0.050 σ^2: 0.008(1) Δr: -0.030(8)
$Sc_2Mo_3O_{12}$	1.752 x2, 1.758 x2	*R*: 0.010 σ^2: 0.0019(6) Δr: -0.004(4)	-	*R*: 0.004 σ^2: 0.0021(3) Δr: 0.000(2)	-
$Sc_2Mo_3O_{12}$	1.792	*R*: 0.009 σ^2: 0.0018(5) Δr: -0.043(3)	*R*: 0.074 σ^2: 0.008(2) Δr: -0.033(11)	*R*: 0.003 σ^2: 0.0021(3) Δr: -0.038(2)	*R*: 0.062 σ^2: 0.008(2) Δr: -0.034(9)
trigonal $ZrMo_2O_8$	1.690, 1.762, 1.763, 1.767	*R*: 0.008 σ^2: 0.0019(5) Δr: 0.014(3)	-	*R*: 0.004 σ^2: 0.0022(3) Δr: 0.019(2)	-
trigonal $ZrMo_2O_8$	1.792	*R*: 0.009 σ^2: 0.0031(6) Δr: -0.031(4)	*R*: 0.065 σ^2: 0.010(2) Δr: -0.020(10)	*R*: 0.005 σ^2: 0.0034(4) Δr: -0.026(3)	*R*: 0.057 σ^2: 0.010(2) Δr: -0.022(9)
cubic $ZrMo_2O_8$ @ RT	1.702 x1, 1.792 x3	*R*: 0.011 σ^2: 0.002(1) Δr: -0.015(4)	-	*R*: 0.004 σ^2: 0.0025(4) Δr: -0.009(2)	-
cubic $ZrMo_2O_8$ @ RT	1.792	*R*: 0.011 σ^2: 0.0038(7) Δr: -0.035(4)	*R*: 0.063 σ^2: 0.011(2) Δr: -0.024(10)	*R*: 0.005 σ^2: 0.0041(4) Δr: -0.029(3)	*R*: 0.043 σ^2: 0.011(2) Δr: -0.025(8)
amorphous $ZrMo_2O_8$ @ RT	cubic model, 1.702 x1, 1.792 x3	*R*: 0.034 σ^2: 0.006(1) Δr: -0.004(7)	-	*R*: 0.030 σ^2: 0.007(1) Δr: -0.003(7)	-
amorphous $ZrMo_2O_8$ @ RT	trigonal model, 1.690, 1.762, 1.763, 1.767	*R*: 0.031 σ^2: 0.007(1) Δr: 0.020(7)	-	*R*: 0.027 σ^2: 0.007(1) Δr: 0.021(6)	-
amorphous $ZrMo_2O_8$ @ RT	mon. model, 1.679 (σ^2), 1.760,1.862 x2 (σ_2^2)	*R*: 0.009 σ^2: 0.22 ± 2.59 σ_2^2: 0.0009(7) Δr: -0.075(4)	-	*R*: 0.009 σ^2: 0.57± 7088 σ_2^2: 0.0015(6) Δr: -0.070(4)	-

Table 5.4 (Continued)

Sample	Starting model / Mo - O path lengths (Å)	R space fit		Q space fit	
		4-coord.	6-coord.	4-coord.	6-coord.
amorphous $ZrMo_2O_8$ @ RT	1.792	*R*: 0.032 σ^2: 0.008(1) Δr: -0.025(7)	*R*: 0.118 σ^2: 0.018(3) Δr: -0.009(15)	*R*: 0.029 σ^2: 0.008(1) Δr: -0.023(7)	*R*: 0.099 σ^2: 0.017(3) Δr: -0.016(14)
MoO_3	1.553 x4 (σ^2), 1.786 x2 (σ_2^2)	-	*R*: 0.049 σ^2: 0.010(2) σ_2^2: 0.003(2) Δr: 0.156(10)	-	*R*: 0.134 σ^2: 0.010(3) σ_2^2: 0.003(3) Δr: 0.152(16)
MoO_3	1.792	*R*: 0.136 σ^2: 0.020(4) Δr: 0.020(19)	*R*: 0.139 σ^2: 0.030(5) Δr: 0.038(19)	*R*: 0.228 σ^2: 0.024(5) Δr: 0.023(26)	*R*: 0.243 σ^2: 0.034(6) Δr: 0.033(28)
$MoO_2(acac)_2$	1.633 x3 (σ^2), 1.703, 1.943, 1.987 (σ_2^2)	-	*R*: 0.153 σ^2: 0.011(3) σ_2^2: 0.000(3) Δr: 0.062(16)	-	*R*: 0.252 σ^2: 0.013(4) σ_2^2: 0.0006(24) Δr: 0.064(21)
$MoO_2(acac)_2$	1.792	*R*: 0.658 σ^2: 0.041(22) Δr: 0.039(87)	*R*: 0.621 σ^2: 0.051(21) Δr: 0.064(79)	*R*: 0.864 σ^2: 0.059(50) Δr: 0.119(195)	*R*: 0.834 σ^2: 0.067(44) Δr: 0.126(166)

In Table 5.5 we present the average Mo-O bond lengths from our fits. The derived average Mo – O bond lengths show an increasing trend with coordination similar to that seen for the tungsten compounds at the W L_{III}-edge. The average Mo-O distance in amorphous $ZrMo_2O_8$ is only marginally greater than in the cubic material. Within the error limits on the values, they are basically equivalent. This suggests that the average Mo coordination in the amorphous material is very close to, or is still, tetrahedral. Unfortunately, there is a very large error associated with the refined Mo-O distances for $MoO_2(acac)_2$. This may be due to the large difference between the half path length value (1.792) chosen by us and the actual half path length calculated by the FEFF program for two of the six paths responsible for the first-shell peak (1.633 and 1.703) in this material. It may also reflect that there are a wide variety of Mo-O distances in the compound. These results are consistent with the XANES data and the Fourier filtered EXAFS data (see Figures 5.11 and 5.14).

Table 5.5: First-shell average Mo – O bond lengths obtained from room temperature EXAFS data for compounds with different Mo coordination. The fits were carried out in Fourier-filtered k-space using only 1 scattering path (k-range: 2.5 – 15 $Å^{-1}$, R-range: 0.9-2.0 Å).

Sample	**Average Mo-O bond length (Å)**	
	4-coord.	**6-coord.**
$Sc_2Mo_3O_{12}$ (tetrahedral)	1.753(2)	1.757(9)
$Na_2MoO_4 \cdot 2H_2O$ (tetrahedral)	1.758(2)	1.762(8)
Cubic $ZrMo_2O_8$ (tetrahedral)	1.762(3)	1.766(8)
Trigonal $ZrMo_2O_8$ (tetrahedral)	1.766(3)	1.770(9)
Amorphous $ZrMo_2O_8$	1.768(7)	1.776(14)
MoO_3 (distort. octahedr.)	1.815(26)	1.824(28)
$MoO_2(acac)_2$ (octahedral)	1.911(195)	1.918(166)

5.3.3 Zr K-edge data

5.3.3.1 Zr K-edge XANES

XANES spectroscopy at the Zr K-edge has been used before for qualitative comparison of species with different Zr coordination environments.[29, 30] The XANES indicate a change in Zr coordination on amorphization for both ZrW_2O_8 and $ZrMo_2O_8$ (see Figure 5.18). By visual examination of the absorption edges, an average coordination of ~7 could be estimated in both amorphous materials based on the great resemblance of their edge features to that of ZrO_2, which contains Zr in 7 coordination.[6] The difference between 6 (the cubic tungstate and molybdate), 7 (ZrO_2) and 8 ($ZrSiO_4$)[7] coordination is clearly distinguishable.

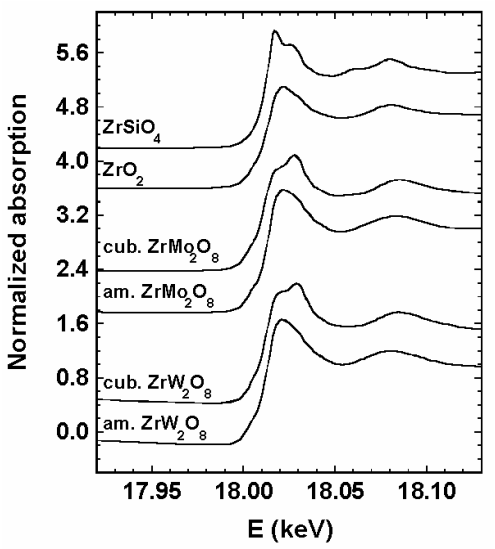

Figure 5.18: Zr K-edge XANES spectra for cubic and amorphous ZrW_2O_8 and $ZrMo_2O_8$ containing 6-coordinate Zr along with two reference compounds with 7 (ZrO_2) and 8 ($ZrSiO_4$) Zr coordination.

5.3.3.2 Zr K-edge EXAFS

The kχ(k)-k curves shown in Figure 5.19 are consistent with the XANES spectra. Both cubic-amorphous sample pairs show the same change in the shape of the first peak. The curves for the amorphous samples are very similar to that of ZrO_2 suggesting that their average coordination number may also be about 7.

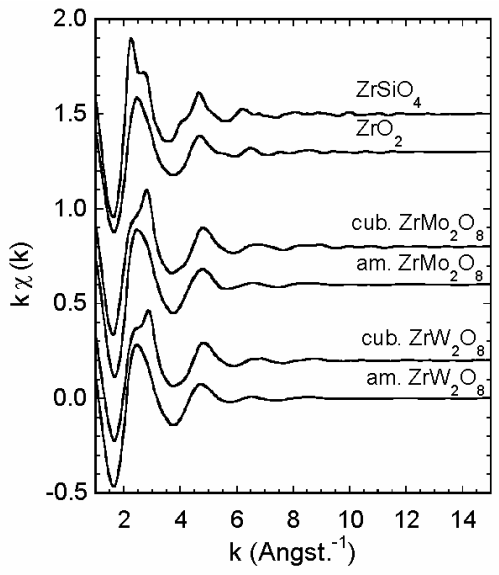

Figure 5.19: Zr K-edge kχ(k)-k curves for cubic and amorphous ZrW_2O_8 and $ZrMo_2O_8$, resp., along with two reference compounds with 7 and 8 Zr coordination.

The Fourier transformed kχ(k) curves (FT magnitudes) for the two model compounds and for cubic and amorphous ZrW_2O_8 and $ZrMo_2O_8$ are shown in Figure 5.20. There are dramatic changes in the Zr coordination environment in both ZrW_2O_8 and $ZrMo_2O_8$ on amorphization.

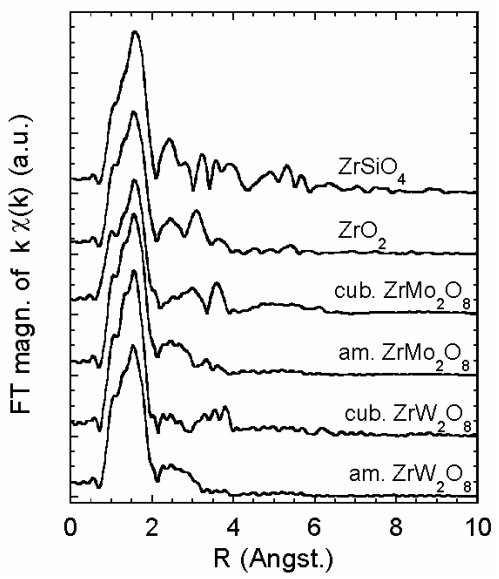

Figure 5.20: FT magnitudes for cubic and amorphous ZrW_2O_8 and $ZrMo_2O_8$, resp., along with two reference compounds with 7 (ZrO_2) and 8 ($ZrSiO_4$) coordination.

In order to verify what changes this involves, let us examine the scattering path contributions responsible for the features of the FT magnitude curves. The scattering contributions in both cubic ZrW_2O_8 and $ZrMo_2O_8$ were examined in great detail for the data obtained at the corresponding absorption edges. As we look at the exact same structures, only from the Zr's point of view this time, instead of listing all of the scattering paths that make up the EXAFS, let us focus on the major contributions. The most important scattering effects are shown for both cubic ZrW_2O_8 and $ZrMo_2O_8$ at the Zr K-edge in Figure 5.21. There are three main groups of scattering contributions in each case: the single Zr-O scattering that contributes to the first peak, the multiple and single Zr-O scattering that contributes to the second feature, and the metal-metal single and multiple scattering responsible for the feature (or group of features) in the graphs.

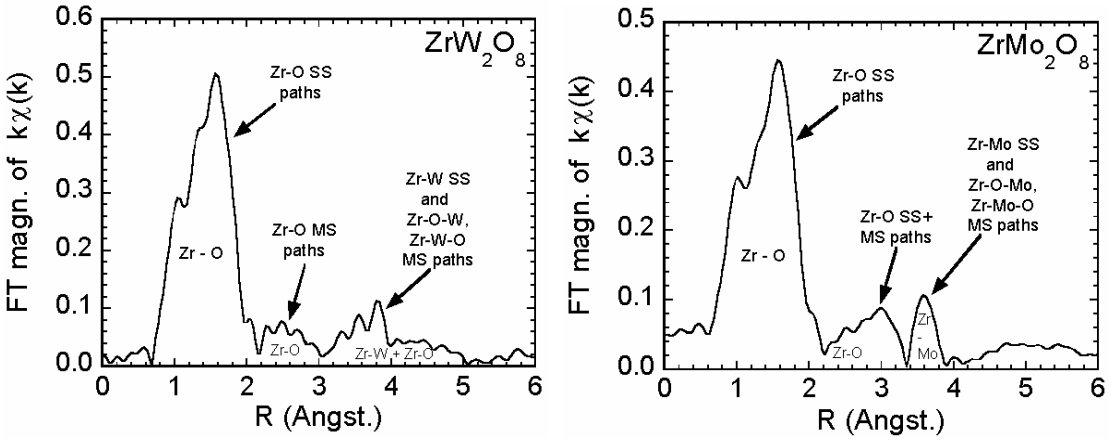

Figure 5.21: Contribution of the different metal-oxygen and metal-metal single (SS) and multiple scattering (MS) paths to the FT magnitude spectrum of cubic ZrW_2O_8 (left) and cubic $ZrMo_2O_8$.

Based on Figure 5.20, we can say that the metal-metal peaks in amorphous ZrW_2O_8 that can be seen in the cubic material between 3-4 Å are almost completely washed out and the scattering can basically be described by using only Zr – O paths. As proof, see Figure 5.22, which shows that the FT magnitude of amorphous ZrW_2O_8 can be very well modeled using only Zr-O (single and multiple) scattering paths in the fit. The fit was carried out in the k-range of 2.5 – 15 $Å^{-1}$ and an R-range of 1-4.1 Å using Zr-O scattering paths with path lengths in the 2.042-4.151 Å range. This fit suggests that there is practically no Zr-W or Zr-Zr interference in amorphous ZrW_2O_8. (The latter one is rather insignificant even in the cubic materials and thus not shown in Figure 5.21.) This, in turn means that the weak peaks we see in the 3-4 Å region of the FT magnitude plot of the material at the W L_{III}-edge (Figure 5.7) are probably due to W-W scattering in addition to the obvious W-O scattering. This was not clear from the fits presented in Figure 5.9, which seemed insensitive to which metal-metal scattering we include in the fit in addition to the W-O paths.

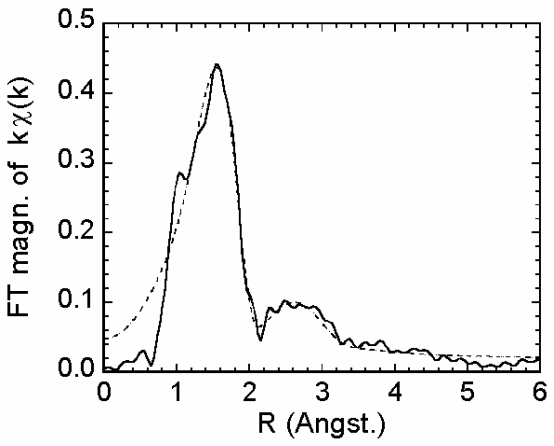

Figure 5.22: EXAFS fit to the data on amorphous ZrW_2O_8 collected at the Zr K-edge indicating that the structure can be quite well modeled using only Zr-O scattering paths in the fit. The solid line is the data, and the dotted line is the fit.

There seems to be some residual in amorphous $ZrMo_2O_8$ of the metal-metal scattering that occur between 3-4 Å in the cubic material. Still, the dramatic reduction of the large magnitude Zr-Mo peaks suggests a significant change in the Zr coordination environment within the material, quite in contrast to the very little change in the Mo-coordination. The fact that the metal-metal scattering still contributes to the scattering in amorphous $ZrMo_2O_8$ is also supported by the fit shown in Figure 5.23. The fit is not as good as in the case of ZrW_2O_8 (see Figure 5.22), because the residual peaks from the metal-metal scattering between 3 and 4 Å are not fully accounted for.

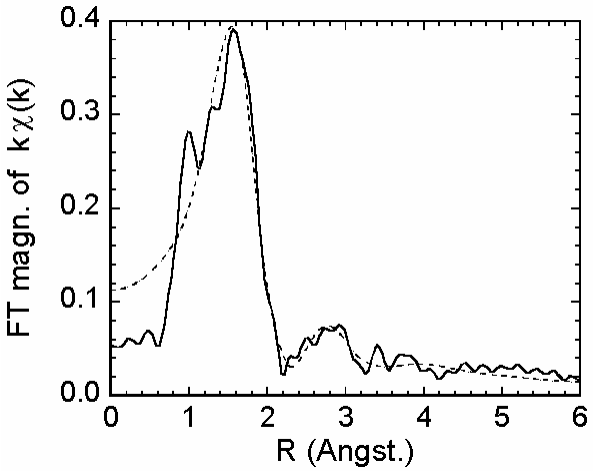

Figure 5.23: EXAFS fit to the data on amorphous $ZrMo_2O_8$ collected at the Zr K-edge, indicating that the structure can be approximately modeled using only Zr-O scattering paths in the fit, but there remain some metal-metal scattering not accounted for. The solid line is the data, and the dotted line is the fit.

An EXAFS analysis similar to the Mo K-edge and W L_{III}-edge case was carried out. Data for the reference compounds and the amorphous samples recovered from high pressure were fitted using very simple models. The models and the results from the fits are shown in Table 5.6. For all of the samples, fits were carried out using only scattering paths that contribute to the first (Zr-O) coordination shell as well as fits using an even simpler model consisting of a single Zr-O path (with a distance of 2.102 Å) with a degeneracy of both 6 and 8. The average bond lengths were calculated as the sum of the starting path length value (2.102) and Δr from the fitting (values in the shaded cells of the table were used). The variation in the refined Zr-O distance from the analysis was used as an indicator of the Zr-coordination.

Table 5.6: Details of the EXAFS fits at the Zr K-edge. The structural models that were used along with the resulting quality of fit indicator (*R*-factor), Debye-Waller factor (σ^2) and change in half-path length (Δr) are presented. Fixed values of S_0 and E_0 were used unless otherwise indicated: S_0: 1.34 (R-space), 1.28 (q-space); E_0: 5.61 eV (R-space), 7.45 eV (q-space). For all the fits a k-range of 2.9 – 15 $Å^{-1}$ and an R-range of 0.90-2.25 Å were employed. Values in the shaded cells were used to calculate the average W – O bond lengths shown in Table 5.7.

Sample	**Starting model / W-O path lengths (Å)**	**R space fit**		**q space fit**	
		6-coord.	**8-coord.**	**6-coord.**	**8-coord.**
ZrO_2	2.051 - 2.285; σ^2 =0.008	*R*: 0.035 S_0: 1.34(10) E_0: 5.61(147) Δr: -0.055(21)		*R*: 0.032 S_0: 1.28(10) E_0: 7.45(163) Δr: -0.037(21)	
ZrO_2	2.102	*R*: 0.060 σ^2: 0.011(2) Δr: -0.026(10)	*R*: 0.045 σ^2: 0.016(2) Δr: -0.022(9)	*R*: 0.047 σ^2: 0.010(2) Δr: -0.002(8)	*R*: 0.038 σ^2: 0.015(2) Δr: 0.000(8)
$ZrSiO_4$	2.130 x4, 2.267 x4	-	*R*: 0.043 σ^2: 0.008(2) Δr: -0.059(9)	-	*R*: 0.043 σ^2: 0.007(2) Δr: -0.042(8)
$ZrSiO_4$	2.102	*R*: 0.068 σ^2: 0.008(2) Δr: 0.016(11)	*R*: 0.052 σ^2: 0.013(2) Δr: 0.020(10)	*R*: 0.060 σ^2: 0.007(2) Δr: 0.039(9)	*R*: 0.051 σ^2: 0.012(2) Δr: 0.040(9)
cubic ZrW_2O_8 @ RT	2.042 x3, 2.108 x3	*R*: 0.048 σ^2: 0.006(2) Δr: -0.031(9)	-	*R*: 0.042 σ^2: 0.005(1) Δr: -0.019(7)	-
cubic ZrW_2O_8 @ RT	2.102	*R*: 0.057 σ^2: 0.007(2) Δr: -0.067(9)	*R*: 0.050 σ^2: 0.013(2) Δr: -0.064(9)	*R*: 0.042 σ^2: 0.006(1) Δr: -0.046(8)	*R*: 0.037 σ^2: 0.011(1) Δr: -0.045(7)
amorphous ZrW_2O_8 @ RT	cubic model, 2.042 x3, 2.108 x3	*R*: 0.428 σ^2: 0.011(8) Δr: 0.250(38)	-	*R*: 0.322 σ^2: 0.012(5) Δr: 0.241(28)	-
amorphous ZrW_2O_8 @ RT	orth. Model, 1.953, 2.030, 2.055, 2.074, 2.125, 2.150	*R*: 0.051 σ^2: 0.005(2) Δr: 0.009(10)	-	*R*: 0.032 σ^2: 0.005(1) Δr: 0.031(7)	-
amorphous ZrW_2O_8 @ RT	2.102	*R*: 0.055 σ^2: 0.010(2) Δr: -0.024(10)	*R*: 0.036 σ^2: 0.015(2) Δr: -0.019(8)	*R*: 0.043 σ^2: 0.009(1) Δr: -0.010(8)	*R*: 0.031 σ^2: 0.014(1) Δr: -0.008(7)
cubic $ZrMo_2O_8$ @ RT	2.035 x3, 2.102 x3	*R*: 0.043 σ^2: 0.005(1) Δr: -0.026(8)	-	*R*: 0.028 σ^2: 0.004(1) Δr: -0.006(6)	-
cubic $ZrMo_2O_8$ @ RT	2.102	*R*: 0.042 σ^2: 0.006(1) Δr: -0.058(8)	*R*: 0.038 σ^2: 0.011(1) Δr: -0.054(7)	*R*: 0.027 σ^2: 0.005(1) Δr: -0.039(6)	*R*: 0.027 σ^2: 0.010(1) Δr: -0.037(6)
amorphous $ZrMo_2O_8$ @ RT	cubic model, 2.035 x3, 2.102 x3	*R*: 0.073 σ^2: 0.007(2) Δr: -0.005(12)	-	*R*: 0.052 σ^2: 0.007(2) Δr: 0.021(9)	-
amorphous $ZrMo_2O_8$ @ RT	2.102	*R*: 0.072 σ^2: 0.009(2) Δr: -0.037(11)	*R*: 0.045 σ^2: 0.014(2) Δr: -0.033(9)	*R*: 0.051 σ^2: 0.008(2) Δr: -0.012(9)	*R*: 0.033 σ^2: 0.013(1) Δr: -0.010(7)

The derived average Zr – O bond lengths show an increasing trend with coordination. As the average Zr-O distance in both amorphous materials is close to the value obtained for ZrO_2, we presume that the average Zr-coordination changed from 6 to around 7 as the materials went from cubic to amorphous on compression. These data are in accordance with the XANES results (see Figure 5.18).

Table 5.7: First-shell average Zr – O bond lengths obtained from room temperature EXAFS data for cubic and amorphous ZrW_2O_8 and $ZrMo_2O_8$, resp., along with two reference compounds with 7 (ZrO_2) and 8 ($ZrSiO_4$) coordination. The fits were carried out in Fourier-filtered k-space using only 1 scattering path (k-range: 2.9 – 15 $Å^{-1}$, R-range: 0.90-2.25 Å).

Sample	**Average Zr-O bond length (Å)**	
	6-coord.	**8-coord.**
Cubic ZrW_2O_8 (tetrahedral)	2.056(8)	2.057(7)
Cubic $ZrMo_2O_8$ (tetrahedral)	2.063(6)	2.065(6)
Amorphous ZrW_2O_8	2.092(8)	2.094(7)
Amorphous $ZrMo_2O_8$	2.090(9)	2.092(7)
ZrO_2 (7-coordinate)	2.100(8)	2.101(8)
$ZrSiO_4$ (8-coordinate)	2.140(9)	2.142(9)

5.4 Discussion

Our W L_{III}-edge XAS results on amorphous ZrW_2O_8 that had been amorphized in a multi-anvil press and recovered from 7.5 GPa pressure to ambient conditions are in agreement with the ex-situ and in-situ results for ZrW_2O_8 reported in Chapter 4. Both the W L_I-edge XANES and the W L_{III}-edge EXAFS data are inconsistent with a view of the pressure-induced amorphization as a result of polyhedral tilting because the WO_4

polyhedra become distorted on amorphization, which is manifested in an increase of the average W-O bond length and thus the average coordination of tungsten. As the tungsten coordination environment in the amorphous material is apparently different from that in WO_3, a kinetically hindered pressure-induced decomposition is not a very likely driving force for the amorphization. However, a kinetically frustrated decomposition could be imagined as mechanism if we view the W coordination in the amorphous material as a distorted version of that of WO_3 on a pathway to demixing. Comparison of the Fourier-transformed EXAFS data for the amorphous material with that of cubic ZrW_2O_8 revealed that the metal-metal scattering contributions, although some were still present, became much less important relative to the scattering along paths containing only W and O. Although the metal-metal paths had to be included in the fitting in order to better describe the scattering from the amorphous material, it was possible to fit the EXAFS of the material reasonably well using only W-O scattering. From the W L_{III}-edge EXAFS it was not clear whether the W-Zr or the W-W scattering is more important in the amorphous material, probably because their importance was rather low compared to W-O scattering and their calculated scattering path lengths are close to one another in the model used. The Zr K-edge XAS results indicated a distortion of the ZrO_6 octahedra, which further supports the invalidity of a simple polyhedral tilting model for the amorphization. The increase in the coordination number of Zr from 6 to ~7 does not exclude a kinetically frustrated decomposition as mechanism, given that the Zr in ZrO_2 is 7-coordinated.[6] The results for ZrW_2O_8 may be compatible with the highly irregular 6+1 coordination reported for the metals in the α-U_3O_8-type ZrW_2O_8 mentioned in section 5.1,[2] as the amorphous material may be viewed as an intermediate on a pathway to that high-pressure

phase with higher coordination. The Zr K-edge EXAFS provided useful insight into which metal-metal peaks might still be present in the EXAFS of the amorphous material. As practically no metal-metal scattering was needed to adequately fit the Zr K-edge EXAFS for amorphous ZrW_2O_8, we believe that the metal-metal contribution to the more significant W-O scattering in the material is W-W scattering (single and multiple paths). This means that the distribution of Zr-W distances became large on the loss of long-range order, but the distribution of W-W distances is not so large.

The Mo K-edge XAS results on amorphous $ZrMo_2O_8$ amorphized in a multi-anvil apparatus at 5 GPa and recovered to ambient conditions are in agreement with the high-pressure *in-situ* and *ex-situ* results for $ZrMo_2O_8$ discussed in Chapter 4. The behavior of cubic $ZrMo_2O_8$ on amorphization is clearly different from that of ZrW_2O_8. The Mo K-edge XANES and EXAFS demonstrate that the pressure-induced amorphization of cubic $ZrMo_2O_8$ is not accompanied by any dramatic changes in the molybdenum coordination on amorphization. There are few signs of the tetrahedral coordination shifting to a higher average coordination, including a marginal increase in the average Mo-O bond length (the values actually agree with the cubic bond length within error) and the suppression of the metal-metal scattering contributions to the EXAFS spectrum of the amorphous material. This suppression of the metal-metal scattering contribution is evidently smaller than in amorphous ZrW_2O_8, resulting in worse fitting results when we tried to use only Mo-O scattering contributions in the fit. The Zr K-edge data revealed that the average Zr coordination increases from 6 to approximately 7, similarly to the case of ZrW_2O_8. This suggests that the ZrO_6 octahedra distort more easily, that is expectedly at lower pressure, than the MoO_4. This observation is in agreement with an earlier proposition by Pryde *et*

al.,[1] who predicted for cubic ZrW_2O_8 that the ZrO_6 octahedra were more liable to distort than the WO_4 tetrahedra, and thus major coordination changes involving the zirconium were more likely than those involving tungsten. This raises an interesting point: as the pressure employed by us to amorphize cubic $ZrMo_2O_8$ (5 GPa) was lower than that used to amorphize ZrW_2O_8 (7.5 GPa), could the difference be only due to the different synthesis pressures? Could higher coordination be achieved in amorphous $ZrMo_2O_8$ using pressures higher than 5 GPa? We do not know, but in the sense the amorphization pressures were similar in both cases: they were chosen so that we were above the pressure of the amorhization for both ZrW_2O_8 (reported amorphization range 2.3-7.6 GPa)[31] and $ZrMo_2O_8$ (1.7-4.1 GPa range).[32] Although the increase in the Zr coordination might support a possible mechanism involving a kinetically hindered decomposition, the fact that the Mo coordination in amorphous $ZrMo_2O_8$ is very far from anything that shows resemblance to centrosymmetric, the pressure-induced amorphous material can not be considered as an intermediate along the pathway towards decomposition into its binary oxides. Based on the results of the present Chapter and of Chapter 4, the amorphous $ZrMo_2O_8$ might best be viewed as a metastable intermediate on the pathway to another crystalline zirconium molybdate.

5.5 Conclusions

The amorphization behavior of cubic ZrW_2O_8 and cubic $ZrMo_2O_8$ is different from one another. While pressure-induced amorphization is accompanied by a significant increase in the average tungsten coordination in the tungstate, the average molybdenum coordination in $ZrMo_2O_8$ barely changes. All the scattering paths in the amorphous

materials have smaller amplitudes, but the metal-metal correlations are relatively much less pronounced, especially the W-Zr ones in amorphous ZrW_2O_8, relative to the cubic polymorphs. The Zr K-edge data added useful information to our picture of the pressure-induced amorphization in the two materials. It revealed that the Zr coordination increases in both materials on amorphization indicating a distortion of the ZrO_6 octahedra. This, based on the results on amorphous $ZrMo_2O_8$, where the MoO_4 tetrahedra remained relatively undistorted, seems to happen independently of the extent of distortion of the tetrahedral units suggesting that the ZrO_6 octahedra are more prone to distortion on compression. These results are in accordance with our *in-situ* and *ex-situ* results discussed in Chapter 4. A mechanism for the pressure-induced amorphization involving a kinetically frustrated phase transformation to a high-pressure phase with higher metal coordination numbers seems to be the likely driving force. However, a kinetically hindered pressure-induced decomposition can not be ruled out completely given the observed increases in metal coordination.

5.6 References

[1] A. K. A. Pryde, M. T. Dove, and V. Heine: Simulation studies of ZrW_2O_8 at high pressure. *J. Phys.: Condens. Matter* **10**, 8417 (1998).

[2] A. Grzechnik, W. A. Crichton, K. Syassen, et al.: A New Polymorph of ZrW_2O_8 Synthesized at High Pressures and High Temperatures. *Chem. Mater.* **13**, 4255 (2001).

[3] B. Ravel, ATHENA - EXAFS Data Processing, computer code Athena, Naval Research Laboratory, Washington, D.C. (2005).

[4] M. Newville: Interactive XAFS analysis and FEFF fitting. *J. Synchrotron Radiat.* **8**, 322 (2001).

[5] B. Ravel, ARTEMIS - EXAFS Data Analysis, computer code Artemis, Naval Research Laboratory, Washington, D.C., WA (2005).

[6] D. K. Smith and H. W. Newkirk: The Crystal Structure of Baddeleyite (Monoclinic ZrO_2) and its Relation to the Polymorphism of ZrO_2. *Acta Crystallogr.* **18**, 983 (1965).

[7] R. M. Hazen and L. W. Finger: Crystal structure and compressibility of zircon at high pressure. *Am. Mineral.* **64**, 196 (1979).

[8] C. Lind, A. P. Wilkinson, Z. Hu, et al.: Synthesis and Properties of the Negative Thermal Expansion Material Cubic Zirconium Molybdate. *Chem. Mater.* **10**, 2335 (1998).

[9] T. A. Mary, J. S. O. Evans, T. Vogt, et al.: Negative Thermal Expansion from 0.3 to 1050 Kelvin in ZrW_2O_8. *Science* **272**, 90 (1996).

[10] J. S. O. Evans, T. A. Mary, and A. W. Sleight: Negative Thermal Expansion in $Sc_2(WO_4)_3$. *J. Solid State Chem.* **137**, 148 (1998).

[11] K. Okada, H. Morikawa, F. Marumo, et al.: Crystal structure of $Na_2WO_4.2H_2O$. *Bull. Tokyo Inst. Technol.*, 7 (1974).

[12] D. E. Cox, G. Shirane, and B. C. Frazer: Neutron-Diffraction Study of Antiferrromagnetic Ba_2CoWO_6 and Ba_2NiWO_6. *J. Appl. Phys.* **38**, 1459 (1967).

[13] P. M. Woodward, A. W. Sleight, and T. Vogt: Structure refinement of triclinic tungsten trioxide. *J. Phys. Chem. Solids* **56**, 1305 (1995).

[14] v. H. D'Amour and R. Allman: Die Kristallstruktur des Ammoniumparawulframat-tetrahydrats. *Z. Kristallogr.* **136**, 23 (1972).

[15] V. N. Serezhkin, V. A. Efremov, and V. K. Trunov: The Crystal Structure of α-$Zr(MoO_4)_2$, the High-tempertuare Modification of Zirconium Molybdate. *Russ. J. Inorg. Chem.* **32**, 1566 (1987).

[16] E. M. McCarron III and J. C. Calabrese: The growth and single crystal structure of a high pressure phase of molybdenum trioxide: MoO_3-II. *J. Solid State Chem.* **91**, 121 (1991).

[17] O. N. Krasochka, Y. A. Sokolova, and L. O. Atovmyan: Crystal and molecular structures of molybdenum bic-acetylacetonate, $MoO_2(C_5H_7O_2)_2$. *J. Struct. Chem.* **16**, 648 (1975).

[18] J. S. O. Evans, Z. Hu, J. D. Jorgensen, et al.: Compressibility, Phase Transitions, and Oxygen Migration in Zirconium Tungstate, ZrW_2O_8. *Science* **275**, 61 (1997).

[19] J. Wong, F. W. Lytle, R. P. Messmer, et al.: K-edge absorption spectra of selected vanadium compounds. *Phys. Rev. B* **30**, 5596 (1984).

[20] A. Balerna, E. Bernieri, E. Burattini, et al.: EXAFS studies of MeO_{3-x} (Me = W, Mo, Re, Ir) crystalline and amorphous oxides. *Nucl. Instrum. Methods Phys. Res.* **A308**, 234 (1991).

[21] J. A. Horsley, I. E. Wachs, J. M. Brown, et al.: Structure of Surface Tungsten Oxide Species in the WO_3/Al_2O_3 Supported Oxide System from X-ray Absorption Near-edge Spectroscopy and Raman Spectroscopy. *J. Phys. Chem.* **91**, 4014 (1987).

[22] F. Hilbrig, H. E. Gobel, H. Knozinger, et al.: X-ray Absorption Spectroscopy Study of the Titania- and Alumina-Supported Tungsten Oxide System. *J. Phys. Chem.* **95**, 6973 (1991).

[23] V. S. Filip'ev, G. E. Shatalova, and E. G. Fesenko: Determination of bond lengths in tungstates with the perovskite structure. *Kristallografiya* **19**, 386 (1974).

[24] D. Cao, F. Bridges, G. R. Kowach, et al.: Correlated atomic motions in the negative thermal expansion material ZrW_2O_8: A local structure study. *Phys. Rev. B* **68**, 014303 (2003).

[25] D. Cao, F. Bridges, G. R. Kowach, et al.: Frustrated Soft Modes and Negative Thermal Expansion in ZrW2O8. *Phys. Rev. Lett.* **89**, 215902 (2002).

[26] C. Meade, R. J. Hemley, and H. K. Mao: High-Pressure X-Ray Diffraction of SiO_2 Glass. *Phys. Rev. Lett.* **69**, 1387 (1992).

[27] J. P. Itie, A. Polian, C. Jauberthie-Carillon, et al.: High-pressure phase transition in gallium phosphide: an x-ray absorption spectroscopy study. *Phys. Rev. B* **40**, 9709 (1989).

[28] S. Allen and J. S. O. Evans: Negative thermal expansion and oxygen disorder in cubic ZrMo2O8. *Phys. Rev. B* **68**, 134101 (2003).

[29] G. Mountjoy, R. Anderson, R. J. Newport, et al.: The effect of zirconia content on the structure of zirconia-silica xerogels as determined by x-ray and neutron diffraction and Zr K-edge EXAFS and XANES. *J. Phys.: Condens. Matter* **12**, 3505 (2000).

[30] H. Kanai, Y. Okumura, K. Utani, et al.: Epoxidation of 1-octene with *tert*-butyl hydroperoxide catalyzed by ZrO_2/Aerosil-SiO_2. *Catal. Lett.* **76**, 207 (2001).

[31] T. Varga, A. P. Wilkinson, C. Lind, et al.: Pressure-induced amorphization of cubic ZrW_2O_8 studied in-situ and ex-situ by synchrotron x-ray absorption spectroscopy and diffraction. *submitted to Phys. Rev. B*, (2005).

[32] T. Varga, A. P. Wilkinson, C. Lind, et al.: Pressure-induced amorphization of cubic $ZrMo_2O_8$ studied in-situ by x-ray absorption spectroscopy and diffraction. *submitted to Solid State Commun.*, (2005).

CHAPTER 6

SYNTHESIS, STRUCTURE AND THERMAL BEHAVIOR OF STUFFED ZIRCONIUM PYROPHOSPHATES WITH THE FORMULA $M^{I}_{x}Zr_{1-x}M^{III}_{x}P_2O_7$

Abstract

A phase transition between a low-temperature (ordered) structure that has normal positive thermal expansion and a high-temperature (disordered) structure with lower thermal expansion occurs at about 300 ^{o}C in cubic ZrP_2O_7. From an applications point of view, it is desirable to lower the temperature of this phase transition preferably below room temperature. Chemical modification of the structure through the replacement of some Zr(IV) by M^{III} cations and the simultaneous insertion of small cations such as Li^{+} into interstitial spaces was used to lower the phase transition temperature and thus control the thermal expansion behavior of ZrP_2O_7. Some new compositions of the formula $M^{I}_{x}Zr_{1-x}M^{III}_{x}P_2O_7$ (M^{I}= Li, Na, K; M^{III}= Ga, Y, In, Eu and Nd) have been synthesized and trends in their thermal behavior were examined. However, we were unable to lower the phase transition temperature by more than ~40 ^{o}C using this method. The upper limit of doping appears to be ~20 molar% (i.e. x = 0.2) in most cases based on DSC data, but could not be definitively concluded in the absence of a definitive characterization of the phases' chemical composition. The linear thermal expansion coefficient of the high-temperature form increased on chemical modification.

6.1 Introduction

Materials with the cubic AM_2O_7 (zirconium pyrophosphate/pyrovanadate) structure have been under investigation since the work of Levi and Peyronel in 1935.[1] Their diffraction pattern can be indexed, at least approximately, on a cubic unit cell with ~8 Å dimensions. At low temperature, nearly all of the compounds show a superstructure, which typically involves a 3 x 3 x 3 enlargement of the basic cubic unit cell. In some cases, the lattice is only approximately metrically cubic (e.g. GeP_2O_7).[2] The nature of these superstructures is still an active area of investigation, as already discussed in 1.2.1. Many of the compounds undergo a phase transition from the low-temperature phase to a high-temperature phase on heating. This transformation involves the loss of the superstructure.

Most AM_2O_7 compounds, including the prototype ZrP_2O_7, crystallize in the cubic space group $Pa\bar{3}$, which implies that the thermal expansion behavior has to be isotropic. This phase exhibits normal positive thermal expansion between room temperature and the temperature of the phase transition to the high-temperature structure.[3, 4] The structure of cubic ZrP_2O_7 is closely related to that of cubic zirconium tungstate (ZrW_2O_8), the material which has become well-known due to its isotropic negative thermal expansion over a wide temperature range (see Figure 6.1).[5, 6]

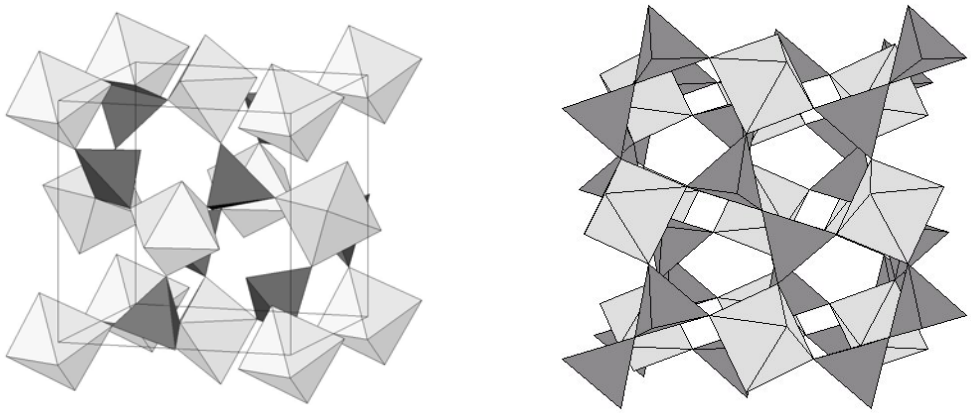

Figure 6.1: Crystal structure of α-ZrW_2O_8 (on the left; bright ZrO_6 octahedra and dark WO_4 tetrahedra sharing corners) and ideal (high-temperature) crystal structure of ZrP_2O_7 (on the right; bright ZrO_6 octahedra and dark PO_4 tetrahedra sharing corners). The two cubic structures are closely related.

The thermal expansion of cubic AM_2O_7 phases can be very low and even negative in the temperature range where there is no superstructure.[3, 4, 7] Pure phosphates AP_2O_7 with lighter elements have a decreased α (CTE) above the phase transition from the superstructure to the normal structure, but still exhibit positive expansion. For ZrP_2O_7 this phase transition occurs at ~290 ^oC.[7] After the phase transition, the coefficient of thermal expansion (CTE or α) becomes quite low (~$3.5x10^{-6}$ K^{-1}), but still can only be considered low intermediate CTE based on the classification of Roy.[8] Thermal expansion data suggest only one phase transition for ZrP_2O_7, nonetheless there are actually two transitions as the material goes through an intermediate incommensurate structure.[9] The thermal expansion actually becomes negative in the radioactive uranium and thorium analogues as well as in ZrV_2O_7 and HfV_2O_7 at high temperatures.[10-13] Above 102 °C, the vanadates exhibit strong NTE with a change in slope at ~600 °C.[3, 4] The thermal expansion for several cubic AM_2O_7 compounds is shown in Figure 6.2.

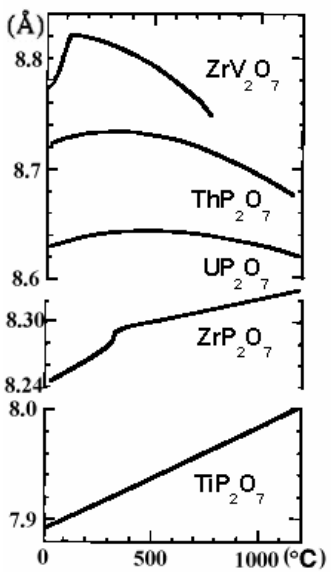

Figure 6.2: Thermal expansion for some cubic AM_2O_7 compounds. ZrV_2O_7, ThP_2O_7 and UP_2O_7 exhibit NTE at high temperatures. Taken from Sleight.[3]

The wide variety of 4+ cations that can be accommodated in the cubic AM_2O_7 framework are listed in section 1.2.1. The list includes some transition metals in less than their maximum oxidation states, e.g. Re,[14] W[15] and Nb.[16] Niobium pyrophosphate can be prepared with the transition metal in a range of oxidation states. As the metal is oxidized, phosphorous vacancies are introduced to maintain charge balance.[16, 17] There have also been reports of materials with mixed M^{III}/M^{V} cations such as $Bi_{0.5}Ta_{0.5}P_2O_7$, $Bi_{0.5}Nb_{0.5}P_2O_7$ and $Nd_{0.5}Ta_{0.5}P_2O_7$ (see next chapter of this thesis).[18] A small number of isostructural vanadates (ZrV_2O_7,[19] HfV_2O_7[20]) and arsenates ($ZrAs_2O_7$, $HfAs_2O_7$) has also been reported.[21]

Interest in the thermal expansion properties of materials related to ZrP_2O_7 started with the work of Harrison in 1954,[22] after a report on the formation of a low thermal expansion material in experiments examining the addition of P_2O_5 to ZrO_2 ceramic bodies.[23] Later, the thermal expansion of TiP_2O_7,[24] ZrV_2O_7,[10, 11] UP_2O_7,[25] ThP_2O_7[26] and

$Zr_{1-x}Th_xP_2O_7$[27] were studied. Even greater interest was generated by the work of Korthuis *et al*. on thermal expansion in the solid solution series $ZrV_{2-x}P_xO_7$ in 1995.[12] In compounds with smaller cation size, such as TiP_2O_7[28] and GeP_2O_7,[2] the thermal expansion is positive at all reported temperatures. As materials with larger unit cells are examined, the behavior becomes more interesting as was already mentioned for ZrP_2O_7, ZrV_2O_7, UP_2O_7 and ThP_2O_7.

For the phosphates, the unit cell size varies in an almost linear fashion with the radius of the octahedral cation (see Figure 6.3).[15, 29, 30]

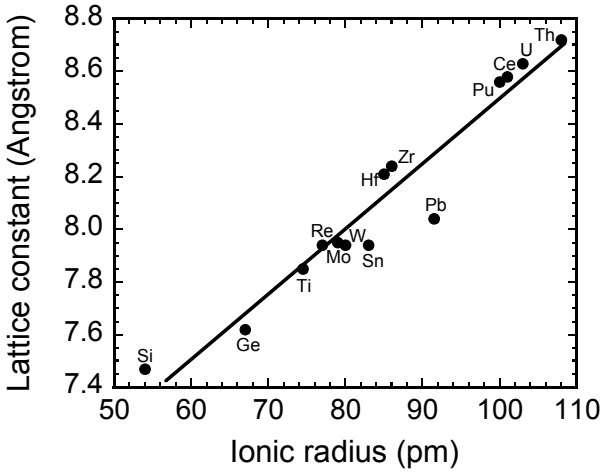

Figure 6.3: Unit cell size versus ionic radius of the octahedral A^{4+} cation in cubic AP_2O_7 compounds. The data were taken from Tillmans[31] and Withers,[9, 31, 32] but also includes our own data on CeP_2O_7 kindly provided by Kathy White.

For the phosphates, in general, increasing the weight/size of the A^{4+} cation lowers the phase transition temperatures and leads to a lower thermal expansion coefficient for the ideal (high-temperature) structure. The expansion behavior of AM_2O_7 compounds can be attributed to their unusual crystal structure, which can be viewed as related to the NaCl structure with A^{4+} as the cation and $(M_2O_7)^{4-}$ as the anion. The ordering of the

M_2O_7 units lowers the space group symmetry to $Pa\bar{3}$, the highest possible symmetry for this framework. In the high-temperature structure, this centrosymmetric space group constrains the M-O-M bond angles to be 180° on average, as the M_2O_7 units are located on a three-fold axis with the bridging oxygen on the inversion center. In the 3 x 3 x 3 superstructure, this constraint is released on most of the M_2O_7 units, and M-O-M bond angles range from ~130 to 165°. The superstructure shows normal (positive) expansion behavior. Above the phase transition, which in most cases occurs between 100 and 400 °C depending on the identity of A and M, all M_2O_7 units must have an average M-O-M angle of 180°. As a 180° bond angle is unfavorable, both static displacements leading to disorder and thermal motion are likely to release the strain. Considering the low or negative CTEs of the AM_2O_7 compounds, it seems likely that the relaxation occurs by transverse thermal motion of the oxygens in analogy to the low and negative expansion materials discussed in 1.2.6. This is also supported by theoretical studies, which predict a rotation of the VO_4 tetrahedra causing a distortion of the ZrO_6 octahedra in ZrV_2O_7.[33] In their study, Pryde *et al.* argue that the effect of the tetrahedral rotations in pulling in the rest of the structure (causing contraction) will decrease with decreasing size of the tetrahedra, which explains why the expansion of most phosphates is positive, whereas the vanadates contract on heating. This suggests that the trend seen for the A^{4+} cation (more negative expansion with increasing weight/size) is valid for the tetrahedral M atom (P, V, As), and would imply that the arsenates should show even more negative expansion than the vanadates.

From the applications point of view, the low CTE of the high-temperature phase is desirable over a wide temperature range possibly including room temperature, thus we

were interested in lowering the temperature of the phase transition in order to stabilize the high-temperature disordered structure to lower temperatures.

One way to stabilize certain structures or control phase transitions is chemical modification, during which ions can be replaced (substitution) and/or new additional ions inserted (stuffing), and thus crystal defects created. Previous work done on β-quartz to suppress the unwanted transformation to α-quartz was already mentioned in Chapter 1 (see section 1.5.1) along with solid solution formation in the $ZrV_{2-x}P_xO_7$ and $HfV_{2-x}P_xO_7$ systems and the substitution of Zr^{4+} in cubic ZrW_2O_8 by trivalent cations leading to a decrease in the temperatures of the corresponding phase transitions.

There has been some previous work on the preparation of stuffed ZrP_2O_7. Sacks et al.[34] examined substitutions involving the replacement of Zr^{4+} by a combination of an alkali metal ($M^I = Li^+$, Na^+, K^+) or Ag^+, and a trivalent cation, such as In^{3+}, Y^{3+} or Eu^{3+} (M^{III}) giving $M^I_xZr_{1-x}M^{III}_xP_2O_7$ compositions. The substitution of phosphorous by alkali plus silicon was also tried ($M^I_xZrM^{III}_xP_{2-x}O_7$), but with no success. In their standard solid state synthesis, they applied the phosphate-containing compound $NH_4H_2PO_4$ in significant excess. For $M^I_xZr_{1-x}Eu_xP_2O_7$ compositions, a solid solubility limit of x = 0.20 was estimated. In some other cases ($M^I_xZr_{1-x}(Y,In)_xP_2O_7$ higher levels of substitution were claimed (up to 35 molar% or x = 0.35). The authors noticed that the phase transition temperature in ZrP_2O_7 was lowered on stuffing. These materials were examined as potential fast ion conductors and as their conductivity was found to be low, no further work seems to have been done on them.

Ota and Yamai also studied the effect of solute ions in ZrP_2O_7 solid solutions.[35] They reported that the replacement of Zr^{4+} ions by larger ions and the stuffing of cations

into the cavities of the framework stabilized the high-temperature structure or, as they call it, the expanded structure and consequently the thermal expansion was reduced in $Ce_xZr_{1-x}P_2O_7$ or $(Li,Y)_xZr_{1-x}P_2O_7$ solid solutions. For their $(Li,Y)_xZr_{1-x}P_2O_7$ solid solutions, they estimated a solubility limit of x = 0.2. There is very little detail in both papers on the thermal expansion behavior of the new compositions.

In common with most materials that display negative or very low thermal expansion, the high-temperature structure of ZrP_2O_7 is of relatively low density. We have performed a preliminary examination of this structure using some very simple modeling tools (ATOMS void searching tool[36]) and confirmed that there are cavities big enough to accommodate a small ion such as Li^+.

In this work, we explored the possibility of stabilizing the high-temperature low thermal expansion structure of cubic ZrP_2O_7 to room temperature by putting univalent cations (Li^+, Na^+ or K^+) into the interstitial spaces of the structure and compensating for the charge by substituting trivalent ions (e.g. Eu^{3+}, Nd^{3+}) for Zr^{4+}. The systems that Sacks *et al.*[34] explored were reexamined in the present work as well as new $M^I_x(Zr_{1-x}M^{III}_x)P_2O_7$ compositions. We looked at how the substitutions influenced the phase transition behavior and the thermal expansion using thermal analysis and powder diffractometry.

6.2 Experimental

6.2.1 Syntheses

Direct syntheses of $M^I_xZr_{1-x}M^{III}_xP_2O_7$ compounds (M^I= Li^+, Na^+ and K^+; M^{III}=Ga^{3+}, Y^{3+}, In^{3+}, Nd^{3+} and Eu^{3+}) have been carried out using standard solid state techniques

from Li_2CO_3 (or Na_2CO_3, K_2CO_3), $ZrO(NO_3)_2.xH_2O$, a salt or oxide of the M^{III} ion (e.g. Ga_2O_3, $Y(NO_3)_3$, $In(NO_3)_3$, etc.) and $NH_4H_2PO_4$ based on the method of Sacks *et al*.[34] Stoichiometric quantities of the alkali-, zirconium- and M^{III}-containing ingredients were mixed with excess $NH_4H_2PO_4$ and finely ground (pressed into pellets in some cases), put into a covered ceramic crucible and heated up to 1100 ^oC for 12-15 hours. The product was quenched in air, reground with some additional $NH_4H_2PO_4$ and refired at 1200 ^oC for 20-30 minutes. The excess of $NH_4H_2PO_4$ was used to because P_2O_5 is lost at the high temperatures of the reaction.[22, 34] The samples prepared this way cover the $0.1 \leq x \leq 0.4$ stuffing range and are listed in Table 6.1 along with the specific synthesis conditions. $Li_xZr_{1-x}Nd_xP_2O_7$ and $Li_xZr_{1-x}Ga_xP_2O_7$ compositions have never been reported before.

Some of the compositions already synthesized by Sacks et al.[34] as well as Ota and Yamai were revisited[35] due to the limited information on the materials' thermal behavior and contradicting values for solubility limits in the two papers. A set of samples covering the $0.03 \leq x \leq 0.2$ composition range has been synthesized by Michael M. Morant (Winthrop University), an undergraduate student working with our group in the summer of 2004, using an alternative synthesis method. The difference in the synthesis procedure was that no excess $NH_4H_2PO_4$ (due to our concerns about the formation of glassy or impurity phases when excess phosphate is added, see section 6.3.4) was used and that the mixture was slowly heated to 600 ^oC before regrinding. This synthesis procedure was only used for $Li_xZr_{1-x}Eu_xP_2O_7$ samples (see Table 6.2).

Table 6.1: List of $M^{I}_{x}(Zr_{1-x}M^{III}_{x})P_2O_7$ compositions prepared with $0.1 \leq x \leq 0.4$. Many more samples were prepared, sometimes using modified synthesis conditions, but only the ones that appeared relatively pure by initial XRD and thus suitable for further studies are listed.

Sample ID	x	Target composition	Special condition
VTLZIP1 and 5	0.1	$Li_{0.1}Zr_{0.9}In_{0.1}P_2O_7$	8-10 % initial excess of $NH_4H_2PO_4$, regrinding w/ extra 7 % before refiring
VTLZEP1		$Li_{0.1}Zr_{0.9}Eu_{0.1}P_2O_7$	
VTLZYP1		$Li_{0.1}Zr_{0.9}Y_{0.1}P_2O_7$	
VTLZNP2	0.1	$Li_{0.1}Zr_{0.9}Nd_{0.1}P_2O_7$	12 % initial excess of $NH_4H_2PO_4$ at 1120 ^oC, regrinding w/ extra 10 % before refiring at 1220 ^oC
VTLZEP3	0.2	$Li_{0.2}Zr_{0.8}Eu_{0.2}P_2O_7$	
VTLZNP1	0.2	$Li_{0.2}Zr_{0.8}Nd_{0.2}P_2O_7$	10 % initial excess of $NH_4H_2PO_4$, regrinding w/ extra 10 % before refiring
VTLZIP4	0.2	$Li_{0.2}Zr_{0.8}In_{0.2}P_2O_7$	Pressed into pellet w/ 12 % excess of $NH_4H_2PO_4$ at 1300 ^oC, regrinding w/ extra 10 %, refiring at 1350 ^oC
VTNZEP1	0.2	$Na_{0.2}Zr_{0.8}Eu_{0.2}P_2O_7$	10-11 % initial excess of $NH_4H_2PO_4$, regrinding w/ extra 12-15 % before refiring
VTKZEP1		$K_{0.2}Zr_{0.8}Eu_{0.2}P_2O_7$	
VTNZIP1		$Na_{0.2}Zr_{0.8}In_{0.2}P_2O_7$	
VTKZIP1		$K_{0.2}Zr_{0.8}In_{0.2}P_2O_7$	
VTNZYP1		$Na_{0.2}Zr_{0.8}Y_{0.2}P_2O_7$	
VTKZYP1		$K_{0.2}Zr_{0.8}Y_{0.2}P_2O_7$	
VTLZIP2	0.3	$Li_{0.3}Zr_{0.7}In_{0.3}P_2O_7$	12 % initial excess of $NH_4H_2PO_4$, regrinding w/ extra 12 % before refiring
VTLZEP2		$Li_{0.3}Zr_{0.7}Eu_{0.3}P_2O_7$	
VTLZYP2		$Li_{0.3}Zr_{0.7}Y_{0.3}P_2O_7$	
VTLZNP3	0.3	$Li_{0.3}Zr_{0.7}Nd_{0.3}P_2O_7$	14 % initial excess of $NH_4H_2PO_4$ at 1140 ^oC, regrinding w/ extra 12 % before refiring at 1250 ^oC
VTLZNP7 and 8	0.3	$Li_{0.3}Zr_{0.7}Nd_{0.3}P_2O_7$	Mix. dried at 300-350^oC for 4 hrs w/ 12 % initial excess of $NH_4H_2PO_4$, pellet pressed, 1120 ^oC reground w/ 14 % before refiring at 1220 ^oC
VTLZGP1 and 4	0.3	$Li_{0.3}Zr_{0.7}Ga_{0.3}P_2O_7$	
VTLZGP2 and 6	0.4	$Li_{0.4}Zr_{0.6}Ga_{0.4}P_2O_7$	
VTLZNP9	0.1	$Li_{0.1}Zr_{0.9}Nd_{0.1}P_2O_7$	10-15 % initial excess of $NH_4H_2PO_4$, pellet pressed, reground w/ extra 5-10 % before refiring at 1150-1175 ^oC
VTLZEP4	0.1	$Li_{0.1}Zr_{0.9}Eu_{0.1}P_2O_7$	
VTLZNP10	0.2	$Li_{0.2}Zr_{0.8}Nd_{0.2}P_2O_7$	
VTLZEP5	0.3	$Li_{0.3}Zr_{0.7}Eu_{0.3}P_2O_7$	

Table 6.2: List of $Li_x(Zr_{1-x}Eu_x)P_2O_7$ ($0.03 \leq x \leq 0.2$) compositions prepared by Michael Morant.

Sample ID	x
MMM2_ZrPO (ZrP_2O_7)	0
MMM3_LiEu03	0.03
MMM5_LiEu03	0.03
MMM8_LiEu045	0.045
MMM12_1_LiEu045	0.045
MMM12_2_LiEu045	0.045
MMM1_LiEu06	0.06
MMM1_LiEu06_2	0.06
MMM4_LiEu12	0.12
MMM6_LIEu15	0.15
MMM6_LiEu15_2	0.15
MMM10_LiEu2	0.2

6.2.2 X-ray powder diffraction

Laboratory powder X-ray diffraction patterns were recorded for all of the samples using a Scintag X1 diffractometer. This instrument was equipped with a Cu Kα radiation source and a Scintag Peltier-cooled solid state detector. For most of the reported data sets, a scan rate of 2.5°/min and a step size of 0.02° were employed along with a 251 mm diffractometer radius, 2/1 mm slits on the tube side and 0.5/0.3 mm slits on the detector side. Data with better statistics, used for Rietveld refinement purposes, were collected with scan rates of 0.1-0.2°/min. The variable temperature measurements made use of a Scintag High-Low temperature stage that allowed data collection between –196 °C (with liquid nitrogen) and 300 °C under vacuum (see section 2.1.1).

Data for $Li_{0.4}Zr_{0.6}Ga_{0.4}P_2O_7$ (VTLZGP6) were collected at the High Temperature Materials Laboratory (HTML), Oak Ridge National Laboratory (Oak Ridge, TN) on a Philips X'Pert PRO MPD x-ray diffractometer with copper K_α radiation, a high count rate proportional detector (Miniprop) and an Anton-Paar XRK900 high-temperature

stage. Polycapillary lens optics (10 mm x 10 mm aperture) and a 0.09^{o} parallel plate collimator with Soller slits were used on the incident and diffracted beam sides, respectively.

6.2.3 Synchrotron x-ray powder diffraction

High-temperature synchrotron x-ray diffraction measurements on $Li_xZr_{1-x}Eu_xP_2O_7$ samples were carried out at beamline X14A of the National Synchrotron Light Source, Brookhaven National Laboratory (BNL), Upton, NY. An x-ray wavelength of 0.7285 Å was selected using a Si(111) double-crystal monochromator. A gas proportional counter with krypton and CO_2 gas was used as detector. The samples were loaded into capillaries and placed in a capillary furnace for variable temperature measurements.

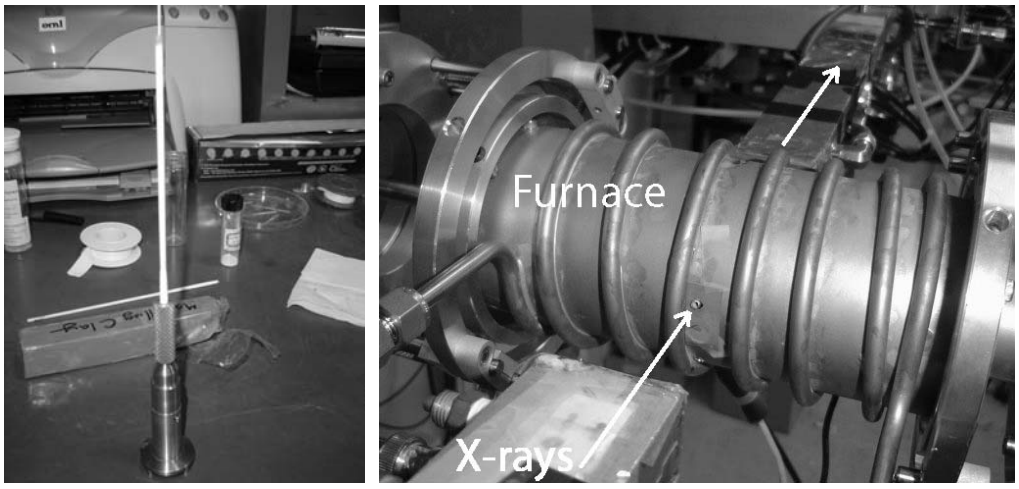

Figure 6.4: Sample holder with the capillary containing the powder sample inserted on the top of the alumina tube (left) and the capillary furnace at X14A, NSLS, Upton, NY (right).

6.2.4 Neutron powder diffraction

Variable temperature neutron powder diffraction data for samples with the $Li_{0.3}Zr_{0.7}Nd_{0.3}P_2O_7$ (VTLZNP8) and $Li_{0.4}Zr_{0.6}Ga_{0.4}P_2O_7$ (VTLZGP6) nominal

composition were collected on the BT-1 high resolution powder diffractometer at the National Center for Neutron Research (NCNR) at NIST, Gaithersburg, MD (see Figure 2.7). A Cu(311) monochromator with 15' arcmin of in-pile collimation was used to select an incident wavelength of 1.5401 Å. This monochromator setting was chosen as it provides an optimal balance between intensity and resolution and is widely used to collect data for the Rietveld refinement of structures.

6.2.5 Analysis of the diffraction data

The powder diffraction data were analyzed using the program GSAS[37] with the EXPGUI interface.[38] Lattice parameters, site occupancies and phase fractions were determined by Rietveld refinement. For samples where no quantitative phase analysis was done, the lattice constants were extracted by Le Bail fitting.

6.2.6 Thermal analysis

Thermal analysis measurements were made with a Seiko 220 DSC instrument in the School of Polymer, Textile & Fiber Engineering, Georgia Tech. The instrument can be used for experiments up to 600 °C in nitrogen, oxygen or in air. The temperature calibration was checked with the ICTA (International Center for Thermal Analysis) standard set 759. All DSC peaks were observed at temperatures of ± 3 °C of the certified value, indicating that the instrument was well calibrated.

6.3 Results and discussion

6.3.1 Synthesis problems and impurity phases

Difficulties were encountered preparing phase pure samples with the desired $M^{I}_{x}Zr_{1-x}M^{III}_{x}P_2O_7$ composition. In many cases, even after repeated grinding, pellet-pressing and firing cycles, the samples contained impurities that were clearly visible in the x-ray pattern. As Table 6.1 indicates, many different synthesis conditions were tried, but even the ones that seemed to work better than others did not always reproduce the same result. In addition, it turned out that even when the sample looked phase-pure by diffraction at room temperature, crystalline impurity phase(s) started to appear when the sample was heated (see section on high-temperature synchrotron experiments). This observation indicated the presence of some glassy component in the sample that was invisible in the room temperature x-ray pattern, but started to crystallize at higher temperatures. There are several possible reasons for these difficulties as outlined below:

(1) The use of excess of $NH_4H_2PO_4$ raised the question whether it leads to the formation of unwanted products. Solid state reactions are limited by the slow diffusion in solids. In order to get reasonable diffusion, high temperatures are required, but high temperatures may lead to loss of certain reactants. P_2O_5 is volatile at high temperatures, and excess phosphate was employed by Harrison *et al.*[22] and Sacks *et al.*,[22, 34] to account for the phosphate loss at the high temperatures of the reaction. However, based on some impurity phases (e.g. $LiEuP_4O_{12}$, $Eu(PO_3)_3$) found in some of the samples where a significant excess of $NH_4H_2PO_4$ (up to 15 weight%) was used, we considered $NH_4H_2PO_4$ a possible cause of the formation of glassy and crystalline impurities. In addition, in samples with higher x's ($x \geq 0.3$), where greater excess phosphate was used,

the amount of crystalline impurities seemed to be smaller, suggesting the possibility that more glassy material formed and the impurities ended up in the amorphous phase. Therefore, the synthesis of a set of samples with the $Li_xZr_{1-x}Eu_xP_2O_7$ composition in the low doping concentration range ($0.03 \leq x \leq 0.2$) was attempted with no excess phosphate used (see Table 6.3 for a list of samples). (2) Solid solubility in ZrP_2O_7 is limited as suggested by previous reports on similar materials.[34, 35] For instance, if the structure of a phase that forms is not related to cubic ZrP_2O_7, than the formation of that phase may pose a limit to the solid solubility. (In our case, if its structure is not related to cubic ZrP_2O_7, then it is considered as impurity.) (3) Alternative defect mechanisms (e.g. formation of oxygen or phosphorous vacancies) can also lead to undesired products. (4) Solid solution formation can be kinetically unfavorable.

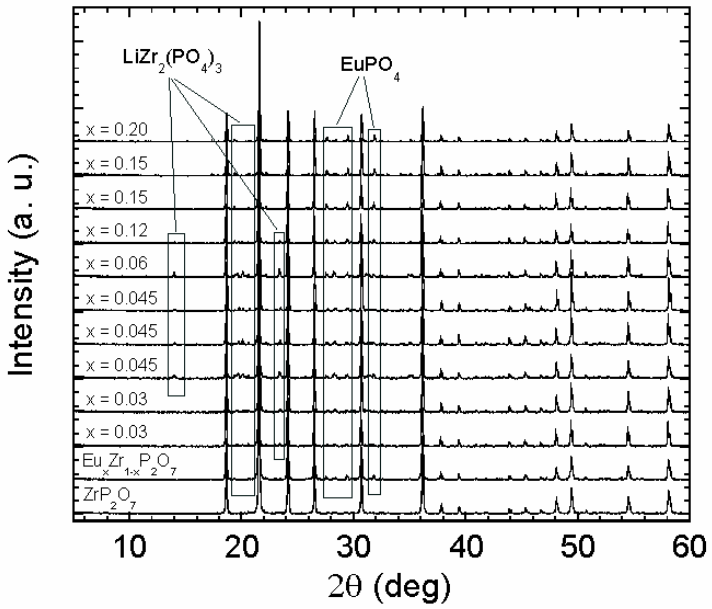

Figure 6.5: Impurities found in $Li_xZr_{1-x}Eu_xP_2O_7$ samples ($0 \leq x \leq 0.2$): $LiZr_2(PO_4)_3$ and $EuPO_4$. Data obtained by Michael Morant.

The impurity phases present were investigated in $Li_xZr_{1-x}Eu_xP_2O_7$ samples with $0.03 \leq x \leq 0.2$ (see Figure 6.5). $LiZr_2(PO_4)_3$ and $EuPO_4$ were identified as the main impurities. The following observations were made based on the presence of these two compounds and the variation of their quantities throughout the $0 \leq x \leq 0.2$ range: (a) the Li-containing impurity $LiZr_2(PO_4)_3$ disappeared above $x = 0.12$; (b) the presence of the Eu-containing impurity $EuPO_4$ appears to be independent of the presence of the Li-containing impurity. This means that using dopant concentrations above 12 molar%, we can get samples with less crystalline impurities, but we can not get rid of the Eu-containing impurity in this composition range using our synthesis method.

6.3.2 Calorimetric studies of the order-disorder phase transition

The effect of stuffing on the temperature of phase transition was studied by differential scanning calorimetry (DSC). DSC is a useful tool for studying some phase transformations in small amounts of solid samples, as the DSC curve often shows a peak at the temperature of the phase transition. In the case of the order-disorder phase transition in ZrP_2O_7-type materials, where transformation requires an input of energy, the peak in the DSC is an endotherm. In order to check the effect of the individual stuffing species in $Li_xZr_{1-x}Eu_xP_2O_7$ compositions, samples doped with only Eu and only Li, respectively, were prepared. No decrease in the temperature of phase transition was achieved in a sample with $Li_{0.2}Zr_{0.95}P_2O_7$ nominal composition (but two transitions were seen), and a depression of only about 10 ^oC was seen in $Eu_{0.06}Zr_{0.94}P_2O_7$ as shown by their DSC curves (see Figure 6.6a). The change in the temperature of the phase transition with the amount of doping in the $Li_xZr_{1-x}Eu_xP_2O_7$ samples with nominal 0.03

≤ x ≤ 0.2 is illustrated in Figure 6.6b. The trend is not uniform with the nominal composition, which suggests that the actual compositions may be different. The introduction of Li and Eu into ZrP_2O_7 with a nominal amount of 20 molar% decreased the transition temperature by about 44 °C. The two datasets together suggest that the presence of both Li and Eu was needed to have any significant decreasing effect on the transition.

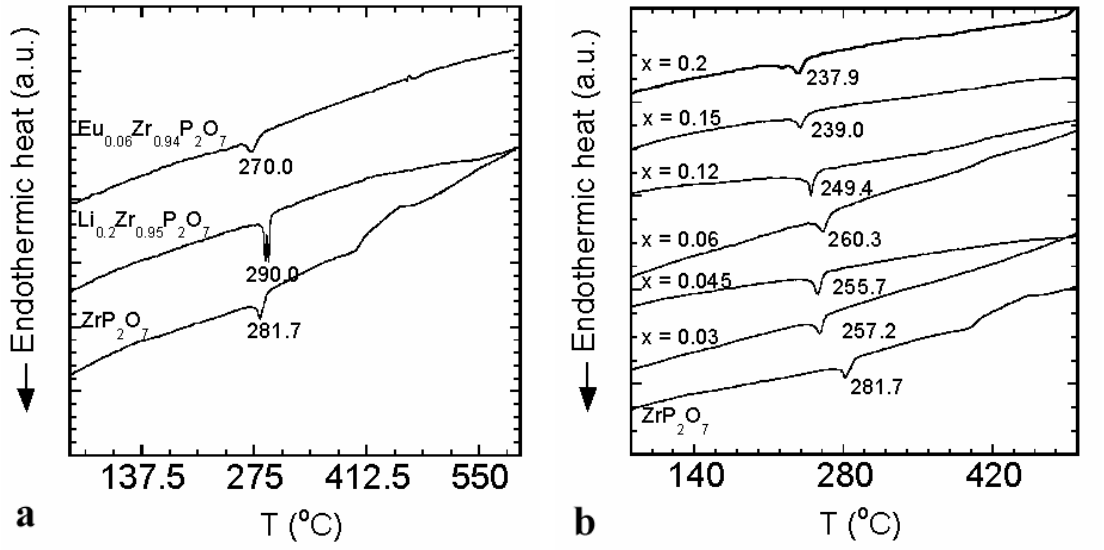

Figure 6.6: The effect of doping by Li and Eu only, respectively, on the phase transition in ZrP_2O_7. The $Li_{0.2}Zr_{0.95}P_2O_7$ sample shows two phase transitions. (a); Change of the phase transition temperature with x in $Li_xZr_{1-x}Eu_xP_2O_7$ samples ($0.03 \leq x \leq 0.2$) (b).

The phase transition temperatures from the DSC data in Figure 6.6b along with the lattice constants determined by diffraction for $Li_xZr_{1-x}Eu_xP_2O_7$ samples with $0.03 \leq x \leq 0.2$ are tabulated in Table 6.3. The table includes data for ZrP_2O_7 and samples with x = 0.1 and 0.2 prepared with excess phosphate (in italics) for comparison purposes. The reasonably good agreement between the lattice constants and phase transition

temperatures for samples prepared using different synthesis conditions indicates that both synthesis procedures provide similar samples in this stuffing (x) range. The overall trend in the temperature of the phase transition indicates that Li and Eu were incorporated into ZrP_2O_7.

Table 6.3: Lattice constants and phase transition temperatures for $Li_xZr_{1-x}Eu_xP_2O_7$ samples ($0.03 \leq x \leq 0.2$). Results on another ZrP_2O_7 sample and two samples prepared with phosphate excess (in italics) are included for comparison. Data for "MMM" samples were provided by M. Morant.

Sample ID	X	Lattice constant (Å)	Temp. of transition (°C)
MMM2_ZrPO	0	8.2419(3)	281.7
KMW122	*0*	*8.2416(2)*	*282.0*
MMM3_LiEu03	0.03	8.2459(2)	257.2
MMM8_LiEu045	0.045	8.2425(3)	262.6
MMM12_1_LiEu045	0.045	8.2453(1)	255.7
MMM12_2_LiEu045	0.045	8.2458(1)	255.6
MMM1_LiEu06	0.06	8.2456(2)	260.4
MMM1_LiEu06_2	0.06	8.2442(2)	260.3
VTLZEP4	*0.1*	*8.2460(2)*	*250.9*
MMM4_LiEu12	0.12	8.2464(2)	249.4
MMM6_LIEu15	0.15	8.2487(2)	239.0
MMM6_LiEu15_2	0.15	8.2476(2)	238.4
MMM10_LiEu2	0.2	8.2466(2)	237.9
VTLZEP3	*0.2*	*8.2478(2)*	*246.5*

The DSC data of Table 6.3 are plotted in Figure 6.7a. The graph shows how the temperature of phase transition decreases as the amount of Li/Eu added increases.

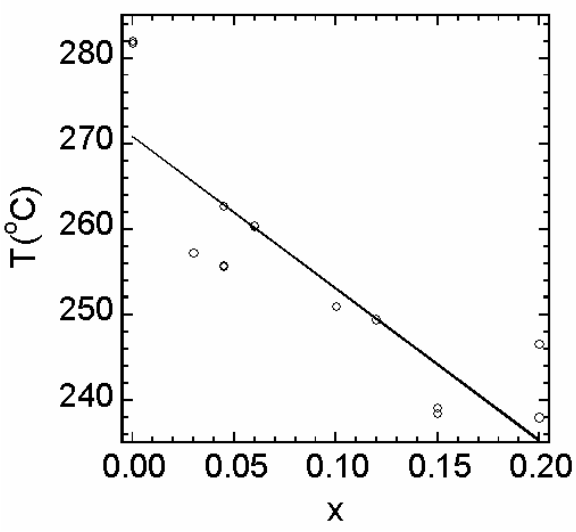

Figure 6.7: Change of the phase transition temperature with the amount of doping cations in $Li_xZr_{1-x}Eu_xP_2O_7$ with $0.03 \leq x \leq 0.2$. Data for "MMM" samples were provided by Michael Morant.

By extrapolating the straight line in Figure 6.7 to x = 1.0, we can crudely estimate the lowest phase transition temperature theoretically achievable by stuffing. The linear extrapolation suggests that even if all the Zr(IV) was substituted by Eu(III) and one Li^+/formula unit was inserted, the temperature of the phase transition would be about 80 ^oC.

$M^I_xZr_{1-x}M^{III}_xP_2O_7$ (M^I= Li, Na, K; M^{III}= Ga, Eu and Nd) samples have been prepared with nominal $0.1 \leq x \leq 0.4$ values using excess $NH_4H_2PO_4$ as recommended by Sacks *et al*.,[34] with rigorous regrinding and refiring steps and higher temperatures in the synthesis. Phase transition temperatures as given by DSC and room temperature lattice constants extracted from Rietveld analysis of the data are given in Table 6.4.

In samples with $0.1 \leq x \leq 0.4$, the maximum depression achieved in the temperature of the phase transition was 35.5 ^oC, for $Li_{0.2}Zr_{0.8}Eu_{0.2}P_2O_7$. The greater the targeted extent of doping was, the greater the shift to lower temperatures up to a limit of about x

= 0.2 (see Figure 6.8). The DSC data for $Li_xZr_{1-x}Eu_xP_2O_7$ ($0.1 \leq x \leq 0.3$) show a significant depression in the phase transition temperature going from the undoped ZrP_2O_7 to the composition with x = 0.2. For the sample with x = 0.3 ($Li_{0.3}Zr_{0.7}Eu_{0.3}P_2O_7$), no further depression in the phase transition temperature was seen. In fact, the transition temperature was similar to those of the x = 0.1 samples. This suggests that actual substitution/insertion does not occur to x's greater than 0.2. These DSC results are consistent with the lattice constant data of Table 6.4, which indicate that the lattice constant for the 0.3 sample is much smaller than expected (suggesting very incomplete incorporation for that sample).

Table 6.4: Temperatures of phase transition as well as lattice constants from XRD and neutron (denoted with "N") data for $M^{I}_{x}Zr_{1-x}M^{III}_{x}P_2O_7$ samples with $0.1 \leq x \leq 0.4$. Where the low-temperature structure was used in the structural refinement, the lattice constant was divided by 3 for the sake of comparability. Cation size is given as the average size of M^{III} and Zr (in octahedral coordination) weighted by their amount per formula unit.

Sample	x	Cation size (pm)	Temp. of ph. tr. (^{o}C)	RT lattice constant (Å)
ZrP_2O_7 KMW122	0	86	282.0	8.2416(2) 8.2475(1)[7]
$Li_{0.1}Zr_{0.9}Eu_{0.1}P_2O_7$ VTLZEP4	0.1	88.3	250.9	8.2460(2)
$Li_{0.2}Zr_{0.8}Eu_{0.2}P_2O_7$ VTLZEP3	0.2	90.5	246.5	8.2478(2)
$Li_{0.3}Zr_{0.7}Eu_{0.3}P_2O_7$ VTLZEP5	0.3	92.8	250.4	8.2443(2)
$Li_{0.2}Zr_{0.8}Nd_{0.2}P_2O_7$ VTLZNP1b	0.2	91.3	276.2	8.2323(2)
$Li_{0.3}Zr_{0.7}Nd_{0.3}P_2O_7$ VTLZNP8	0.3	93.9	279.2	8.2383(1) N: 8.2478(2)
$Li_{0.3}Zr_{0.7}Ga_{0.3}P_2O_7$ VTLZGP4	0.3	83	278.3	8.2314(1)
$Li_{0.4}Zr_{0.6}Ga_{0.4}P_2O_7$ VTLZGP6	0.4	82	n/a*	8.2449(2) N: 8.2425(3)
$Na_{0.2}Zr_{0.8}Eu_{0.2}P_2O_7$ VTNZEP1b	0.2	90.5	249.5	8.2394(2)
$K_{0.2}Zr_{0.8}Eu_{0.2}P_2O_7$ VTKZEP1	0.2	90.5	276.5	8.2330(2)

*not measured

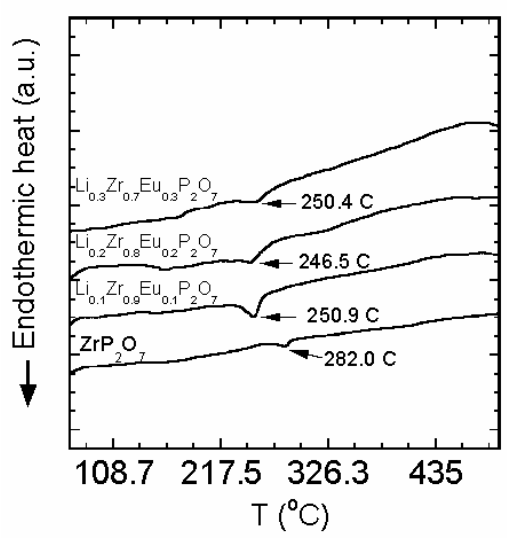

Figure 6.8: Phase transition temperatures of different $Li_xZr_{1-x}Eu_xP_2O_7$ samples with $0.1 \leq x \leq 0.3$. The data suggest a solubility limit around x = 0.2.

When this experiment was repeated with another set of samples of the same composition, it gave identical results. The apparent solubility limit of x ~ 0.2 is in accordance with earlier reports for $Li_xZr_{1-x}Eu_xP_2O_7$ materials.[34] It is also consistent with the suspected formation of an additional glassy component, whose amount at higher doping concentrations is larger. Unfortunately, no compositions have been examined with x values between 0.2 and 0.3, therefore a more exact solubility limit can not be stated based on our data. As not all of the doping cations go into the pyrophosphate structure when higher concentrations are used, the question arises: can we be sure about full cation incorporation in the case of lower doping concentrations (such as x = 0.1 or 0.2)? An attempt to address this issue is discussed in section 6.3.4, where we attempt to check the composition of the crystalline phase in selected samples by diffraction methods.

We investigated whether any trends can be established in the temperature of phase transition as a function of the size of both the alkali and the trivalent cations. In the light of the above observations regarding a possible solubility limit, stuffed samples with different M^{III} cations and 20 molar% incorporation ($Li_{0.2}Zr_{0.8}Eu_{0.2}P_2O_7$ and $Li_{0.2}Zr_{0.8}Nd_{0.2}P_2O_7$ compositions) were compared (see Figure 6.9). These comparisons are made with the assumption that the amount of cation incorporated is the same in all samples with x = 0.2. For the Eu^{3+} cation (radius: 108.7 pm), which is of smaller size than Nd^{3+} (112.3 pm), a greater negative shift was found in the phase transition temperature. This can mean two things: (a) it might suggest that smaller cation size makes the disordered high-temperature structure more favorable. However, more data would be needed for drawing a reliable conclusion, (b) it could indicate better incorporation with a smaller-sized cation.

Comparison of the DSC results for stuffed samples containing different M^+ cations (Li^+, Na^+ and K^+) with x = 0.2 suggests that as the univalent cation gets smaller, the temperature of the phase transition decreases (see Figure 6.10). This is in agreement with the tendency observed for our pair of M^{3+} cations, and, again, may suggest that smaller-sized stuffing ions make the high-temperature ideal structure more favorable, or a better incorporation with the small-size ion. The apparent difference in the sharpness of the endothermic peak for the phase transition could actually be due to a more homogeneous composition achieved with the smallest-size cation of the three; Li^+.

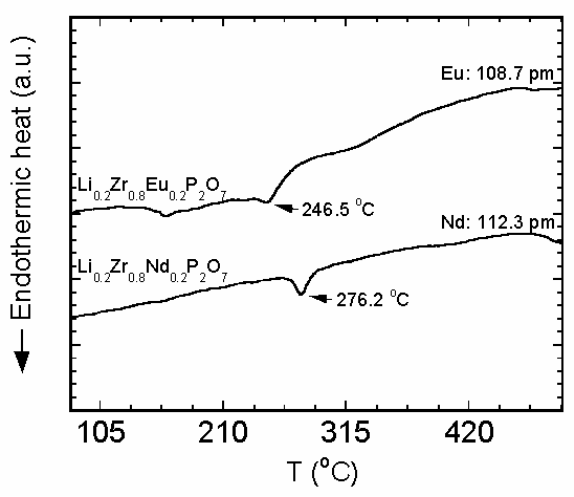

Figure 6.9: Phase transition temperatures in $Li_xZr_{1-x}M_xP_2O_7$ compounds with different M cations; Nd^{3+} and Eu^{3+} (x = 0.2). The radii are for octahedral coordination from Shannon and Prewitt.[39]

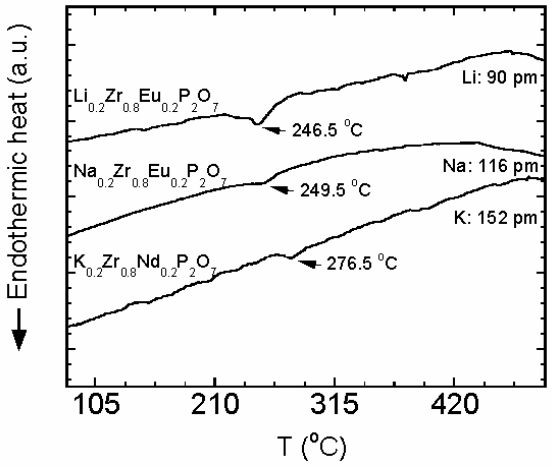

Figure 6.10: Phase transition temperatures in $M_{0.2}Zr_{0.8}Eu_{0.2}P_2O_7$ samples with different M^+ cations (Li^+, Na^+ and K^+) as seen by DSC. The radii are six-coordinate cation radii from Shannon and Prewitt.[39]

6.3.3 Variation of unit cell size with stuffing

In general, the larger the size of the 4+ cation, the larger the unit cell, as was shown in Figure 6.3 for different pyroposphates with 4+ cations ranging from Si to Th (54-108

pm). Figure 6.11a shows the same, approximately linear trend in the size of the unit cell with the nominal amount of Li and Eu incorporated for all samples up to x = 0.2. In Figure 6.11b, lattice constants for $Li_xZr_{1-x}Eu_xP_2O_7$ samples with x = 0.1, 0.2 and 0.3 measured at 350 ^oC are plotted. Although these data are not representative of the actual amount of cations incorporated into the structure, the increase of unit cell size with increasing nominal concentration of the doping species indicates that some fraction of the Li and Eu ions actually go into the pyrophosphate framework. It should be noted that Figure 6.11b is not in accordance with Figure 6.8: according to the DSC results, essentially no greater decrease in the phase transition temperature was seen for the x = 0.3 sample than for the 0.1 sample, while the increased lattice constant of the 0.3 sample indicates that the stuffing cations were incorporated to a greater extent than for the 0.1 and 0.2 samples. These results seem to be contradictory, and they question the mechanism by which stuffing acts on the thermal behavior of the samples. Stuffing is expected to increase the thermal expansion coefficient of the material (see section 6.3.5), but as the amount of incorporated cations in the (nominal) $Li_{0.3}Zr_{0.7}Eu_{0.3}P_2O_7$ sample is smaller than in the 0.2 sample, its lattice constant should also be smaller than that of $Li_{0.2}Zr_{0.8}Eu_{0.2}P_2O_7$ sample at all temperatures. (The data in Figure 6.11b were obtained from high-temperature XRD measurements carried out at 350 ^oC, while the data of Table 6.4 are room temperature results.)

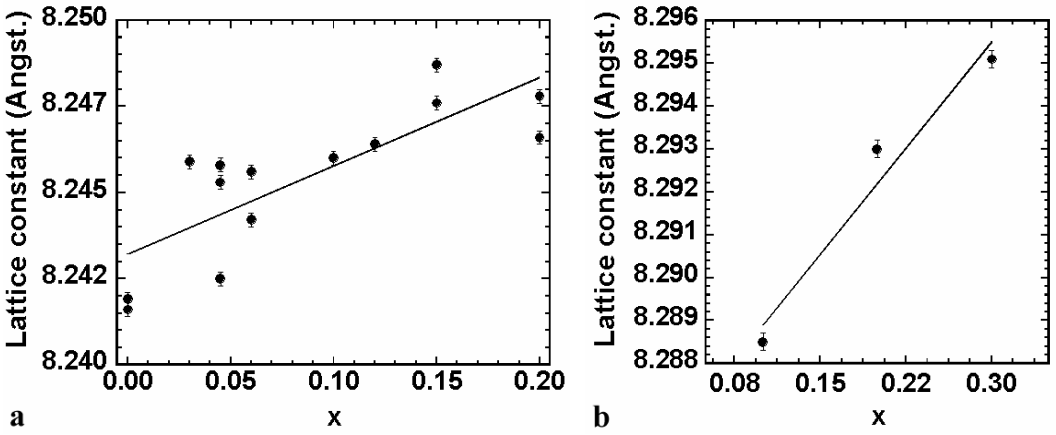

Figure 6.11: Change of the lattice parameter with the amount of doping species in $Li_xZr_{1-x}Eu_xP_2O_7$ compounds, where $0 \leq x \leq 0.2$ prepared with no excess P_2O_5, from room T XRD (a); Lattice constant versus x for $Li_xZr_{1-x}Eu_xP_2O_7$ compounds with x = 0.1, 0.2 and 0.3 prepared with excess P_2O_5, based on synchrotron XRD data at 350 ^oC.

The variation of the temperature of the phase transition with the lattice constant for all $Li_xZr_{1-x}Eu_xP_2O_7$ compositions is given in Figure 6.12. This is just another way of looking at how the thermal behavior of the samples changes with doping. The decreasing trend in the temperature of phase transition is in agreement with the trend from transition temperature vs. dopant concentration (x) graph (see Figure 6.7) and also with the relationship between the lattice constant and transition temperature (see Figure 6.11). Doping with Li and Eu with up to 20 molar% nominal concentration resulted in a depression of the phase transition temperature in ZrP_2O_7, which is unfortunately not very significant from a practical point of view.

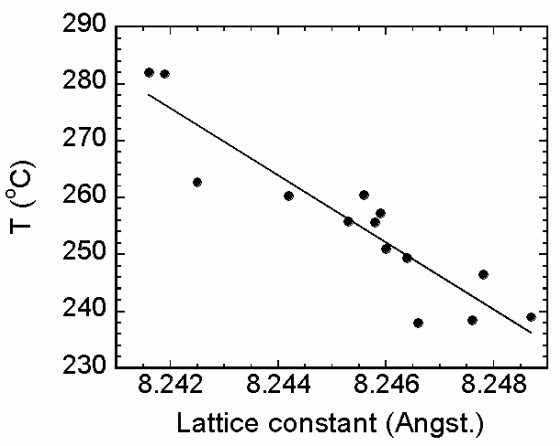

Figure 6.12: Phase transition temperature vs. lattice constant for all $Li_xZr_{1-x}Eu_xP_2O_7$ compositions with $x \leq 0.2$. Data from Michael Morant.

6.3.4 X-ray and neutron diffraction studies to confirm sample composition

For the studies to determine the composition of our crystalline phases, room and high-T laboratory XRD, synchrotron XRD and neutron diffraction were used. All the prepared $M^{I}_xZr_{1-x}M^{III}_xP_2O_7$ compositions could be indexed based on the cubic unit cell (using space group $Pa\bar{3}$).

The analysis of the room and high temperature laboratory XRD data gave unreliable results; the extracted values for x varied from sample to sample, even in the case of the same nominal composition, or were unreasonable. Due to this uncertainty in the laboratory x-ray results, we carried out synchrotron x-ray powder diffraction experiments on selected samples at 350 ^{o}C, above the expected phase transition temperature (where the simpler structure should describe the cubic pyrophosphate phase). Unfortunately, these measurements did not provide reliable site occupancy estimates either. The problem with the XRD data was most likely due to correlations between site occupancies, scale factors and thermal parameters. In the case of the laboratory XRD data, this was probably worsened by relatively poor statistics and the

difficulties to obtain a good quality fit to the low-temperature superstructure, which is far more complex than the high-temperature disordered one.

Neutron diffraction can be used to locate lighter atoms in structures, because neutrons are scattered by the atomic nucleus and not the electrons, and thus the neutron scattering cross section does not vary systematically with the atomic number. Neutron diffraction has been used to locate lithium in, for instance, different polymorphs of $LiZr_2(PO_4)_3$.[40, 41] Our goal was to locate the inserted Li^+ ions in the structure with the hope that by knowing where the lithium goes, we might be able to learn about how stuffing actually works in changing the thermal properties of the materials from a structural point of view. Rietveld analysis of the data was carried out without including Li in the structural model. The Fourier calculation option in the program GSAS[37] was used to locate negative peaks in the difference Fourier map (Li has a negative neutron scattering length). The potential Li positions, which were at physically reasonable distances from the other atoms, were used in the subsequent refinement. However, the extracted Li-occupancies were unreasonably small. In addition, due to the noisiness of the neutron data, there was a large error associated with them, making the numbers of questionable value.

The high-temperature synchrotron experiments provided us with important information regarding the sample preparation. In the samples with nominal composition $Li_{0.2}Zr_{0.8}Eu_{0.2}P_2O_7$ and $Li_{0.3}Zr_{0.7}Eu_{0.3}P_2O_7$, that were studied at 350 ^oC, a secondary phase $LiEu(PO_3)_4$ was found to grow in upon heating. As no significant amount of any crystalline impurity phase seemed to be present at room temperature, this suggests that $LiEu(PO_3)_4$ crystallized from an amorphous component that was present initially, but

was not detectable by room temperature x-ray diffraction. In the $Li_{0.2}Zr_{0.8}Eu_{0.2}P_2O_7$ sample (VTLZEP3), the amount of the impurity phase was estimated to be 24 weight%, representing ~50% of the added Eu.

The bottomline is that our structural analysis attempts failed to determine reliable compositions for the samples studied and thus failed to confirm the presumed solubility limit of x = 0.2.

6.3.5 The thermal expansion of $Li^{I}_{x}Zr_{1-x}M^{III}_{x}P_2O_7$ phases

The linear coefficient of thermal expansion (CTE) was determined for several $Li_xZr_{1-x}M^{III}_{x}P_2O_7$ samples based on variable temperature neutron and x-ray diffraction measurements. The CTE was calculated using the lattice constants obtained from structural analysis by Rietveld refinement method or Le Bail fitting.

Thermal expansion studies were carried out on a few samples that were available at the time of the experiments. It is unfortunate that at the time of these measurements we were quite convinced (based on the XRD patterns) that successful doping was carried out up to x = 0.4. The following data are for $M^{I}_{x}Zr_{1-x}M^{III}_{x}P_2O_7$ samples with x = 0.1 - 0.4. However, we have to keep in mind the results of the DSC and structural characterization (carried out at a later time) suggest a solubility limit of x = 0.2 - 0.3 when drawing conclusions about the thermal expansion behavior of these phases.

The lattice constants at different temperatures are tabulated in Table 6.6. Neutron data are only available for a limited number of temperature points. This is because the primary goal of the neutron experiments was to find the Li in the structure, and

therefore long data collection times (4-5 hours) were employed for better counting statistics.

Table 6.5: Lattice constants (cell parameter *a*) for samples with nominal composition $Li_{0.4}Zr_{0.6}Ga_{0.4}P_2O_7$ and $Li_{0.3}Zr_{0.7}Nd_{0.3}P_2O_7$ as obtained from variable temperature x-ray and neutron diffraction measurements.

Temp. (°C)	**$Li_{0.4}Zr_{0.6}Ga_{0.4}P_2O_7$ (VTLZGP6)**		**$Li_{0.3}Zr_{0.7}Nd_{0.3}P_2O_7$ (VTLZNP8)**
	***a* (Å) – X-ray**	***a* (Å) – Neutron**	***a* (Å) – Neutron**
25	8.2449(2)	8.2425(2)	8.2478(2)
50	8.2437(2)	-	-
100	-	8.2454(4)	8.2558(4)
110	8.2472(2)	-	-
170	8.2517(3)	-	-
200	8.2572(3)	-	-
260	8.2643(3)	-	-
290	8.2703(3)	-	-
294	-	8.2666(2)	8.2867(6)
320	8.2780(3)	-	-
340	-	-	8.2886(1)
350	8.2794(2)	-	-
375	-	8.2847(3)	-
400	8.2823(3)	-	-
430	-	8.2887(4)	8.2923(4)
500	8.2888(4)	-	-
600	8.2908(3)	-	-

The variation of the lattice constant with temperature for the sample with nominal composition $Li_{0.4}Zr_{0.6}Ga_{0.4}P_2O_7$ is shown in Figure 6.16 (bottom graph). We compare the thermal expansion curve for the material with that of cubic ZrP_2O_7 (top graph). There is a change in the slope of the thermal expansion curve with temperature, which shows some resemblance to that seen for ZrP_2O_7, but with a smaller discontinuity at the transition and a greater slope at high temperature.

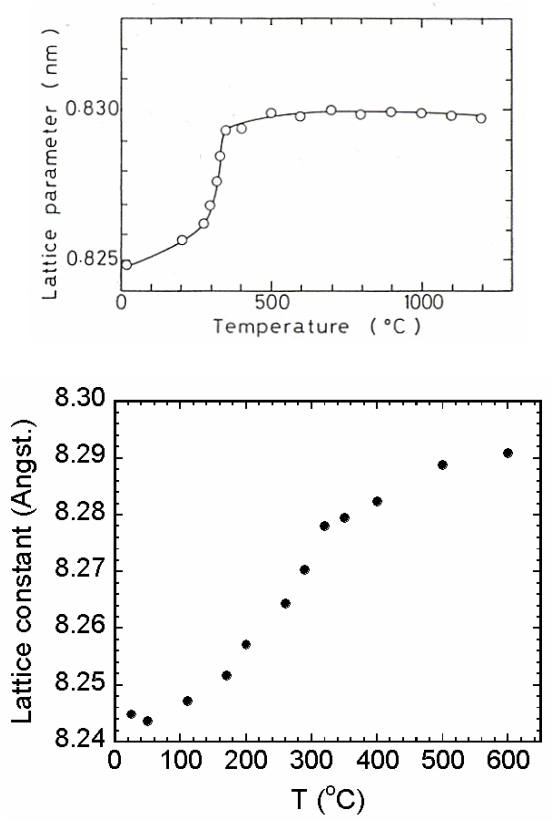

Figure 6.13: Change of unit cell constant with temperature for $Li_{0.4}Zr_{0.6}Ga_{0.4}P_2O_7$ (variable T x-ray data) compared to that of ZrP_2O_7.[35]

A straight line was fit to the two regions of different slopes in all cases and the corresponding thermal expansion coefficients were calculated (see Figure 6.15). It should be noted that dividing the curves into two regions and fitting straight lines to them is somewhat biased by the expectation that these materials, similarly to cubic ZrP_2O_7, show a phase transition somewhere around 300 ^oC. Fitting straight lines to the regions of apparently different slope and obtaining the linear thermal expansion coefficients is a simplified, yet informative, view of the changes in the thermal behavior of the material. By looking at the graphs in Figures 6.14 and 6.15, it can be argued that they can be divided into three regions instead of two. In that case an intermediate (transition) range would be considered between ~ 200 and 300 ^oC in Figure 6.15.

However, fitting three ranges to this kind of data does not appear to be the common way of interpreting the thermal expansion behavior of two phases of materials that display a phase transition.[3, 4] The intermediate phase in the transition range exists over a rather narrow temperature range and therefore not interesting from a practical point of view. Due to the limited number of data points, these graphs do not precisely determine the temperature of the phase transition.

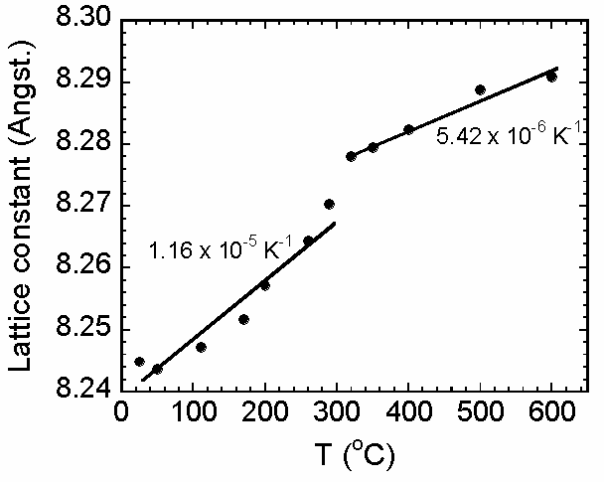

Figure 6.14: Variation of the lattice constant with temperature for $Li_{0.4}Zr_{0.6}Ga_{0.4}P_2O_7$ (variable T x-ray data). Straight lines are fitted to the curve over the low- and high-temperature regions, respectively, and the corresponding CTEs are given. The CTE gets smaller above 290 °C. Errors on the numbers and a comparison to the CTE of ZrP_2O_7 are given in Table 7.6.

If we plot the unit cell parameters from our variable temperature neutron diffraction measurements versus temperature for the sample with $Li_{0.2}Zr_{0.7}Nd_{0.3}P_2O_7$ nominal composition (VTLZNP8), we also get a change in slope around 300 °C (see Figure 6.16). Although the available data is very limited, the difference between the thermal expansion coefficients in the two regions is evident. From the very similar difference in the slopes over the two regions compared to that seen for $Li_{0.4}Zr_{0.6}Ga_{0.4}P_2O_7$ in Figure

6.15, we can infer that the phase transition in the two samples is of similar nature, but may be different from that in cubic ZrP_2O_7.

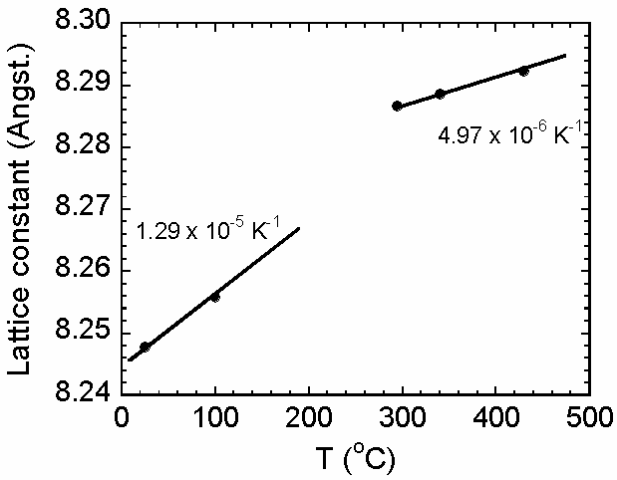

Figure 6.15: Variation of the lattice constant with temperature for $Li_{0.3}Zr_{0.7}Ga_{0.3}P_2O_7$ (variable T neutron data). Straight lines are fitted to the curve over the low- and high-temperature regions, respectively, and the corresponding CTEs are given. The CTE gets smaller above 294 °C. Errors on the numbers and a comparison to the CTE of ZrP_2O_7 are given in Table 7.6.

The calculated linear thermal expansion coefficients along with literature results for some cubic pyrophosphates are tabulated in Table 7.6. The γ-polymorph of GeP_2O_7 is actually monoclinic, but very close to, and previously reported as, cubic, and shows practically isotropic thermal expansion.[2] Both GeP_2O_7[2] and UP_2O_7[3, 25] display practically linear thermal expansion in the tabulated ranges. We consider the region below the temperature of the phase transition (or apparent change in the CTE) as the low-temperature region. For the $M^{I}_{x}Zr_{1-x}M^{III}_{x}P_2O_7$ compounds, the phase transition should fall between the end temperature of the low-temperature range and the beginning of the high-temperature range. Based on what is expected for cubic ZrP_2O_7-type materials, the high-temperature phase should have lower thermal expansion. This is

well seen in both $Li_{0.4}Zr_{0.6}Ga_{0.4}P_2O_7$ (CTE decreased by about 50 % based on the high-temperature XRD data) and $Li_{0.3}Zr_{0.7}Nd_{0.3}P_2O_7$ (a decrease by 60 %).

The CTEs for the low-temperature structure of our synthesized compositions are basically identical to the low-temperature CTE of ZrP_2O_7. In the high-temperature region, which is of more interest to us, the thermal expansion, although lower than in the low-temperature region, is greater than that of ZrP_2O_7. Stuffing seems to work against the mechanism for low thermal expansion in the high-temperature form. This is to be expected as the inserted Li^+ probably blocks free space in the interstitials (our idea of suppressing the phase transition was based on this). It is not possible to say anything about the dependence of the thermal expansion on the identity of the stuffing ions and their concentration based on the data for $Li_{0.4}Zr_{0.6}Ga_{0.4}P_2O_7$ and $Li_{0.3}Zr_{0.7}Nd_{0.3}P_2O_7$ only, because the CTEs are very close to one another (at least in the low-temperature region, but can also be very close in the high-temperature region considering the errors on the numbers) and the the exact composition of the major crystalline phase in the samples is not known.

Table 6.6: Linear thermal expansion coefficients for different pyrophosphate phases; Those for ZrP_2O_7, GeP_2O_7 and UP_2O_7 are literature values. The cation size refers to the radius of the 3+ cation in the octahedral coordination. In $M^{I}_{x}Zr_{1-x}M^{III}_{x}P_2O_7$ compounds, it is the weighted average radius of the 3+ and Zr(IV) cations. N denotes neutron diffraction data. Low-temperature and high-temperature data are separated within the table.

Compound / ID	Cation size (pm)	T range (^{o}C)	CTE (K^{-1})
Low-temperature data			
$Li_{0.4}Zr_{0.6}Ga_{0.4}P_2O_7$ VTLZGP6	Zr-Ga: 82	25 – 290 25 – 294	$1.16(30) \times 10^{-5}$ $1.09(33) \times 10^{-5}$ (N)
ZrP_2O_7[7]	Zr: 86	25 – 227	$1.20(25) \times 10^{-5}$
$Li_{0.3}Zr_{0.7}Nd_{0.3}P_2O_7$ VTLZNP8	Zr-Nd: 94	25 – 100	$1.29(90) \times 10^{-5}$ (N)
UP_2O_7[25]	U: 103	27 – 400	$4.88(*) \times 10^{-6}$
High-temperature data			
GeP_2O_7[2]	Ge: 67	295 – 970	$1.11(*) \times 10^{-5}$
$Li_{0.4}Zr_{0.6}Ga_{0.4}P_2O_7$ VTLZGP6	Zr-Ga: 82	320 – 600 340 – 430	$5.42(30) \times 10^{-6}$ $8.78(100) \times 10^{-6}$ (N)
ZrP_2O_7[7]	Zr: 86	290 – 610	$3.47(9) \times 10^{-6}$
$Li_{0.3}Zr_{0.7}Nd_{0.3}P_2O_7$ VTLZNP8	Zr-Nd: 94	294 – 430	$4.97(100) \times 10^{-6}$ (N)

* not reported

6.3.6 Phase transition as seen by synchrotron x-ray diffraction

A short set of measurements during our synchrotron studies on $Li_{0.1}Zr_{0.9}Eu_{0.1}P_2O_7$ and $Li_{0.3}Zr_{0.7}Eu_{0.3}P_2O_7$ nominal compositions, confirmed the results obtained by DSC for these samples by following the phase transition *in-situ* (see Figure 6.17). At the onset of the phase transition, the peak width gets larger. The temperature where the strongest peak gets narrower and simultaneously gets more intense was taken as the

temperature of the phase transition. Based on the following plots, the phase transition temperature is estimated to be around 250 ^{o}C for both samples. This temperature value is confirmed by our DSC studies on the same samples (250.9 ^{o}C for $Li_{0.1}Zr_{0.9}Eu_{0.1}P_2O_7$ and 250.4 ^{o}C for $Li_{0.3}Zr_{0.7}Eu_{0.3}P_2O_7$). These data thus further confirm the counterintuitive observations pointed out in section 6.3.3: the transition temperatures for the x = 0.1 and 0.3 samples are almost identical by DSC and XRD, but their lattice constants at 350 ^{o}C are different. The phase with $Li_{0.3}Zr_{0.7}Eu_{0.3}P_2O_7$ nominal composition, that contains less incorporated cations, should have smaller lattice constant (and thermal expansion) than the x = 0.2 sample. If none of the determined lattice constants are in error, this means that the nature of the mechanism by which stuffing acts in suppressing the phase transition is questionable. The phase transition is reversible as it seemed to be reproducible on cooling.

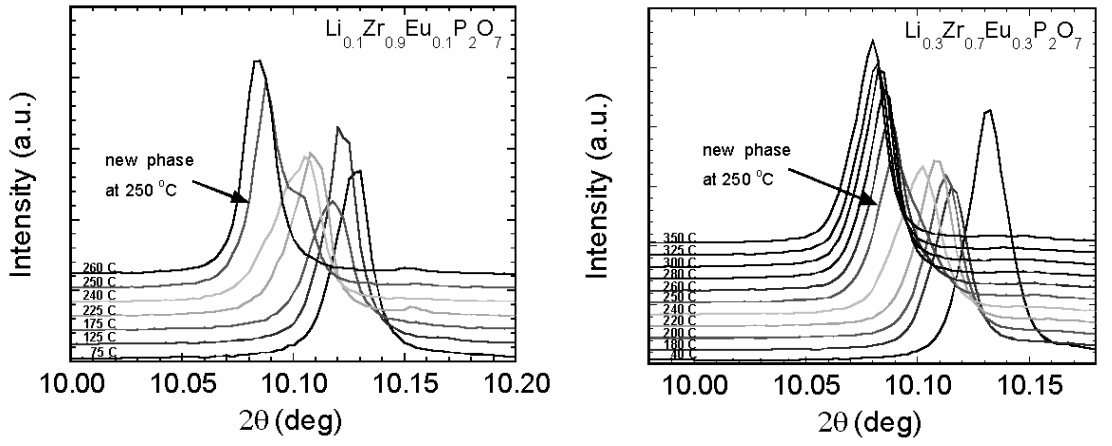

Figure 6.16: The evolution of the phase transition in $Li_{0.1}Zr_{0.9}Eu_{0.1}P_2O_7$ and $Li_{0.3}Zr_{0.7}Eu_{0.3}P_2O_7$. Based on changes in the shape of the strongest peak of with temperature, a temperature of ~250 ^{o}C was estimated.

6.4 Conclusions

The suppression of the order-disorder phase transition in ZrP_2O_7 was attempted by chemical modification. Through the partial substitution of Zr(IV) by a trivalent cation and the simultaneous insertion of Li^+ into the interstitial spaces of the structure some new $M^{I}_{x}Zr_{1-x}M^{III}_{x}P_2O_7$ compounds were prepared. However, difficulties were encountered preparing phase pure samples with the targeted compositions. Due to several factors that may have affected the outcome of the synthesis, such as reagent excess/loss leading to formation of impurities, limit to the solid solubility, kinetics and possible alternative defect mechanisms, the compositions could not even be made in a reproducible fashion. The apparent solubility limit for these solid solutions was estimated to be around x = 0.2 (x being the lower index in the above chemical formula) based on DSC data. This solubility limit is in accordance with previous reports on similar phases. However, this upper limit of doping could not be verified by our structural analysis results.

Although the temperature of the phase transition was lowered in the prepared samples relative to ZrP_2O_7 (by 44 ^{o}C at most), suppressing it to or below room temperature is not feasible with this method. With an increased unit cell size, a suppression of the phase transition and thus the stabilization of the high-temperature structure are expected. Although, increased nominal x, which also means increased unit cell size, leads to a greater depression in the phase transition temperature, unit cell size does not seem to be the only controlling factor in the thermal behavior; the identity of the cation is also important in the feasibility of the incorporation (size) along with the corresponding chemistry affecting the sample preparation.

The phase transition in $M^{I}_{x}Zr_{1-x}M^{III}_{x}P_2O_7$ compounds may not be of the same nature as seen in cubic ZrP_2O_7, as the shape of its lattice parameter versus temperature curve is different from that of the prototype compound as the discontinuity in the lattice constant at the transition is less pronounced. The high-temperature form of the compounds examined has smaller thermal expansion than that of the low-temperature phase, but larger than that of ZrP_2O_7. This means that stuffing, probably through blocking free interstitial space within the structure, acts against the mechanism that leads to low thermal expansion. This general statement can be made without knowing the exact composition of the phases that were examined.

Further phase analysis using Rietveld refinement on samples with $0.03 \leq x \leq 0.2$ and new samples in the $0.2 \leq x \leq 0.3$ range, as well as variable temperature diffraction studies on more samples, particularly with doping concentrations lower than 0.3, could improve our picture with regards to what the exact solubility limits are and how stuffing works (mechanistically) in controlling the thermal expansion behavior. However, this would only help if samples with good purity could be prepared in a reproducible fashion. In the light of our present results, further work on stuffed systems is probably not worthwhile.

6.5 References

1 G. R. Levi and G. Peyronel: Struttura Cristallografica del Gruppo Isomorfo (Si^{4+}, Ti^{4+},Zr^{4+},Sn^{4+},Hf^{4+})P_2O_7. *Z. Kristallogr.* **92**, 190 (1935).

2 E. R. Losilla, A. Cabeza, S. Bruque, et al.: Syntheses, Structures, and Thermal Expansion of Germanium Pyrophosphates. *J. Solid State Chem.* **156**, 213 (2001).

3 A. W. Sleight: Compounds that Contract on Heating. *Inorg. Chem.* **37**, 2854 (1998).

4 A. W. Sleight: Isotropic Negative Thermal Expansion. *Annu. Rev. Mater. Sci.* **28**, 29 (1998).

5 C. Martinek and F. A. Hummel: Linear Thermal Expansion of Three Tungstates. *J. Am. Ceram. Soc.* **51**, 227 (1968).

6 T. A. Mary, J. S. O. Evans, T. Vogt, et al.: Negative Thermal Expansion from 0.3 to 1050 Kelvin in ZrW_2O_8. *Science* **272**, 90 (1996).

7 N. Khosrovani, V. Korthuis, A. W. Sleight, et al.: Unusual 180^o P-O-P Bond Angles in ZrP_2O_7. *Inorg. Chem.* **35**, 485 (1996).

8 R. Roy, D. K. Agrawal, and H. A. McKinstry: Very Low Thermal Expansion Coefficient Materials. *Annu. Rev. Mater. Sci.* **19**, 59 (1989).

9 R. L. Withers, J. S. O. Evans, J. Hanson, et al.: An *In Situ* Temperature-Dependent Electron and X-ray Diffraction Study of Structural Phase transitions in ZrV_2O_7. *J. Solid State Chem.* **137**, 161 (1998).

10 D. F. Craig and F. A. Hummel: Zirconium Pyrovanadate Transitions. *J. Am. Ceram. Soc.* **55**, 532 (1972).

11 R. C. Buchanan and G. W. Walter: Properties of Hot-Pressed Zirconium Pyrovanadate Ceramics. *J. Electrochem. Soc.* **130**, 1905 (1983).

[12] V. Korthuis, N. Khosrovani, A. W. Sleight, et al.: Negative Thermal Expansion and Phase Transitions in the $ZrV_{2-x}P_xO_7$ Series. *Chem. Mater.* **7**, 412 (1995).

[13] D. Taylor: Thermal Expansion Data: IV Binary Oxides with the silica structures. *Br. Ceram. Trans. J.* **83**, 129 (1984).

[14] E. Banks and R. Sacks: ReP_2O_7: A New Isomorph of ZrP_2O_7. *Mat. Res. Bull.* **17**, 1053 (1982).

[15] Z. S. Teweldemedhin, K. V. Ramanujachary, and M. Greenblatt: New Tungsten Pyrophosphate with Cubic Zirconium Pyrophosphate-Type Structure. *Mat. Res. Bull.* **28**, 427 (1993).

[16] J. J. Zah-Letho, S. Oyetola, A. Verbaere, et al.: Defect structure of the so-called "niobium V diphosphate". Diffraction and spectroscopic studies. *Eur. J. Solid State Chem.* **31**, 1009 (1994).

[17] H. Fukuoka, H. Imoto, and T. Saito: Preparation of Cubic Niobium Pyrophosphate Containing Nb(IV) and Topotactic Extraction of Phosphorus Atoms. *J. Solid State Chem.* **119**, 98 (1995).

[18] S. Oyetola, A. Verbaere, D. Guyomard, et al.: New ZrP_2O_7-like diphosphates of either mixed ($M^{III}_{0.5}M'^{V}_{0.5}$) cations (M=Sb,Bi,Hd,Eu; M'=Sb,Nb,Ta) or M'^{V} cations (M'=Ta, Nb): synthesis and structure. *Eur. J. Solid State Inorg. Chem.* **28**, 23 (1991).

[19] J. S. O. Evans, J. C. Hanson, and A. W. Sleight: Room-Temperature Superstructure of ZrV_2O_7. *Acta Crystallogr.* **B54**, 705 (1998).

[20] E. J. Baran: The unit cell of hafnium divanadate. *J. Less Common Met.* **46**, 343 (1976).

[21] H. Onken: Uber Zirkonpyroarsenat. *Die Naturwissenschaften* **52**, 344 (1965).

[22] D. E. Harrison, H. A. McKinstry, and F. A. Hummel: High-Temperature Zirconium Phosphates. *J. Am. Ceram. Soc.* **37**, 277 (1954).

[23] G. R. Pole, A. W. Beinlich, and N. Gilbert: Physical Properties of some High-Temperature Refractory Compositions. *J. Am. Ceram. Soc.* **29**, 208 (1946).

[24] D. E. Harrison and F. A. Hummel: Reactions in the System TiO_2-P_2O_5. *J. Am. Ceram. Soc.* **42**, 487 (1959).

[25] H. P. Kirchner, K. M. Merz, and W. R. Brown: Thermal Expansion of Uranium Pyrophosphate and Ceramic Bodies in the System UO_2-P_2O_7. *J. Am. Ceram. Soc.* **46**, 137 (1963).

[26] K. Laud and F. A. Hummel: The system ThO_2-P_2O_5. *J. Am. Ceram. Soc.* **54**, 296 (1971).

[27] K. R. Laud and F. A. Hummel: Subsolidus Relations in the System ZrO_2-ThO_2-P_2O_5. *J. Am. Ceram. Soc.* **54**, 407 (1971).

[28] D. Taylor: Thermal Expansion Data: XIII Complex Oxides with chain, ring and layer structures and apatites. *Br. Ceram. Trans. J.* **87**, 88 (1988).

[29] C.-H. Huang, O. Knop, and D. A. Othen: Pyrophosphates of Tetravalent Elements and a Mossbauer Study of SnP_2O_7. *Can. J. Chem.* **53**, 79 (1975).

[30] N. Kinomura, M. Hirose, N. Kumada, et al.: Molybdenum (IV) Pyrophosphate Isostrucutral with ZrP_2O_7. *Mat. Res. Bull.* **20**, 379 (1985).

[31] E. Tillmans, W. Gebert, and W. H. Baur: Computer Simulations of Crystal Structures Aplied to the Solution of the Superstructure of Cubic Silicondiphosphate. *J. Solid State Chem.* **7**, 69 (1973).

[32] R. L. Withers, Y. Tabira, J. S. O. Evans, et al.: A New Three-Dimensional Incommensurately Modulated Cubic Phase (in ZrP_2O_7) and it Symmetry Characterization via Temperature-Dependent Electron Diffraction. *J. Solid State Chem.* **157**, 186 (2001).

[33] A. K. A. Pryde, K. D. Hammonds, M. T. Dove, et al.: Origin of the Negative Thermal Expansion in ZrW_2O_8 and ZrV_2O_7. *J. Phys. Condens. Matter* **8**, 10973 (1996).

[34] R. Sacks, Y. Avigal, and E. Banks: New Solid Electrolytes Based on Cubic ZrP_2O_7. *J. Electrochem. Soc.* **129**, 726 (1982).

[35] T. Ota and I. Yamai: Thermal expansion of ZrP_2O_7 and related solid solutions. *J. Mater. Sci.* **22**, 3762 (1987).

[36] E. Dowty, computer code ATOMS, Shape Software, Kingsport, TN (2000).

[37] A. C. Larson and R. B. Von Dreele, computer code General Structural Analysis System, Los Alamos National Laboratory, Los Alamos, NM (2000).

[38] B. H. Toby: EXPGUI, a graphical user interface for GSAS. *J. Appl. Crystallogr.* **34**, 210 (2001).

[39] R. D. Shannon and C. T. Prewitt: Effective Ionic Radii in Oxides and Fluorides. *Acta Crystallogr., Sect. B* **25**, 925 (1969).

[40] M. Catti and S. Stramare: Lithium location in NASICON-type Li^+ conductors by neutron diffraction. II. Rhombohedral α-$LiZr_2(PO_4)_3$ at T = 423 K. *Solid State Ionics* **136-137**, 489 (2000).

[41] M. Catti, S. Stramare, and R. Ibberson: Lithium location in NASICON-type Li^+ conductors by neutron diffraction. I. Tricilinic α'-$LiZr_2(PO_4)_3$. *Solid State Ionics* **123**, 173 (1999).

CHAPTER 7

THERMAL EXPANSION AND PHASE TRANSITIONS IN $(M^{III}_{0.5}M^{V}_{0.5})P_2O_7$-TYPE COMPOUNDS

Abstract

Cation ordering/disordering can significantly affect the properties (phase transitions, thermal and electric behavior, etc.) of solid materials. In $(M^{III}_{0.5}M^{V}_{0.5})P_2O_7$-type compounds with the cubic ZrP_2O_7 structure, a disordered arrangement of the cations was expected to suppress the typical phase transition seen in ZrP_2O_7-related materials and stabilize the high-temperature low thermal expansion structure. Also, by controlling the ordering of the M^{III}/M^{V} cations in the structure we hoped to control the thermal expansion properties of the materials. In this study, a range of $M^{III}M^{V}(P_2O_7)_2$ compounds (M^{III}= Al^{3+}, Fe^{3+}, Ga^{3+}, In^{3+}, Y^{3+}, Nd^{3+} and Bi^{3+}; M^{V}= Nb(V), Ta(V)) have been prepared including several new compositions. Different heat treatments have been used in an attempt to manipulate the cation ordering. Thermal history seems to have little effect on cation ordering. We found that the thermal expansion of the high-temperature phase can be lowered relative to that for ZrP_2O_7 through the substitution of Zr by a combination of M^{III} and M^{V} cations in the case of $Y_{0.5}Nb_{0.5}P_2O_7$. However, different cation combination led to different thermal expansion behavior. A decrease in thermal expansion at higher temperature, suggesting that there may be an order-disorder type phase transition similar to that in ZrP_2O_7, was only observed for $Y_{0.5}Nb_{0.5}P_2O_7$. The materials $Al_{0.5}Ta_{0.5}P_2O_7$ and $In_{0.5}Nb_{0.5}P_2O_7$ show increased thermal expansion at high temperatures compared to ZrP_2O_7.

7.1 Introduction

Cation ordering can significantly affect the properties (phase transitions, thermal and electric behavior, etc.) of solid materials. The influence of M^{III} and M^{V} cation ordering on ferroelectric properties has been shown in the perovskite ferroelectrics $PbIn_{0.5}Nb_{0.5}O_3$ (PIN)[1-4] and $PbSc_{0.5}Ta_{0.5}O_3$ (PST, see section 1.5.2).[5-9]

The structure and thermal behavior of cubic ZrP_2O_7, which will be our prototype compound for this chapter, was already discussed in sections 1.2.1 and 6.1. The material undergoes a phase transition from an ordered superstructure with normal positive thermal expansion to a disordered high-temperature (also referred to as "ideal") structure that exhibits low intermediate thermal expansion (CTE = $3.5x10^{-6}$ K^{-1}) at ~290 ^{o}C (see Figure 7.1).[10]

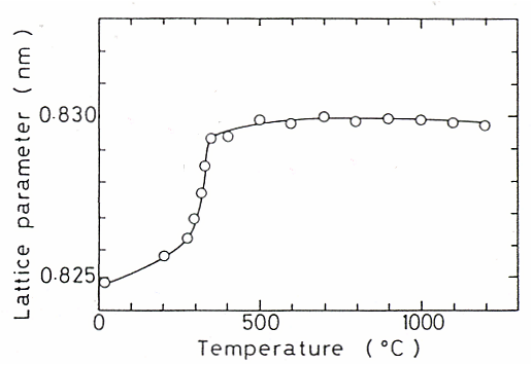

Figure 7.1: Thermal expansion of cubic ZrP_2O_7. There is a dramatic change in the CTE through the phase transition. Taken from Ota and Yamai.[11]

There have been prior reports of pyrophosphate materials with mixed M^{III}/M^{V} cations. Oyetola *et al.* have reported the preparation of $(M^{III}_{0.5}M^{V}_{0.5})P_2O_7$ compositions (where M^{III} = Sb, Bi, Nd or Eu and M^{V} = Nb, Sb or Ta), having structures closely related to that of cubic ZrP_2O_7.[12, 13] These materials can be thought of as ZrP_2O_7 with the Zr "replaced" by two metal ions, an M^{III} and an M^{V}, in 1:1 molar ratio. They reported long-

range ordering of the M^{III}/M^{V} cations in some of their samples with the β-SbP_2O_7 structure (closely related to cubic ZrP_2O_7), and short-range ordering in their cubic $Eu_{0.5}Ta_{0.5}P_2O_7$ sample. Oyetola *et al.* speculated that cation ordering occurs due to size differences.[12] Although, in materials of this type, the dominant driving force for ordering is likely to be the requirement of local charge balance, size differences may also play an important role. In analogy to previous observations in the perovskite ferroelectrics,[1-3, 7, 8] it seemed possible that the degree of cation ordering in the material could be manipulated by the heat treatment conditions used during sample preparation as well as the choice of the metal ions (M^{III} and M^{V}). If the sample is cooled down from the synthesis temperature very slowly, it might be expected to show at least partial cation ordering. On the other hand, quenched samples are expected to display a "frozen" snapshot of the high-temperature disordered state.

It should be noted that cation ordering, that has to do with the occupancy of the cations among crystallographic sites, should be distinguished from ordering of the structure in the context of an disorder-order phase transition, which in the case of ZrP_2O_7, involves the order of P_2O_7 units, in particular the bending of the P-O-P bond angles to avoid the unfavorable 180^o angles present in the high-temperature superstructure.

To the best of our knowledge, no studies have been done on the thermal expansion and phase transition behavior of the reported $(M^{III}_{0.5}M^{V}_{0.5})P_2O_7$ phases. However, cubic $Bi_{0.5}Ta_{0.5}P_2O_7$ made by Oyetola *et al.* appears to adopt the ideal (high-temperature) ZrP_2O_7-structure at room temperature as they did not observe extra reflections indicative of a superstructure.[12] Manipulating the degree of ordering in the M^{III}/M^{V} cation arrangement was investigated as a mean for tuning both the thermal expansion properties

and phase transitions seen in these materials. A disordered arrangement of the cations was expected to suppress the typical phase transition seen in ZrP_2O_7-related materials and stabilize the high-temperature low thermal expansion structure.

In the present work, the synthesis of several new $(M^{III}_{0.5}M^{V}_{0.5})P_2O_7$ phases was accomplished, and their thermal expansion as well as their phase transition behavior was studied by a combination of x-ray diffraction and thermal analysis methods.

7.2 Experimental

7.2.1 Syntheses

The $(M^{III}_{0.5}M^{V}_{0.5})P_2O_7$ phases were prepared by a solution/sol-gel route with the exception of $Bi_{0.5}Ta_{0.5}P_2O_7$. The solution route made use of a very reactive 5+ cation source, tantalum or niobium pentaethoxide, and involved the dissolution of a salt of the 3+ cation (usually nitrate pentahydrate) in absolute ethanol and the use of the chelating agent acethyl acetonate (2,4-pentanedione or acac) to slow down the hydrolysis of the ethoxide. A mixture containing the M^{V}-pentaethoxide, ethanol and acac in a 1:10:2 ratio was added to an ethanolic solution of the M^{III} cation while stirring. The amount of ethanol used to dissolve the salt of the M^{III} cation was kept to the minimum needed to dissolve all the salt (typically ~5-6 ml was needed per mmol cation). Finally, a stoichiometric amount of $(NH_4)_2HPO_4$, dissolved in the minimum amount of water necessary, was quickly added to the mixture, and a gelatinous precipitate formed. A xerogel was obtained by drying the mixture at 100 ^{o}C overnight. The xerogel was decomposed by heating to 350 ^{o}C for 4 hours. Finally, the powder was fired at 1000 ^{o}C overnight.

For the preparation of $Bi_{0.5}Ta_{0.5}P_2O_7$, a "slurry" was made from the Ta-pentaethoxide:ethanol:acac 1:10:2 mixture, crystalline $Bi(NO_3)_3 \cdot 5H_2O$ and concentrated (85 %) phosphoric acid in a platinum crucible. The slurry was stirred for 20 minutes, dried at 200 ^oC overnight then heated at 700 ^oC for 12 hours.

"Fast-cooled" and "slow-cooled" samples were prepared in order to examine the effect of thermal history on cation ordering. Fast-cooled samples were taken out of the furnace and were air-quenched to room temperature. Slow-cooled samples were cooled in the furnace at a rate of ~1 ^oC/min.

For the studies of cation ordering on prolonged annealing (see section 7.3.4), four portions of selected samples as loose powders were heated to 600, 700, 800 and 900 ^oC, respectively, in covered crucibles and held at those temperatures for 19 days. These samples were cooled down in air (fast cooling).

7.2.2 Laboratory x-ray diffraction

Laboratory powder X-ray diffraction patterns were recorded for all of the samples using a Scintag X1 diffractometer. This instrument was equipped with a Cu Kα radiation source and a Scintag Peltier-cooled solid state detector. For most of the reported data sets, a scan rate of 2.5^o/min and a step size of 0.02° were employed along with a 251 mm diffractometer radius, 2/1 mm slits on the tube side and 0.5/0.3 mm slits on the detector side. Data with better statistics used for Rietveld refinement purposes were collected with scan rates of 0.1-0.2^o/min. The variable temperature in-house measurements made use of a Scintag High-Low variable temperature stage attachment that allowed data collection between -196 ^oC (with liquid nitrogen) and 300 ^oC under vacuum (see section 2.1.1).

High-temperature powder x-ray diffraction experiments were also carried out using two other instruments with optical systems that eliminated problems due to the variation of sample height with temperature. Early data for $In_{0.5}Nb_{0.5}P_2O_7$ and $Y_{0.5}Nb_{0.5}P_2O_7$ were collected at the High Temperature Materials Laboratory (HTML), Oak Ridge National Laboratory (Oak Ridge, TN) on a Philips X'Pert PRO MPD x-ray diffractometer with copper K_α radiation, a high count rate proportional detector (Miniprop) and an Anton-Paar XRK900 high-temperature stage. Polycapillary lens optics (10 mm x 10 mm aperture) and a 0.09^o parallel plate collimator with Soller slits were used on the incident and diffracted beam sides, respectively.

Additional data for $Al_{0.5}Ta_{0.5}P_2O_7$, $In_{0.5}Nb_{0.5}P_2O_7$ and $Y_{0.5}Nb_{0.5}P_2O_7$ were collected on an X'Pert PRO MPD diffractometer from PANalytical in the X-ray Analysis Group, Materials Science and Engineering, Georgia Tech with Cu Kα radiation from a 1.8 kW special ceramic copper tube. A parallel beam configuration (PreFIX optics) with 0.04 degree Soller slits was used on the incident beam side and 0.09 degree parallel plate collimators on the diffracted beam side. A scintillation detector was used during data collection. An Anton-Paar HTK1200 high-temperature furnace was used for the measurements (see Figure 2.2). For temperature calibration, two NIST DTA temperature standards (NIST, Gaithersburg, MD) were used: $KClO_4$ and Ag_2SO_4 (standard # 8759).

Analysis of the diffraction data to extract lattice constants and peak profile parameters were carried out by Le Bail fitting using the program GSAS[14] with the EXPGUI interface.[15]

7.2.3 Thermal analysis

Thermal analysis measurements were made with a Seiko 220 DSC instrument in the School of Polymer, Textile & Fiber Engineering, Georgia Tech. The instrument can be used for experiments up to 600 °C in nitrogen, oxygen or in air. Temperature calibration was checked with the ICTA (International Center for Thermal Analysis) standard set 759. All DSC peaks were observed at temperatures of ± 3 °C of the certified value, indicating that the instrument was well calibrated.

7.3 Results and discussion

7.3.1 Phase identification and variation of lattice constants with cation size

The room temperature lattice constant and average cation size are listed for all samples prepared in Table 7.1. The compositions $Al_{0.5}Ta_{0.5}P_2O_7$, $Ga_{0.5}Ta_{0.5}P_2O_7$, $Fe_{0.5}Ta_{0.5}P_2O_7$, $In_{0.5}Nb_{0.5}P_2O_7$ and $Y_{0.5}Nb_{0.5}P_2O_7$ have been prepared for the first time. The lattice constants show a trend with the average size of the cations substituting for Zr^{4+}: the larger the cations are, the larger the unit cell (see also Figure 7.3). $In_{0.5}Nb_{0.5}P_2O_7$ has a smaller unit cell than ZrP_2O_7, the "parent" compound with the same average octahedral cation size. This may be due to differences in the ordering of different size cations. $Bi_{0.5}Ta_{0.5}P_2O_7$ also displays a smaller lattice constant than expected based on the size of Bi^{3+}. However, the quality of the $Bi_{0.5}Ta_{0.5}P_2O_7$ sample was rather poor based on its x-ray diffraction pattern and it is possible that the phase does not have the exact target composition. A composition with more Ta than Bi in the octahedral sites, coupled with a necessary number of crystal defects (cation vacancies) to maintain charge balance, could result in a unit cell size smaller than expected.

Table 7.1: Ionic radii and lattice constants for $(M^{III}_{0.5}M^{V}_{0.5})P_2O_7$ compounds prepared by quenching. The ionic radii are given as the average radii of the M^{3+} and M^{5+} cations (six-coordination). The lattice constants were determined from Le Bail fitting of room temperature diffraction data. Sample KMW122 was kindly provided by Kathy White. Cation radii are taken from Shannon and Prewitt.[16] For Fe^{3+}, the high-spin radius was used as Fe^{3+} is more likely to be in the high-spin state in similar oxides.

Sample	Cation size (pm)	RT lattice constant (Å)
$Al_{0.5}Ta_{0.5}P_2O_7$ VTAlTa3	72.8	7.8863(5)
$Ga_{0.5}Ta_{0.5}P_2O_7$ VTGaTa6	77	7.9233(12)
$Fe_{0.5}Ta_{0.5}P_2O_7$ VTFeTa1	78.2	7.9807(3)
ZrP_2O_7 KMW122	86	8.2416(2)
$In_{0.5}Nb_{0.5}P_2O_7$ VTInNb1	86	8.0896(1)
$Y_{0.5}Nb_{0.5}P_2O_7$ VTYNb1	91	8.2617(2)
$Nd_{0.5}Ta_{0.5}P_2O_7$ VTNdTa7	95.2	8.3047(5)
$Bi_{0.5}Ta_{0.5}P_2O_7$ VTBiTa10	97.5	8.2334(3)

$In_{0.5}Nb_{0.5}P_2O_7$, $Y_{0.5}Nb_{0.5}P_2O_7$ and $Al_{0.5}Ta_{0.5}P_2O_7$ were prepared successfully with only small amounts of impurities (see Figure 7.2a). Traces of $InPO_4$ and $TaPO_5$ as well as $AlPO_4$ and $TaPO_5$ were found in $In_{0.5}Nb_{0.5}P_2O_7$ and $Al_{0.5}Ta_{0.5}P_2O_7$, respectively. A small amount of an impurity phase was found in $Y_{0.5}Nb_{0.5}P_2O_7$ by XRD which was not successfully identified. These three samples were further examined by variable temperature XRD and DSC. The samples $Fe_{0.5}Ta_{0.5}P_2O_7$, $Bi_{0.5}Ta_{0.5}P_2O_7$, $Ga_{0.5}Ta_{0.5}P_2O_7$ and $Nd_{0.5}Ta_{0.5}P_2O_7$ (see Figure 7.2b) contained larger amounts of impurities ($TaPO_5$ and $NdPO_4$) and/or were not well crystallized and therefore were not used further.

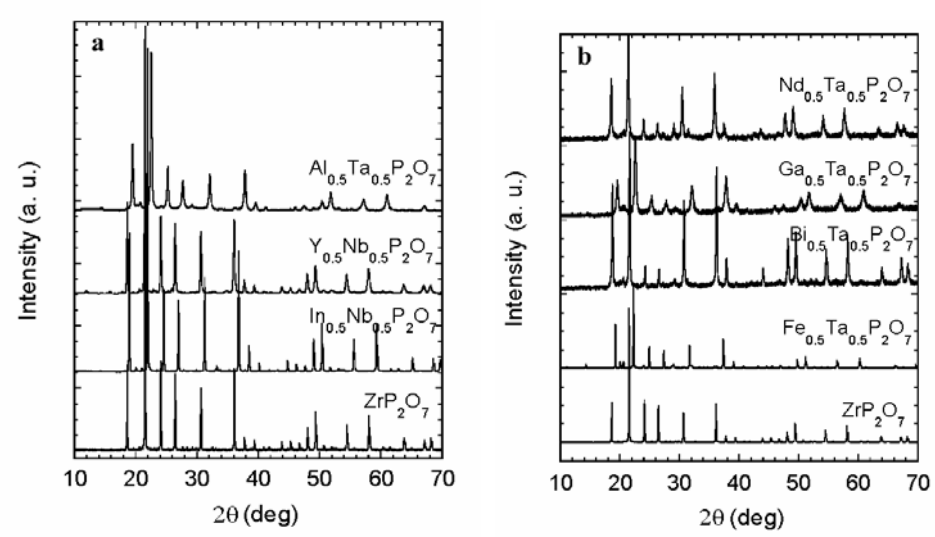

Figure 7.2: X-ray patterns of the samples prepared by quenching; a) samples with almost no impurities - $In_{0.5}Nb_{0.5}P_2O_7$, $Y_{0.5}Nb_{0.5}P_2O_7$ and $Al_{0.5}Ta_{0.5}P_2O_7$; b) samples with more impurities - $Fe_{0.5}Ta_{0.5}P_2O_7$, $Bi_{0.5}Ta_{0.5}P_2O_7$, $Ga_{0.5}Ta_{0.5}P_2O_7$ and $Nd_{0.5}Ta_{0.5}P_2O_7$.

The lattice constants were determined by Le Bail fitting of the laboratory x-ray diffraction data. As was discussed in Chapter 6, the unit cell size of cubic pyrophosphates varies in an almost linear fashion with the radius of the octahedral cation. We made a comparison with the data for MP_2O_7 compounds (Figure 6.3), in order to see whether the trend is valid for $(M^{III}_{0.5}M^{V}_{0.5})P_2O_7$ compounds when the radii of the M^{III} and M^{V} cations are averaged. Figure 7.3a shows the lattice constant as a function of cation radius for our $M^{III}_{0.5}M^{V}_{0.5}P_2O_7$ compositions, while Figure 7.3b shows the same data along with the lattice constants for the MP_2O_7 compounds, where M is a 4+ cation. The variation of our M^{III} / M^{V} lattice constants with average ionic radius (closed circles in Figure 7.2b) follows the same trend as the MP_2O_7 compounds.

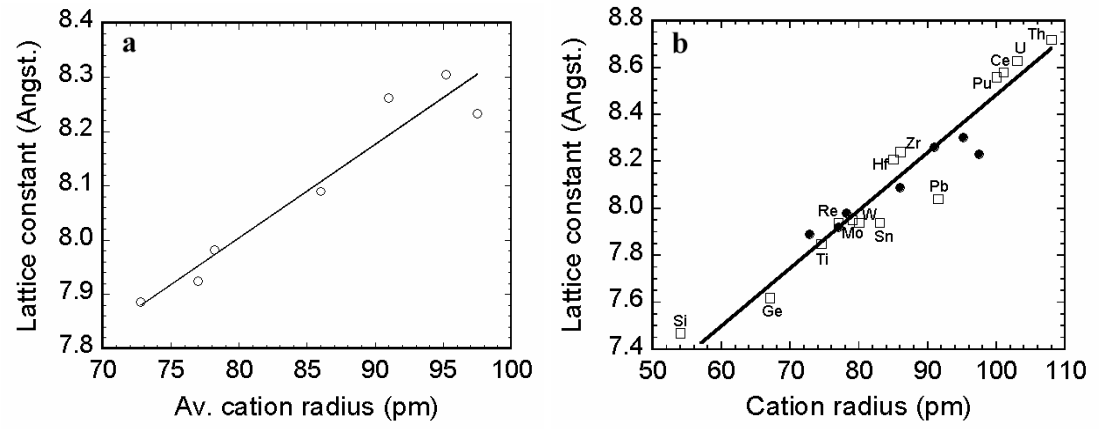

Figure 7.3: Variation of the lattice constant for different $(M^{III}_{0.5}M^{V}_{0.5})P_2O_7$ phases with the average size of the substituting cations (data from Table 7.1); (a); Lattice constant vs. size of the M^{4+} ion for cubic MP_2O_7 compounds (open symbols) and vs. the average cation size for $(M^{III}_{0.5}M^{V}_{0.5})P_2O_7$ samples (closed symbols) (b).

7.3.2 The effect of replacing M^{IV} by $(M^{III}_{0.5}M^{V}_{0.5})$ on the order-disorder phase transition in $M^{III}_{0.5}M^{V}_{0.5}P_2O_7$ compositions

DSC analysis of quenched $In_{0.5}Nb_{0.5}P_2O_7$ and $Y_{0.5}Nb_{0.5}P_2O_7$ showed no endothermic peak at all (see Figure 7.4) suggesting that an order-disorder phase transition typical of ZrP_2O_7 either occurred over a very wide temperature range so that is was not visible in the DSC, or it did not occur at all. It is possible that these compounds adopt the high-temperature ideal cubic ZrP_2O_7 structure even at room temperature as reported for $Bi_{0.5}Ta_{0.5}P_2O_7$ by Oyetola *et al.*[12] If the ideal disordered structure was adopted by these materials at room temperature, it might be advantageous relative to ZrP_2O_7, as this structure has a low thermal expansion coefficient.

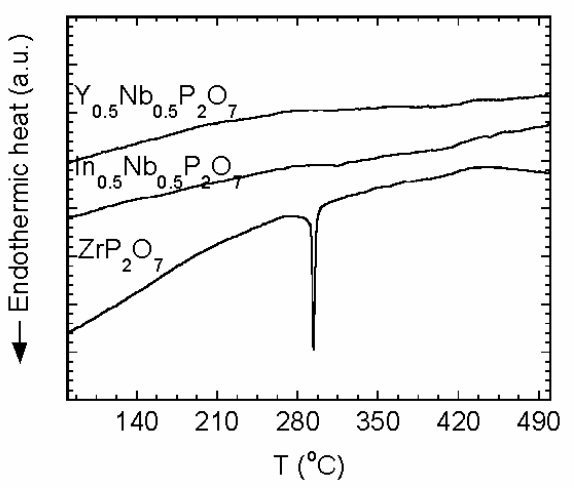

Figure 7.4: DSC of quenched $In_{0.5}Nb_{0.5}P_2O_7$ and $Y_{0.5}Nb_{0.5}P_2O_7$ compared with that of ZrP_2O_7.

In order to explore the possibility of cation ordering in the samples, with the goal of examining the effect of cation ordering on the thermal properties, the samples of $In_{0.5}Nb_{0.5}P_2O_7$ and $Y_{0.5}Nb_{0.5}P_2O_7$ were split into two halves and held at the synthesis temperature (1000 ^oC) for 30 minutes. One half was then quenched rapidly to room temperature, while the other half was let to cool down in the furnace very slowly. Comparison of the DSC of the fast- and slow-cooled samples showed only very small differences (see Figure 7.5).

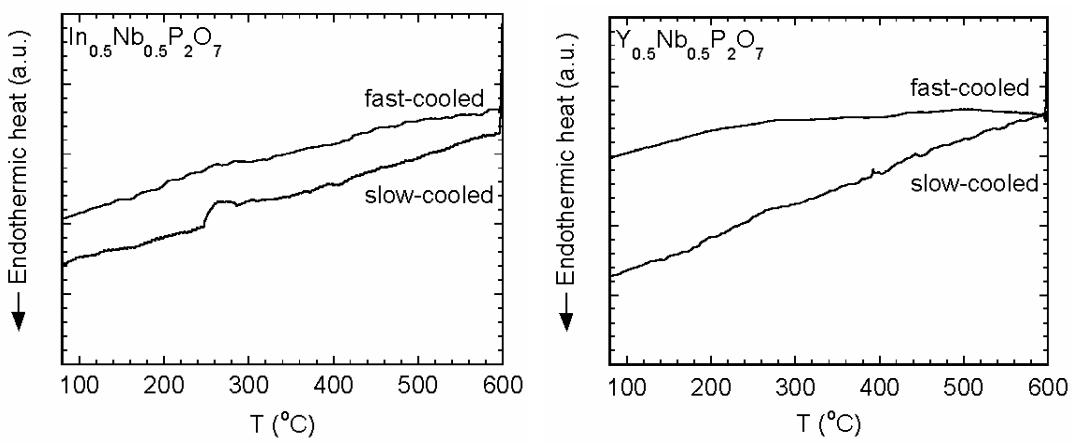

Figure 7.5: Effect of heat treatment conditions on the thermal properties in $In_{0.5}Nb_{0.5}P_2O_7$ and $Y_{0.5}Nb_{0.5}P_2O_7$ as seen by DSC.

If ordering of the cations was achieved to a significant extent upon slow-cooling of the material, one would expect a difference between the DSC curves of the samples with a less ordered and a more ordered arrangement of cations, respectively. Provided that, similarly to ZrP_2O_7, both the ordered 3 x 3 x 3 superstructure and the disordered structure is possible in these materials, the ordered sample would show an endotherm marking the phase transition to the disordered structure at some temperature. However, no apparent sign of a phase transition is visible in the DSC graphs for any of the samples. Careful inspection of the graphs around the 300 ^oC region (where the transition occurs in ZrP_2O_7) shows a bump in the "slow-cooled" curve between 250 and 300 ^oC. A broad bump is clearly visible in the case of $In_{0.5}Nb_{0.5}P_2O_7$, which rather looks like an experimental/instrumental artifact. However, the feature was reproducible upon repeating the measurement. Still, these features cannot be considered as proof of a phase transition.

7.3.3 The effect of slow cooling on cation ordering as seen by XRD

Comparison of the room temperature x-ray diffraction patterns for fast-cooled and slow-cooled $In_{0.5}Nb_{0.5}P_2O_7$ and $Y_{0.5}Nb_{0.5}P_2O_7$ samples, respectively, shows an interesting result (see Figure 7.6). The peak positions for the slow-cooled samples were slightly shifted to higher 2θ values in all cases suggesting that the lattice constant got slightly smaller. The fact that it was observed in all sample pairs studied (at least five: samples VTInNb1-2, VTYNb1-2 and VTYNb3) suggests that the finding is not an experimental artifact due to sample packing differences or instrument problems. This shift meant a change of 0.1 degree 2θ in the case of $In_{0.5}Nb_{0.5}P_2O_7$ (strongest peak shifted from 22.060 to 22.160 degrees) resulting in lattice parameter change of about a hundredth of an Angstrom from 8.0878(2) to 8.0808(2). The same ~0.1 degree shift for $Y_{0.5}Nb_{0.5}P_2O_7$ (21.554 to 21.667) resulted in a change in the lattice constant of about the same magnitude, from 8.2613(3) to 8.2480(3).

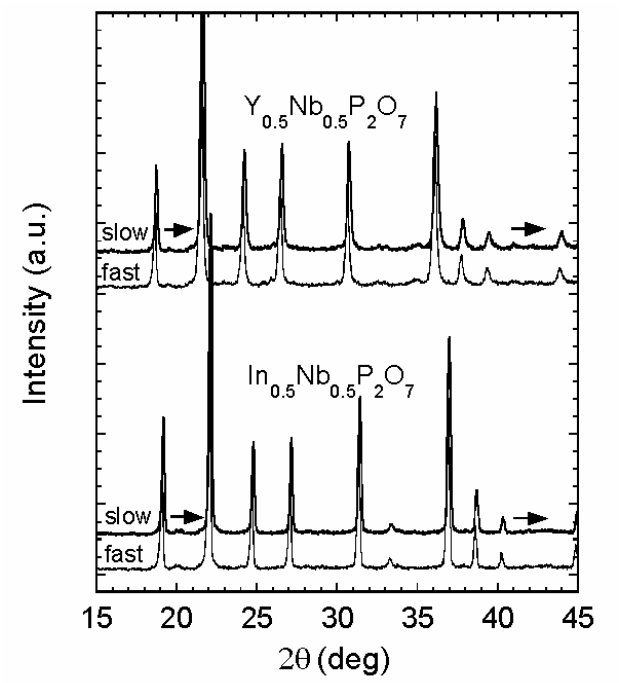

Figure 7.6: Shift of the positions of the diffraction peaks to higher angles for $In_{0.5}Nb_{0.5}P_2O_7$ and $Y_{0.5}Nb_{0.5}P_2O_7$ samples indicating a slightly smaller unit cell size in the slow-cooled samples.

The more ordered the structure, the smaller the size of the unit cell. Therefore, this observation suggests a difference in the degree of cation ordering between the fast-cooled and slow-cooled samples. When the sample undergoes slow cooling, the ions have more time to move around and find the sites corresponding to higher degree of ordering, because higher temperature required for thermal motion is maintained for longer. Ordering could be accompanied by an appearance of extra diffraction peaks as cations sites that used to be equivalent in the disordered state become unique. However, if the ordering does not take place over a long range, then the extra reflections are so broad that they are not visible in the x-ray pattern. These results, therefore, suggest that the cation ordering that occurred on slow-cooling, if any, was only on a short length scale.

7.3.4 Study of cation ordering on annealing

Equal portions of $In_{0.5}Nb_{0.5}P_2O_7$, $Y_{0.5}Nb_{0.5}P_2O_7$ and $Al_{0.5}Ta_{0.5}P_2O_7$ sample were held at four different temperatures (600, 700, 800 and 900 ^oC) for 19 days in order to look for cation ordering on prolonged annealing. All samples were air-quenched from the temperature of the heat treatment. Visual examination of the diffraction patterns for the annealed samples did not reveal any obvious differences in the positions of the peaks (see Figure 7.7). Had there been a change in cation ordering with the temperature of heat treatment, a change in peak positions or maybe extra superstructure reflections would have occurred.

However, changes in sample composition were observed for two of the materials. In $Y_{0.5}Nb_{0.5}P_2O_7$, as the annealing temperature increased, the amount of impurity phases/decomposition products also increased. The sample that was annealed at 900 ^oC seemed to contain some remaining cubic pyrophosphate phase and decomposition products, from which only $NbPO_5$ was positively identified. The impurities in the $Al_{0.5}Ta_{0.5}P_2O_7$ sample also became quite significant on annealing. Only the $In_{0.5}Nb_{0.5}P_2O_7$ (all temperatures) and $Y_{0.5}Nb_{0.5}P_2O_7$ (up to the 800 ^oC sample) were of sufficient quality after annealing for Rietveld analysis to look for cation ordering.

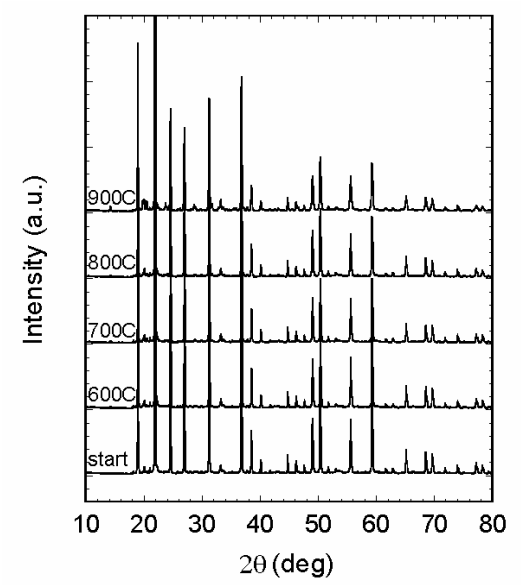

Figure 7.7: Diffraction patterns for $In_{0.5}Nb_{0.5}P_2O_7$ samples after different heat treatment conditions. The starting sample is the one synthesized at 1000 ^oC and quenched in air. The other samples were held for 19 days at the temperatures indicated in the figure. No major changes were detected.

Le Bail fitting of the diffraction data for the $In_{0.5}Nb_{0.5}P_2O_7$ and $Y_{0.5}Nb_{0.5}P_2O_7$ samples showed that the lattice constants remained practically unchanged as the annealing conditions varied, and actually all values agree with earlier lattice constants for the as-synthesized samples (see Table 7.1). An analysis of the peak shapes and widths, the Gaussian (GW) and Lorentzian (LY) peak parameters, showed no observable trend in the GWs (see Table 7.2). However, the LY component of our model related to the microstrain in the material showed an increase with annealing temperature. As the "as synthesized" sample had the smallest LY value, this suggests that the microstrain may have increased due to phosphate loss on prolonged heating. The higher the temperature of the heat treatment, the greater the phosphate loss may have been and thus the degree of microstrain. The lack of change in the lattice constants on annealing at any temperature

suggests that cation ordering, or the lack of it, is not sensitive to the annealing conditions examined.

Table 7.2: Fitting results on XRD data of $In_{0.5}Nb_{0.5}P_2O_7$ and $Y_{0.5}Nb_{0.5}P_2O_7$ samples exposed to a series of different heat treatments. Portions of the "as made" samples synthesized at 1000 ^oC were heated at 600, 700, 800 and 900 ^oC for 19 days.

$In_{0.5}Nb_{0.5}P_2O_7$ (VTInNb1)		**$Y_{0.5}Nb_{0.5}P_2O_7$** (VTYNb1)	
As made (1000 ^oC)	a = 8.0893(1) Å GW = 13.3(3) **LY = 9.0(3)**	As made (1000 ^oC)	a = 8.2607(3) Å GW = 36.6(9) **LY = 27.6(5)**
600 ^oC	a = 8.0885(1) Å GW = 14.6(3) **LY = 13.4(2)**	600 ^oC	a = 8.2604(2) Å GW = 24.8(7) **LY = 38.4(4)**
700 ^oC	a = 8.0903(1) Å GW = 10.2(3) **LY = 15.6(2)**	700 ^oC	a = 8.2610(2) Å GW = 19.4(7) **LY = 41.2(4)**
800 ^oC	a = 8.0912(1) Å GW = 12.8(3) **LY = 16.3(2)**	800 ^oC	a = 8.2596(2) Å GW = 20.6(8) **LY = 42.3(4)**
900 ^oC	a = 8.0893(2) Å GW = 15.4(5) **LY = 21.8(3)**		

7.3.5 Thermal expansion in $(M^{III}_{0.5}M^{V}_{0.5})P_2O_7$ compounds

In the light of the DSC results discussed in section 7.3.2, we were eager to determine the thermal expansion coefficients for some of our $(M^{III}_{0.5}M^{V}_{0.5})P_2O_7$ phases. The variation of the lattice constants with temperature is also very sensitive to phase transformations (see Figure 6.2), thus the change in (or the invariance of) thermal

expansion can decide whether the lack of an endothermic peak in the DSC indicates the non-existence of a phase transition.

Several variable temperature x-ray studies have been carried out on the samples $In_{0.5}Nb_{0.5}P_2O_7$ and $Y_{0.5}Nb_{0.5}P_2O_7$ in the 25 – 600 ^oC and the -200 – 600 ^oC temperature range, respectively, as well as one experiment on $Al_{0.5}Ta_{0.5}P_2O_7$ between 25 – 600 ^oC. Lattice constants were obtained using Le Bail fits at each temperature. The data are tabulated in Table 7.3. The variation of the lattice constant with temperature for all three materials is shown in Figures 7.8-7.11. In all three cases, we see a change in the slope the thermal expansion curves with temperature. This change is rather slight for $Al_{0.5}Ta_{0.5}P_2O_7$ and $In_{0.5}Nb_{0.5}P_2O_7$ and appears to be an increase in slope from around 285 and 260 ^oC, respectively. For $Y_{0.5}Nb_{0.5}P_2O_7$, the slope of the curve becomes smaller at higher temperature. These changes in the thermal expansion of all samples were reproducible. In Figures 7.9 and 7.10, two datasets from two different experiments carried out on the same samples but different instruments are plotted. A straight line was fit to the two regions of different slopes in all cases and the corresponding thermal expansion coefficients were calculated.

Table 7.3: Lattice constants (*a*) for $(M^{III}_{0.5}M^{V}_{0.5})P_2O_7$ samples as a function of temperature as obtained by Le Bail fitting of the variable temperature XRD data. Top table: MSE, Georgia Tech data (GT) and HTML, Oak Ridge data (HTML); bottom table: data collected in-house on the Scintag instrument.

Temp. (°C)	**$Al_{0.5}Ta_{0.5}P_2O_7$ (VTAlTa1)**	**$In_{0.5}Nb_{0.5}P_2O_7$ (VTInNb2)**	**$Y_{0.5}Nb_{0.5}P_2O_7$ (VTYNb1)**	**Temp. (°C)**	**$In_{0.5}Nb_{0.5}P_2O_7$ (VTInNb2)**	**$Y_{0.5}Nb_{0.5}P_2O_7$ (VTYNb1)**
	a (Å) - GT	***a (Å) – GT***	***a (Å) - GT***		***a (Å) - HTML***	***a (Å) - HTML***
20	7.8855(3)	-	-	25	8.0862(2)	8.2557(2)
25	-	8.0895(1)	8.2583(2)	50	8.0903(2)	8.2597(3)
30	7.8865(2)	8.0897(1)	-	110	8.0929(2)	8.2621(4)
40	-	-	8.2580(2)	170	8.0967(2)	8.2652(5)
55	7.8876(3)	8.0921(1)	8.2593(2)	200	8.0989(3)	8.2671(4)
105	7.8915(3)	8.0965(1)	8.2619(2)	260	8.1037(3)	8.2700(3)
155	7.8966(3)	8.1017(1)	8.2646(2)	290	8.1067(3)	8.2705(3)
210	7.9003(3)	8.1065(1)	8.2667(2)	320	8.1087(3)	8.2721(3)
260	7.9049(3)	8.1117(1)	8.2689(2)	350	8.1109(3)	8.2734(3)
285	7.9064(3)	8.1142(2)	8.2701(2)	400	8.1165(4)	8.2747(4)
310	7.9082(3)	8.1169(1)	8.2712(2)	500	8.1263(5)	8.2760(4)
335	7.9107(3)	8.1194(1)	8.2721(2)	600	8.1350(6)	8.2778(4)
360	7.9130(3)	8.1220(1)	8.2729(3)			
410	7.9176(3)	8.1274(1)	8.2750(3)			
460	7.9234(3)	8.1332(1)	8.2767(3)			
510	7.9283(3)	8.1389(1)	8.2784(3)			
560	7.9345(3)	8.1447(1)	8.2800(3)			
610	7.9397(3)	8.1494(1)	8.2814(3)			

Temp. (°C)	**$Y_{0.5}Nb_{0.5}P_2O_7$ (VTYNb1)**	**Temp. (°C)**	**$Y_{0.5}Nb_{0.5}P_2O_7$ (VTYNb1)**
	a (Å)		***a (Å)***
-196	8.2547(3)	-25	8.2606(4)
-185	8.2543(3)	0	8.2608(5)
-165	8.2544(3)	25	8.2618(3)
-145	8.2551(3)	50	8.2605(3)
-125	8.2559(3)	110	8.2654(3)
-105	8.2563(3)	170	8.2688(3)
-85	8.2562(3)	200	8.2698(3)
-65	8.2576(3)	260	8.2724(3)
-45	8.2580(3)	290	8.2730(3)

It should be noted that dividing the curves into two regions and fitting straight lines to them is somewhat biased by the expectation that these materials, similarly to cubic ZrP_2O_7, may show a phase transition somewhere around 300 °C. Therefore, for a more

objective representation of the data, a graph without the straight lines was also included for each compound. The change of the thermal expansion coefficient can also be represented by a smoothly bending curve, which might be expected for a phase transition occurring over a broad temperature range (DSC results). Fitting straight lines to the regions of apparently different slope and obtaining the linear thermal expansion coefficients is a simplified, yet informative, view of these changes.

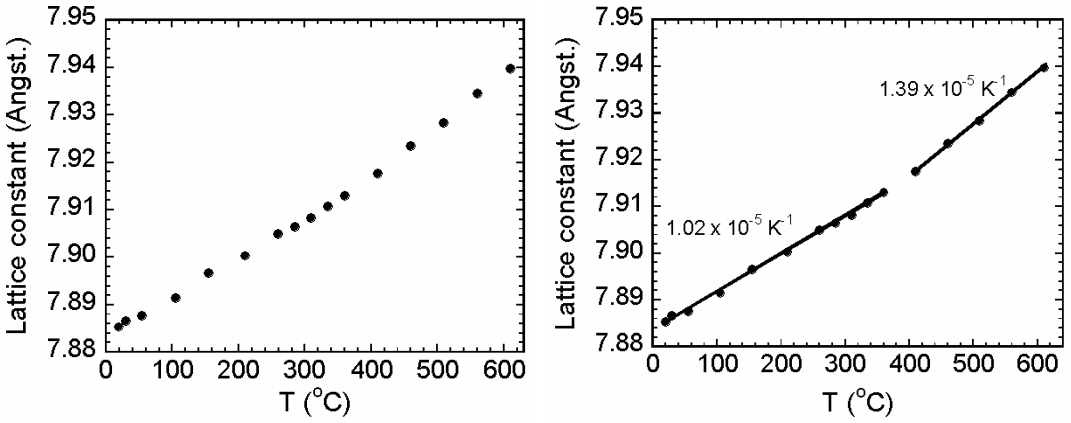

Figure 7.8: Variation of the lattice constant with temperature in $Al_{0.5}Ta_{0.5}P_2O_7$. Straight lines are fitted to the curve over the low- and high-temperature regions, resp. The thermal expansion coefficient gets larger above 360 °C. Data collected on the PANalytical instrument of MSE, Georgia Tech.

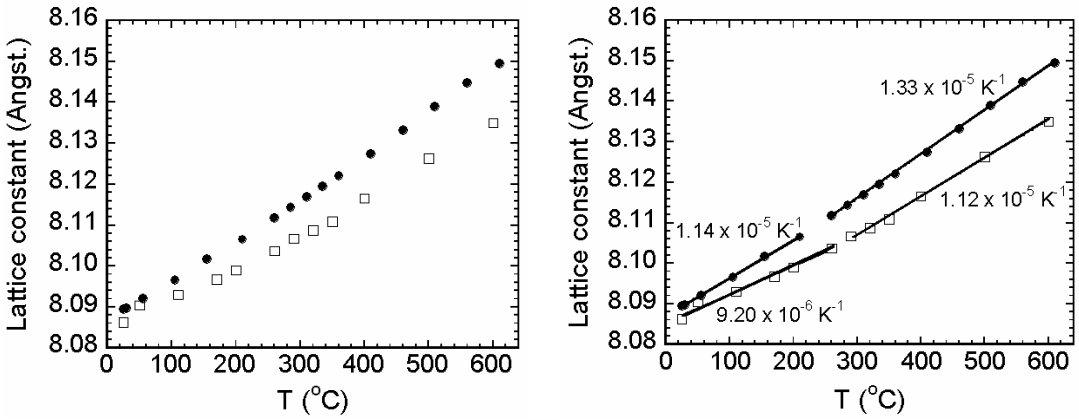

Figure 7.9: Variation of the lattice constant with temperature in $In_{0.5}Nb_{0.5}P_2O_7$. Data from two different experiments are plotted: Philips X'Pert PRO, HTML, Oak Ridge (open symbols), PANalytical instrument, MSE, Georgia Tech (closed symbols). Straight lines are fitted to the curve over the low- and high-temperature regions, resp. The thermal expansion coefficient gets larger from ~260 °C.

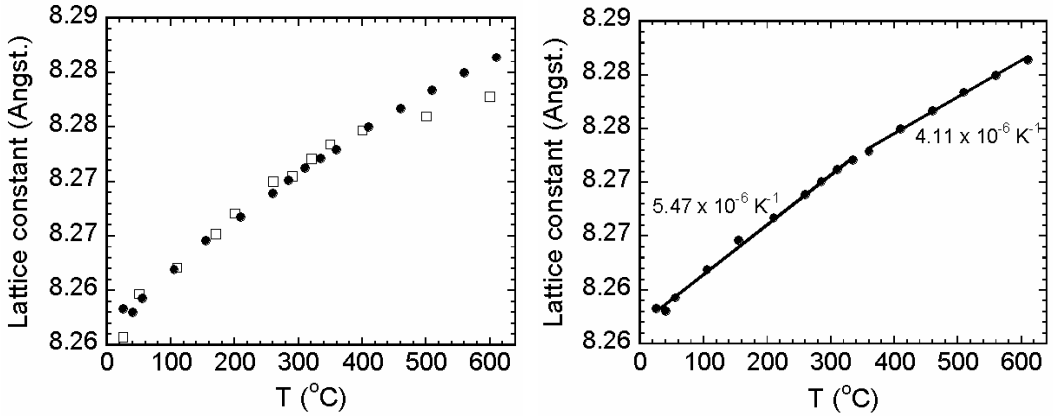

Figure 7.10: Variation of the lattice constant with temperature for $Y_{0.5}Nb_{0.5}P_2O_7$. Data from two different experiments are plotted: Philips X'Pert PRO, HTML, Oak Ridge (open symbols), PANalytical instrument, MSE, Georgia Tech (closed symbols). Straight lines are fitted to the curve for the MSE data over the low- and high-temperature regions, resp. The thermal expansion coefficient gets smaller above 360 °C.

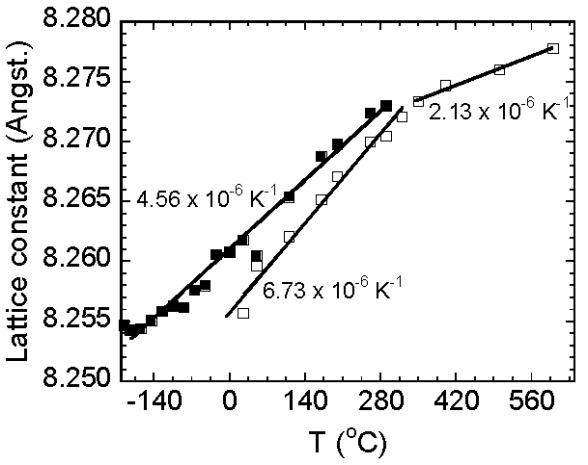

Figure 7.11: Variation of the lattice constant with temperature for $Y_{0.5}Nb_{0.5}P_2O_7$. Data from two different experiments are plotted: Philips X'Pert PRO, HTML, Oak Ridge (open symbols), Scintag instrument, Wilkinson Group, Georgia Tech (closed symbols). Straight lines are fitted to the curve for the data over the low- and high-temperature regions, resp. The thermal expansion coefficient gets smaller above ~320 °C.

The two datasets plotted for $In_{0.5}Nb_{0.5}P_2O_7$ differ from one another in slope, but they give similar temperatures for the change in slope. The data at room temperature are actually in good agreement and also agree with the data of Table 7.1, which were collected with our in-house diffractometer. For $Y_{0.5}Nb_{0.5}P_2O_7$, deviations are seen at higher temperature in Figure 7.10 and also between the slopes of the thermal expansion curves at room temperature in Figure 7.11. The fact that the deviations are not systematic in any of the cases suggests that it may be due to differences in instrumental configuration. The most likely instrumental cause of a difference in lattice constants obtained from different powder x-ray diffraction measurements on the same sample is the variation of sample height with temperature. However, in the case of both Figure 7.9 and 7.10, data collected with instruments presumably insensitive to sample height variations are plotted. Thus, in those cases the origin of the slight differences may be due to other instrumental factors such as for example temperature calibration. The data from our in-

house instrument plotted in Figure 7.11 (closed symbols) were collected using optics that can not eliminate the effect of sample height displacements on the lattice constants. For those data, sample height variations were accounted for by the use of an internal standard mixed into the sample as described in section 2.1.1. The difference between these two datasets might be a result of a combination of errors due to inadequate sample height correction and again the different instruments. Nevertheless, the temperature dependence of the thermal behavior of the materials is equally well reflected in data from all sources.

The calculated linear thermal expansion coefficients along with literature results for some cubic pyrophosphates are tabulated in Table 7.4. The γ-polymorph of GeP_2O_7 is actually monoclinic, but very close to, and previously reported as, cubic, and shows practically isotropic thermal expansion.[17] We consider the region below the temperature of the apparent change in the CTE as the low-temperature region. For the $(M^{III}_{0.5}M^{V}_{0.5})P_2O_7$ compounds, the phase transition, if any, should fall between the end temperature of the low-temperature range and the beginning of the high-temperature range. However, as the temperature regions were taken from the lattice constant vs. temperature data based on visual examination of the graphs, this is a rather subjective and crude way of estimating the temperature of phase transition. Also, we have to keep in mind that no phase transition was seen by DSC, thus, if there is one, it probably happens over a wide temperature range.

Table 7.4: Linear thermal expansion coefficients for different $(M^{III}_{0.5}M^{V}_{0.5})P_2O_7$ phases along with literature values for ZrP_2O_7, GeP_2O_7 and UP_2O_7. The cation size refers to the radius of the 3+ cation in the octahedral coordination. In $(M^{III}_{0.5}M^{V}_{0.5})P_2O_7$ compounds it is the average radius of the 3+ and 5+ cations. Low-temperature and high-temperature data are separated within the table. HTML: data with open symbols from the graphs, GT: data with solid symbols, HOME: data with solid symbols in Figure 7.11.

Compound/Sample	Cation size (pm)	T range (^{o}C)	CTE (K^{-1})
Low-temperature region			
ZrP_2O_7[10]	Zr: 86	25 – 277	1.20(25) x 10^{-5}
$Al_{0.5}Ta_{0.5}P_2O_7$ VTAlTa3	Al-Ta: 72.8	20 – 360	1.02(26) x 10^{-5} (GT)
$In_{0.5}Nb_{0.5}P_2O_7$ VTInNb2	In-Nb: 86	25 – 260 25 – 210	9.20(30) x 10^{-6} (HTML) 1.14(16) x 10^{-5} (GT)
$Y_{0.5}Nb_{0.5}P_2O_7$ VTYNb1	Y-Nb: 91	25 – 320 30 – 335	6.73(30) x 10^{-6} (HTML) 5.47(20) x 10^{-6} (GT)
UP_2O_7[18]	U: 103	27 – 400	4.88(*) x 10^{-6}
High-temperature region			
GeP_2O_7[17]	Ge: 67	295 – 970	1.11(*) x 10^{-5}
$Al_{0.5}Ta_{0.5}P_2O_7$ VTAlTa3	Al-Ta: 72.8	410 – 610	1.39(30) x 10^{-5} (GT)
ZrP_2O_7[10]	Zr: 86	290 – 610	3.47(9) x 10^{-6}
$In_{0.5}Nb_{0.5}P_2O_7$ VTInNb2	In-Nb: 86	290 – 600 260 – 610	1.12(42) x 10^{-5} (HTML) 1.33(9) x 10^{-5} (GT)
$Y_{0.5}Nb_{0.5}P_2O_7$ VTYNb1	Y-Nb: 91	350 – 600 360 – 610	2.13(44) x 10^{-6} (HTML) 4.11(24) x 10^{-6} (GT)

* not reported

$Al_{0.5}Ta_{0.5}P_2O_7$ and $In_{0.5}Nb_{0.5}P_2O_7$ show very similar behavior. Above ~360 ^{o}C and ~260 ^{o}C, respectively, the slope of the thermal expansion curve slightly increases (see Figures 7.8 and 7.9). For $Al_{0.5}Ta_{0.5}P_2O_7$, the linear coefficient of thermal expansion changes from 1.02 x 10^{-5} (20-360 ^{o}C range) to 1.39 x 10^{-5} K^{-1} (260-610 ^{o}C range). An

increase of similar magnitude is seen for $In_{0.5}Nb_{0.5}P_2O_7$. These changes are very small, especially in the light of the errors on the CTE values. The CTE for the low- temperature range calculated from data collected on the same instrument (GT data) is almost identical for the two materials, and the same is true for the high-temperature values. The observation that the CTE is slightly greater at high temperature is surprising, as the high-temperature ZrP_2O_7 structure is known to show decreased thermal expansion compared to the low-temperature one.[10, 19] Notable is the difference in the graphs of Figures 8 and 9 from the shape of the thermal expansion curve of cubic ZrP_2O_7 (see Figure 7.1): practically no discontinuity is seen in the thermal expansion of these materials. Both these observations suggest that the observed change in the CTE is not indicative of a phase transition from an ordered to a disordered structure analogous to that of ZrP_2O_7. This is accordance with the thermal analysis data as well, which did not show any sign of a well-defined phase transition such as the order-disorder transition in cubic ZrP_2O_7. In the low-temperature region, both $In_{0.5}Nb_{0.5}P_2O_7$ and $Al_{0.5}Ta_{0.5}P_2O_7$ seems to have a slightly smaller CTE than ZrP_2O_7 (cannot be definitively stated due to the errors on the CTE's). The average cation size in $Al_{0.5}Ta_{0.5}P_2O_7$ (72.8 pm) is smaller than the size of the Zr^{4+} in octahedral coordination (86 pm), in $In_{0.5}Nb_{0.5}P_2O_7$ it is 86 pm. For a smaller unit cell size, larger thermal expansion is expected. The smaller thermal expansion relative to ZrP_2O_7 can only be explained by an effect of the presence of two different cations in the octahedral sites and their disorder. However, even with a disordered arrangement of the cations the unit cell of both $In_{0.5}Nb_{0.5}P_2O_7$ and $Al_{0.5}Ta_{0.5}P_2O_7$ seems to remain smaller than that of ZrP_2O_7 at all temperatures, as indicated by the comparison of our and Khosrovani's data,[10] and as a consequence of the cation sizes (Zr(IV): 86 pm, Al^{3+}: 67.5

pm, In^{3+}: 94 pm, both Ta(V) and Nb(V): 78 pm[16]). The greater CTE at high temperature compared to ZrP_2O_7 follows the general trend that was also seen in the stuffed pyrophosphates (see Chapter 6); thermal expansion increases as the unit cell gets smaller.

The behavior of $Y_{0.5}Nb_{0.5}P_2O_7$ is different from that of $In_{0.5}Nb_{0.5}P_2O_7$ and $Al_{0.5}Ta_{0.5}P_2O_7$. $Y_{0.5}Nb_{0.5}P_2O_7$ shows a decrease in the thermal expansion coefficient above 320-360 ^oC. The material may display low thermal expansion at high temperature, but due to the relatively large difference between the CTE determined at HTML, Oak Ridge ($2.13x10^{-6}$ K^{-1}) and the one determined at Georgia Tech ($4.11x10^{-6}$ K^{-1}), it cannot be stated with certainty if it is smaller than that of ZrP_2O_7. The low-temperature CTE is definitely smaller than in ZrP_2O_7, and those calculated for $In_{0.5}Nb_{0.5}P_2O_7$ and $Al_{0.5}Ta_{0.5}P_2O_7$. The trend in the thermal expansion with average cation size (Y^{3+}: 104 pm[16]) in the three materials is in accordance with the previous observation that CTE decreases with increasing unit cell size, except that the CTEs for $In_{0.5}Nb_{0.5}P_2O_7$ and $Al_{0.5}Ta_{0.5}P_2O_7$ are practically the same. Although, the behavior of $Y_{0.5}Nb_{0.5}P_2O_7$ is similar to that of ZrP_2O_7 in the sense that a decrease in CTE is expected in the high-temperature from, the shape of the thermal expansion curve is largely different from the discontinuous curve characteristic of ZrP_2O_7. The substitution of Zr^{4+} in ZrP_2O_7 by a combination of 3+ and 5+ cations with a larger average radius lowers the thermal expansion coefficient of the material.

We examined the x-ray diffraction pattern of $Y_{0.5}Nb_{0.5}P_2O_7$ before and after the phase transition looking for any evidence of extra reflections that might appear due to formation of a superstructure. However, no evidence of any changes was found (see Figure 7.12).

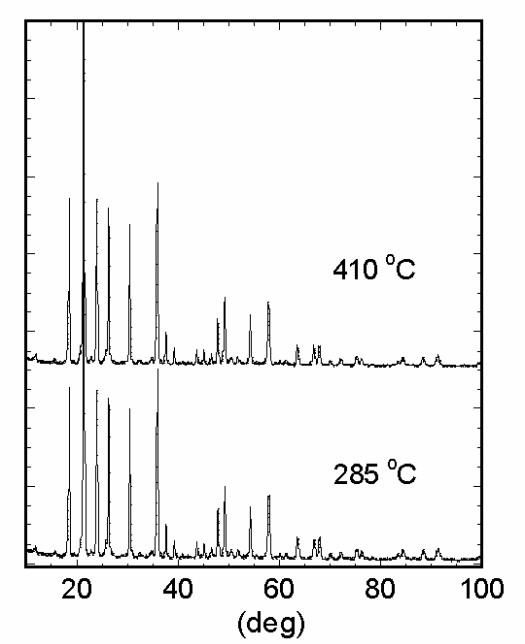

Figure 7.12: X-ray diffraction pattern for $Y_{0.5}Nb_{0.5}P_2O_7$ (sample VTYNb1) before (285 °C) and after (410 °C) the change in slope of lattice constants versus temperature. No changes in the pattern are detected. Data collected using the PANalytical instrument in MSE, Georgia Tech.

7.4 Conclusions

Zr(IV) in ZrP_2O_7 can be substituted by a combination of different 3+ and 5+ cations resulting in $(M^{III}_{0.5}M^{V}_{0.5})P_2O_7$ compositions with the cubic ZrP_2O_7 structure. Synthesis/heat treatment conditions seems to have little effect on the ordering of the cations; slower cooling resulted in only short-range ordering as indicated by x-ray diffraction. In addition, prolonged heating at higher temperatures seems to results in microstrain and decomposition possibly due to phosphate loss. This suggests that the manipulation of cation ordering through the synthesis conditions is not an effective way of controlling the thermal expansion in cubic pyrophosphate materials. However, the choice of M^{III} cation apparently has a significant effect on the physical properties. Although thermal analysis of our $(M^{III}_{0.5}M^{V}_{0.5})P_2O_7$ compositions indicated no apparent

phase transition in the materials, variable temperature XRD revealed changes in their thermal expansion with temperature. This change may be an increase in the coefficient of thermal expansion at higher temperatures for $In_{0.5}Nb_{0.5}P_2O_7$ and $Al_{0.5}Ta_{0.5}P_2O_7$, while a reduction in the CTE was seen for $Y_{0.5}Nb_{0.5}P_2O_7$ at higher temperature. This contrasting behavior can only be explained by both taking into consideration the cation sizes and the fact that two cations of different size are present in the octahedral sites as opposed to ZrP_2O_7. In the samples with smaller average cation size ($In_{0.5}Nb_{0.5}P_2O_7$ and $Al_{0.5}Ta_{0.5}P_2O_7$), the smaller low-temperature CTE compared to ZrP_2O_7 can only be rationalized by assuming that the 3+ and 5+ cations of different size have a somewhat disordered arrangement. The difference in the variation of the lattice constant with temperature for all $(M^{III}_{0.5}M^{V}_{0.5})P_2O_7$ compositions relative to ZrP_2O_7 suggests that a phase change occurs in the 260-360 ^oC temperature range and it is not strictly analogous to the order-disorder phase transition seen in cubic ZrP_2O_7.

Unfortunately the temperature of change in CTE for $Y_{0.5}Nb_{0.5}P_2O_7$ is no lower than that seen for cubic ZrP_2O_7, which makes this material impractical for real-life applications such as use in low-expansion ceramics. Nonetheless, the low CTE of the high-temperature structure of $Y_{0.5}Nb_{0.5}P_2O_7$ indicates that by full substitution of Zr(IV) in ZrP_2O_7, the thermal expansion can be lowered, and the size of the substituting cations (unit cell size) is an important controlling factor in the thermal expansion behavior of these materials.

Calorimetric measurements using better instrumentation under controlled conditions as well as careful electron diffraction studies could be helpful in providing a better picture of the level of order in these materials.

7.5 References

[1] A. A. Bokov, I. P. Rayevskii, V. G. Smotrakov, et al.: Kinetics of Compositional Ordering in $Pb_2B'B''O_6$ Crystals. *Phys. Status Solidi A* **93**, 411 (1986).

[2] P. Groves: The influence of B-site cation order on the phase transition behaviour of antiferroelectric lead indium niobate. *J. Phys. C: Solid State Phys.* **19**, 5103 (1986).

[3] P. Groves: Structural phase transitions and long-range order in ferroelectric perovskite lead indium niobate. *J. Phys. C: Solid State Phys.* **19**, 111 (1986).

[4] N. Yasuda and S. Shibuya: Ferroelectricity in disordered $Pb(In_{1/2}Nb_{1/2})O_3$. *J. Phys.: Condens. Matter* **1**, 10613 (1989).

[5] K. Z. Baba-Kishi, G. Cressey, and R. J. Cernik: X-ray and Electron Diffraction Studies of the Structure of Pseudo-Perovskite Compounds $Pb_2(Sc, Ta)O_6$ and $Pb_2(Mg,W)O_6$. *J. Appl. Crystallogr.* **25**, 477 (1992).

[6] L. E. Cross: Relaxor ferroelectrics. *Ferroelectrics* **76**, 241 (1987).

[7] M. P. Harmer, J. Chen, P. Peng, et al.: Control of Microchemical Ordering in Relaxor Ferroelectrics and Related Compounds. *Ferroelectrics* **97**, 263 (1989).

[8] N. Setter and L. E. Cross: The role of B-site cation disorder in diffuse phase transition behavior of perovskite ferroelectrics. *J. Appl. Phys.* **51**, 4356 (1980).

[9] N. Setter and L. E. Cross: The contribution of structural disorder to diffuse phase transitions in ferroelectrics. *J. Mater. Sci.* **15**, 2478 (1980).

[10] N. Khosrovani, V. Korthuis, A. W. Sleight, et al.: Unusual 180° P-O-P Bond Angles in ZrP_2O_7. *Inorg. Chem.* **35**, 485 (1996).

[11] T. Ota and I. Yamai: Thermal expansion of ZrP_2O_7 and related solid solutions. *J. Mater. Sci.* **22**, 3762 (1987).

[12] S. Oyetola, A. Verbaere, D. Guyomard, et al.: New ZrP_2O_7-like diphosphates of either mixed $(M^{III}_{0.5}M'^{V}_{0.5})$ cations (M=Sb,Bi,Hd,Eu; M'=Sb,Nb,Ta) or M'^{V}

cations (M'=Ta, Nb): synthesis and structure. *Eur. J. Solid State Inorg. Chem.* **28**, 23 (1991).

[13] A. Verbaere, S. Oyetola, D. Guyomard, et al.: New Mixed-Valence Antimony Phosphates: α- and β-$Sb^{III}Sb^{V}(P_2O_7)_2$. *J. Solid State Chem.* **75**, 217 (1988).

[14] A. C. Larson and R. B. Von Dreele, computer code General Structural Analysis System, Los Alamos National Laboratory, Los Alamos, NM (2000).

[15] B. H. Toby: EXPGUI, a graphical user interface for GSAS. *J. Appl. Crystallogr.* **34**, 210 (2001).

[16] R. D. Shannon and C. T. Prewitt: Effective Ionic Radii in Oxides and Fluorides. *Acta Crystallogr., Sect. B* **25**, 925 (1969).

[17] E. R. Losilla, A. Cabeza, S. Bruque, et al.: Syntheses, Structures, and Thermal Expansion of Germanium Pyrophosphates. *J. Solid State Chem.* **156**, 213 (2001).

[18] H. P. Kirchner, K. M. Merz, and W. R. Brown: Thermal Expansion of Uranium Pyrophosphate and Ceramic Bodies in the System UO_2-P_2O_7. *J. Am. Ceram. Soc.* **46**, 137 (1963).

[19] A. W. Sleight: Compounds that Contract on Heating. *Inorg. Chem.* **37**, 2854 (1998).

CHAPTER 8

FLUORINERT AS A PRESSURE-TRANSMITTING MEDIUM FOR HIGH-PRESSURE DIFFRACTION STUDIES

Abstract

Fluorinert is widely used as a liquid pressure-transmitting medium in high-pressure diffraction work. A systematic study of five different fluorinerts was carried out using single-crystal X-ray diffraction in a diamond anvil cell in order to determine the pressure range over which they provide a hydrostatic stress state to the sample. It was found that none of the fluorinerts studied can be considered hydrostatic above 1.2 GPa, a lower pressure than reported previously.

8.1 Introduction

For high pressure diffraction experiments (either single-crystal or powder), it is often necessary to ensure that the force applied to the sample crystal(s) is homogeneous and that the sample is free of any differential stress or shear strain. To achieve this, the crystal(s) within the pressure chamber must be immersed in a medium that displays hydrostatic behavior, for example a liquid or gas, under all conditions of interest. Nonhydrostatic stress leads to significant broadening and shifts in the position of the diffraction peaks from the sample and, thus, inaccurate unit cell data.[1-4] It can also promote or suppress phase transitions.[5-9] Although the degree of diffraction line broadening depends sensitively upon a number of factors, including the physical state and the elastic constant tensor of the sample, this limitation of the cell/medium invariably degrades the quality of the resulting diffraction pattern by means of a loss of effective instrumental resolution.[10] The practice of neglecting the nonhydrostatic compression effect and taking the lattice parameter as the average of the lattice parameters calculated from the measured d-spacings of the observed reflections results in overestimation of the lattice parameter and the standard deviation in the lattice parameter.[4] Furthermore, the apparent pressure registered by internal pressure standards can also be affected by nonhydrostatic stresses,[2, 3, 11-14] resulting in incorrect equation of state parameters being determined from pressure-volume data.

Diamond anvil cells (DACs) are used extensively to record X-ray diffraction patterns from samples compressed to high pressures. These experiments give interesting information on the phase transitions and equations of state of materials over wide pressure ranges. A well-characterized stress state (ideally hydrostatic pressure) is

essential for a rigorous interpretation of the diffraction data. The need for hydrostaticity made the use of fluid pressure media, although more difficult to use and load than solid media, quite important for high pressure X-ray diffraction measurements. In DACs, a metal gasket to contain the sample and the pressure-transmitting medium between the diamond anvils is commonly used to render the stress state of the sample hydrostatic, at least up to the solidification pressure of the pressure-transmitting medium. However, the use of fluid pressure-transmitting medium does not always result is hydrostatic pressure. As the pressure is raised above the solidification point of the medium, the stress state of the sample begins to deviate from hydrostatic. Pressure-transmitting media usually exhibit a continuous increase in viscosity with increasing pressure prior to solidifying into a glassy state, so the onset of nonhydrostatic pressure is also expected to be gradual.[4] Even at lower pressures, the stress state can become nonhydrostatic if the sample starts bridging the anvils due to excessive thinning of the gasket or due to large initial thickness of the sample. In this context, knowing whether the stress state of the sample is hydrostatic or nonhydrostatic is very important as it greatly affects the diffraction data to be analyzed.

One of the most commonly used pressure media for single-crystal diffraction studies is the (water-saturated) 4:1 methanol:ethanol mixture, which is generally believed to remain at least quasihydrostatic to its glass transition at 10.4 GPa[11]. Miletich *et al.*[15] gave an overview on the most frequently used pressure-transmitting media. Their comparison shows that for pressures above 10-15 GPa there is no ambient-pressure liquid available and thus successful application to single-crystal work is necessarily tied to relaxation of nonhydrostatic stresses with time or at elevated temperature, or to the use of gaseous

pressure media. They reported the maximum pressure of (quasi)hydrostaticity for several fluid pressure media including silicone oil, water, isopropyl alcohol, glycerine-water mixture, petroleum ether, pentane-isopentane mixture, methanol, methanol-ethanol mixture and methanol-ethanol-water mixture, in the list silicone oil being at the low end with <2.0 GPa and methanol-ethanol-water at the high end with 14.5 GPa. If alcohol in known to react or dissolve the sample, then a number of alkane-based fluids can be used, such as petroleum ether or a mixture of pentane and isopentane.[15-17] However, while all of these compounds can be used for x-ray diffraction measurements, they are all hydrogenated and thus give rise to incoherent scattering and high backgrounds in neutron diffraction experiments.

Fluorinerts, the brand name for a range of products supplied by 3M (St. Paul, MN), are completely fluorinated aliphatic compounds, contain no hydrogen and, thus, are ideal for neutron diffraction experiments. They also have the advantage that they are chemically inert and can, therefore, be employed with a wide variety of samples that may dissolve or react with the more commonly used pressure media. Fluorinerts thus became widely used as pressure-transmitting media in high-pressure neutron diffraction experiments, especially in pressure cells of the Paris-Edinburgh design.[18, 19] In this particular cell design, the nonhydrostaticity of the pressure medium also served to reduce stress on the anvils; in its original configuration maximum pressures of only 2-3 GPa could be achieved with hydrostatic pressure media compared to 9-10 GPa with fluorinert.[10]

Recent experiments suggest that fluorinert is hydrostatic to 0.6 GPa,[20, 21] but evidence for a low hydrostatic limit of fluorinert goes back at least to the work of Decker *et al.*[22]

They showed that the use of fluorinert completely suppresses the monoclinic-to-rhombohedral phase transition in lead phosphate that normally occurs at 1.8 GPa (room temperature) under hydrostatic conditions and had therefore transmitted shear stresses to the lead phosphate sample that stabilized the monoclinic ferroelastic phase. More recently, line broadening in high-pressure neutron powder diffraction experiments has been attributed to the nonhydrostaticity of fluorinert, but estimates of the pressure range at which broadening starts range between 0.7 and 5 GPa.[17, 23-26]

Part of this variation may be due to the many types of commercially available fluorinerts, of which the grades FC-70, FC-75 and FC-77 and sometimes a mixture of FC-70 and FC-77, have been used for high-pressure studies. But there has been no systematic determination of the maximum pressure to which they provide hydrostatic pressure conditions. In addition, the use of fluorinert as a pressure medium had been considered for high-pressure x-ray diffraction experiments in a DAC for this thesis work, and was actually used by our group before (see section 4.3.2.1). We have, therefore, performed experiments on five different grades of fluorinert in order to determine the pressure range over which they provide hydrostatic conditions. This was achieved by compressing a quartz single-crystal using each of these fluorinerts as a pressure medium in a DAC and monitoring the changes in the positions and widths of the diffraction peaks as a function of pressure.

8.2 Experimental

Fluorinert samples were obtained commercially; FC-40, FC-70, FC-72 and FC-75 from Acros Organics (Fisher Scientific, Pittsburgh, PA) and FC-77 from Sigma Aldrich

(St. Louis, MO). Gem-quality single crystals of twin-free natural quartz were also obtained commercially. The same quartz sample was used for all of the fluorinerts. "BGI" (Bayerisches Geoinstitut, Bayreuth, Germany) and "ETH" (Swiss Federal Institute of Technology, Zurich, Switzerland) designs of diamond anvil cell (DAC)[15, 27] were used (see Figure 8.1). The single-crystal was mounted in the DAC along with the fluorinert and sealed. The gasket in each experiment was 250 μm thick stainless steel (Inconel) that was preindented to a thickness of 92 μm. The sample whole was drilled in the steel gasket using a spark-erosion drilling machine. The diamond anvils had a culet face diameter of 0.6 mm. Pressure adjustment was achieved by turning two pairs of right- and left-handed bolts in the cell.

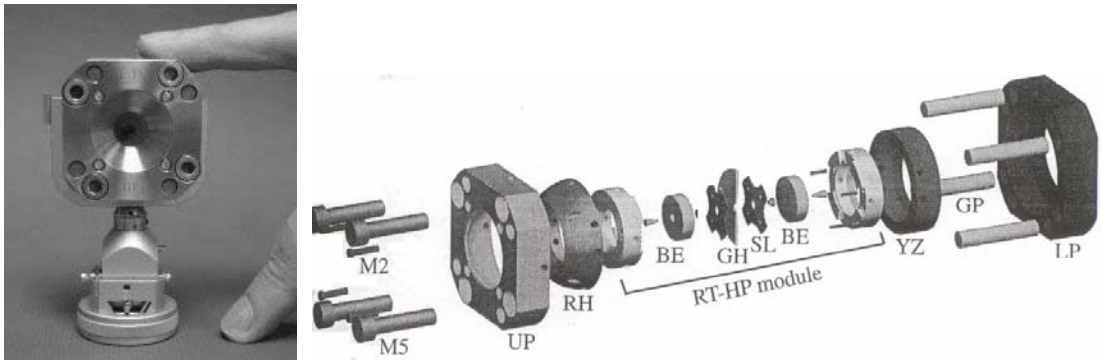

Figure 8.1: Picture and exploded view of the ETH diamond anvil cell. RT: room temperature, HP: high pressure, M2: alignment screws, M5: bolts, UP: upper platen, RH: rocking hemisphere, BE: beryllium seat, GH: gasket holder, SL: spring leaf, YZ: translation stage, GP: guide pins, LP: lower platen.[15]

8.2.1 Single crystal x-ray diffraction

Single-crystal diffraction measurements were performed at room temperature and high pressures using Huber four-circle diffractometers with Eulerian-cradles (see Figure 8.2), one at Virginia Tech (Blacksburg, VA) and one at the Bayerisches Geoinstitut

(Bayreuth, Germany). The measurements at the Bayerisches Geoinstitut were carried out by Ross J. Angel, our collaborator on this work. The physical parameters of the diffractometer at Virginia Tech are very similar to that in Bayreuth.[28] These instruments are optimized for extremely precise measurements of lattice parameters at high-pressures in diamond-anvil cells.[29] The four-circle goniometers were built from model 511.1 χ circles with an offset φ drive mounted on two model 420 bases for ω and 2θ motions. The ω and χ circles are driven with stepper motors with 0.00125^{o} steps, the 2θ and φ axes with 0.0025 steps. Final peak profiles are made by scanning the ω axis, keeping the 2θ and φ axes stationary, so that the 0.0025^{o} step size of the latter did not degrade the resolution. The diffractometers are equipped with unfiltered Mo sealed-tube X-ray source (Mo K_{α} radiation, 50 kV, 40 mA) without a monochromator to provide clean, stable and reproducible peak-profile shapes. The source-to-crystal distance was 40 cm and the crystal-to-detector distance was 35 cm. The incident beam was collimated using a 0.5 mm aperture close to the source, and the detector area was defined by adjustable parallel slits. For the experiments in this paper the slits defining the divergence in the 2θ plane were kept at 9 mm width, and the perpendicular set was at 2 mm spacing. Of particular importance is that the instrument configurations lead to a full width at half maximum (FWHM) of the individual components of the α_1-α_2 doublet of the diffracted beams from the quartz sample of approximately 0.05^{o} under hydrostatic conditions. This means the broadening of the peaks due to strain or any other cause is readily detectable.

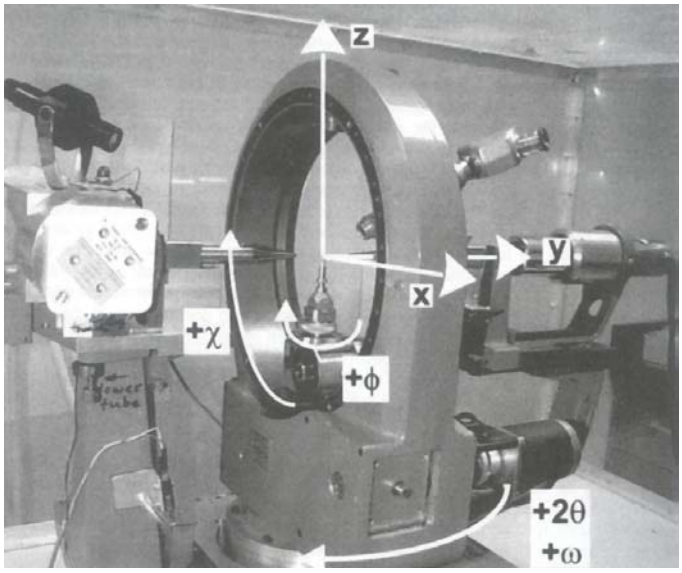

Figure 8.2: An Eularian four-circle goniometer with all circles positioned at zero. The axes of the Cartesian coordinate system of Busing and Levy[30] are superimposed. The circle motions for positive parities are indicated.[29]

Both diffractometers were driven by the *SINGLE* program.[29] The algorithm used for centering diffraction peaks is described in full in an earlier work of Angel *et al*.[28] The determination of the setting angles for an individual peak started with an initial determination of approximate positions 2θ, ω and χ by the iteration of a sequence of relatively coarse scans of these axes coupled with parabolic fits to determine the positions of maximum intensity. The final step scan of a diffraction peak is performed with the ω circle and the resulting profile is fitted with a constrained pair of pseudo-Voigt functions that represent the contribution of the $K\alpha_1$ and $K\alpha_2$ components of the x-ray spectrum.[29] This refinement procedure provides the peak position of the $K\alpha_1$ component to a precision better than 0.01^{o}, as well as the refined FWHM of the individual components. Each diffracted beam was centered in eight positions on the diffractometer, and the setting angles were determined following the method of King and Finger[31] to eliminate

the effects of diffractometer circle zero-offsets, crystal offsets and aberrations in the diffractometer alignment.

The body of the diamond anvil cell limits the angles of the incident and diffracted x-ray beams to within ~45^{o} of the cell axis. Therefore, the number of accessible reflections from the crystal is limited. With the 010 face of the quartz lying approximately parallel to the culet faces of the diamond anvils, up to 15 low-angle reflections are accessible (100, 101, 10-1, 110, -210, 012, -102, 102, -112, 1-12, 112, -212, 11-2, 2-12, -212), although some of these become inaccessible at higher pressures due to either increases in 2θ values or small rotations of the crystal within the cell. For each fluorinert sample a series of measurements at different pressures was carried out up to a pressure at which significant peak broadening had occurred. After each pressure adjustment, a two-position centering was carried out on the diffractometer of the 101 or 10-1 reflection to get an idea of the extent of pressure change. If the pressure was close to the target value, an eight-position centering was carried out usually using two reflections to get more reliable estimates of the peak widths and positions. The 2θ value of the quartz 101 and 10-1 peaks determined in this way allowed pressure determination with a precision of better than 0.01 GPa via the known variation of the cell parameters with pressure.[28] The reported peak widths at each pressure are the average of the widths refined at each of the eight positions and the estimated uncertainty is calculated as the standard deviation of these values.

As the primary object of these measurements was to detect the onset of line broadening of the diffraction peaks from the quartz crystal as a result of non-hydrostatic stresses applied by the pressure medium, cell parameters were not determined at every pressure point. If more than two reflections were centered then vector least-squares fits[32]

were performed to the values of all the setting angles (2θ, ω and χ) to determine unit cell parameters unconstrained by symmetry.

8.3 Results and discussion

The five different fluorinerts that were studied, FC-75, FC-70, FC-72, FC-40 and FC-77, essentially cover the entire range of physical properties available with this class of compounds (see Table 8.1).

Table 8.1: Typical physical properties (from the Selection Guide for 3M™ Fluorinert™ Electronic Liquids) of the fluorinert grades studied.

Fluorinert Grade	**FC-72**	**FC-77**	**FC-75**	**FC-40**	**FC-70**
Average molecular weight (g/mol)	340.0	415.0	420.0	650.0	820.0
Typical boiling point (^{o}C)	56.0	97.0	102.0	155.0	215.0
Density (g/cm^3)	1.68	1.78	1.77	1.87	1.94
Kinematic viscosity (cs)	0.4	0.8	0.8	2.2	14.0
Vapor pressure (Torr)	232.0	42.0	31.0	3.0	<0.1

With each fluorinert, the pressure in the DAC was gradually increased until significant peak broadening was observed (typically amounting to a doubling of the peak width), and then gradually released until the initial peak width was recovered. Diffraction data were collected at several pressure points during both compression and release. The change of the full peak width at half maximum (FWHM) for the most intense reflection (101) with pressure was followed in each experiment. All scans were ω-scans, thus the

plotted FWHM values are ω-width values. The full peak width at half maximum values as a function of pressure for the fluorinert grades studied are tabulated in Table 8.2.

Table 8.2: Full peak widths at half maximum (FWHM) for the (101) reflection of the quartz single crystal compressed in different fluorinert grades as a function of pressure.

FC-72		FC-77		FC-75		FC-40		FC-70	
P (GPa)	FWHM (101) (^{O})	P (GPa)	FWHM (101) (^{O})	P (GPa)	FWHM (101) (^{O})	P (GPa)	FWHM (101) (^{O})	P (GPa)	FWHM (101) (^{O})
0.56	0.051(3)	0.25	0.046(3)	0.00	0.056(5)	0.60	0.046(4)	0.01	0.052(3)
0.61	0.051(3)	0.44	0.046(3)	1.03	0.054(3)	0.73	0.047(4)	0.32	0.052(3)
0.67	0.051(3)	0.61	0.046(3)	1.22	0.061(5)	0.85	0.045(4)	0.41	0.052(3)
0.76	0.051(3)	0.66	0.048(3)	1.39	0.058(3)	0.95	0.046(4)	0.53	0.052(3)
0.93	0.051(3)	0.76	0.047(4)	1.40	0.058(2)	1.07	0.057(5)	0.96	0.085(4)
1.07	0.054(5)	0.86	0.045(3)	1.45	0.057(2)	1.22	0.065(5)	1.12	0.082(3)
1.37	0.074(10)	0.93	0.047(3)	1.47	0.062(3)	1.40	0.073(6)	1.02	0.080(3)
1.60	0.103(13)	1.24	0.066(8)	1.90	0.081(3)	1.67	0.083(7)	0.86	0.134(4)
1.90	0.151(20)	1.62	0.150(40)	2.06	0.093(4)	1.88	0.095(9)	0.85	0.079(4)
1.64	0.131(13)	2.24	0.214(60)	2.41	0.148(13)	1.79	0.079(8)	0.33	0.051(3)
1.59	0.078(13)	2.13	0.196(50)	1.67	0.081(7)	1.70	0.085(7)	0.23	0.055(3)
0.62	0.051(3)	2.00	0.112(40)	1.51	0.071(7)	1.53	0.101(6)	0.50	0.054(3)
0.32	0.049(3)	1.17	0.070(7)	1.39	0.074(8)	0.08	0.047(4)	0.86	0.079(7)
0.00	0.045(3)	0.51	0.047(4)	-	-	0.015	0.048(4)	1.60	0.097(7)
-	-	0.07	0.046(3)	-	-	-	-	1.80	0.134(8)
								2.26	0.187(10)
								2.02	0.142(8)
								1.77	0.095(7)
								0.31	0.059(4)

Upon increasing the pressure, the widths of the diffraction peaks from the quartz sample initially remain the same as at room pressure. Above a given pressure, the peak widths increase with increasing pressure, up to a point at which it is no longer possible to reliably determine either their widths or positions. We associate a nominal "hydrostatic limit" with either the first detection of broadening, or the pressure at which the broadening is extrapolated back to zero (see Table 8.3). We observed two types of behavior on pressure release that may also affect the apparent hydrostatic limit of these pressure media. For three of the samples (FC-72, FC-77 and FC-75) the peak width

recovers on pressure reduction (sometimes with some hysteresis), indicating that the mechanism of broadening is essentially reversible on the time scale of a few hours of the experiments (see Figure 8.3-8.5).

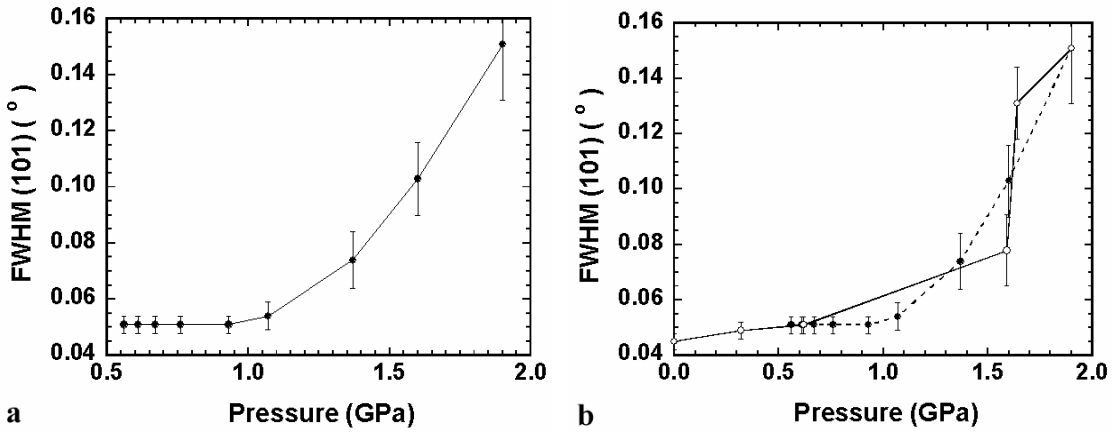

Figure 8.3: Change of average peak width (FWHM) of the quartz (101) reflection with pressure for fluorinert FC-72 upon compression (a) and decompression (b – with the compression curve shown with dotted line). The straight lines drawn between the points serve as a guide to the eye.

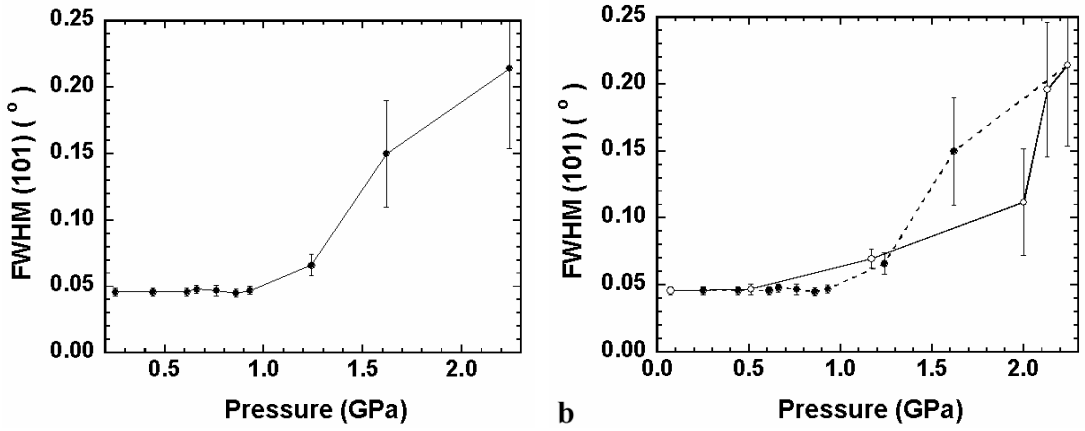

Figure 8.4: Change of average peak width (FWHM) of the quartz (101) reflection with pressure for fluorinert FC-77 upon compression (a) and decompression (b – with the compression curve shown with dotted line). The straight lines drawn between the points serve as a guide to the eye.

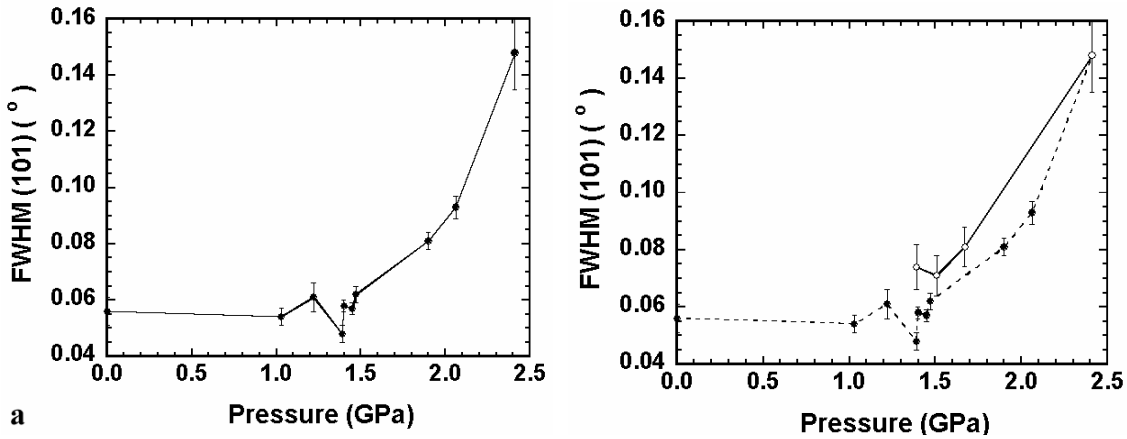

Figure 8.5: Change of average peak width (FWHM) of the quartz (101) reflection with pressure for fluorinert FC-75 upon compression (a) and decompression (b – with the compression curve shown with dotted line). The straight lines drawn between the points serve as a guide to the eye.

By contrast, for FC-70, which was the most viscous fluorinert with the highest boiling point, upon releasing pressure for the first time, an increase in peak width was observed at about 0.85 GPa (see Figure 8.6). When compressed for the second time, the sample displayed two significant peak width increases but the sudden jump during pressure-release was absent (see Figure 8.7). Similar but less pronounced behavior was also observed with FC-40, the second most viscous fluorinert (see Figure 8.8). This non-reversibility seems to be more pronounced in the more viscous fluorinerts, which suggests that it may be alleviated by temperature annealing. Without such annealing, it means that the hydrostatic limit on subsequent pressure cycles maybe lower than that observed on the first pressurization.

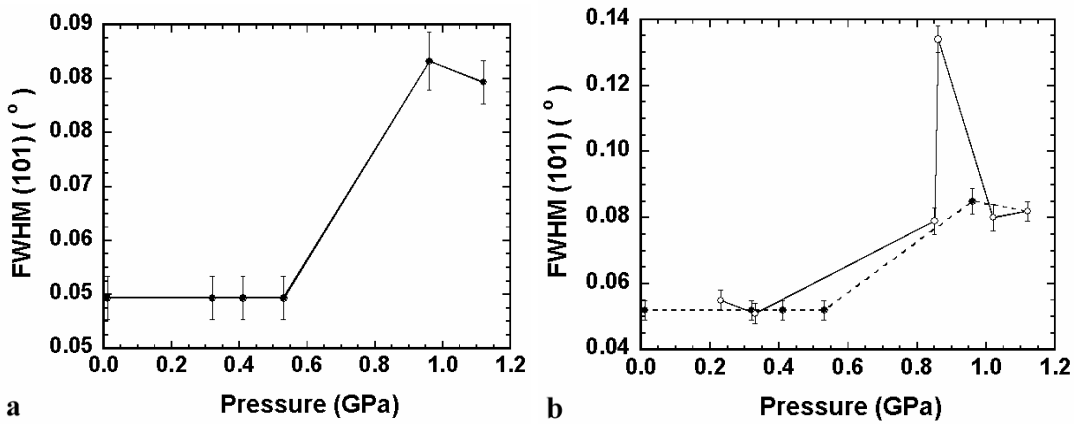

Figure 8.6: Change of average peak width (FWHM) of the quartz (101) reflection with pressure for fluorinert FC-70 during compression (a) and pressure release (b – with compression also shown). An increase in peak width was observed at about 0.85 GPa. The straight lines drawn between the points serve as a guide for the eyes.

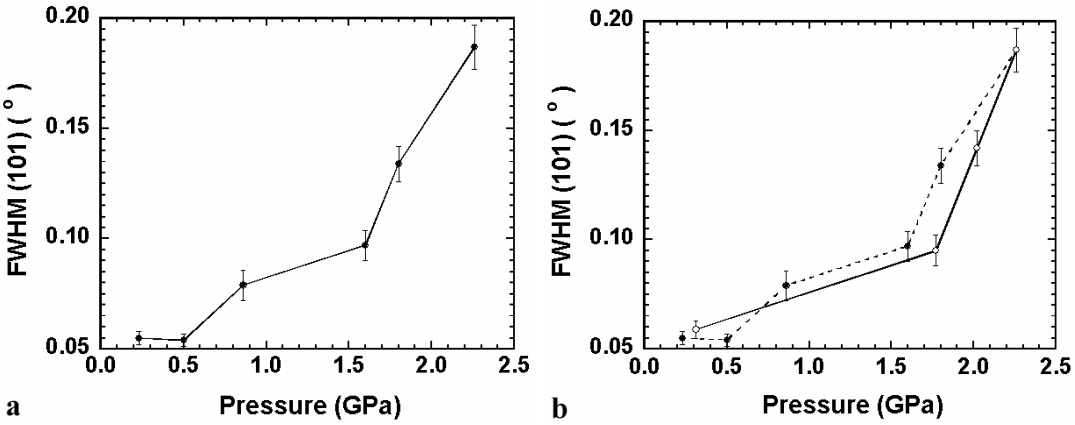

Figure 8.7: Change of average peak width (FWHM) of the quartz (101) reflection with pressure for fluorinert FC-70 during the second compression (a) and pressure release (b – with compression also shown). The increase in peak width on decompression was absent this time. The straight lines drawn between the points serve as a guide for the eyes.

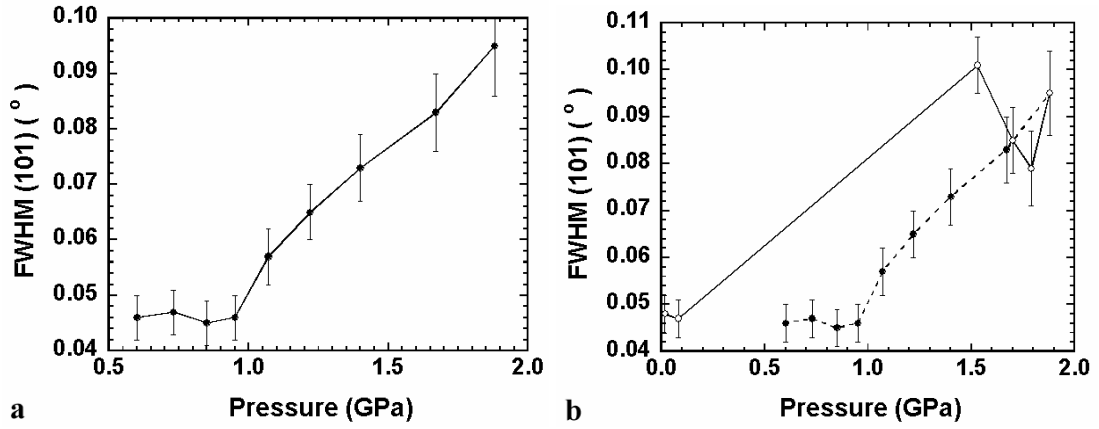

Figure 8.8: Change of average peak width (FWHM) of the quartz (101) reflection with pressure for fluorinert FC-40 during compression (a) and pressure release (b – with compression also shown). An increase in peak width was observed at about 1.5 GPa. The straight lines drawn between the points serve as a guide for the eyes.

All fluorinerts studied led to significant peak broadening beginning from a pressure of around 1 GPa or lower. From the physical properties point of view, FC-70, which was the most viscous fluorinert with the highest boiling point, provided hydrostatic conditions until about 0.6 GPa only. FC-72 is from the other end of the series regarding physical properties, it has the smallest boiling point and viscosity, it is the most volatile fluorinert among the samples. As expected based on this, the peaks started to broaden at a higher pressure (around 1.1 GPa), indicating that FC-72 requires a higher pressure to solidify. However, despite the quite different physical properties of FC-40 and FC-77 (FC-40 has a boiling point higher by 60 degrees, an average molecular weight greater by 235 and its kinematic viscosity is three times greater than that of FC-77), their behavior under pressure didn't seem to reflect this difference, as both fluorinerts showed peak broadening from about the same pressure, just below 1 GPa (see Table 8.3).

Table 8.3: Observed hydrostatic limits for the fluorinert grades studied. A nominal hydrostatic limit was associated with either the first detection of broadening or the pressure at which the broadening was extrapolated back to zero.

Fluorinert grade	**FC-72**	**FC-77**	**FC-75**	**FC-40**	**FC-70**
Hydrostatic limit (GPa)	~1.05	~0.95	~1.20	~0.95	~0.55

8.4 Conclusions

The precise mechanism of peak broadening due to non-hydrostatic pressure media in a single-crystal diffraction experiment is not fully understood, although it is clear that it must differ from that in a powder diffraction experiment.[4] Furthermore, the degree of broadening is presumably also a function of the components of the elastic tensor of the sample crystal, its orientation with respect to the stress field of the pressure medium, and the stress state of the medium. Nonetheless, the detection of peak broadening in a single-crystal experiment is proof that a non-hydrostatic stress has been applied to the sample crystal. The absence of broadening, however, does not prove that the medium is truly hydrostatic. The pressures that we found for the onset of broadening (see Table 8.3) are, therefore, upper limits on the pressures to which the various fluorinert compounds remain hydrostatic pressure media at room temperatures. Our results show that all of the fluorinerts that we studied become non-hydrostatic at pressures of less than 1.2 GPa, that being the limit observed for the FC-75 grade, while the FC-70 grade becomes non-hydrostatic below 0.6 GPa. However, there does not appear to be a strong correlation between the physical properties and the hydrostatic limit of these fluorinerts. We also note that not all of the broadening is immediately reversible upon pressure release at room temperature.

8.5 References

[1] Y. Yamamoto, M. Nomura, and H. Fujiwara: Effect of Nonhydrostaticness of Pressure on Lattice Contraction of Silicon. *Jpn. J. Appl. Phys.* **16**, 397 (1977).

[2] T. Kenichi: Evaluation of the hydrostaticity of a helium-pressure medium with powder x-ray diffraction techniques. *J. Appl. Phys.* **89**, 662 (2001).

[3] N. Sata, G. Shen, M. L. Rivers, et al.: Pressure-volume equation of state of the high-pressure B2 phase of NaCl. *Phys. Rev. B* **65**, 104114 (2002).

[4] A. K. Singh and T. Kenichi: Measurement and analysis of nonhydrostatic lattice strain component in niobium to 145 GPa under various fluid pressure-transmitting media. *J. Appl. Phys.* **90**, 3269 (2001).

[5] T.-C. Wu, W. A. Bassett, P. C. Burnley, et al.: Shear-Promoted Phase Transitions in Fe_2SiO_4 and Mg_2SiO_4 and the Mechanism of Deep Earthquakes. *J. Geophys. Res.* **98**, 19767 (1993).

[6] N. Funamori, M. Funamori, R. Jeanloz, et al.: Broadening of x-ray powder diffraction lines under nonhydrostatic stress. *J. Appl. Phys.* **82**, 142 (1997).

[7] T. Taniguchi, T. Sato, W. Utsumi, et al.: Effect of nonhydrostaticity on the pressure induced phase transformation of rhombohedral boron nitride. *Appl. Phys. Lett.* **70**, 2392 (1997).

[8] H. Libotte and J.-P. Gaspard: Pressure-induced distortion of the β-Sn phase in silicon: Effects of nonhydrostaticity. *Phys. Rev. B* **62**, 7110 (2000).

[9] L. Dubrovinsky, N. Dubrovinskaia, S. Saxena, et al.: X-ray diffraction under non-hydrostatic conditions in experiments with diamond anvil cell: wüstite (FeO) as an example. *Mater. Sci. Eng.* **A288**, 187 (2000).

[10] W. G. Marshall and D. J. Francis: Attainment of near-hydrostatic compression conditions using the Paris-Edinburgh cell. *J. Appl. Crystallogr.* **35**, 122 (2002).

[11] G. J. Piermarini, S. Block, and J. D. Barnett: Hydrostatic limits in liquids and solids to 100 kbar. *J. Appl. Phys.* **44**, 5377 (1973).

[12] M. Chai and J. M. Brown: Effects of static non-hydrostatic stress on the R lines of ruby single crystals. *Geophys. Res. Lett.* **23**, 3539 (1996).

[13] B. Reynard, G. Fiquet, J.-P. Itié, et al.: High-pressure X-ray diffraction study and equation of state of $MgSiO_3$ ilmenite. *Am. Mineral.* **81**, 45 (1996).

[14] G. J. Piermarini: High Pressure X-ray Crystallography With the Diamond Cell at NIST/NBS. *J. Res. NIST* **6**, 889 (2001).

[15] R. Miletich, D. Allan, R., and W. Kuhs, F.: High-Pressure Single-Crystal Techniques. *Rev. Mineral. Geochem.* **41**, 445 (2001).

[16] H. B. Vanfleet and R. J. Zeto: Comparison of the Bismuth I-II Phase Transformations in Liquid and Solid High-Pressure Systems. *J. Appl. Phys.* **42**, 4955 (1971).

[17] T. P. Russell, P. J. Miller, G. J. Piermarini, et al.: High-Pressure Phase Transition in γ-Hexanitrohexaazaisowurtzitane. *J. Phys. Chem.* **96**, 5509 (1992).

[18] J. M. Besson, R. J. Nelmes, G. Hamel, et al.: Neutron powder diffraction above 10 GPa. *Physica B* **180, 181**, 907 (1992).

[19] R. J. Nelmes, J. S. Loveday, R. M. Wilson, et al.: Neutron diffraction study of the structure of deuterated ice VIII to 10 GPa. *Phys. Rev. Lett.* **71**, 1192 (1993).

[20] J. Mizuki, M. Takai, H. Takakashi, et al.: Pressure dependence of superconductivity in simple-cubic Na_2CsC_{60}. *Phys. Rev. B* **50**, 3466 (1994).

[21] H. Takakashi, N. Môri, T. Matsumoto, et al.: Development of a high-pressure cell for the neutron powder diffractometer (HRP) at KEK. *Physica B* **213 & 214**, 1028 (1995).

[22] D. L. Decker, S. Petersen, D. Debray, et al.: Pressure-induced ferroelastic phase-transition in $Pb_3(PO_4)_2$: A neutron diffraction study. *Phys. Rev. B* **19**, 3552 (1979).

[23] J. B. Parise, K. Leinenweber, D. J. Weidner, et al.: Pressure-induced H bonding: Neutron diffraction study of brucite, $Mg(OD)_2$, to 9.3 GPa. *Am. Mineral.* **79**, 193 (1994).

[24] J. B. Parise, B. Theroux, R. Li, et al.: Pressure dependence of hydrogen bonding in metal deuteroxides: a neutron powder diffraction study of $Mn(OD)_2$ and β-$Co(OD)_2$. *Phys. Chem. Mineral.* **25**, 130 (1998).

[25] M. D. Welch and W. G. Marshall: High-pressure behavior of clinochlore. *Am. Mineral.* **86**, 1380 (2001).

[26] G. A. Lager and R. B. Von Dreele: Neutron powder diffraction study of hydrogarnet to 9.0 GPa. *Am. Mineral.* **81**, 1097 (1996).

[27] D. R. Allan, R. Miletich, and R. J. Angel: A diamond-anvil cell for single-crystal X-ray diffraction studies to pressures in excess of 10 GPa. *Rev. Sci. Instrum.* **67**, 840 (1996).

[28] R. J. Angel, D. R. Allan, R. Miletich, et al.: The Use of Quartz as an Internal Pressure Standard in High-Pressure Crystallography. *J. Appl. Crystallogr.* **30**, 461 (1997).

[29] R. J. Angel, R. T. Downs, and L. W. Finger: High-Temperature - High-Pressure Diffractometry. *Rev. Miner. Geochem.* **41**, 559 (2001).

[30] W. R. Busing and H. A. Levy: Angle calculations for 3- and 4-circle X-ray and neutron diffractometers. *Acta Crystallogr.* **22**, 457 (1967).

[31] H. E. King and L. W. Finger: Diffracted beam crystal centering and its application to high-pressure crystallography. *J. Appl. Crystallogr.* **12**, 374 (1979).

[32] R. L. Ralph and L. W. Finger: A Computer Program for Refinement of Crystal Orientation Matrix and Lattice Constants from Diffractometer Data with Lattice Symmetry Constraints. *J. Appl. Crystallogr.* **15**, 537 (1982).

CHAPTER 9

POSSIBILITIES FOR FUTURE WORK

Some possibilities for further investigations have already been pointed out at the end of the conclusions for certain chapters. At the end of Chapter 3, during the examination of the high-pressure behavior of $A_2M_3O_{12}$ compounds with two different A^{3+} cations we pointed out that the trends in the phase transition temperature and pressure, as well as the compressibility could not be fully explained by considering only the physical properties of the ions (such as size and electronegativity) and the packing densities of the compounds. A comprehensive understanding of the effect of the chemistry of the cations can probably only be achieved by considering also the thermodynamics; both entropic as well as enthalpic factors. We presume that there is a significant loss of vibrational entropy on going from the orthorhombic to the monoclinic phase, which entropy change will be dependent on the identity of A^{3+}. The entropy of the orthorhombic to monoclinic phase transition could be studied by either inelastic neutron scattering or calorimetry. For example, heat capacity calorimetry measurements could be used to obtain the entropy of the transition and that, combined with scanning calorimetry to obtain the enthalpy of the phase transition, would allow us to compare the contribution of both entropic and enthalpic factors to the phase changes. Also, the dependence of the vibrational entropy on chemistry could be determined. From a proper DSC study, the order of the orthorhombic to monoclinic phase transition could be confirmed as well. For an even more complete picture, it would be of value to study the pressure-dependence of the vibrational entropy

of the different (orthorhombic and monoclinic) phases. The latter would require the use of high-pressure inelastic neutron diffraction methods or high-pressure heat capacity experiments.

Valuable thermodynamic information could also be gained about the pressure-amorphized phases using thermochemistry. The determination of the free energies and enthalpies of formation for amorphous ZrW_2O_8, $ZrMo_2O_8$ and $A_2M_3O_{12}$-type compounds would complement our studies of the pressure-induced amorphization, as it would provide insight into the thermodynamics of the amorphization. For amorphous ZrW_2O_8 and $ZrMo_2O_8$, we know that the amorphous phase can be recovered to ambient conditions. The above thermodynamic quantities could be determined using scanning calorimetry and drop solution calorimetry. The use of molten solvents would be necessary as these materials are only partially soluble in common acids or bases. The metastability of most cubic AM_2O_8 phases prohibits any experiment that requires equilibration of the sample at high temperature prior to the experiments. For these reasons, drop solution calorimetry should be the method of choice for these kinds of experiments.

The questions regarding the existence of a crystalline to crystalline phase transition in $ZrMo_2O_8$ before the amorphization, as discussed in Chapter 4, could be addressed by another in-situ high-pressure XRD experiment, this time using a hydrostatic pressure-transmitting medium such as nitrogen gas.

In Chapter 7, we saw that the size of the substituting cations (unit cell size) in the $(M^{III}_{0.5}M^{V}_{0.5})P_2O_7$ compositions is an important controlling factor in the thermal expansion behavior of these materials. Particularly, our results on $Y_{0.5}Nb_{0.5}P_2O_7$ indicated

that by full substitution of Zr(IV) in ZrP_2O_7 by a combination of larger-sized cations, the thermal expansion may be lowered. Samples with bigger 3+ (and maybe 5+) cations such as lanthanide ions could be prepared. The coefficient of thermal expansion could be significantly lowered in those compositions relative to cubic ZrP_2O_7. In addition, differential scanning calorimetric measurements using better instrumentation under controlled conditions as well as careful electron diffraction studies could be helpful in providing a better picture of the level of cation ordering in these materials.

APPENDIX A

STRUCTURAL MODELS USED FOR THE ANALYSIS OF THE STRUCTURE OF $A_2M_3O_{12}$ COMPOUNDS USING DIFFRACTION DATA

For the Rietveld and Le Bail fitting of the x-ray and neutron diffraction data for $Sc_2W_3O_{12}$ (see Tables 3.1, 3.2 and 3.3, respectively), for $Sc_2Mo_3O_{12}$ (see Table 3.8) and for $Al_2W_3O_{12}$ (see Table 3.9) in Chapter 3, two different structural models were used. As starting point for the orthorhombic model for all three compounds, the unit cell parameters and atomic coordinates reported by Abrahams and Bernstein[1] were used. For fitting the data for the monoclinic forms of all three compounds, the structural model of $Sc_2Mo_3O_{12}$ as reported by Evans and Mary[2] was used as starting point. The unit cell parameters and atomic coordinates for both structural models as well as nearest-neighbor interatomic distances and bond angles for the orthorhombic structure are given in this Appendix in a tabulated form.

A.1 Orthorhombic model

Table A.1: Cell parameters for orthorhombic $Sc_2W_3O_{12}$ at 298 K by Abrahams and Bernstein[1] in space group Pnca. All angles are 90^o.

	a	b	c
Lattice constant (Å)	9.596(4)	13.330(3)	9.512(4)

Table A.2: Fractional atomic coordinates for orthorhombic $Sc_2W_3O_{12}$ at 298 K by Abrahams and Bernstein[1] in space group Pnca.

Atom	x	y	z
Sc	0.46643(42)	0.38133(20)	0.25010(28)
W1	0.2500	0.0000	0.47300(8)
W2	0.11657(9)	0.35594(4)	0.39454(6)
O1	0.0921(19)	0.1407(11)	0.0780(11)
O2	0.1186(17)	0.0647(11)	0.3766(13)
O3	0.0086(20)	0.2616(10)	0.3174(20)
O4	0.3338(12)	0.4172(7)	0.0785(9)
O5	0.0790(16)	0.3322(13)	0.3631(17)
O6	0.3017(16)	0.3322(13)	0.3631(17)

Table A.3: Nearest-neighbor interatomic distances in orthorhombic $Sc_2W_3O_{12}$ at 298 K by Abrahams and Bernstein[1] in space group Pnca. Oxygen-oxygen distances greater than 3.4 Å are not listed. All distances are in angstroms.

W1-O2	1.782(15)	Sc-O1	2.053(15)
W1-O4	1.695(9)	Sc-O2	2.026(15)
W2-O1	1.762(11)	Sc-O3	2.051(13)
W2-O3	1.787(15)	Sc-O4	2.124(10)
W2-O5	1.751(16)	Sc-O5	2.103(16)
W2-O6	1.829(16)	Sc-O6	2.020(16)
Sc-W1	3.710(3)	O2-O4	2.777(20)
Sc-W1	3.797(4)	O2-O4	2.786(17)
Sc-W2	3.643(4)	O2-O4	2.830(17)
Sc-W2	3.737(3)	O2-O3	2.885(22)
Sc-W2	3.846(3)	O2-O5	2.920(22)
O1-O6	2.865(24)	O2-O2	3.055(32)
O1-O6	2.890(24)	O3-O5	2.885(23)
O1-O5	2.902(20)	O3-O6	2.907(25)
O1-O3	2.903(21)	O3-O6	2.998(24)
O1-O3	2.913(21)	O3-O4	3.078(19)
O1-O5	2.957(23)	O4-O4	2.731(18)
O1O2	3.026(17)	O4-O5	2.836(19)
O5-O6	2.869(24)	O4-O6	2.951(16)
O5-O6	2.883(25)	O5-O5	3.366(37)

Table A.4: Tetrahedral and octahedral bond angles in orthorhombic $Sc_2W_3O_{12}$ at 298 K by Abrahams and Bernstein[1] in space group Pnca. All angles are in degrees.

O2-W1-O2	118.10(9)	O1-Sc-O6	89.40(6)
O2-W1-O4	106.50(7)	O2-Sc-O3	90.10(7)
O2-W1-O4	109.00(6)	O2-Sc-O4	84.00(5)
O4-W1-O4	107.40(5)	O2-Sc-O5	90.00(7)
O1-W2-O3	110.30(9)	O3-Sc-O4	95.00(6)
O1-W2-O5	111.40(8)	O3-Sc-O6	91.20(8)
O1-W2-O6	107.20(8)	O4-Sc-O5	84.30(6)
O3-W2-O5	109.30(9)	O4-Sc-O6	90.80(5)
O1-W2-O6	112.00(8)	O5-Sc-O6	88.70(8)
O5-W2-O6	106.50(8)	O1-Sc-O4	175.00(5)
O1-Sc-O2	95.80(6)	O2-Sc-O6	174.70(6)
O1-Sc-O3	90.00(7)	O3-Sc-O5	179.20(8)
O1-Sc-O5	90.70(7)		

A.2 Monoclinic model

Table A.5: Unit cell parameters for monoclinic $Sc_2Mo_3O_{12}$ at 50 K by Evans and Mary[2] in space group $P2_1/a$. Angles α and γ are 90^o.

	a (Å)	b (Å)	c (Å)	β (^{o})
Lattice parameter	16.22715(9)	9.58051(6)	18.9208(1)	125.3988(4)

Table A.6: Fractional atomic coordinates for monoclinic $Sc_2Mo_3O_{12}$ at 50 K by Evans and Mary[2] in space group $P2_1/a$.

Atom	x	y	z
Mo1	-0.00572(22)	0.24647(34)	0.48730(17)
O11	-0.0720(7)	0.3827(10)	0.4120(5)
O12	0.0491(6)	0.1391(10)	0.4498(6)
O13	0.0917(7)	0.3157(9)	0.5897(5)
O14	-0.0887)7)	0.1513(9)	0.4979(6)
Mo2	0.35949(22)	0.12616(33)	0.13478(16)
O21	0.4807(7)	0.0879(9)	0.1628(6)
O22	0.3307(8)	0.2982(10)	0.0968(6)
O23	0.2715(7)	0.0076(9)	0.0521(6)
O24	0.3587(7)	0.1080(10)	0.2279(6)
Mo3	0.13997(20)	0.11233(33)	0.25461(15)
O31	0.1215(7)	0.1011(9)	0.3378(6)
O32	0.2304(6)	-0.0089(9)	0.2738(6)
O33	0.0276(7)	0.0750(9)	0.1553(6)
O34	0.1797(7)	0.2793(9)	0.2510(5)
Mo4	0.15002)22)	0.61710(35)	0.38255(16)
O41	0.2478(7)	0.5345(9)	0.4814(5)
O42	0.1616(7)	0.5686(9)	0.2997(6)
O43	0.0298(7)	0.5638(9)	0.3566(6)
O44	0.1623(8)	0.7969(10)	0.3937(6)
Mo5	0.35246(20)	0.62609(31)	0.21615(15)
O51	0.4619(7)	0.5742(9)	0.3121(5)
O52	0.3618(7)	0.5992(10)	0.1292(6)
O53	0.2481(7)	0.5308(10)	0.1972(6)
O54	0.3380(7)	0.8050(10)	0.2246(5)
Mo6	0.00274(22)	0.74472(34)	0.010909(17)
O61	0.0509(7)	0.6568(9)	0.1156(6)
O62	0.1044(7)	0.8120(10)	0.0189(6)
O63	-0.0684(7)	0.6304(9)	-0.0700(6)
O64	-0.0741(6)	0.8846(10)	0.0099(6)
Sc1	0.3789(5)	0.9675(7)	0.31727(39)
Sc2	0.3718(4)	0.4590)6)	0.04934(35)
Sc3	0.1201(5)	0.4694(7)	0.18618(39)
Sc4	0.1090(4)	0.9779(7)	0.42039(33)

A.3 References

[1] S. C. Abrahams and J. L. Bernstein: Crystal Structure of the Transition-Metal Molybdates and Tungstates. II. Diamagnetic $Sc_2(WO_4)_3$. *J. Chem. Phys.* **45**, 2745 (1966).

[2] J. S. O. Evans and T. A. Mary: Structural phase transitions and negative thermal expansion in $Sc_2(MoO_4)_3$. *Int. J. Inorg. Mater.* **2**, 143 (2000).

VITA

Tamás Varga was born on July 13, 1972 in Debrecen, Hungary to Zoltán Varga and Zoltánné Varga. He graduated with a M.S. in Chemistry from the University of Debrecen, Debrecen, Hungary in 1995. His minor was English-Hungarian Special Translation. After five years of working for two different industrial companies in Hungary and earning his second diploma (M.S. in Economics, University of Miskolc, Miskolc, Hungary) he took a graduate assistantship offered by the School of Chemistry and Biochemistry at the Georgia Institute of Technology, Atlanta, Georgia to earn his Ph.D. His Ph.D. thesis work was directed by Dr. Angus P. Wilkinson. He graduated with a Ph.D. in Chemistry in 2005.